Investigating the electrical conductivity structure of the San Andreas fault system in the Parkfield-Cholame region, central California, with 3D magnetotelluric inversion

Kristina Tietze

Dissertation

zur Erlangung des akademischen Grades
doctor rerum naturalium (Dr. rer. nat.)
im Fachbereich Geowissenschaften
der Freien Universität Berlin

Berlin, November 2012

Gutachter:

PD Dr. Oliver Ritter (1. Gutachter)
Freie Universität Berlin, Deutsches GeoForschungsZentrum Potsdam

Jun. Prof. Dr. Michael Becken (2. Gutachter)
Westfälische Wilhelms-Universität Münster

Tag der Disputation: 13.11.2012

Abstract

This thesis presents the application of 3D MT inversion to an array data set of more than 250 sites from central California to image the electrical conductivity structure of the San Andreas fault (SAF) system in the Parkfield-Cholame region where the fault changes its mechanical state. Previous extensive two-dimensional (2D) inversion revealed a high-conductivity region in the upper mantle and lower crust, which has a connection to the SAF in the northern, transitional-to-creeping section, whereas it is confined to lower-crustal to upper-mantle levels in the transitional-to-locked section. The highly conductive region and the connecting channel were interpreted as migration path for fluids rising from mantle depth into the SAF system where they are considered to contribute to the low-frictional strength of the creeping fault segment. The new 3D inversion results confirm the high-conductive zones of the 2D results and strongly support the presence of a fluid channel into the SAF system in the creeping segment. However, conductivity structures obtained with 3D inversion also showed a great non-uniqueness depending on the inversion setup. Satisfying models (in terms of data fit) could only be recovered if the inversion parameters were tuned in accordance with the particularities of the data set.

Based on the Parkfield MT data and complementary synthetic 3D data sets, the model space was explored by testing the influences of a wide range of inversion settings. The results show that in presence of a pronounced regional 2D structure, 3D inversion of the complete impedance tensor still depends on the coordinate system. 2D subsurface structures can vanish if data are not aligned with the regional strike-direction. A priori models and data weighting, i.e. how strongly individual components of the impedance tensor and/or vertical magnetic field transfer functions dominate the solution, are crucial controls for the outcome of 3D inversion. If deviations from a prior model are heavily penalized, regularization is prone to result in erroneous and misleading 3D inversion models, particularly in the presence of strong conductivity contrasts. Reliable and meaningful 3D inversion models can only be recovered if data misfit is assessed systematically in the frequency-space domain.

Galvanic distortion can impair 3D inversion models and result in spurious structures at depth. A new tool for automatic identification of static shift was developed and applied to synthetic and real world data, making use of the spatial coherence of MT responses. For the Parkfield data set, identification and removal of static shift improved the outcome of subsequent 3D inversion for the near-surface layers. Inversion of phase tensor and apparent resistivity & phase data was implemented into the 3D inversion scheme and proved to be a valuable asset for obtaining reliable subsurface images from galvanically distorted data, while not requiring any data preprocessing.

Kurzfassung

In der vorliegenden Arbeit ist die Anwendung eines dreidimensionalen (3D) magnetotellurischen (MT) Inversionsschemas auf einen Array-Datensatz von mehr als 250 Stationen aus Zentralkalifornien (USA) dargestellt. Die Untersuchungen hatten zum Ziel, die elektrische Leitfähigkeitsstruktur der San Andreas-Verwerfung (SAF) in der Region zwischen Parkfield und Cholame, in der sich das mechanische Verhalten der Verwerfung ändert, abzubilden. Vorangegangene zweidimensionale (2D) Inversionen des Datensatzes zeigten eine Region hoher elektrischer Leitfähigkeit im Tiefenbereich des oberen Mantel und der unteren Kruste, die im nördlichen Teil des Messgebiets hin zum kriechenden Segment mit der seismogenen SAF verbunden ist. Im Übergang zum blockierten Verwerfungsabschnitt Richtung Süden ist diese leitfähige Region in der Tiefe dagegen von der oberkrustalen Deformationszone abgeschnitten. Die Bereiche erhöhter Leitfähigkeit und die kanalartige Verbindung im Norden wurden als Migrationspfade für Fluide interpretiert, die aus dem Mantel in das SAF System aufsteigen. Es wird vermutet, dass Fluide wesentlich zur mechanischen Schwäche der SAF im kriechenden Segment beitragen. Die neuen, 3D Inversionsergebnisse bestätigen die elektrisch leitfähige Zone aus den 2D Modellen und unterstützen die Existenz eines Fluidkanals in das SAF-System im kriechenden Abschnitt. Jedoch zeigten die 3D Leitfähigkeitsmodelle starke Variationen der abgebildeten Strukturen, die mit der Wahl der Inversionsparameter zusammenhingen. Zufriedenstellende Modelle (im Sinne der Datenanpassung) konnten nur ermittelt werden, wenn die Inversionsparameter auf die Besonderheiten des Datensatzes abgestimmt waren.

Basierend auf den MT-Daten aus Kalifornien sowie komplementären synthetischen 3D Datensätzen wurde der Einfluss der Inversionsparameter auf den Modellraum untersucht. Die Ergebnisse zeigen, dass die 3D Inversion in Gegenwart einer ausgeprägten, regionalen 2D Struktur von der Orientierung des Koordinatensystems abhängt, auch wenn alle vier Komponenten des Impedanztensors in der Inversion verwendet werden. 2D Untergrundstrukturen können gänzlich verschwinden, wenn das Koordinatensystem nicht an der regionalen geoelektrischen Streichrichtung ausgerichtet ist. A priori-Modelle und Datengewichtung, welche bestimmt, wie stark einzelne Komponenten des Impedanztensors und der vertikalen magnetischen Übertragungsfunktionen die Lösung dominieren, sind wichtige Steuerungselemente für das 3D Inversionsergebnis. Werden Abweichungen von einem a priori-Modell stark regularisiert, führt dies leicht zu verfälschten und irreführenden 3D Inversionsergebnissen, insbesondere wenn starke Leitfähigkeitskontraste im Untergrund vorhanden sind. Verlässliche und aussagekräftige Modelle können nur ermittelt werden, wenn eine systematische Auswertung der Datenanpassung im Frequenz-Orts-Bereich vorgenommen wird.

Galvanische Verzerrung von MT-Daten kann die Qualität von 3D Inversionsmodellen beeinträchtigen und zum Aufreten artifizieller Strukturen bis in große Tiefe führen. Zur Identifizierung von Static Shift wurde ein neues Schema entwickelt, das auf der räumlichen Kohärenz

von MT-Daten basiert, und sowohl auf synthetische als auch auf Messdaten angewendet. Für den Kalifornien-Datensatz verbesserte die Entfernung von Static Shift die nachfolgenden 3D Inversionsergebnisse. Die Inversionen von Phasentensoren und scheinbaren Widerständen & Phasen, die in das 3D Inversionspaket implementiert wurden, sind ein wertvoller Gewinn für die verlässliche Abbildung von Untergrundsstrukturen, ohne dafür verzerrte Daten vorbehandeln zu müssen.

Acknowledgements

This work would not have been possible without the support of the kind people around me, to only some of whom it is possible to give particular mention here.

First and foremost, I am grateful to my PhD advisor PD Dr. Oliver Ritter, who patiently provided the vision, encouragement and advice necessary for me to proceed through the dissertation project and complete my thesis. He has been a strong and supportive advisor to me, while giving me great freedom to pursue independent work. I am thankful for the opportunities he provided me to discuss my work at international conferences and during visits to colleagues in the U.S. and to participate in several MT field campaigns all over the world.

Dr. Naser Meqbel introduced me to the world of 3D MT inversion and the implementation of ModEM. I am deeply indebted to him for innumerable discussions over the past years, in which he greatly increased my understanding of 3D MT inversion and helped to clarify ideas finally presented in this thesis.

I am thankful to Dr. Ute Weckmann for a number of stimulating suggestions on tackling static shift and exchange on experience with 3D MT inversion. I would also like to acknowledge her introduction to 2D MT inversion while supervising my previous work on MT data from South Africa.

I owe sincere gratitude to Dr. Michael Becken for his achievements at all stages of the California MT projects from data acquisition to 2D interpretation of the result. Since handing over the projects, he has been continuously following up on the 3D results and available to discuss the 2D results. He has also assumed the task to review my thesis as an external reviewer.

During my PhD time, I had the opportunity to visit Prof. Gary Egbert and his working group at Oregon State University, Corvallis, USA. I gratefully acknowledge his introduction to fundamental principles of the ModEM software package as well as valuable discussions on general aspects of 3D MT inversion and of results from California. In this respect, I would also like to thank Dr. Anna Kelbert for sharing here experiences with ModEM3DMT inversion during my time in Corvallis. Moreover, Prof. Egbert kindly made ModEM available to the Geo-Electromagnetics working group for several years before it went into public domain recently.

I would like to express my sincere thanks to Prof. Steve Constable and Brent Wheelock at Scripps Institution of Oceanography, La Jolla CA, USA. We openly exchanged on results from marine (Scripps) and on-land (GFZ) MT data from the San Andreas fault during my visit to

Scripps, conferences, and Prof. Constable's visits to Potsdam. Discussions with them provided valuable insights into marine electromagnetic methods. I thank Dr. Karen Weitemeyer for her hospitality during my visit to Scripps.

I would like to express my thanks to Dr. Gerard Muñoz for explaining theoretical backgrounds of MT which increased my understanding of the method. Warmest thanks go to Dirk Brändlein with whom I enjoyed sharing the office and even more a great many conversations on geophysics and beyond. I remember good advice on data visualization and two fantastic field trips to "his" observatory sites in the Atacama desert.

I would like to thank all my present and former colleagues in the Geo-Electromagnetics working group at GFZ for creating such an inspiring and friendly working atmosphere both in the office and in the field. In particular, I would like to acknowledge those who provided helpful feedback on earlier versions of this thesis.

I would like to thank the MT working group (MT-AG) consisting of the Geo-Electromagnetics working groups of Free University Berlin (Dr. Heinrich Brasse) and GFZ Potsdam for the many opportunities to present and discuss aspects of my work in our MT-AG meetings.

Finally, I would like to express my gratitude to all people from Germany and the U.S. (Scripps, USGS) who helped to collect the MT data in California during the field campaigns in 2005, 2007, and 2008, while enduring weeks of rain (2008) and fighting the impacts of cows and ground squirrels on the equipment. Funding for the field campaigns came from the Deutsche Forschungsgemeinschaft (DFG) and the German Research Centre for Geosciences Potsdam (GFZ). The instruments for the experiments were provided by the Geophysical Instrument Pool Potsdam (GIPP).

Contents

Abstract iii

Acknowledgements vii

List of Figures xi

List of Tables xiii

Introduction xv

1 Electromagnetic fields in magnetotellurics 1
- 1.1 From Maxwell's equations to the diffusion equation . . . 1
- 1.2 The transfer functions . . . 3
- 1.3 Galvanic distortion . . . 5

2 Magnetotelluric study of the San Andreas fault 11
- 2.1 Geology of California . . . 14
  - 2.1.1 Major geologic units in Central California . . . 14
  - 2.1.2 Tectonic evolution of the San Andreas fault system . . . 16
  - 2.1.3 Locked and creeping segments of the San Andreas fault . . . 20
  - 2.1.4 Non-volcanic tremors observed in the San Andreas fault system . . . 22
- 2.2 Magnetotelluric data set . . . 23
  - 2.2.1 Field setup and data processing . . . 24
  - 2.2.2 2D data analysis and interpretation . . . 24

3 3D inversion and forward modelling 27
- 3.1 Data properties of the California MT array . . . 30
- 3.2 ModEM3DMT . . . 35
  - 3.2.1 Implementation of phase tensor and apparent resistivity & phase inversion 38
  - 3.2.2 3D ObliqueOne test model . . . 42
  - 3.2.3 Inversion of phase tensors . . . 43
  - 3.2.4 Inversion of apparent resistivities and phases . . . 48
- 3.3 Setting up 3D inversion for the California MT array data set . . . 54
- 3.4 3D inversion tests with a synthetic data set . . . 59
  - 3.4.1 The SYNPRK 3D model . . . 59
  - 3.4.2 Orientation of the coordinate system . . . 59
  - 3.4.3 Model regularization . . . 67
  - 3.4.4 Site distribution . . . 71
  - 3.4.5 Setup of data-weighting for single and joint data type inversion . . . 73

3.5 Inversion of the California MT array data . . . 75
3.5.1 Inversion of single components . . . 76
3.5.2 Influence of regional structures on VTF responses . . . 78
3.5.3 Further single and joint inversion results . . . 81
3.5.4 Resolution studies . . . 88
3.5.5 Preferred 3D model . . . 94
3.6 Comparison of 3D and 2D results . . . 96
3.7 Discussion . . . 100

4 Modelling static shift in magnetotellurics 105
4.1 Substitute structures for static shift . . . 109
4.1.1 2D modelling . . . 110
4.1.2 3D modelling . . . 114
4.2 AIDE – Automatized identification and estimation of static shift . . . 118
4.3 Using spatial coherence of data to correct for static shift . . . 121
4.3.1 Testing AIDE parameters and influence of statistical properties of static shift values . . . 122
4.3.2 2D subsurface structure . . . 126
4.3.3 3D subsurface structure . . . 130
4.4 Application to the California MT array . . . 133
4.5 Discussion . . . 139

5 Summary 141

Bibliography 145

List of Figures

1 Electrical resistivity sections across the central San Andreas fault near Parkfield obtained from 2D MT inversion xviii

1.1 Graphical representation of phase tensors 5
1.2 Galvanic effect of subsurface inhomogeneity 7

2.1 The San Andreas fault in California 12
2.2 Distribution of principal basement rocks in California 15
2.3 Tectonic evolution of the San Andreas fault 17
2.4 Schematic illustration of Monterey microplate capture in central California . . 18
2.5 Schematic evolution of the California continental margin 19
2.6 Locations of MT sites at the San Andreas fault near Parkfield 23
2.7 Electrical resistivity sections across the central San Andreas fault near Parkfield obtained from 2D MT inversion 25
2.8 High resolution MT resistivity model from 2D inversion near the SAFOD . . . 26

3.1 Distribution of more than 250 MT sites in the vicinity of Parkfield and Cholame 29
3.2 Phase tensor properties of the California data set 31
3.3 Ratios of impedance tensor elements (real parts) 32
3.4 Vertical magnetic transfer functions 33
3.5 Period range of the California MT array 169-site data set in 3D inversion . . . 34
3.6 Schematic overview of the Modular Electromagnetic Inversion (ModEM) system 38
3.7 ObliqueOne 3D model and data set 42
3.8 Convergence behaviour of 3D inversion for different prior models 44
3.9 Comparison of ObliqueOne PT data and final inversion responses for inversion runs with different prior models 45
3.10 Resistivity models obtained from inversion of phase tensors (ObliqueOne data) 47
3.11 Influence of vertical smoothing on the outcome of PT inversion 48
3.12 Resistivity models obtained from inversion of apparent resistivities & phases (RP) of the ObliqueOne data set 50
3.13 Statistical distribution of synthetic distortion parameters c_{xx} and c_{yy} 51
3.14 3D resistivity models obtained from inversion of synthetically distorted ObliqueOne data 53
3.15 Comparison of data and inversion model responses obtained for the shifted ObliqueOne data set 55
3.16 Resistivity image of the Parkfield region revealed by joint and individual inversion of impedance and VTF data for two inversion coordinate setups 56
3.17 Comparison of observed data and responses of impedance-only inversion results obtained in the geographic and strike-aligned coordinate system 58

3.18 SYNPRK model 60
3.19 Resistivity distribution recovered by four component impedance inversion of the SYNPRK data set in different coordinate systems 61
3.20 Influence of the HCZ of the SYNPRK model on impedance and VTF components in dependence of the orientation of the coordinate system 63
3.21 Responses of SYNPRK, SYNPRK-h, and a resistivity inversion model obtained from SYNPRK data in the north-east coordinate system 64
3.22 3D inversion of VTF and PT data of the SYNPRK data set 65
3.23 Influence of HCZ on phase tensor data 67
3.24 3D inversion results of SYNPRK data set for various setups of model regularization 69
3.25 Systematic analysis of data misfits of SYNPRK inversion results in the frequency-space domain 71
3.26 3D resistivity models obtained from inversion of SYNPRK data sets using different site distributions 72
3.27 Influence of data-weighting on 3D inversion results of the SYNPRK data set . . 74
3.28 3D resistivity models from separate inversion of each off-diagonal impedances and vertical magnetic transfer functions 77
3.29 Ocean and sediments of the San Joaquin valley dominate VTF behaviour across strike 78
3.30 Influence of the Pacific Ocean on VTF responses 79
3.31 Simulation of lateral variations of surface conductors based on topography. . . 80
3.32 Influence of conductive sedimentary overburden on long-period VTF data of the California MT array 82
3.33 3D resistivity models obtained from California MT data with two site layouts . 84
3.34 Comparison of near-surface structure along profile 2 of various inversion models 86
3.35 3D resistivity structures obtained from inversion of the California data using 2D inversion models as a priori information 87
3.36 Illustration of 3D forward modelling tests investigating the along-strike extent of the HCZ 89
3.37 Conductive path between HCZ and SAF? 90
3.38 Resistivity models obtained from 3D and 2D inversion results of SYNPRK-path data sets 92
3.39 Preferred 3D inversion model of the California data set (PRK-3D) and data misfits 95
3.40 Comparison of PRK-3D and 2D resistivity models along profiles 2 and 6 97
3.41 Comparison of PRK-3D and 2D model responses at sites along profiles 2 and 6 99

4.1 Effect of static shift on 2D MT inversion. 108
4.2 1D layered half-space model 110
4.3 Conceptional conductive 2D substitute structures for galvanic scatterers and FWD responses 111
4.4 Conceptional resistive 2D substitute structures for galvanic scatterers and FWD responses 112
4.5 Horizontal slice through 3D ObliqueOne model at 2.56 km depth illustrating the main structural features 115
4.6 Effect of 3D box-shaped near-surface anomalies on MT responses above a 3D subsurface structure 116

4.7 Influence of complex shaped 3D inhomogeneities on 3D ObliqueOne responses . 117
4.8 Identification and estimation of static shift with the AIDE scheme 119
4.9 Distribution of synthetic static shift values. 123
4.10 AIDE-N shift value estimates for 1D LH data compromised with three different sets of randomly distributed static shift 124
4.11 Comparison of distributions of original shift values and AIDE-N estimates for the LH data set 125
4.12 AIDE-N shift estimates for synthetically shifted TE and TM data of the 2D BBL model 127
4.13 $\Delta_{ij}(\omega_k)$-estimate distributions for three sites of the 2D BBL data set 129
4.14 Cumulated shift estimates for iterative application of AIDE-N method to the BBL data set 130
4.15 Main structural features of ObliqueOne model and distribution of reference sites 131
4.16 Application of AIDE-N method to the shifted 3D ObliqueOne data set 132
4.17 Distribution of reference sites and AIDE-N shift estimates for the California MT array data set 135
4.18 Comparison of 3D inversion results for 169-site California data set obtained with original and shift-corrected data 136
4.19 Original and shift-corrected data of the California data set and corresponding inversion responses 138

List of Tables

4.1 Overview of AIDE parameters 121

Introduction

The San Andreas fault (SAF) is one of the major transform faults in the world. It passes 1,100 km through nearly the entire length of the state of California, USA, and forms the tectonic boundary at which the North American and Pacific plates move past each other. The fault is infamous for having been the origin of a series of disastrous earthquakes; most noteworthy are the great San Francisco earthquake of 1906 (M 7.8), Fort Tejon 1857 (M 7.9), and Loma Prieta 1989 (M 6.9). Within the last 150 years, more than 30 major earthquakes with magnitudes above M 6.0 ruptured large segments of the SAF (Toppozada et al., 2002), making California one of the most earthquake-prone regions on earth.

The 175 km long segment between San Juan Bautista and Cholame in central California stands out from the entire SAF system, in that here slip is released through a combination of continuous aseismic creep and small-magnitude earthquakes (Bakun & Lindh, 1985; Thatcher, 1990). Recently, tectonic non-volcanic tremors (NVT) were discovered in this area below seismogenic depths (Nadeau & Dolenc, 2005). NVT events primarily cluster at the transition between the locked and creeping sections of the SAF near Cholame (Nadeau & Guilhem, 2009; Zhang et al., 2010). In addition, characteristic, M ∼6 earthquakes have been observed recurring on average every 22 years since 1857 (Bakun & McEvilly, 1984) towards the segment's southeastern end near Parkfield.

Consequently, the SAF has been subject of a great amount of geoscientific studies which aimed to unravel the physical, chemical and tectonic processes controlling the mechanical state of the SAF system. An outstanding research initiative of the last decades is the San Andreas Fault Observatory at Depth (SAFOD) near Parkfield, central California. For the first time, a borehole pierced an active fault and finished up in a source zone of repeating M ∼2 earthquakes to study directly the processes governing faulting and earthquake generation (Hickman et al., 2004; Zoback et al., 2011). Though the SAF is the best studied fault zone in the world, fundamental properties of the fault system such as fault strength, fault geometry at deeper levels, and NVT source mechanisms remain elusive. Yet a key component in most models explaining fault creep and NVTs is the presence of a significant amount of fluids within the fault system (e.g. Irwin & Barnes, 1975; Kennedy et al., 1997; Fulton & Saffer, 2009).

Presence of a fluid phase within rocks lowers their strength by a variety of processes. One of the most important factors is the pore-fluid pressure, because it controls the effective normal stress (e.g. Hubbert & Rubey, 1959). Increasing pore-fluid pressure will lower the rock

strength mechanically and promote brittle failure at low stress levels, in particular if porosity is interconnected (Bürgmann & Dresen, 2008). In addition, fluids can react with the host rock to produce weak mineral phases and reduce fault strength chemically (Scholz, 2002). For the SAF system both mechanical and chemical weakening mechanisms related to fluids have been proposed and are subject of ongoing research.

Models explaining fault creep in the SAF system with the presence of high pore-fluid pressures within the upper-crustal deformation zone call on different fluid sources and permeability patterns within and around the fault system. Rice (1992) suggested that the shear zone acts as low-permeable conduit for fluids infiltrating the seismogenic fault from deep crustal or mantle depths at superhydrostatic pressures. Such fluids may be mantle volatiles (Kennedy et al., 1997; Pili et al., 2010) or products of metamorphic processes (Pili et al., 2010) such as dehydration of a serpentinized mantle wedge (Fulton & Saffer, 2009). Alternatively, metamorphic fluids released in the upper crust and kept below a low-permeable layer may flow laterally towards the relatively permeable fault gouge and enter the fault system in response to rupture (Irwin & Barnes, 1975). In the model of Byerlee (1990) fluids originating from the crustal host rock penetrate the fault zone, where they become trapped by mineral reactions. High fluid pressure is re-established by compressive tectonic forces and successive compaction of the sealed fault zone materials. In this case, the fault would act as a barrier for both horizontal and vertical fluid flow.

The concept of Rice (1992) is supported by isotope ratios observed for noble gas, carbon, and oxygen isotopes, which can only be explained with influx of fluids such as water and CO_2 from mantle depths (Kennedy et al., 1997; Pili et al., 2010) and low transverse permeability of the fault (Wiersberg & Erzinger, 2007, 2011). Wiersberg & Erzinger (2007) point out that limited permeability occurs parallel to the fault direction, but the majority of fluids probably rise up through other more permeable faults of the SAF system. High pore-fluid pressures were observed in country rocks northeast of the central SAF (e.g. Yerkes et al., 1985; Johnson & McEvilly, 1995); in the SAFOD drillhole, however, pore-fluid pressures did not reach lithostatic levels (Zoback et al., 2011). Lithological (Zoback, 2006) and geochemical (Wiersberg & Erzinger, 2007, 2008) observations suggest that the SAF at SAFOD is an impermeable barrier for both horizontal and vertical fluid flow. Hence, Zoback et al. (2011) argue that high pressures are not the primary cause for the apparent weakness of the fault. Yet observations at the depth and location where the drillhole intersects the SAF may not be representative for the deeper parts of the fault zone.

Evidence for chemical weakening and mineral trapping of water was provided by findings of hydrous clay coatings such as talc (Moore & Rymer, 2007) and smectite (Schleicher et al., 2010) in rock samples from the deformation zone at SAFOD. Mechanical simulations of Moore & Rymer (2007), however, suggest that the bare presence of talc cannot fully account for the extremely low frictional strength of the creeping SAF segment.

The source mechanism of NVT is poorly understood. Correlation in space and time of episodes of NVT with local earthquakes (Nadeau & Guilhem, 2009), teleseismic events (Ghosh et al., 2009; Peng et al., 2009), and tides (Thomas et al., 2009) suggest that NVT occur in response to stress field perturbations in the deep SAF fault system. Various authors suggest the presence of high-pore fluid pressures at NVT source depth which would make segments of the deep fault extremely weak and enable deep fault shear failure at low stress levels (e.g. Nadeau & Guilhem, 2009; Shelly, 2010). Pore-fluid overpressure at these depth was suggested to result from ongoing fluid supply from deeper regions, e.g. mantle volatiles or dehydration of a serpentinized mantle wedge (Nadeau & Guilhem, 2009; Shelly, 2010) and fluids may be trapped below an impermeable layer (Becken et al., 2011).

Distribution of fluids on a regional scale and implications on pore pressure levels and fluid pathways are often inferred from geophysical surveys (e.g. Johnson & McEvilly, 1995; Zhao et al., 1996; Becken et al., 2011). Imaging of the electrical conductivity structure is particularly useful in this respect. Fluid phases usually have significantly higher electrical conductivity than the rock matrix and bulk electrical conductivity of rocks is dominated by interconnected fluid networks (Guéguen & Palciauskas, 1994). Fluid conductivity depends on its temperature and composition. Hence, regional scale images of the electrical conductivity structure can be used to constrain the volume of available fluids and the permeability of the host rock. The magnetotelluric (MT) method which is based on electromagnetic induction in the Earth is the only method capable of imaging the electrical conductivity structure between shallow crust and upper mantle depths. Thus MT may be one of the best means to image fluid networks over wide regions directly and to yield information on the deep hydraulic system. Overviews of relations between electrical conductivity images obtained from MT data, distribution of fluids, and rock deformation and how these can be used for inferences on tectonic processes are given among others in Jiracek et al. (2007) and Unsworth (2010).

Along the SAF, various MT studies revealed zones of high electrical conductivity at upper-crustal depths which were associated with fluids and could be related to tectonic processes (see review of Becken & Ritter, 2012, and references therein).

This work is based on MT data collected in the transitional region of the SAF between Parkfield and Cholame, where the fault's mechanical state changes from creeping to being locked. Between 2005 and 2008, the Geo-Electromagnetics working group of GFZ Potsdam deployed more than 250 MT sites along seven parallel profiles across the SAF system, covering an area of 130 km $\times$ 60 km across and along strike, respectively. These regional scale surveys aimed to investigate deep structural "along-strike" variations of the transitional segment of the SAF and to probe for the first time with MT the source region of NVT. Two-dimensional (2D) inversion of the MT data by Becken et al. (2011) revealed a highly conductive region in the upper mantle and lower crust, which is linked to the upper-crustal, brittle deformation zone of the SAF along the three northern profiles across the transitional-to-creeping segment

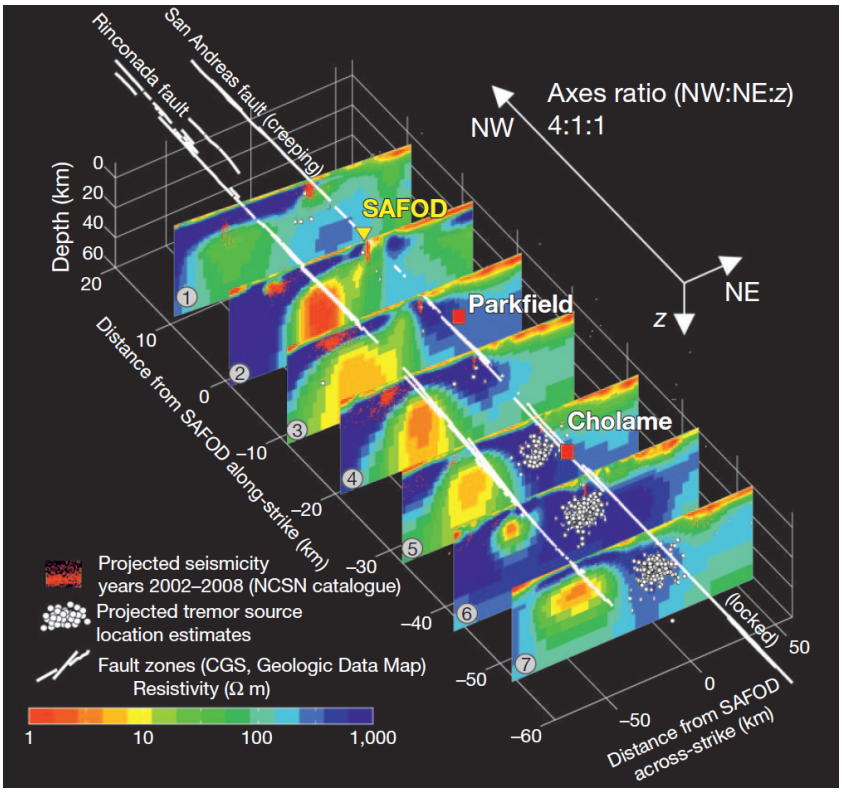

Figure 1: Electrical resistivity sections across the central San Andreas fault obtained from 2D inversion. The high conductivity (red and yellow colours) in the lower crust and upper mantle (20 - 40 km) was attributed to hot saline fluids, which can rise into the creeping SAF near SAFOD. Near the locked segment, fluids seem to be trapped adjacent to the main tremor zone (white dots, Zhang et al., 2010) and to be prevented from escaping into the upper crustal portion of the SAF. The along-strike variation of the 2D models indicates underlying 3D structure. Figure taken from Becken et al. (2011).

by a narrow, subvertical high-conductive feature (profiles ① - ③ in Fig. 1). This subvertical conductive channel is interpreted as a zone where fluids can migrate into the SAF system (Becken et al., 2011). Interestingly, the crustal fluid channel is absent at the transitional-to-locked segment of the SAF (profiles ⑤ - ⑦ in Fig. 1). The three southern profiles consistently show that the mantle conductor is separated from the seismogenic SAF by a deep-reaching resistive zone. In this area, NVT occur (white circles in Fig. 1) and are thought to be related to overpressured fluids (e.g. Nadeau & Guilhem, 2009; Shelly, 2010). Becken et al. (2011) speculate that fluids may be trapped beneath an impermeable layer and NVT events are caused by episodic release of fluids into the surrounding units.

Although the predominant geo-electrical strike direction of the data coincides with the orientation of the SAF, significant along-strike variations inferred from the 2D conductivity models clearly indicate underlying 3D structures. For 2D inversion, however, data components containing information on 3D structures have to be discarded as only three of the six magnetotelluric

data components (impedances and vertical magnetic transfer functions) can be used and additionally 3D effects in the remaining components had to be downweighted (Becken et al., 2011). The main aim of this work is to derive a coherent 3D image of the electrical conductivity structure in the Parkfield-Cholame area using the full information contained in the data set. Therefore, a 3D MT inversion scheme (ModEM3DMT, Egbert & Kelbert, 2012) is applied to the Parkfield MT array data set and all six MT components are used.

For surveys such as in California the great amount of data and the dimensions of the area require huge models and enormous computational resources, when attempting full 3D MT inversion. Today, many of the controlling factors for the outcome of 3D inversion of real-world data are little explored.

A key focus of this work is the assessment and development of strategies for application of 3D inversion to real world data sets. Based on the Parkfield array data and a complementary synthetic data set, the inversion process is examined with respect to model and data setup. In particular, the influences of inversion coordinate system, model regularization (trade-off between fitting details of the data and keeping structures coherent), and background conductivity structure including integration of a priori information are tested. Investigation of data parameters includes the contribution of individual data components to the resolution of subsurface structures as well as of the setup of data weighting (error bounds) in general and within a particular data set.

In this context, inversion of two alternative representations of the magnetotelluric impedance – the phase tensor (Caldwell et al., 2004) and apparent resistivity & phase – are implemented into ModEM3DMT and used for the first time in 3D. Inversion of these data has advantages if MT impedance data are affected by galvanic distortion due to small-scale near-surface inhomogeneities. The phase tensor is derived from the observed impedance, but it is independent of galvanic distortion. Its invariants provide distortion-free information about the dimensionality of the underlying conductivity structure, which can be obtained directly from the observed distorted data. However, the dimensionless phase tensor components describe only variations of the conductivity structure. Thus, when inverting these data, particular care has to be taken of the conductivity structure in the a priori model, which provides the reference when transferring the information from phase tensors into absolute conductivity values. In situations, where galvanic distortion is expressed as static shift, only the amplitude of MT impedances (apparent resistivities) are affected, the phase relation is preserved. Inversion of apparent resistivity & phase data using higher weight on the undistorted phases allows to reduce the influence of static shift on the inversion, while maintaining some of the information about the absolute subsurface conductivity contained in the apparent resistivity data. The latter has proven successful in 2D inversion (e.g. Becken et al., 2008b; Ritter et al., 2003; Tauber et al., 2003).

Though galvanic distortion has long been recognized an obstacle for MT interpretation and been subject of research, it has experienced little attention in 3D MT inversion so far. Some

workers argue that static shift does not have to be considered in 3D inversion as 3D near-surface inhomogeneities can be integrated into the model by the inversion scheme (e.g. Farquharson & Craven, 2009; Newman et al., 2008; Xiao et al., 2010). However, discretization of the subsurface with sufficiently fine detail which allows for modelling of such small-scale heterogeneities is often impractical in 3D as the number of model parameters very rapidly exceeds manageable sizes. Effective strategies for handling galvanically distorted MT data have been developed mainly for 2D inversion (deGroot-Hedlin, 1991; Ogawa & Uchida, 1996). Preliminary results for 3D joint inversion for subsurface conductivity and galvanic distortion parameters were presented by Avdeeva et al. (2012).

Alternatively, a second group of methods aims at removing galvanic distortion from the measured data prior to inversion to improve the resolution of absolute conductivities of the subsurface structure. However, the problem of distortion is non-unique. Approaches for distortion removal often represent partial remedies only (e.g. Groom & Bailey, 1989; Bahr, 1991; McNeice & Jones, 2001; Becken & Burkhardt, 2004; Bibby et al., 2005) and/or are based on assumptions, e.g concerning the conductivity structure of the subsurface (Bahr, 1991; Groom & Bailey, 1989; Jones, 1988), or additional information on near-surface conductivities obtained with other geophysical methods (e.g. Sternberg et al., 1988; Torres-Verdín & Bostick, 1992). This work presents a newly developed approach which identifies and estimates static shift-type galvanic distortion based on spatial coherency of data. The scheme is tested with synthetic data and used for removal of static shift from the California MT array data set.

1 Electromagnetic fields in magnetotellurics

Magnetotellurics (MT) is an electromagnetic method to image the electrical conductivity structure of the subsurface, which uses natural variations of the electric and magnetic fields measured at the Earth's surface. The method was introduced in the 1950s by Cagniard (1953) and Tikhonov (1950) and is based on the physical principle of electromagnetic induction.

1.1 From Maxwell's equations to the diffusion equation

The behaviour of electromagnetic fields is described by Maxwell's equations:

$$\nabla \times \mathbf{E} = -\dot{\mathbf{B}} \tag{1.1}$$

$$\nabla \times \mathbf{H} = \dot{\mathbf{D}} + \mathbf{j} \tag{1.2}$$

$$\nabla \cdot \mathbf{D} = \bar{\rho} \tag{1.3}$$

$$\nabla \cdot \mathbf{H} = 0, \tag{1.4}$$

where $\mathbf{E}$ is the electric field, $\mathbf{B}$ the magnetic flux density, $\mathbf{H}$ the magnetic field, $\mathbf{D}$ the electric displacement field, $\mathbf{j}$ the current density, and $\bar{\rho}$ the charge density.

In addition, the quantities are linked by the constitutive relations

$$\mathbf{D} = \epsilon_0 \epsilon_r \mathbf{E} = \epsilon \mathbf{E} \tag{1.5}$$

$$\mathbf{B} = \mu_0 \mu_r \mathbf{H} = \mu \mathbf{H} \tag{1.6}$$

and Ohm's law for homogeneous isotropic media

$$\mathbf{j} = \sigma \mathbf{E}. \tag{1.7}$$

where ϵ_0 is the permittivity of the free space, ϵ_r the relative permittivity, μ_0 the permeability of the free space, ϵ_r the relative permeability, and σ the electrical conductivity.

For the investigation of the Earth with MT, following simplifying assumptions can be made:

- The electromagnetic sources lie outside the investigated medium, i.e. the Earth: $\bar{\rho} = 0$.
- Within the Earth, relative permeability and permittivity can be considered as frequency-independent, scalar quantities $\mu_r \approx 1$ and $\epsilon_r < 80$ and will be neglected in the following: $\mu = \mu_0$ and $\epsilon = \epsilon_0$.

With these constraints, Maxwell's equations can be transformed as follows: Multiplying the first equation (1.1) with $\nabla\times$ and eliminating $\mathbf{B}$ using (1.6) and subsequently (1.2) yields a second order differential equation for the electric field:

$$\nabla \times (\nabla \times \mathbf{E}) = -\nabla \times \dot{\mathbf{B}} = -\mu_0(\dot{\mathbf{j}} + \ddot{\mathbf{D}}). \tag{1.8}$$

This equation can be rewritten as

$$\nabla(\nabla \cdot \mathbf{E}) - \Delta\mathbf{E} = -\mu_0(\sigma\dot{\mathbf{E}} + \epsilon_0\ddot{\mathbf{E}}) \tag{1.9}$$

using the vector identity $\nabla\times(\nabla\times\mathbf{A}) = \nabla(\nabla\cdot\mathbf{A}) - \Delta\mathbf{A}$, Ohm's law (1.7), and the constitutional relation (1.5). As the electromagnetic sources lie outside the Earth ($\nabla \cdot \mathbf{E} = 0$), the electric field $\mathbf{E}$ is described by a wave equation in (1.9). Similarly, a wave equation for the magnetic field $\mathbf{H}$ can be derived starting from (1.2). Hence,

$$\Delta\mathbf{F} = \mu_0(\sigma\dot{\mathbf{F}} + \epsilon_0\ddot{\mathbf{F}}),$$

with $\mathbf{F}$ representing either of the fields $\mathbf{E}$ or $\mathbf{H}$. As the penetration depth of the fields is small compared to the source dimensions (Schmucker, 1987), the electromagnetic fields can be considered a homogeneous plane wave in the survey area with a time dependency of $e^{i\omega t}$. Thus, in frequency domain the formulation of the wave equation simplifies

$$\Delta\tilde{\mathbf{F}} = \mu_0\sigma(i\omega - \frac{\epsilon_0\omega^2}{\sigma})\tilde{\mathbf{F}}, \tag{1.10}$$

with $\tilde{\mathbf{F}}$ denoting the fourier transform of $\mathbf{F}$. As frequencies used in magnetotellurics are below 1000 Hz and conductivities σ of the subsurface < 10 S/m, the oscillating part of the wave equation ($\frac{\epsilon_0\omega^2}{\sigma}$) is much smaller than the term describing the diffusion process ($i\omega$) so that (1.10) reduces to the diffusion equation

$$\Delta\tilde{\mathbf{F}} = i\omega\mu_0\sigma\tilde{\mathbf{F}} = k^2\tilde{\mathbf{F}}, \tag{1.11}$$

where $k^2 = i\omega\mu_0\sigma$ is the complex wave number. (1.11) describes the propagation of electric and magnetic fields as diffusion in a homogeneous medium of conductivity σ. As the source

fields can be considered as surface parallel plane waves (Schmucker, 1987) equation (1.11) has the two following independent solutions

$$\tilde{\mathbf{F}} \propto \exp(\pm kz), \tag{1.12}$$

which describe the behaviour of the field with depth z. Horizontal variations of the observed electric and magnetic fields arise due to the subsurface conductivity structure $\sigma = \sigma(x, y, z)$. In the notation used here, e^{-kz} describes the down-going and e^{+kz} up-going wave. In either case, the amplitude of such solutions will decay exponentially. The penetration depth of the electromagnetic fields can be characterized by the skin depth p

$$p = \sqrt{\frac{2}{\mu_0 \sigma \omega}} = \sqrt{\frac{2\rho}{\mu_0 \omega}} \tag{1.13}$$

at which the amplitude of the fields has decayed to $\frac{1}{e}$ of some initial surface value; $\rho = \sigma^{-1}$ is the electrical resistivity.

1.2 The transfer functions

For analysis of the subsurface conductivity structure through the induction behaviour of the electric and magnetic[1] field components, following linear transfer functions between the field components are defined in the frequency domain[2]:

$$\begin{pmatrix} E_x \\ E_y \end{pmatrix} = \begin{pmatrix} Z_{xx} & Z_{xy} \\ Z_{yx} & Z_{yy} \end{pmatrix} \cdot \begin{pmatrix} B_x \\ B_y \end{pmatrix} \tag{1.14}$$

$$\mathbf{E} = \mathbf{Z} \cdot \mathbf{B}$$

$$B_z = \begin{pmatrix} T_x & T_y \end{pmatrix} \cdot \begin{pmatrix} B_x \\ B_y \end{pmatrix} \tag{1.15}$$

$$B_z = \mathbf{T} \cdot \mathbf{B}$$

All quantities are complex functions of frequency. The impedance tensor $\mathbf{Z}$ describes a linear relationship between the horizontal electric and magnetic fields. Equation (1.14) constitutes the basis of the magnetotelluric method. The analysis of $\mathbf{T}$ (1.15), the induction vector or vertical magnetic transfer function (VTF), originally emerged as independent Geomagnetic Depth Sounding (GDS) method (Parkinson, 1959; Wiese, 1962). Nowadays, GDS is usually considered part of MT in a wider sense.

In MT measurements, time series of the local magnetic and electric field variations are recorded at each survey site[3]. Following the physical relationships described above a Fourier

[1] Henceforth, I will use the common term *magnetic field* when referring to the magnetic flux density $\mathbf{B}$.

[2] From now on, explicit denotation of the Fourier transform of the quantities by $\tilde{}$ is omitted.

[3] The magnetic field is recorded vectorially along the three axis of the coordinate system; for the electrical field only the horizontal components are recorded (see chapter 2.2).

transform is applied to the time series and transfer functions are estimated in the frequency domain using a bivariate approach.

For graphical representation, the complex impedances are often described as apparent resistivity ρ_a and phase ϕ values (Cagniard, 1953)

$$\rho_{a,ij}(\omega) = \frac{\mu_0}{\omega}|Z_{ij}(\omega)|^2 \tag{1.16}$$

$$\phi_{ij}(\omega) = \arctan\frac{\Im(Z_{ij})}{\Re(Z_{ij})}, \tag{1.17}$$

analogue to the representation of complex numbers as absolute value and phase. The apparent resistivity $\rho_a(\omega)$ represents an average of the electrical resistivity within the induction volume of the electromagnetic fields.

The phase relation of the impedance tensor can be alternatively expressed by the phase tensor Φ (Caldwell et al., 2004)

$$\Phi = \mathbf{X}^{-1}\mathbf{Y}, \tag{1.18}$$

with $\mathbf{X}$ and $\mathbf{Y}$ real and imaginary parts of the impedance tensor $\mathbf{Z} = \mathbf{X} + i\mathbf{Y}$. Φ is a real, second rank tensor and is characterized by a direction and three independent scalar coordinate invariants. Caldwell et al. (2004) suggest to use maximum (Φ_{max}) and minimum (Φ_{min}) tensor values and the tensor skew β

$$\beta = \frac{1}{2}\arctan\left(\frac{\Phi_{xy} - \Phi_{yx}}{\Phi_{xx} + \Phi_{yy}}\right) \tag{1.19}$$

as coordinate invariants. Using this notation, the phase tensor can be rewritten as

$$\Phi = \mathrm{R}^T(\alpha - \beta)\begin{pmatrix}\Phi_{max} & 0\\ 0 & \Phi_{min}\end{pmatrix}\mathrm{R}(\alpha + \beta), \tag{1.20}$$

where $\mathrm{R}(\alpha + \beta)$ is the rotation matrix

$$\mathrm{R}(\alpha + \beta) = \begin{pmatrix}\cos(\alpha + \beta) & \sin(\alpha + \beta)\\ -\sin(\alpha + \beta) & \cos(\alpha + \beta)\end{pmatrix} \tag{1.21}$$

and

$$\alpha = \frac{1}{2}\arctan\left(\frac{\Phi_{xy} + \Phi_{yx}}{\Phi_{xx} - \Phi_{yy}}\right) \tag{1.22}$$

expresses the dependence of the phase tensor on the coordinate system. Phase tensor data are

usually visualized as ellipses where Φ_{max} and Φ_{min} determine the length of major and minor axis, respectively, and $\alpha - \beta$ describes the orientation of the major axis (Fig. 1.1). Information on the dimensionality of the subsurface structure can be directly obtained from the phase tensor invariants. If the phase tensor is symmetric ($\beta = 0$) the subsurface is mirror-symmetric, e.g. one- or two-dimensional. Additionally, in one-dimensional situations $\Phi_{max} = \Phi_{min}$ and phase tensor ellipses are circular.

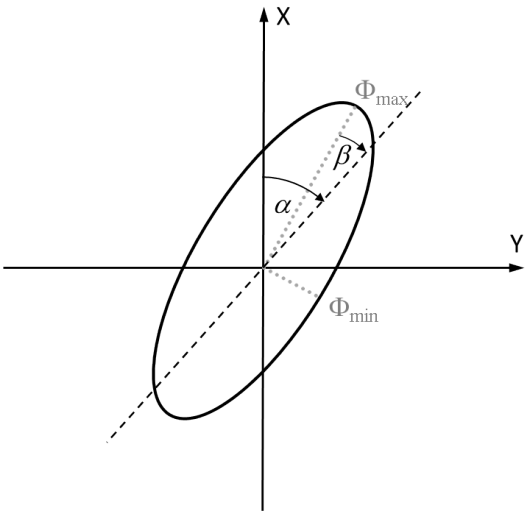

Figure 1.1: Graphical representation of phase tensors. Φ_{max} and Φ_{min} are used to scale major and minor ellipse axis, respectively. The angle $\alpha - \beta$ gives the orientation of the major axis in the observer's coordinate system. In the general case, the angle β represents the rotation of the major axis from an identically shaped ellipse representing a symmetric tensor (black dashed line). Figure drawn after Caldwell et al. (2004).

1.3 Galvanic distortion

In MT surveys, localized small-scale heterogeneities in conductivity of the near-surface can impose significant galvanic distortion on the electric field and subsequently bias the impedance response. Interpretation of these distorted impedance data can be misleading and usually results in erroneous subsurface models.

Any anomaly in a given conductivity structure has both an inductive and a galvanic response. Due to the skin effect the contribution of the inductive response of the anomaly to the overall inductive response of the subsurface depends on the frequency. At high frequencies, i.e. if the anomaly occupies the entire induction volume, the inductive subsurface response is determined by the anomaly. For decreasing frequencies ω, i.e. increasing inductive scale length of the fields, the relative contribution of the inductive response of the anomaly will decay and can be neglected below some threshold frequency ω_c (Jiracek, 1990; West & Edwards, 1985).

The galvanic response is caused by the accumulation of charges at the boundaries of the anomalous body, which arises as a consequence of the electromagnetic field. In the quasi-static

approximation appropriate for MT (cf. section 1.1), we easily obtain

$$\nabla \cdot \mathbf{j} = 0$$

multiplying the second Maxwell equation (1.2) with $\nabla\cdot$. Applying Ohm's Law (1.7) and (1.3) the volume charge density $\bar{\rho}$ describing the accumulation of charges is given by

$$\bar{\rho} = -\frac{\epsilon_0}{\sigma}\mathbf{E}_r \cdot \nabla\sigma = -\frac{1}{\sigma}\mathbf{D}_r \cdot \nabla\sigma. \tag{1.23}$$

Equation (1.23) shows that the accumulation of charges at conductivity gradients is a secondary effect, which occurs only if (i) there is a regional or primary electric field $\mathbf{E}_r$ and (ii) there is a component of the electric field in the direction of the conductivity change, i.e. $\mathbf{E}_r \cdot \nabla\sigma \neq 0$. The charge accumulation generates a secondary electric field, which adds to the observed field. In the quasi-static approximation this secondary electric field $\mathbf{E}_s$ is given by Coulomb's law (cf. Menvielle, 1988)

$$\mathbf{E}_s = -\frac{1}{4\pi\epsilon_0}\int_V \frac{\bar{\rho}}{|\mathbf{r}|^3}\mathbf{r}_0 dV, \tag{1.24}$$

where $\mathbf{r}$ is a vector between a differential volume segment dV and the observation point; $\mathbf{r}_0$ is a unit $\mathbf{r}$ vector. The galvanic field $\mathbf{E}_s$ adds to the regional inductive subsurface response $\mathbf{E}_r$, which is the target observation quantity, and impairs the measurements.

At first sight, the consideration of charge accumulation within the Earth providing a relevant contribution to the measured electric field appears to disagree with the solution of the MT induction problem, where the assumptions of $\bar{\rho} = 0$ and $\mathbf{D} = 0$ were used (cf. section 1.1). In fact, both the electric field causing the accumulation of charges, which is in the order of $\mathbf{D}$ (see (1.23)), and the volume charge density are small and can be neglected. The (secondary) electric field of these charges $\mathbf{E}_s$, however, can be quite large (Price, 1973).

The amplitude of $\mathbf{E}_s$ is proportional to the conductivity difference between the anomaly and the background structure. However, $\mathbf{E}_s$ decays rapidly when moving away from the conductivity interface so that only heterogeneities which are very close to the sampling point do have a significant influence on the measurements. The secondary electric field varies in-phase with the primary background field. In the frequency range used in MT, charge build-up can be considered to happen synchronously with the variation of the primary field (Kaufmann, 1985). Thus, the phase of the measured electric field is the same as that of the background field. In total, both amplitude and orientation of the observed electric field $\mathbf{E}$ differs from the regional electric field $\mathbf{E}_r$, i.e. $\mathbf{E}_s$ distorts the regional electric field. This galvanic distortion of the electric field is constant over frequency and persists at low frequencies, where the inductive response is negligible. For inductive-scale features, the inductive response is usually much larger

than the galvanic response (Kaufmann, 1985). Hence, the galvanic impact on the electric field only is relevant for small-scale structures, *galvanic scatteres*, which are below the inductive scale length and close to a so-called site measurement. In addition, galvanic distortions of the magnetic field can be neglected (Chave & Smith, 1994; Groom & Bahr, 1992; Singer, 1992) and vertical magnetic transfer function $\mathbf{T}$ (1.15) can be considered free of distortion.

Figure 1.2 visualizes the galvanic effect of an anomalous body. The secondary field $\mathbf{E}_s$ associated with the boundary charges of the anomaly adds vectorially to the induction-related primary field $\mathbf{E}_r$. Depending on the sign of the conductivity difference between the anomalous structure of conductivity σ_1 and the regional background (σ_0), the electric field measured above the anomaly is either reduced ($\sigma_1 > \sigma_0$) or increased ($\sigma_1 < \sigma_0$) with respect to the electric field $\mathbf{E}_r$ of the regional structure.

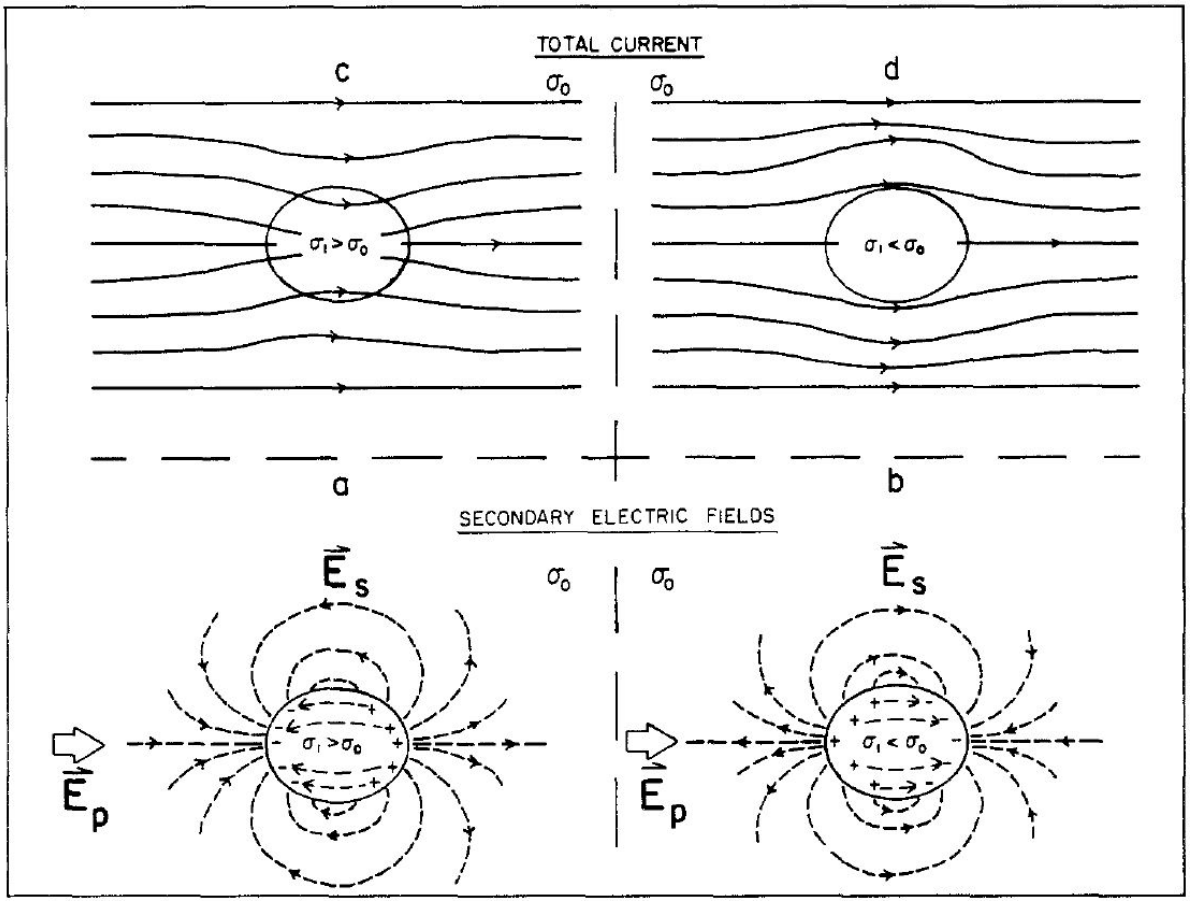

Figure 1.2: Galvanic effect. Boundary charges from the surface of **(a)** conductive inclusion and **(b)** resistive inclusion producing secondary electric fields $\mathbf{E}_s$ (dashed). Primary (or regional) field $\mathbf{E}_p$ and secondary fields $\mathbf{E}_s$ add vectorially to produce total electric field $\mathbf{E}$ resulting in **(c)** current channelling and **(d)** current deflection (from Jiracek (1990)).

Mathematically, the influence of galvanic scatterers on the electric field can be described by a four component distortion tensor $\mathbf{C}$, which relates observed ($\mathbf{E}$) and regional or primary ($\mathbf{E}_r$) electric field, which would be measured in absence of the anomaly (e.g. Bahr, 1988):

$$\mathbf{E} = \mathbf{C} \cdot \mathbf{E}_r = \begin{pmatrix} c_{xx} & c_{xy} \\ c_{yx} & c_{yy} \end{pmatrix} \cdot \begin{pmatrix} E_x^r \\ E_y^r \end{pmatrix}. \tag{1.25}$$

$\mathbf{C}$ is a real, frequency-independent tensor and describes the changes of amplitude and direction of the electric field due to the galvanic scatterer. Equation (1.25) holds if the spatial gradient of the background field is small over the scale size of the inhomogeneity, i.e. the scale of the structure is much smaller than the skin depth of the electromagnetic fields at this period (Groom & Bahr, 1992).

The galvanic distortion of the electric field propagates to the magnetotelluric impedance $\mathbf{Z}$, which describes the amplitude and phase relationship between the horizontal components of the electric and magnetic fields $\mathbf{E} = \mathbf{Z} \cdot \mathbf{B}$ (1.14):

$$\mathbf{E} = \mathbf{C} \cdot \mathbf{E}_r = \mathbf{C} \cdot (\mathbf{Z}_r \cdot \mathbf{B}) = (\mathbf{C} \cdot \mathbf{Z}_r) \cdot \mathbf{B} \tag{1.26}$$

and, thus, the relation between the observed $\mathbf{Z}$ and regional $\mathbf{Z}_r$ impedance is

$$\mathbf{Z}(\omega) = \mathbf{C} \cdot \mathbf{Z}_r(\omega), \tag{1.27}$$

ω indicates frequency dependence. In the general 3D case the observed impedance tensor elements Z_{ij} will be a mixture of two elements of the regional impedance:

$$\mathbf{Z} = \begin{pmatrix} c_{xx}Z_{xx}^r + c_{xy}Z_{yx}^r & c_{xx}Z_{xy}^r + c_{xy}Z_{yy}^r \\ c_{yx}Z_{xx}^r + c_{yy}Z_{yx}^r & c_{yx}Z_{xy}^r + c_{yy}Z_{yy}^r \end{pmatrix}. \tag{1.28}$$

As a consequence, both the amplitude and the phase of the observed impedances differ from the regional values (see also Jones, 2011). Above one-dimensional (1D) or a two-dimensional (2D) underground where the coordinate system is aligned with the geo-electric strike direction the diagonal elements of $\mathbf{Z}_r$ vanish and the distortion problem simplifies to

$$\mathbf{Z}^{\mathrm{1D/2D}} = \begin{pmatrix} c_{xy}Z_{yx}^r & c_{xx}Z_{xy}^r \\ c_{yy}Z_{yx}^r & c_{yx}Z_{xy}^r \end{pmatrix}. \tag{1.29}$$

In this case, the phase relation of the off-diagonal impedance elements, which are used in 2D and 1D interpretation, is preserved and only the impedance amplitudes, i.e. the apparent resistivities are biased. Hence, the galvanic distortion of the measured off-diagonal components will express as vertical offset of the log-apparent-resistivity versus period curves, known as *static*

shift:

$$\rho_{ij,a} = \frac{\mu_0}{\omega}|c_{ii}Z^r_{ij}(\omega)|^2 = {c_{ii}}^2\rho_{ij,a,r} \qquad \log(\rho_a) = \log(\rho_{a,r}) + 2\log(c_{ii}). \tag{1.30}$$

In general, it would be desirable to eliminate the distortion of the observed impedance and determine $\mathbf{Z}_r$ prior to interpretation. Since $\mathbf{C}$ is unknown, the equation system of (1.27) is underdetermined with 12 unknowns of $\mathbf{C}$ and $\mathbf{Z}_r$ in 8 equations for $\mathbf{Z}$ and only partial solutions can be obtained if no further assumptions are made.

The phase relationship of the impedance tensor described by the phase tensor (Caldwell et al., 2004), however, is preserved in the presence of galvanic distortion independent of the dimensionality of the subsurface structure. The regional phase tensor Φ_r (1.18) can be determined directly from the observed impedance. Splitting the impedance tensor $\mathbf{Z} = \mathbf{X} + i\mathbf{Y}$ into real ($\mathbf{X}$) and imaginary ($\mathbf{Y}$) parts, (1.27) can be rewritten as two equations

$$\mathbf{X} = \mathbf{C} \cdot \mathbf{X}_r \qquad \mathbf{Y} = \mathbf{C} \cdot \mathbf{Y}_r.$$

Using the definition of the phase tensor $\Phi = \mathbf{X}^{-1}\mathbf{Y}$ (1.18) we obtain

$$\mathbf{\Phi} = \mathbf{X}^{-1}\mathbf{Y} = (\mathbf{C} \cdot \mathbf{X}_r)^{-1} \cdot (\mathbf{C} \cdot \mathbf{Y}_r) = {\mathbf{X}_r}^{-1} \cdot \mathbf{C}^{-1} \cdot \mathbf{C} \cdot \mathbf{Y}_r = {\mathbf{X}_r}^{-1} \cdot \mathbf{Y}_r = \mathbf{\Phi}_r. \tag{1.31}$$

The measured phase tensor is identical to the regional phase tensor and independent of galvanic effects.

2 Magnetotelluric study of the San Andreas fault

The San Andreas fault (SAF) is one of the major transform faults in the world separating the North American from the Pacific plate. Within the last 150 years, more than 30 major earthquakes with magnitudes above M 6.0 ruptured the fault (Toppozada et al., 2002), of which the most notable ones were the great San Francisco earthquake of 1906, Fort Tejon 1857, Loma Prieta 1989, and Parkfield 2004 (see Fig. 2.1 for epicentre locations). In Los Angeles people are fearfully awaiting "the big one" as the southern segment of the SAF has not been ruptured for a long time and earthquake recurrence statistics show a high probability for a potentially devastating stroke with $M \geq 7.5$ within the next decades (Olsen et al., 2006).

First discovered and described by Lawson (1895), the SAF came into prominence only after the great San Francisco earthquake of 1906. Since then, numerous geological and geophysical studies have been conducted to unravel the fault's dimensions and characteristics, making it one of the most extensively studied plate boundaries in the world.

The SAF extends 1,300 km in northwest-southeast direction from the Mendocino Triple Junction off the coast of Cape Mendocino to the Salton Sea near the Mexican border (cf. Fig. 2.1). Beginning in the Pacific Ocean, the fault trace comes ashore at Point Arena, north of San Francisco, and continues inland roughly parallel to the Californian coastline. South of the Salton Sea, the boundary between the Pacific and the North American plates is continued by a series of spreading centres and transform faults through the Gulf of California unto its end at the Rivera triple junction.

The relative movement between the North American and the Pacific plates in the SAF region is primarily accommodated by the SAF system emerging as right-lateral strike-slip (Thatcher, 1990). The major displacement expresses in recurring intermediate to major earthquakes (Bakun & McEvilly, 1984; Segall & Harris, 1987; Sieh & Jahn, 1984). Large segments of the fault system are in a locked state (cf. Fig. 2.1) and are believed to be able to produce damaging earthquakes. A notable exception is the 175 km long creeping segment between San Juan Bautista and Cholame (cf. Fig. 2.1), where high rates of aseismic slip are observed and large earthquakes above M 6.0 are unknown (Bakun & Lindh, 1985; Thatcher, 1990).

Recently, tectonic non-volcanic tremors (NVT) were discovered in the SAF system in central California (Nadeau & Dolenc, 2005). NVT events primarily cluster at the transition

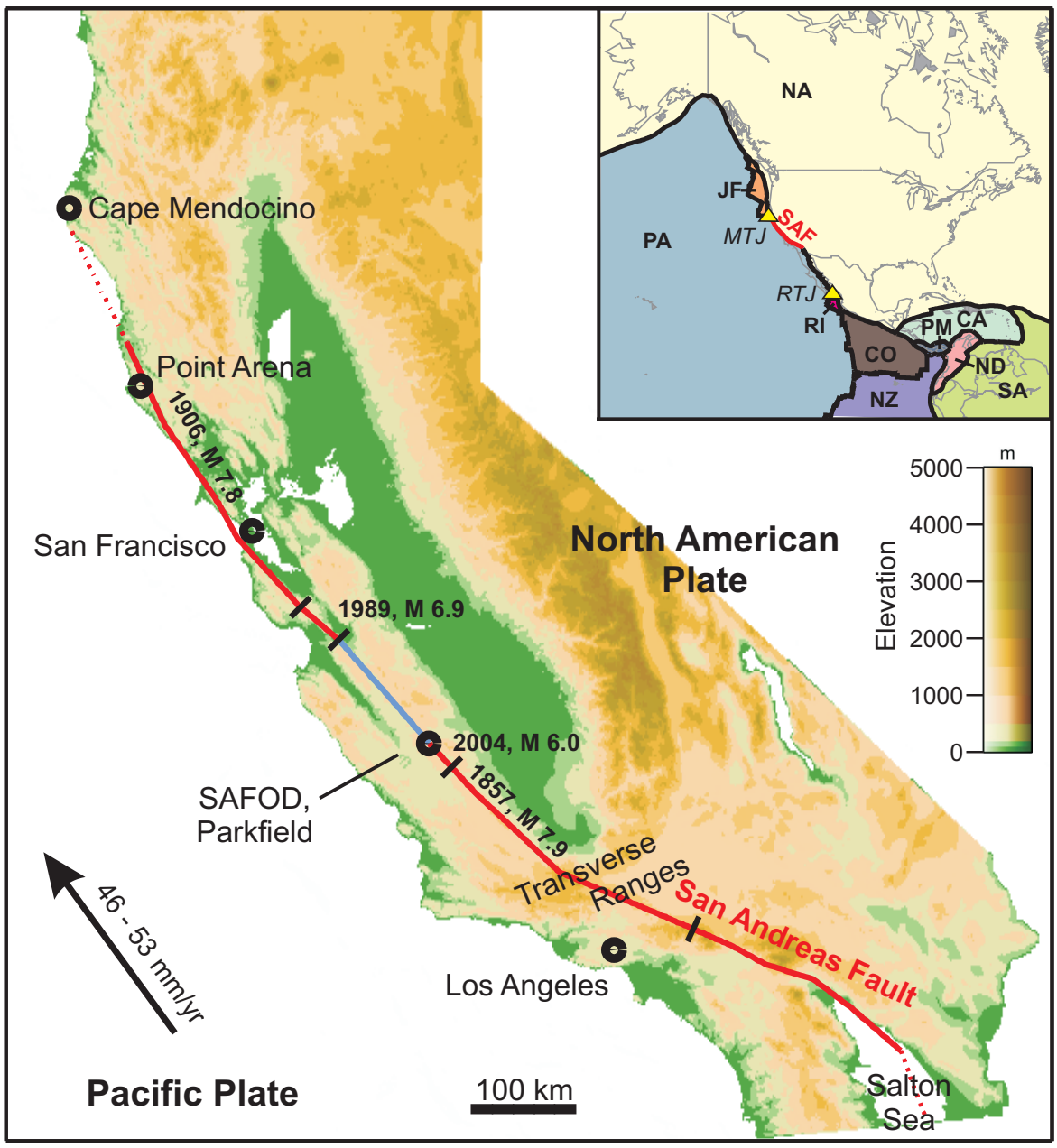

Figure 2.1: Elevation map of California showing the course of the San Andreas fault (SAF). Segments of the SAF that are in a locked state and ruptured in major historical earthquakes are shown in red (Ellsworth, 1990; Langbein et al., 2005), the creeping and microseismically active section of the fault in blue. The relative movement of the Pacific vs. the North American plate is estimated to 46 - 53 mm/yr in N36±2°W direction (Argus & Heflin, 1995; Argus & Gordon, 2001; Atwater & Stock, 1998; DeMets et al., 1990; Ward, 1990). SAFOD San Andreas Fault Observatory at Depth. **Inset:** Location of SAF in context of major tectonic plates (PB2002 model of Bird, 2003). Yellow triangles mark the Mendocino (MTJ) and Rivera (RTJ) triple junctions. PA Pacific plate, NA North American plate, JF Juan de Fuca plate, RI Rivera plate, CO Cocos plate, CA Caribbean plate, PM Panama plate, ND North Andes plate, NZ Nazca plate.

between the locked and creeping sections of the SAF near Cholame (Nadeau & Guilhem, 2009; Zhang et al., 2010). The physical mechanisms of NVT are not yet fully understood, but they are believed to provide new insights in the deep structure of the transform fault system.

The most ambitious project investigating the fault within the last decades is the San Andreas Fault Observatory at Depth (SAFOD) located about 9 km northwest of Parkfield drilling into the fault at seismogenic depths. The SAFOD project is part of the International Continental Scientific Drilling Program (ICDP) and conducted in collaboration with the U.S. Geological Survey. Overviews of the project and related works are given in Hickman et al. (2004, 2007) and Zoback et al. (2011). Forming one component of the EarthScope[1] program, the SAFOD provides new insights in chemical and physical processes that govern the San Andreas fault zone.

Drilling of the SAFOD main-hole was completed in 2004 to 2005. Starting 1.8 km southwest of the SAF surface trace, the borehole goes down vertically to a depth of 1.5 km and then deviates at an angle of 60° to vertical heading for the hypocentral zone of repeating $M \sim 2$ earthquakes on the SAF. The SAFOD crosses the fault at a depth of 2.7 km below surface and continues about 600 m further into the North American plate. Besides the investigation of drill cuttings and real-time analysis of gases in the drilling mud, a series of geophysical downhole measurements (logging-while-drilling and open-hole logs) were conducted. In addition, side-wall cores were retrieved at different depths. Since 2008, seismometers, accelerometers, and tiltmeters are installed within the main hole 100 m above the zone of repeating earthquakes to monitor the SAF at its roots.

In preparation for the SAFOD and still continuing, a tremendous amount of geoscientific studies using all kinds of different methods were conducted around Parkfield and the drill-site aiming to characterize the San Andreas and its surrounding area and trying to unravel its mysteries. The borehole and regional survey results, together forming an unrivalled comprehensive data set, have already yielded in a series of new insights into processes at the active fault and more are to come with work on these data still ongoing.

The magnetotelluric measurements considered here cover a 130 km × 60 km large area of the transitional segment of the SAF around Parkfield and the SAFOD. The survey area extends northeastwards from the Pacific Ocean across the SAF into the Central Valley and southwest beyond the non-volcanic tremor region near Cholame.

[1] Major Earth Science facility program of the United States National Science Foundation designed to investigate the geological processes that shape the North American continent.

2.1 Geology of California

The western coast of the North American continent has always been a very active margin with strong interaction between oceanic and continental crust recognizable by the numerous coast-parallel belts formed by accretion of island-arcs and other micro-plates in mainly Mesozoic times as well as volcanic and plutonic features. In addition, a possibly considerable amount of movement in this zone has been oblique or lateral in an overall northwest-southeast direction (Irwin, 1990). Plates sliding past one another pulled off slices and fragments and displaced them at various distances from their origin.

The most prominent feature of the Californian geology is the SAF running through nearly the entire length of the state (see Figs 2.1 and 2.2). In northern and central California, the fault virtually delineates the lithological contact of the Salinian block of granitic and metamorphic rocks on the west and the Franciscan assemblage and the overlying Great Valley sequence to the east. Further south, the SAF abruptly bends eastward crossing the Transverse Ranges and henceforth, the fault cuts through Precambrian and younger metamorphic and plutonic rocks with blocks on either side of the fault exhibiting rather similar stratigraphy.

2.1.1 Major geologic units in Central California

Figure 2.2 provides an overview of the distribution of the principle basement rocks in California. The following description of the major geologic formations present in central California is summarized from Irwin (1990) and references therein. Numbers in brackets refer to the formation numbers on the map (Fig. 2.2).

Franciscan Complex (5). In northern and central California the eastern wall of the San Andreas fault nearly exclusively consists of Franciscan rocks. Formed in a marine environment in mainly Jurassic to Cretaceous times, it includes dismembered sequences of greywacke, and shale, along with some mafic volcanic rocks, chert, and limestone all assembled heterogeneously due to heavy faulting and shearing. Blueschist and serpentinite can be found in mélange zones, the latter possibly representing sheared-in fragments of Coast Range ophiolite. Paleomagnetic studies suggest that large parts of the complex have been displaced several thousand kilometers northward relative to the North American plate since their formation.

Great Valley sequence (4). Separated by the Coast Range thrust, the Great Valley sequence overlies the Franciscan Complex east of the San Andreas fault. It comprises interbedded marine mudstone, sandstone, and conglomerates which most likely originate from Late Jurassic to Cretaceous submarine fans and turbidite deposits from rapid erosion of the Klamath and Sierra Nevada mountains. The Great Valley sequence reaches a stratigraphic thickness of at

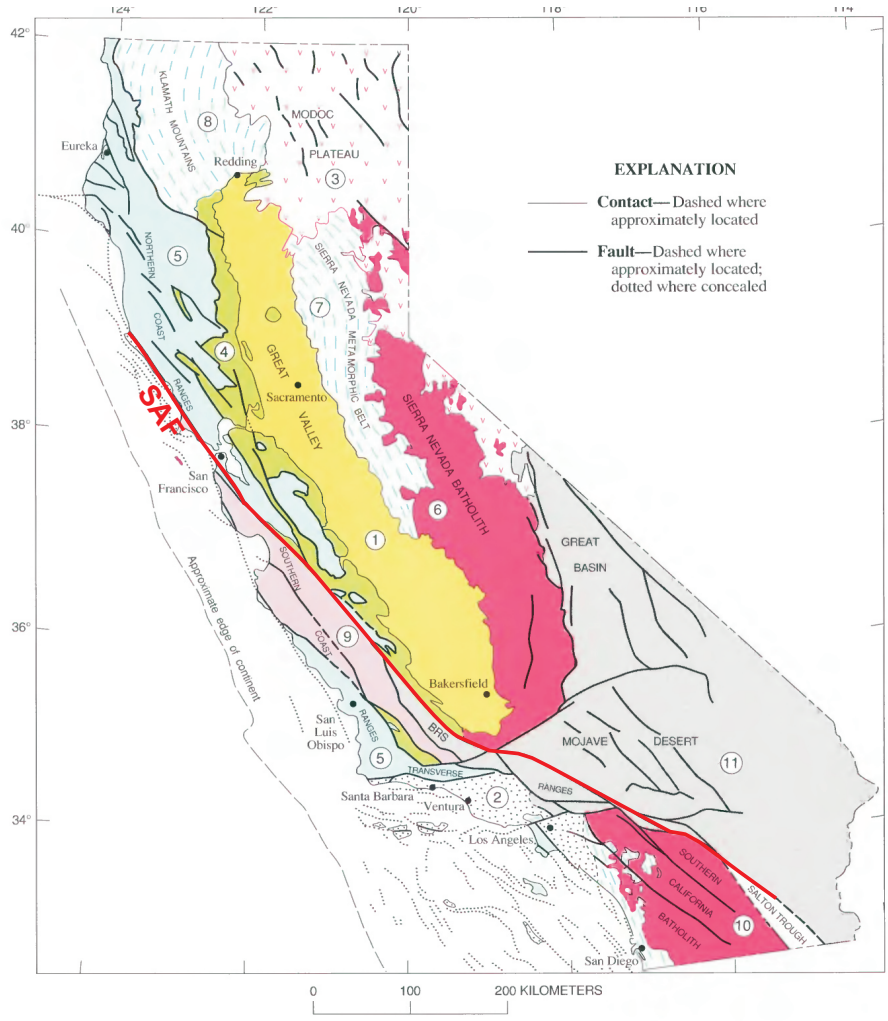

Figure 2.2: Distribution of principal basement rocks in California (modified from Irwin, 1990). Red line marks the SAF. Cenozoic cover not shown except for the Modoc Plateau, northeastern Sierra Nevada, and Santa Barbara-Ventura Basin. **1** Quaternary Alluvium – shown only in Great Valley; **2** basement rocks concealed by thick Upper Cretaceous and Tertiary deposits in the Santa Barbara, Ventura and Los Angeles Basin; **3** Cenozoic volcanic rocks of the Modoc Plateau; **4** Great Valley sequence – Lower Jurassic to Upper Cretaceous strata, including Coast Range ophiolite at base; **5** Franciscan assemblage of Lower Jurassic to Tertiary oceanic rocks; **6** Sierra Nevada batholith – dominantly Cretaceous granitic rocks; **7** Sierra Nevada metamorphic belt – early Paleozoic to Late Jurassic rocks, including fragments of ophiolites, island arcs, and melanges, intruded by early Mesozoic plutons; **8** Klamath Mountains – early Paleozoic to Late Jurassic ophiolites, island arcs, and melanges intruded by early Paleozoic to Cretaceous plutons; **9** Salinian block – dominantly Cretaceous plutons intruding metamorphic rocks of questionable age (Barrett Ridge slice (BRS), commonly shown as part of the Salinian block, is here shown as part of unit 11); **10** Southern California batholith – dominantly Cretaceous plutons intruding sedimentary and volcanic rocks of Jurassic age; **11** mainly Precambrian metamorphic and plutonic rocks, in part overlain by Paleozoic continental shelf deposits and intruded by Mesozoic plutons, locally underthrust in the southwestern part of the region by schist of probably Cretaceous age.

least 12 km at the western edge of the Great Valley. Where it crops out, the Great Valley sequence is generally less deformed than the Franciscan units and has greater lateral continuity.

At the base of the Great Valley sequence a thinned and highly discontinuous layer of Coast Range ophiolites can be found, which must have been close to the equator in Jurassic times. On their northward path towards the North American continent and during accretion they underwent intense shearing and faulting so that only in a few places sequences remained nearly complete, where they reach a stratigraphic thickness of 3 to 5 km. For the most part, the ophiolites are dismembered, thinned, and locally even missing. Serpentinite, probably playing a significant role as a lubricant along creeping segments of the San Andreas and other faults, is mostly related to the ultramafic parts of the Coast Range ophiolite.

Salinian block (9). The rocks of the Salinian block mostly constitute the western wall of the San Andreas fault in central and northern California from the Transverse Ranges to Bodega Head just north of San Francisco and probably extend further north to the latitude of Point Arena overlain in this section by sedimentary rocks. The Salinian block comprises several belts accreted to the North American continent and mainly consists of granitic and moderate- to high-grade metamorphic rocks. In Cretaceous times, granitic and tonalitic rocks locally intruded the Salinian block beginning about 120 - 105 Ma ago in the northwestern part and continuing southeastwards over time leaving the youngest plutons at the Barret Ridge slice about 80 - 75 Ma ago. As rocks are very similar to the Sierra Nevada, the Salinian may represent a displaced fragment of this formation, but paleomagnetic data suggest an origin as far south as the latitude of Central America.

Southern California (10, 11). South of the Transverse Ranges, formed by Precambrian rocks intruded by Mesozoic plutons, the complexity of the San Andreas Fault system increases as it splays into several fault strands cutting through the Cretaceous plutonic rocks of the Southern Californian batholith. Further south the crystalline basement is intersected by the Salton Trough filled with Late Cenozoic and Quaternary deposits. The SAF runs along its eastern edge and terminates as a transform fault where the Salton Trough widens towards the Mexican border and merges into a pull-apart zone, that is the northern end of a series of spreading centres and intermitting transform faults.

2.1.2 Tectonic evolution of the San Andreas fault system

The tectonic evolution of the SAF system started about 30 Ma ago in the mid-Cenozoic (see Fig. 2.3); the trace of the SAF as it is known today, however, has only been existing for 4 to 6 Ma (Powell & Weldon, 1992).

Since at least 80 Ma, the Farallon plate – the ancestor of the present-day Juan de Fuca and Rivera-Cocos plates – has been subducted in northeast direction beneath the western

margin of the North American continent (Bunge & Grand, 2000; Engebretson & Cox, 1984; Liu et al., 2008; Usui et al., 2003). Due to the rapid convergence of the two plates and the accretion of terranes along the coastline, the spreading centre between the Farallon and the Pacific plate gradually approached the North American coast (Fig. 2.3). About 29 Ma ago (Atwater & Molnar, 1973; Powell & Weldon, 1992), the Pacific plate first impinged on the North American plate and started the evolution of the San Andreas fault system. From the time of contact until today, the Pacific plate has been moving in a northwesterly direction relative to the North American plate and roughly parallel to the western margin of the continent (Gordon & Jurdy, 1986; Schellart et al., 2010). Over time, the newly formed Mendocino and Rivera triple junctions migrated northwest- and southeastward, respectively, as a consequence of the ongoing subduction of the Farallon plate successors. Today, the tectonic boundary between the Pacific and the North American plates measures 2,500 km, the northern 1,300 km of which are today's San Andreas fault system. The southern segment is formed by a set of spreading centres and interjacent transform faults running through the Gulf of California and finally merging with the East Pacific Rise near the southern tip of Baja California.

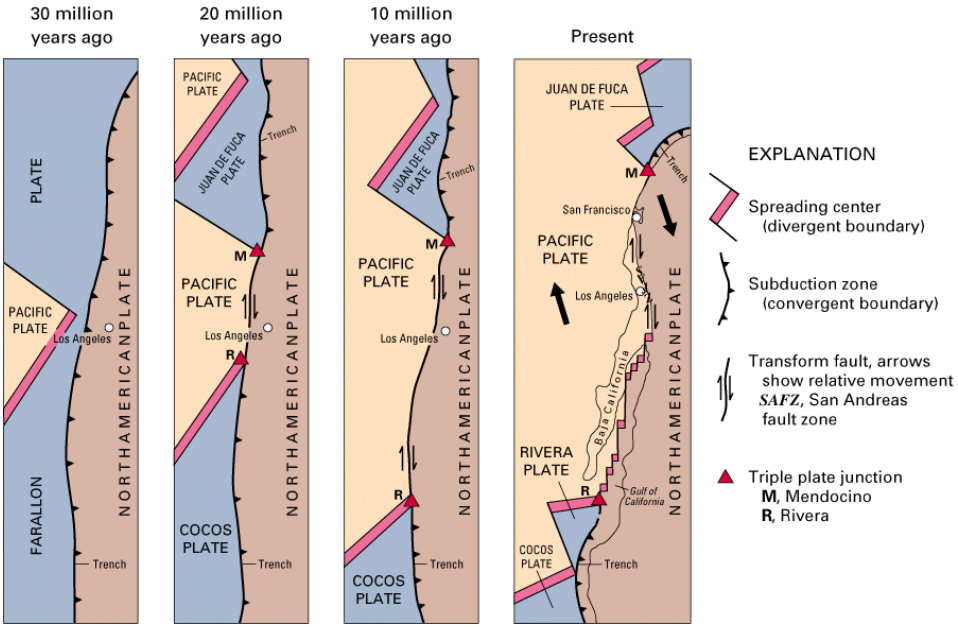

Figure 2.3: Sequential diagrams showing the tectonic evolution of the San Andreas fault [U. S. Geological Survey, modified from Wallace (1990)]. About 29 Ma ago (Atwater & Molnar, 1973; Powell & Weldon, 1992), the spreading centre between the Pacific and the Farallon plate touched the North American plate boundary initiating the development of the San Andreas fault system. Subsequently, the newly evolved Mendocino and the Rivera Triple junctions moved northwest- and southeastward, respectively, toward their current location 2,500 km apart. Over time, the transform faulting has jumped eastward and the present-day San Andreas fault lies within the North American continent.

After its initialization, the new plate boundary gradually developed from an oblique subduction zone into a right-lateral transform fault system. Onland, displacement in the early phase expressed mainly as transtensional deformation with associated volcanism between 26 Ma and 22 to 20 Ma (Powell & Weldon, 1992). Around the time of first contact of the east Pacific ridge and the North American plate 30 Ma ago, the northern part of the Farallon plate began to fragment into several microplates (Nicholson et al., 1994): Subduction of these segments occurred at different velocities depending on the age of the subducted material. As young material gradually approached the coast, subduction and spreading ceased. In parallel, the motion along the plate boundary changed from predominantly oblique subduction to transtensional transform motion initializing strike-slip faults within the North American plate. In central California, where spreading processes finally stopped at around 20 Ma, the Monterey microplate was only partially subducted beneath the North American plate. As it had assumed Pacific plate movement displacement between the Pacific and the North American plate transferred to within the North American plate (cf. Figs 2.4 and 2.5). This microplate capture by the Pacific plate may explain how other parts of California became accreted to the Pacific plate.

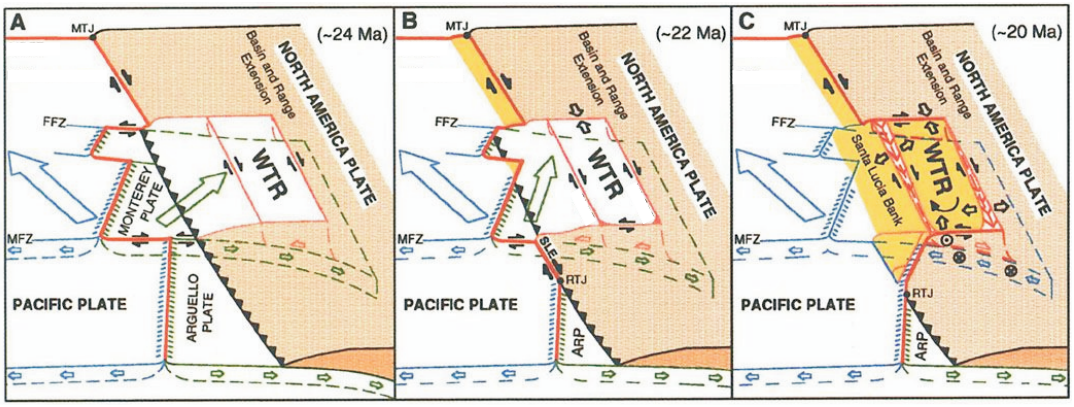

Figure 2.4: Schematic diagram illustrating the capture of Monterey microplate by the Pacific plate in central California. From 24 to 20 Ma, Monterey subduction slows causing subduction (green) to become more oblique until the microplate finally assumes Pacific plate motion (blue). Yellow: North American crust captured by Pacific plate; red: edge to Pacific plate or areas of extension. FFZ, MFZ: Farallon and Morro fracture zones. MTJ and RTJ: Mendocino and Rivera triple junctions; WTR Western Transverse Ranges block. SLE Santa Lucia Escarpment. ARP Arguello plate. Figure modified from Nicholson et al. (1994).

Along the continental margin no transform fault has been identified and there is no clear evidence for a through-going strike-slip plane before 20 Ma (Powell & Weldon, 1992). The interface of the plates is interpreted as a northeastward dipping inactive subduction zone, where oceanic material was subducted beneath the North American plate. Today, the suture zone is overlain by undeformed Miocene strata (e.g. Irwin, 1990).

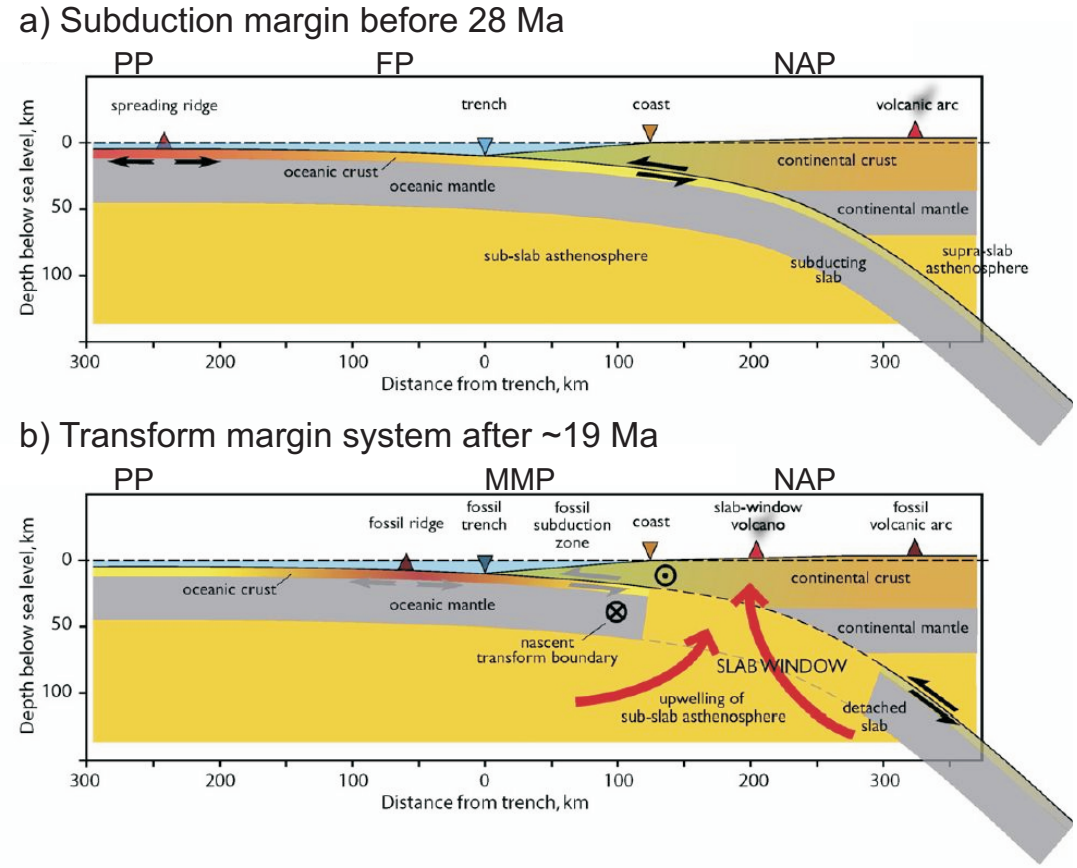

Figure 2.5: Schematic evolution of the California continental margin including capture of the remnant Monterey microplate, formation of a slab window and initiation of the transform margin near the slab tear more than ~19 Ma ago. PP Pacific plate, FP Farallon plate, NAP North American plate, MMP Monterey microplate. Figure modified from McCrory et al. (2009).

With progression of the San Andreas fault system, displacement has occurred along different fault traces as the active slip plane jumped eastward several times to positions within the North American continent. Repeatedly, thin belts have been sliced off and transported northwestward, adding to the present-day appearance of California's geology as dominantly elongated and coast-parallel trending units (cf. Fig. 2.2).

In northern and central California, slip along the modern trace of the San Andreas was only minor until 12.5 to 10 Ma and the fault itself was probably not the dominant slip surface within the transform system until 5 to 7 Ma before present (Dickinson & Snyder, 1979b). Faults within the Coast Ranges between the continental margin and the current San Andreas fault may represent earlier positions of the transform fault (Irwin, 1990).

In southern California, the sudden onset of the opening of the Gulf of California 5 Ma ago

caused the slip surface to leap eastward from a location off the coast to roughly its present position about 100 km inland (Atwater & Molnar, 1973). In conjunction, the course of the San Andreas fault was bent left-laterally in the Transverse Ranges and several left-lateral and reverse faults (cf. Fig. 2.2; Irwin (1990)) were possibly initiated in this section (Powell & Weldon, 1992).

Today, the San Andreas fault system is cutting through the North American continent well inland from the expected margin, but as units on the Pacific side of the fault are moving nearly congruently with the oceanic plate, the San Andreas fault represents the tectonic boundary between the Pacific and the North American plate (Powell & Weldon, 1992).

With progressing evolution of the San Andreas transform system subduction of the Farallon plate ceased. Various studies found evidence for subsequent slab break-off and the development of a slab window (Dickinson & Snyder, 1979a; Fulton & Saffer, 2009; McCrory et al., 2009; Wilson et al., 2005): At triple junctions where a spreading ridge starts to subduct beneath a continental margin, the subducted slab usually parts and a gap or window evolves between the two slabs. The window widens with time as the triple junctions move apart and hot asthenospheric material can upwell to fill the window, which often triggers dehydration of the overlying material and magmatic activity (cf. Fig. 2.5). In Califonia, Cenozoic volcanic activity is known to have occurred in three episodes since 27 Ma till present (Dickinson, 1997). The petrologic character and temporal-spatial distribution of these assemblages suggest that these episodes reflect slab-window magmatism. In addition, fluids released by dehydration of mantle-depth material possibly contribute to high rates of fault creep along some segments of the SAF system in central California and the occurrence of tectonic non-volcanic tremor (Fulton & Saffer, 2009; Nadeau & Dolenc, 2005).

2.1.3 Locked and creeping segments of the San Andreas fault

The present-day movement of the Pacific plate relative to a fixed North American plate in the San Andreas fault region is estimated to 46 - 53 mm/yr in a direction of N36±2°W (e.g. Argus & Heflin, 1995; Argus & Gordon, 2001; Atwater & Stock, 1998; DeMets et al., 1990; Ward, 1990). Since the time of contact 29 - 25 Ma ago, the direction of the movement has been constant (Dubrovine & Tarduno, 2008), the displacement rate, however, varied between 13 and 55 mm/yr (Atwater & Molnar, 1973).

The relative motion between the plates is primarily accommodated by the San Andreas fault system emerging as right-lateral displacement with current rates between 18 and 38 mm/yr along the fault itself (Thatcher, 1990). The residual movement, known as the "San Andreas discrepancy", is taken up in a wide zone both east of the fault as far as the Basin and Range and west of the fault towards the Californian continental margin (e.g. Minster & Jordan, 1987; Page et al., 1998).

Since 20 Ma, the absolute displacement between the North American and the Pacific plates accumulated to 875 ± 70 km (Stock & Molnar, 1988). Displacement estimates for the San Andreas transform fault system range between roughly 300 km for southern and 450 km for central and northern California (Powell & Weldon, 1992, and references therein). Along the fault, prominent evidence for the amount of historical displacement are the 24 Ma old Pinnacle and Neenach Volcanic formations, which are exposed on opposite sides of the San Andreas fault about 315 km apart in central California. Their strikingly similar stratigraphy, lithology, and age suggest that they were contiguous at the time of their formation and displaced afterwards (Matthews, 1976).

The San Andreas fault changes its seismic behaviour along its course through California. Large parts of the fault are mechanically locked, i.e. aseismic slip is small along these segments (2 - 6 mm/yr) and earthquakes occur infrequently (Thatcher, 1990). Major events of $M \geq 8.0$ rupture the fault system at intervals of 100 to 300 years (Ellsworth, 1990; Sieh & Jahn, 1984; Working Group on California Earthquake Probabilities, 1995). The 175 km long segment in central California between San Juan Bautista and Cholame, however, is characterised by strong microseismic activity and high rates of aseismic displacement. For the central 50 km, creep rates reach up to 32 mm/yr and smoothly decrease to the level of the locked sections towards the northwestern and southeastern ends (Burford & Harsh, 1980; Lisowski & Prescott, 1981; Titus et al., 2006). In the entire segment, small earthquakes with $M < 4.0$ occur frequently but larger shocks above magnitude 6 are unknown (Bakun & Lindh, 1985; Thatcher, 1990). At the southeastern end of the creeping segment around Parkfield, characteristic moderate-sized earthquakes recur at intervals of 22 ± 3 years (Bakun & McEvilly, 1984). Since the M 7.9 Fort Tejon earthquake of 1857, six M 5.0 to 6.0 earthquakes have been located in this area (Bakun & McEvilly, 1984; Bakun & Lindh, 1985; Langbein et al., 2005). These events exhibit the same faulting mechanism, magnitude, rupture length, and location.

The seismogenic layer beneath the SAF mostly extends to depths of ∼15 km, except for the Transverse Ranges, where earthquakes at depths > 20 km were observed (Hill et al., 1990). Along the creeping segments, the epicentres of numerous microseismic events form well-defined, narrow “curtains” beneath the surface trace of the SAF and illustrate the fault zone geometry.

Along the creeping segment the SAF exhibits very low frictional strength (Fulton & Saffer, 2009; Sass et al., 1997). The causes are not yet fully understood. Explanations include high pore-fluid pressures within the fault system or the presence of mechanically weak minerals on the fault plane. All studies, however, emphasize the presence of fluids in the fault system.

Irwin & Barnes (1975) suggested that crustal fluids released from metamorphic processes in the Franciscan assemblage increase the pore-fluid pressure in the fault system and thereby reduce the mechanical strength of the fault zone. The location of the creeping segment of the SAF spatially correlates to the region where the Franciscan basement is overlain by the

Coast Range ophiolites and capped by the Great Valley sequence (Irwin & Barnes, 1975, cf. Fig. 2.2). The Great Valley sequence exhibits low permeability and, hence, fluids are forced to penetrate the SAF. Kennedy et al. (1997) find significantly elevated $^3He/^4He$ isotope ratios, which cannot be related to local geology and, hence, provide evidence for fluids migrating into the SAF system from mantle depths.

In cuttings from the SAFOD drillhole, talc minerals were found on the active trace of the SAF and in veins (Moore & Rymer, 2007). Talc results from chemical reactions of serpentine with silicate-rich fluids and exhibits weak shear strengths. Serpentine is found in the Coast Range ophiolite (Irwin & Barnes, 1975) and hydrothermal fluids migrating through the SAF possibly react with these ophiolites. Moore & Rymer (2007) identified talc of recent origin, which implies recent fluid circulation in the fault system.

2.1.4 Non-volcanic tremors observed in the San Andreas fault system

First discovered by Nadeau & Dolenc (2005), various authors have since reported on tectonic non-volcanic tremors (NVT) along the creeping segment of the San Andreas fault (e.g. Nadeau & Guilhem, 2009; Ryberg et al., 2010; Shelly et al., 2009; Shelly, 2010; Shelly & Hardebeck, 2010; Thomas et al., 2009; Zhang et al., 2010). NVT events primarily cluster directly at the transition between the locked and the creeping sections of the SAF near Cholame (cf. Fig. 2.6), where they also exhibit their highest amplitudes (Shelly & Hardebeck, 2010). 5 - 10 % of NVT events occur 65 km northeast of Parkfield near Monarch Peak (Nadeau & Guilhem, 2009; Zhang et al., 2010). The clusters extend ∼30 km across the San Andreas fault system and depth location estimates range from 15 to 40 km, i.e. beneath the seismogenic layer. Shelly (2010) identified source locations within NVT families travelling up to 25 km distance parallel to the SAF strike direction with velocities of 15 to 80 km/h. The results suggest that the SAF is a through-going structure even at its base.

The source mechanisms of NVT are not yet fully understood but as they occur correlated in time with stress-field changes induced by teleseismic earthquakes (e.g. Ghosh et al., 2009; Peng et al., 2008, 2009) or tides (Thomas et al., 2009) their mechanisms are thought to be closely related to earthquake generating processes, i.e. deep fault shear failure. The high sensitivity of the deep fault to stress perturbations can be explained by the presence of high pore-fluid pressures at these depths (Shelly, 2010). High fluid pressure may cause the fault to be extremely weak, possibly permitting patches of the deep fault to deform by brittle rather than ductile failure, and allow localized slip on the deep extension of the SAF.

Earthquakes triggering episodes of NVT and, in turn, changes in NVT activity preceding the 2004 $M6.0$ Parkfield earthquake (Shelly, 2010) illustrate that processes on the deep fault and in the upper crust are coupled and further support that the SAF is through-going.

2.2 Magnetotelluric data set

The magnetotelluric (MT) data set considered here comprises measurements at more than 250 sites recorded along seven parallel profiles during three field campaigns (2005, 2007, 2008) by the Electromagnetics working group of the German Research Centre for Geosciences Potsdam (GFZ) (see Fig. 2.6). The survey area extends 130 km × 60 km in the vicinity of the SAFOD covering the transitional segment of the SAF where it changes its behaviour from creeping to being locked, and where a source area of NVT was located (cf. section 2.1). The distance between neighbouring profiles is roughly 10 km, the site spacing along the profiles varies from 0.5 km in the central parts across the SAF to approximately 10 km towards the profile ends.

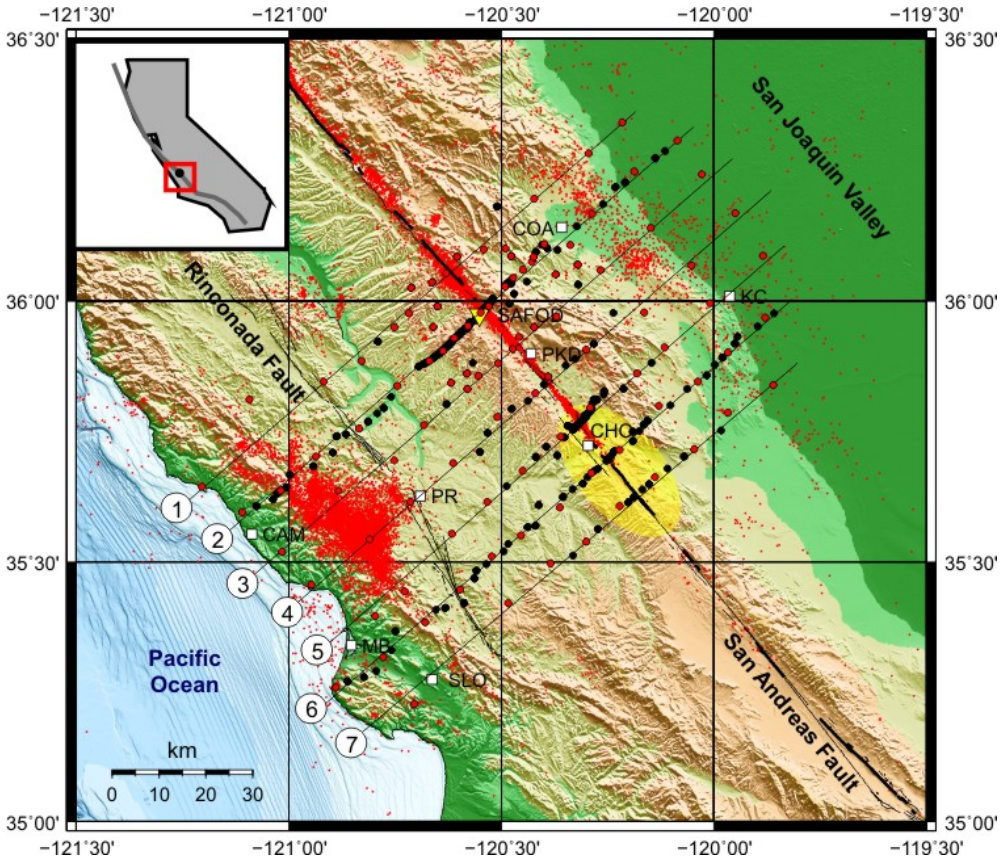

Figure 2.6: Locations of MT sites. More than 250 MT sites deployed along seven profiles cover a 130 km × 60 km large area crossing the SAF in the vicinity of Parkfield. Red filled circles mark combined BB+LMT sites, black filled circles BB-only sites. The location of the SAFOD is indicated by the yellow triangle; red dots show seismicity (NCDEC 2002-2011, M > 1.0). The yellow shaded area outlines the primary cluster of non-volcanic tremors (e.g. Nadeau & Dolenc, 2005; Nadeau & Guilhem, 2009; Zhang et al., 2010). CAM Cambria, CHO Cholame, COA Coalinga, KC Kettleman City, MB Morro Bay, PKD Parkfield, PR Paso Robles, SLO San Luis Obispo.

Measurements, estimation of transfer functions as well as two-dimensional (2D) modelling and interpretation are described in Becken et al. (2008b, 2011); this section contains a summary of their analyses and results. A review of MT surveys along the SAF including previous studies in the vicinity of the SAFOD and in other sections of the fault system can be found in Becken & Ritter (2012).

2.2.1 Field setup and data processing

At all sites, Metronix MFS05/06 induction-coil magnetometers and non-polarisable Ag-AgCl electrodes with horizontal dipole lengths of ∼60 m were deployed. For the long-period magnetotelluric (LMT) measurements 120 of the sites were equipped with Geomagnet flux-gate magnetometers and operated up to 5 weeks. All in all, up to 45 stations were running simultaneously providing a large number of possible combinations for remote reference processing.

Magnetotelluric transfer functions were estimated within a period range of 0.01 s to more than 1,000 s at broadband-only (BB) and 20,000 s at combined BB+LMT sites, respectively, using robust single site and remote reference processing routines (Egbert & Booker, 1986; Egbert, 1997; Ritter et al., 1998; Weckmann et al., 2005). The resulting transfer functions show high quality for periods above 5 s; for shorter periods, however, they were strongly impaired by cultural noise. Closer analysis of the data revealed that the time-series were affected by periodic noise with a fundamental period of ∼5.1 s, which correlates over all channels and wide areas. A likely source of these disturbances are cathodic anti-corrosion currents imposed on gas pipelines, as transfer function quality was especially low in the vicinity of buried pipelines. Hence, a fractional delay filter was applied to the original time-series of the base site and, if applicable, to those of the remote site. Subsequent re-processing of the filtered time-series produced significantly improved transfer functions for periods below 5 s, yielding consistent high-quality transfer functions over four to six decades throughout the array.

2.2.2 2D data analysis and interpretation

The data set was extensively studied by Becken et al. (2008b, 2011) with 2D inversion and FWD modelling. Geo-electric strike analysis revealed a regional strike direction of N41°W, which is parallel to the surface trace of the SAF in this region (Page et al., 1998). The 2D inversion models depict pronounced along-strike variations of the electrical resistivity distribution at the transition from the locked to the creeping segment of the SAF (cf. Fig. 2.7). The most prominent feature in the inversion models is a region of high electrical conductivity (1 to 5 Ωm) located at 15 - 20 km depth. The high-conductivity zone (HCZ) extends along the strike of the SAF, roughly between the surface traces of the Rinconada and the San Andreas faults, with its centre approximately 30 - 40 km southwest of the SAF.

At the northern profiles ① to ③, an upwelling conductive channel of the HCZ appears to be

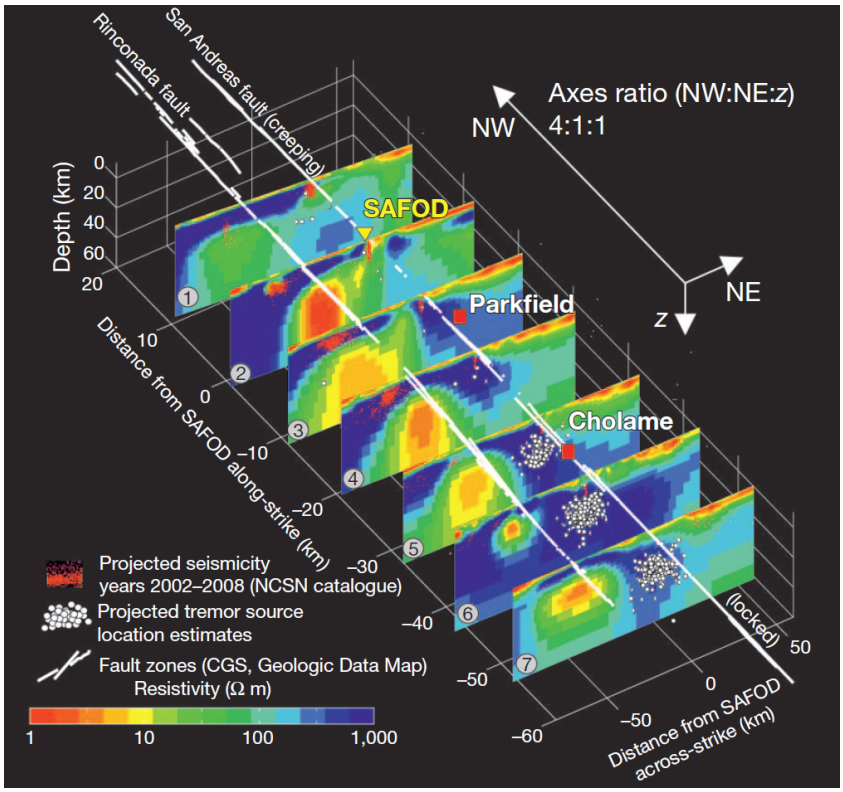

Figure 2.7: Electrical resistivity sections across the central San Andreas fault obtained from 2D inversion. The high conductivity (red and yellow colours) in the lower crust and upper mantle (20 - 40 km) is attributed to hot saline fluids. Fluids can upwell into the creeping SAF near SAFOD. Near the locked segment, fluids seem to be trapped adjacent to the main tremor zone and to be prevented from escaping into the upper crustal portion of the SAF. Tremor source locations (white dots, Zhang et al., 2010) and seismicity (red dots) are superimposed. Figure taken from Becken et al. (2011).

linked with the seismogenic SAF. This is in contrast to the southern profiles ④ to ⑦, where highly resistive (> 500 Ωm) rocks form a resistive cap confining the HCZ to depths below approximately 20 - 40 km.

Becken et al. (2011) interpret the zones of high conductivity at depth as fluids in the lower crust and upper mantle. Dehydration of a serpentinized mantle wedge, a remnant from former subduction of the Farallon plate, is thought to be a possible source for the fluids. These fluids appear to be trapped below a resistive cap in the southern part where the fault is locked and where the highest amplitudes of NVT are observed (Shelly & Hardebeck, 2010). In contrast, the subvertical zones of high conductivity further north could represent possible pathways for fluids migrating from the lower crust and upper mantle into the upper-crustal SAF system. The high resolution 2D resistivity model of Becken et al. (2008b) along the central parts of profile ② suggest that fluids could upwell between the SAF and the Waltham Canyon fault (WCF) located to the northeast and penetrate the SAF system from the eastern side. It is

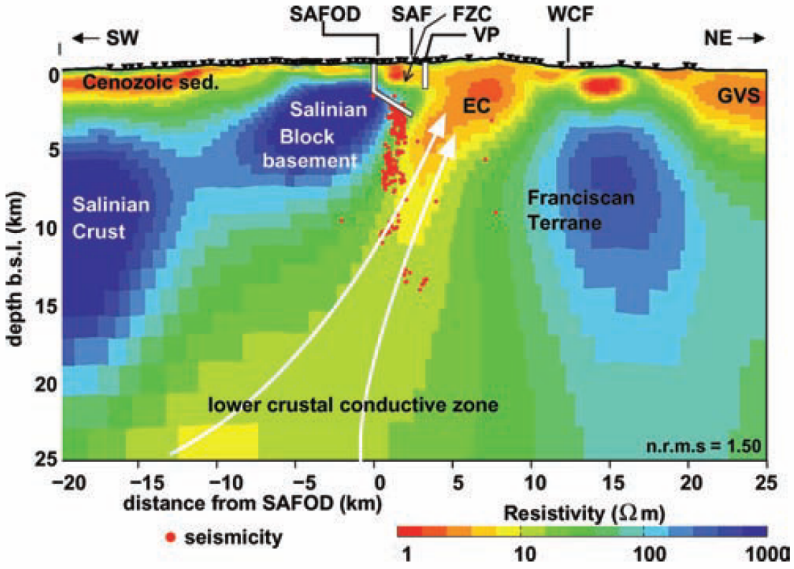

Figure 2.8: High resolution MT resistivity model from 2D inversion near the SAFOD along the central parts of profile ② (cf. Fig. 2.6; Becken et al., 2008b). The low-resistive zone linking the upper-crustal eastern conductor (EC) with the lower-crustal to upper-mantle high-conductivity zone (HCZ) images possible pathways for fluids upwelling from mantle depths (indicated by white arrows) and penetrating the SAF system from the side. The model also recovers the shallow fault-zone conductor (FZC) imaged by previous MT studies (e.g. Unsworth et al., 1997). VP Varian–Philips well, WCF Waltham Canyon fault, GVS Great Valley sequence; red dots indicate the seismicity (Thurber et al., 2006) within 3 km distance from the profile.

possible that these fluids contribute to fault creep northwest of Parkfield (e.g. Fulton & Saffer, 2009). The model also recovers the shallow fault-zone conductor (FZC) imaged by previous MT studies, which focused on the near-surface structure of the SAF system (e.g. Unsworth et al., 1997, 1999; Unsworth & Bedrosian, 2004).

Although data points of some sites showing significant 3D characteristics were down-weighted, not all parts of the data could satisfyingly be explained with 2D inversion, particularly in the southern part of the array. Therefore, Becken et al. (2011) interpolated the 2D inversion results onto a 3D grid and compared 3D forward modelling responses of this model with the measured data. The 3D forward model can reproduce the measured data remarkably well, even some of the 3D features. However, 3D inversion is required to transform all aspects of the 3D data into model structure.

3 3D inversion and forward modelling

With advancing computational resources, three-dimensional (3D) inversion techniques have become practical in recent years and are now a more widely used tool for magnetotelluric (MT) data interpretation. A number of 3D inversion programs using various approaches for both forward modelling and inversion have been developed (e.g. Newman & Alumbaugh, 2000; Zhdanov et al., 2000; Mackie et al., 2001; Sasaki, 2001; Farquharson et al., 2002; Sasaki, 2004; Siripunvaraporn et al., 2005; Sasaki & Meju, 2006; Han et al., 2009; Avdeev & Avdeeva, 2009; Siripunvaraporn & Egbert, 2009; Egbert & Kelbert, 2012). However, full 3D inversion still is very challenging numerically and practically, as typical data sets of modern regional MT studies are huge, affected by noise, and the inversion problem is strongly ill-posed and non-unique.

Many of the existing 3D MT studies focus on local geological features with model grids spanning up to a few tens of square kilometres for investigations of geothermal areas and/or small volcanic complexes (Árnason et al., 2010; Cumming & Mackie, 2010; Heise et al., 2008; Ingham et al., 2009; Newman et al., 2008), ore deposits (Farquharson & Craven, 2009; Tuncer et al., 2006; Xiao et al., 2010), and hydrocarbon reservoirs (He et al., 2010). These targets represent spatially limited structures, which usually have a fairly good station coverage compared to model mesh sizes. Other surveys concentrate on investigating larger scale tectonic structures, e.g. extended volcanic complexes (Hill et al., 2009; Kelbert et al., 2012) and major fault systems (Meqbel, 2009), or a series of major geological units (Bertrand et al., 2012a,b; Heise et al., 2010; Patro & Egbert, 2008, 2011; Türkoğlu et al., 2009; Zhdanov et al., 2010).

The above-mentioned MT studies are based on measurements sampled at 19 (Xiao et al., 2010) and up to 220 (Heise et al., 2010) sites and spanning a period range of 2 to 5 decades. Most of these data sets provide an areal station distribution, but Bertrand et al. (2012b), Meqbel (2009), Patro & Egbert (2011) and Xiao et al. (2010) worked with data from single, two intersecting, and two parallel profiles, respectively. In 3D environments, all four complex components of the impedance tensor (Z) contain information about the subsurface. However, Newman et al. (2008), Tuncer et al. (2006) and Zhdanov et al. (2010) used only the off-diagonal tensor elements for their inversions. Newman et al. (2008) found, that integrating Zxx and Zyy into the data set degrades the performance of the inversion due to the lower magnitudes and therefore lower signal-to-noise-ratios of these elements. Patro & Egbert (2011) compare full-tensor inversion models with results from off-diagonal impedances and magnetic transfer functions only. Recently, first results from joint inversion of impedances and magnetic transfer

functions of field have been presented by Kelbert et al. (2012).

Contrary to 2D modelling, transfer function estimates are often directly taken as input for 3D inversion without making assumptions with respect to strike directions or coordinate systems. The underlying coordinate system matters, however, if only a subset of the impedance tensor is inverted. Árnason et al. (2010), Bertrand et al. (2012a) and Patro & Egbert (2011) present inversion results with data and model grid rotated to the predominant geologic strike direction of the survey area. Árnason et al. (2010) argue that this facilitates a better resolution of the subsurface. Data errors are also handled very differently by various authors. Árnason et al. (2010), Farquharson & Craven (2009), and Patro & Egbert (2008) use the statistically determined variances of the impedance tensor elements; other authors combine impedance variances with pre-set error floors (Bertrand et al., 2012a; Ingham et al., 2009; Meqbel, 2009; Patro & Egbert, 2011; Tuncer et al., 2006; Türkoğlu et al., 2009), or use fixed errors (i.e. a percentage of the data value) (He et al., 2010; Heise et al., 2008, 2010; Hill et al., 2009; Newman et al., 2008; Xiao et al., 2010).

Different approaches have been suggested to handle static shift in 3D inversions. Árnason et al. (2010) and Cumming & Mackie (2010) correct the impedances prior to inversion using time-domain electromagnetic measurements. Heise et al. (2008, 2010), Hill et al. (2009), Ingham et al. (2009) remove distortion from the transfer functions by a tensor decomposition method described by Bibby et al. (2005), arguing that the top-layer cells of the model are too large to properly account for static shift (Heise et al., 2010). Other workers explicitly assume that the 3D inversion solves the problem by adding compensating structures to the surface layers (Farquharson & Craven, 2009; Newman et al., 2008; Xiao et al., 2010). 3D inversion codes solving for static shift as an additional, independent parameter have been demonstrated for synthetic data (Sasaki, 2004; Sasaki & Meju, 2006). Recently Avdeeva et al. (2012) presented 3D joint inversion for subsurface resistivity and galvanic distortion parameters and its successful application to a real world data set.

Model validation or appraisal includes (i) using only subsets of observation sites (Ingham et al., 2009) and period ranges (Farquharson & Craven, 2009; Newman et al., 2008), (ii) varying regularization (smoothing) parameters (Heise et al., 2010; Patro & Egbert, 2008, 2011), (iii) forward modelling sensitivity tests for particular (isolated) features of the inversion result (Bertrand et al., 2012a; Hill et al., 2009; Kelbert et al., 2012; Xiao et al., 2010), and (iv) comparison of 3D forward modelling of principle model structures (Heise et al., 2008; Meqbel, 2009; Tuncer et al., 2006). In addition, a considerable number of 3D models have been examined in view of 2D inversion results, based on subsets of data (Bertrand et al., 2012a; Cumming & Mackie, 2010; Farquharson & Craven, 2009; He et al., 2010; Heise et al., 2010; Hill et al., 2009; Ingham et al., 2009; Newman et al., 2008; Tuncer et al., 2006; Türkoğlu et al., 2009), particularly for data sets recorded along profiles (Bertrand et al., 2012b; Meqbel, 2009; Patro & Egbert, 2011). Most authors found the main structural features of 2D and 3D modelling

results in good agreement, provided the data were prepared appropriately for 2D modelling. However, other studies revealed significant differences between 2D and 3D results which are usually attributed to the limitations of the 2D interpretation (e.g. Heise et al., 2010; Meqbel, 2009; Patro & Egbert, 2011).

The California MT array data set considered here comprises more than 250 MT sites covering a rectangular area of 130 km × 70 km in the vicinity of the San Andreas Fault Observatory at Depth (SAFOD) near Parkfield in central California, USA (Fig. 3.1). From extensive 2D inversion, Becken et al. (2008b, 2011) derived impressive images of along-strike variations of the electrical conductivity structure beneath the San Andreas fault (SAF) system (cf. sec. 2.2). The main interest of the studies presented here, is to better understand 3D effects in the data and 3D inversion of real MT data in practice. For 3D inversion and forward modelling the ModEM package of Egbert & Kelbert (2012) was used. In the framework of my PhD project, I implemented inversion of phase tensors and apparent resistivities and phases into the 3D MT inversion scheme of ModEM.

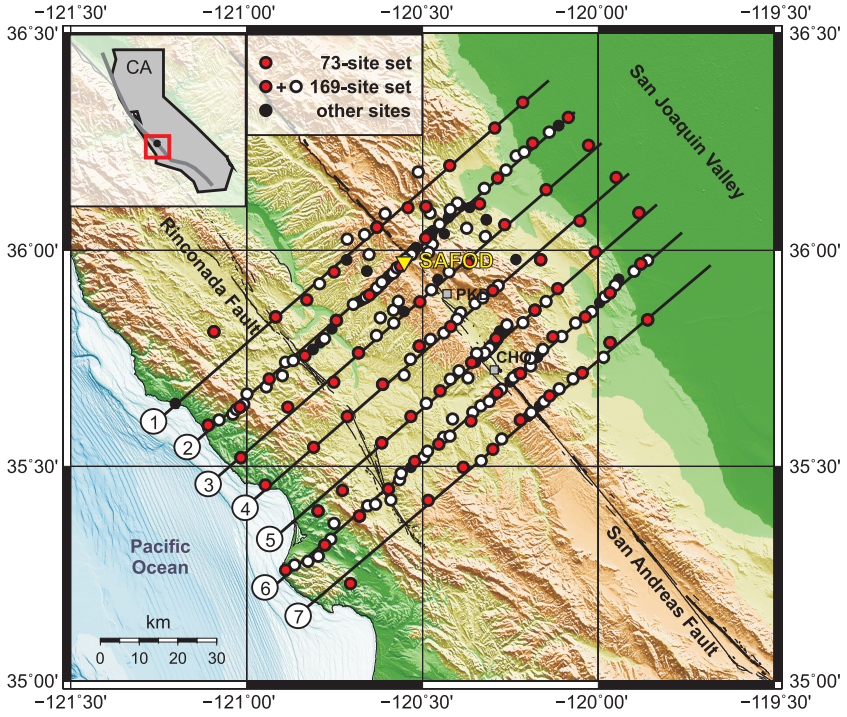

Figure 3.1: More than 250 MT sites (circles) were deployed along seven profiles crossing the San Andreas fault in the vicinity of Parkfield and Cholame. The MT survey covers an area of 130 km × 70 km. For 3D inversion two data subsets comprising 73 sites (red circles) and 169 sites (red + white circles) were used. The location of the San Andreas Fault Observatory at Depth (SAFOD) is indicated by a yellow triangle. CHO Cholame, PKD Parkfield.

3.1 Data properties of the California MT array

The California MT array data set comprises measurements from more than 250 sites in the vicinity of the San Andreas Fault Observatory at Depth (SAFOD) near Parkfield in central California (Fig. 3.1). The MT sites are distributed along seven profiles across the SAF with a distance between neighbouring profiles of roughly 10 km. Site spacing along the profiles varies from 0.5 km in the central parts across the SAF to approximately 10 km towards the profile ends. For 3D interpretation of the data, I use periods in the range between 0.088 s and 11,585 s. Details on data acquisition and time-series processing are described by Becken et al. (2008b, 2011) and are summarized in section 2.2.

To set up the data set for 3D inversion, MT sites were selected from the array aiming at a uniform site spacing of approximately 2 km in the densely sampled areas. Where site density of the array was higher sites were preferred which provide high data quality, cover a wide period range and/or where both impedances and vertical magnetic transfer functions (VTF) are available. The final data set consists of 169 sites (red + white circles in Fig. 3.1). In addition, a 73-site subset was specified which provides a uniform site distance of approximately 10 km over the entire array (red circles).

As outlined in section 2.2, the data set exhibits a predominant geo-electric strike direction of N41°W (Becken et al., 2011), which is consistent with the strike direction of the regional geology (Page et al., 1998). However, significant influence of 3D subsurface structures on the data set is indicated by the large number of data points where the phase tensor beta criterion (Caldwell et al., 2004) significantly deviates from zero (Fig. 3.2). For the 169-site data set, phase tensor (PT) beta values range between $-16°$ and $+8°$ and exceed $\pm 1°$ at 50 % and $\pm 3°$ at 25 % of the data points (Fig. 3.2a). At most sites, the impact of 3D structures manifests at periods > 1 s and is most pronounced in the range between 10 s and 2000 s (Fig. 3.2b). Closer inspection of PT data behaviour across the MT array reveals that significant influences of 3D subsurface structures can be found in all parts of the array for periods above 10 s (blue and red colours in Fig. 3.2c).

At periods above 100 s, PT ellipses in Figure 3.2(c) exhibit a consistent alignment of their axes over large parts of the MT array. This behaviour indicates that despite the 3D nature of the subsurface the electromagnetic fields have a predominant polarization direction at long periods, which is either parallel or perpendicular to the regional geo-electric strike. In addition, orientations of the major PT axes flipping by roughly 90° at the edge of the San Joaquin valley about 100 km inland indicate a pronounced lateral conductivity contrast at intermediate depths in this area (181 s).

A very obvious regional scale structure which contributes to the uniform polarization of the electromagnetic fields at long periods is the Pacific Ocean. The high conductivity contrast between the conductive ocean and the resistive land masses has a well-known effect on the

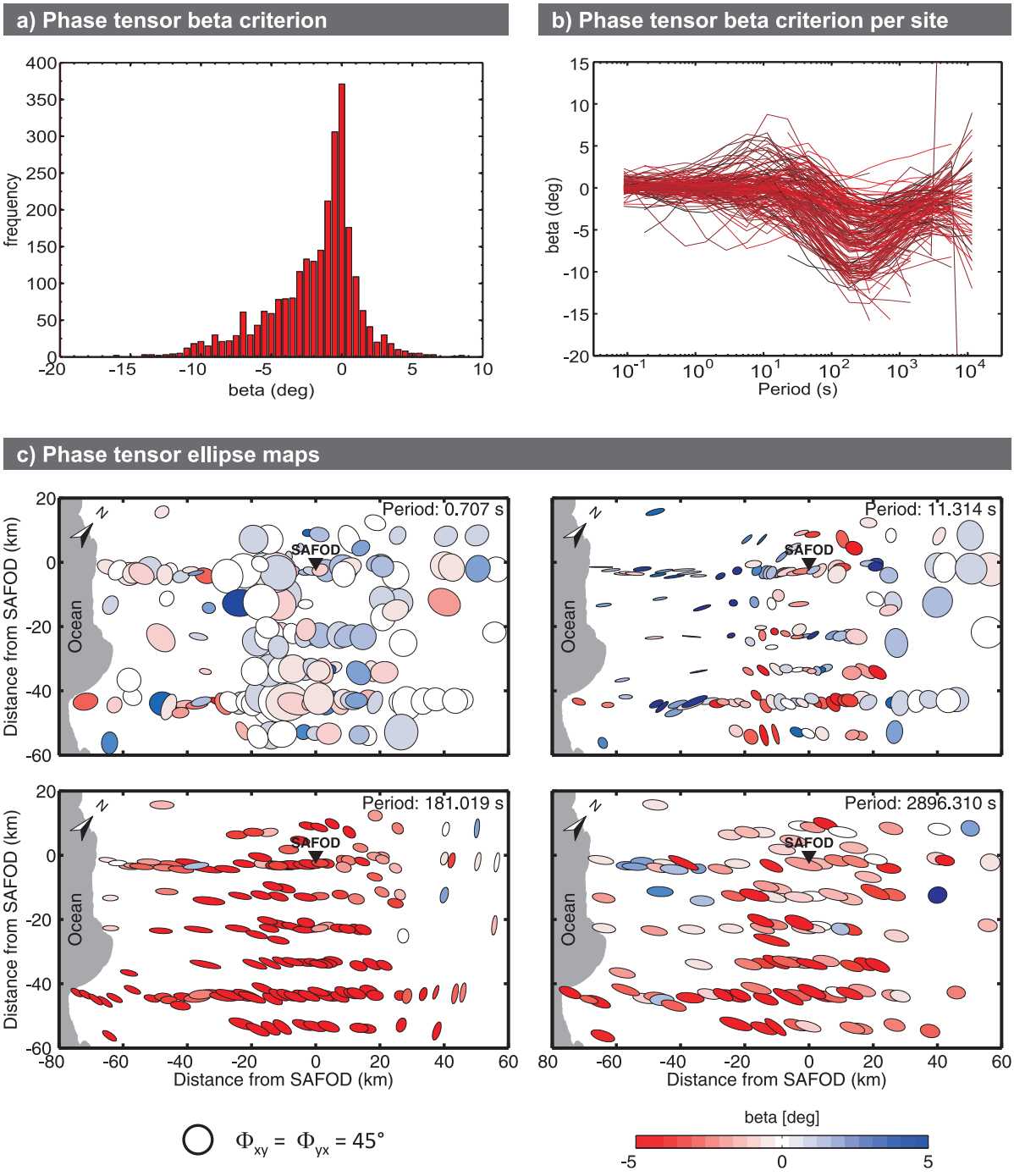

Figure 3.2: Phase tensor (PT) properties of the California data set. **(a)** Distribution of PT beta values for the 169-site data set. 50 % of the points have absolute values above 1°, 25 % above 3°. **(b)** PT beta values vs. period curves vary similarly at each of the 169 sites. Forming a very narrow band around zero at the shortest periods, beta amplitudes increase for periods > 1 s. The strongest influence of 3D structures is observed in the period range between 10 s and 2,000 s. **(c)** PT ellipse map for periods of 0.71 s, 11.3 s, 181 s, and 2,896 s. PT beta values significantly deviating from zero (red and blue colouring) indicate influences of a 3D subsurface for periods > 10 s. At long periods (181 s, 2,896 s), high ellipticities and alignment of PT major axes over larger parts of the array indicate a pronounced polarization of electromagnetic fields parallel or perpendicular to strike (N41°W).

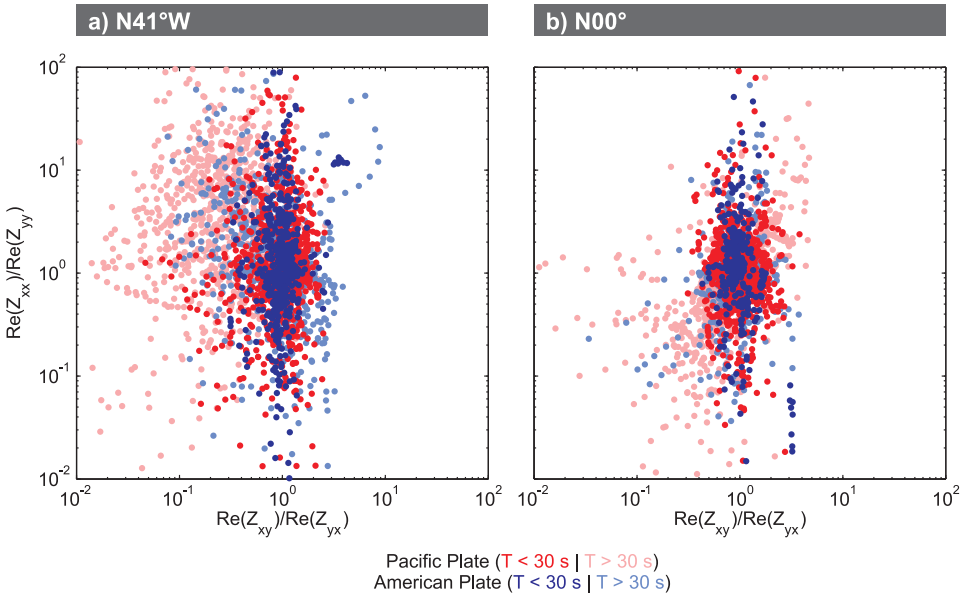

Figure 3.3: Ratios of impedance tensor elements (real parts). **(a)** Data are rotated to N41°W, i.e. the x-direction is roughly parallel to the coast line. For sites located on the Pacific plate (and close to the ocean), the Zyx-component is up to 2 orders of magnitude larger than the Zxy-component. The effect is largest for periods > 30 s (pink dots) but visible at some sites for the shorter periods (red dots). For sites located on the American plate, the distribution is more uniform, the off-diagonal impedance tensor ratios cluster around 1 (light and dark blue dots). **(b)** In the geographic coordinate system, the narrower cluster illustrates that diagonal and off-diagonal components have more similar amplitudes.

impedances, as they split up in small components (currents parallel to the coastline) and large components (currents across the ocean-land contrast) when rotated to the regional geo-electric strike direction. Figure 3.3(a) shows that the ocean effect is clearly visible in the data from California for periods > 30 s. If data are aligned with geographic coordinates, the influence of the ocean distributes evenly between the components. The two off-diagonal impedance components have similar amplitudes Figure 3.3(b).

The Pacific Ocean representing a large conductive body has also a significant influence on VTF data expressing in induction arrows pointing away from the coastline (Wiese convention) at long periods (Fig. 3.4). While for 11.3 s the conductivity contrast along the coastline affects only sites located directly at the coast, the influence of the ocean is visible at more and more sites further inland towards longer periods. For periods above 1,000 s the induction arrows point away from the ocean for most parts of the array and illustrate the far-reaching influence of the ocean.

After processing data are provided in a coordinate system which is aligned with geographic directions, i.e. the x-axis points towards geographic north. For 3D inversion, data were used

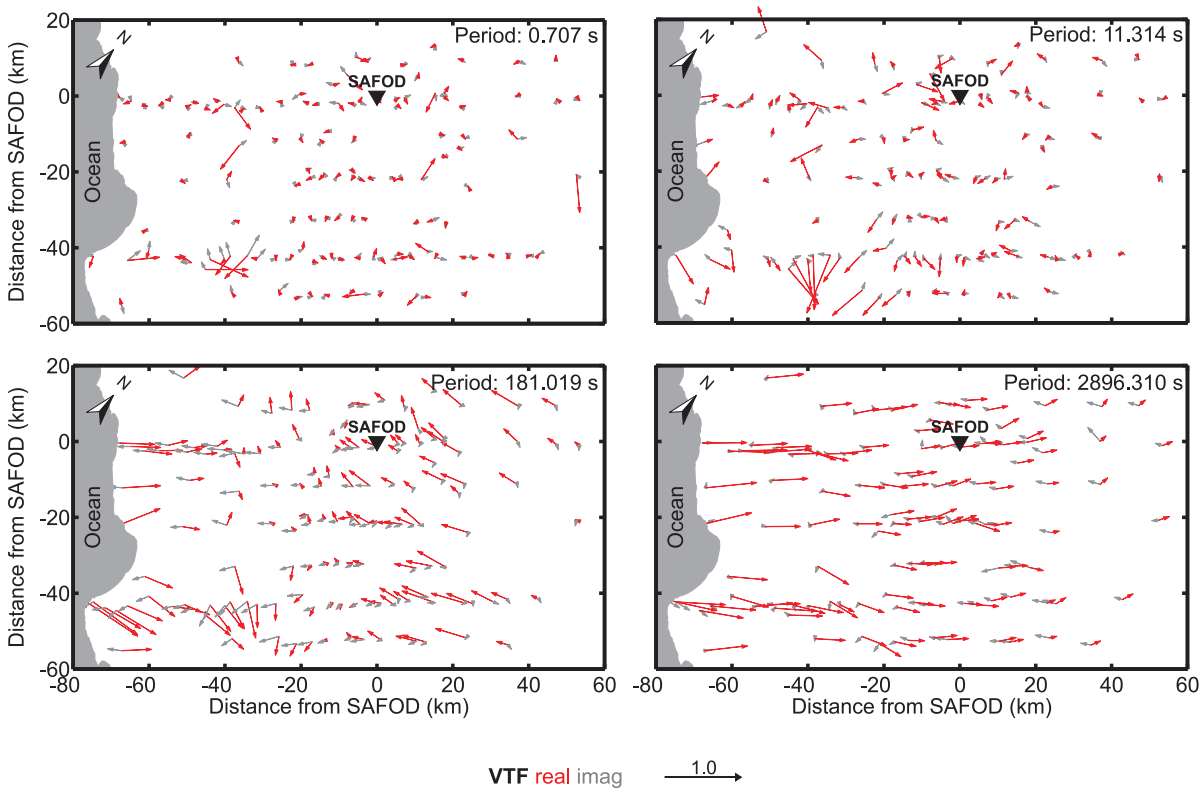

Figure 3.4: Vertical magnetic transfer functions (VTF) for periods of 0.71 s, 11.3 s, 181 s, and 2896 s (Wiese convention). For periods > 1000 s the influence of the conductive seawater of the Pacific Ocean is clearly visible at all sites of the array.

in the original geographic coordinate system as well as rotated to the predominant regional geo-electric strike direction with the x-axis pointing parallel to strike towards N41°W.

In preparation for 3D inversion, impedance tensor elements and VTF data were smoothed independently for both data orientations using a spline function and interpolated to 18 periods distributed evenly on a logarithmic scale in the range between 0.088 s and 11,585 s. Data subsequently underwent manual inspection and data points deviating significantly from the original curves were excluded from the data set. As data quality is high throughout the array, impedance data at most sites cover the full period range (Fig. 3.5). Limitations of the period range are mainly related to the site setup. In total, four-component impedance data are present at 85.2 % of the 3042 data sampling points (169 sites × 18 periods, Fig. 3.5a) and at 1181 of the 1314 points (89.9 %) of the 73-site subset. VTFs were included at 147 sites and 67 sites, respectively, omitting some heavily distorted or noisy sites. VTF data cover a similar period range as the impedance data (Fig. 3.5b).

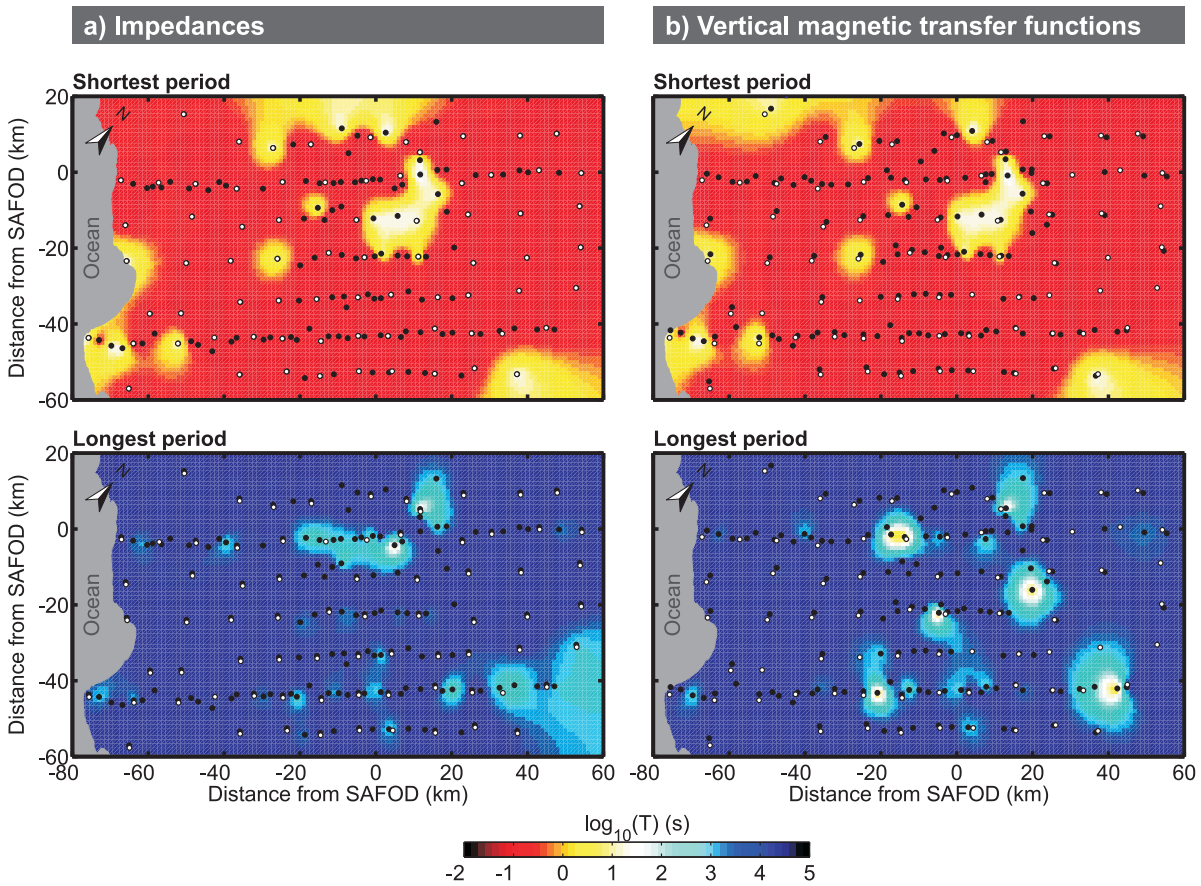

Figure 3.5: Period range of the California MT array 169-site data set in 3D inversion indicated by shortest (top) and longest (bottom) period for each site; in between data are continuous. At most sites, the full period range could be used for both **(a)** impedances and **(b)** vertical magnetic transfer functions.

3.2 ModEM3DMT

In the framework of this thesis I used the Modular Electromagnetic Inversion system (ModEM, Egbert & Kelbert, 2012) for 3D forward modelling and inversion of MT data. The ModEM package comprises computer codes for modelling and inversion of frequency-domain electromagnetic (EM) data with gradient-based search methods. Currently implemented methods solve for 2D and 3D MT, controlled source electromagnetics (CSEM) and global induction problems. The 3D MT modelling scheme (ModEM3DMT) uses a discrete formulation of Maxwells equations (cf. (1.1)-(1.4), p. 1) based on a finite difference approach. Within this work, I used the non-linear conjugate gradient (NLCG) inverse search algorithm. In the following, I will shortly summarize the 3D inversion of MT data with ModEM3DMT and describe the implementation of two new data types – phase tensors and apparent resistivities & phases – into ModEM3DMT. More general and detailed descriptions of the solution of the MT forward and inverse problems and their implementation can be found in e.g. Newman & Alumbaugh (1997), Newman & Alumbaugh (2000), Zhdanov et al. (2000), Siripunvaraporn et al. (2005), Egbert & Kelbert (2012).

The magnetotelluric modelling problem is described by the following equation

$$\mathbf{d} = \mathbf{f}(\mathbf{m}) + \delta, \tag{3.1}$$

where the data $\mathbf{d}$ are reproduced within a distance δ by a forward operator $\mathbf{f}$ working on the model parameters $\mathbf{m}$. The term $\mathbf{f}(\mathbf{m})$ describes the forward problem, in which the electric and magnetic fields are calculated for a known discretized underground $\mathbf{m}$. Solving the inverse problem, a subsurface model has to be found which explains the data, i.e. which minimizes the objective or penalty function

$$\Psi(\mathbf{m}, \mathbf{d}) = (\mathbf{d} - \mathbf{f}(\mathbf{m}))^T {\mathbf{C_d}}^{-1} (\mathbf{d} - \mathbf{f}(\mathbf{m})), \tag{3.2}$$

where $\mathbf{C_d}$ is the covariance of data errors. Solving the MT forward problem requires a large number of model cells to avoid an underparametrization of the system (e.g. Newman & Alumbaugh, 1997). As a consequence, the inverse problem is underdetermined as a large number of unknown model parameters is opposed by a much smaller number of data points. In order to stabilize the solution of the inverse problem and to reduce the number of possible models which would explain the data a model regularization term

$$(\mathbf{m} - \mathbf{m_0})^T {\mathbf{C_m}}^{-1} (\mathbf{m} - \mathbf{m_0}) \tag{3.3}$$

is appended to the penalty function (3.2):

$$\Psi(\mathbf{m},\mathbf{d}) = (\mathbf{d}-\mathbf{f}(\mathbf{m}))^T {\mathbf{C_d}}^{-1}(\mathbf{d}-\mathbf{f}(\mathbf{m})) + \lambda(\mathbf{m}-\mathbf{m_0})^T {\mathbf{C_m}}^{-1}(\mathbf{m}-\mathbf{m_0}), \tag{3.4}$$

where $\mathbf{m_0}$ is a set of prior model parameters, $\mathbf{C_m}$ is the model covariance and describes the model smoothness, and λ is a trade-off parameter. This model regularization removes solutions that are too rough and/or too far away from the prior model by imposing an additional constraint on the data fit. The trade-off parameter λ defines the balance between data fit and model smoothness. In the progress of inversion the model smoothness constraint is reduced by reducing λ. In the beginning, inversion is mainly driven by model smoothness; towards the end it is dominated by the data misfit.

In ModEM3DMT, the data covariance $\mathbf{C_d}$ is a diagonal matrix which contains the inverse of the squared data errors, i.e. the data variances,

$$\mathbf{C_d} = diag(1/{e_i}^2). \tag{3.5}$$

The model covariance $\mathbf{C_m}$ is constructed as a sequence of one-dimensional (1D) smoothing and scaling operators (G. Egbert, pers. comm.):

$$\mathbf{C_m} = \mathbf{c}_x\mathbf{c}_y\mathbf{c}_z\mathbf{c}_z^T\mathbf{c}_y^T\mathbf{c}_x^T \tag{3.6}$$

$\mathbf{C_m} = {\mathbf{C_m}}^{1/2}(\mathbf{C}_m^{1/2})^T$ is symmetric. The 1D smoothing operators are block-diagonal, e.g. for the x-direction

$$\mathbf{c_x} = \begin{pmatrix} c_{11}^x & & & \\ & c_{21}^x & & \\ & & \ddots & \\ & & & c_{NyNz}^x \end{pmatrix}, \tag{3.7}$$

with one block for each x-yz cell pair of the model mesh with Ny and Nz cells in y- and z-directions, respectively. Each block c_{jk}^x is constructed by an autoregression scheme:

$$c_{jk}^x = \begin{pmatrix} 1 & & & \\ \alpha_x & 1 & & \\ \alpha_x^2 & \alpha_x & 1 & \\ \vdots & & & \ddots \\ \alpha_x^{Nx-1} & & \cdots & 1 \end{pmatrix}. \tag{3.8}$$

The model covariance parameter α_x determines the model smoothness in x-direction; analogue, smoothing is set up for y- and z-directions ($0 \leq \alpha_i \leq 1$).

The penalty function is minimized using a least squares approach. Therefore the forward

problem $\mathbf{f}(\mathbf{m})$ has to be linearized using a Taylor series expansion:

$$\mathbf{f}(\mathbf{m}+\Delta\mathbf{m}) = \mathbf{f}(\mathbf{m}) + \left.\frac{\partial \mathbf{f}(\mathbf{m})}{\partial \mathbf{m}}\right|_{\mathbf{m}} \Delta\mathbf{m} = \mathbf{f}(\mathbf{m}) + \mathbf{J}\Delta\mathbf{m}, \tag{3.9}$$

where $\Delta\mathbf{m}$ is a small perturbation around $\mathbf{m_0}$ and $\mathbf{J}$ is the Jacobian or sensitivity matrix. The Jacobian describes the sensitivity of the predicted data $\mathbf{d} = \mathbf{f}(\mathbf{m})$ with respect to small changes of the model parameters.

The NLCG inversion scheme solves iteratively for the subsurface model. At each inversion iteration n, the inversion scheme searches for the steepest gradient of the penalty function (3.4). The gradient of (3.4) at the iteration n is given by

$$\left.\frac{\partial \Psi}{\partial \mathbf{m}}\right|_{\mathbf{m}_n} = -2\mathbf{J}^T\mathbf{r} + 2\lambda {\mathbf{C}_\mathbf{m}}^{-1}\Delta\mathbf{m}_n, \tag{3.10}$$

where $\mathbf{r} = (\mathbf{f}(\mathbf{m}_n) - \mathbf{d})^T\mathbf{C}_d$ is the data residual and $\Delta\mathbf{m}_n = \mathbf{m}_n - \mathbf{m}_0$ is the distance of the current model $\mathbf{m}_n$ to the prior model. Subsequently, the gradient is used to set up a new conjugate search direction in the model space for inversion step $n+1$ which is given by the direction where the gradient is largest.

The ModEM package is implemented in a modular way to facilitate code development. The basic data objects within ModEM are the data vector $\mathbf{d}$, model parameters $\mathbf{m}$, and the solution for the electric field $\mathbf{e}$; if required, the magnetic field is derived from the electric field at observation points. The modules are organized in three layers (Fig. 3.6). The basic layer, depicted on the left hand side, comprises the basic discretization and numerical solution approach used for the forward problem. On the right hand side, you find the more generic routines which are directly applicable to a wide range of EM inverse problems. The interface layer in the centre hides details on the implementation from the right hand side. Each layer contains several boxes representing modules or groups of modules of the actual implementation. Modules such as the inversion algorithms are independent of the data type and discretization. Hence, implementing the new data types – the phase tensor (Caldwell et al., 2004) and apparent resistivity & phase – requires changes to the interface which includes the Data Functionals module (cf. Fig. 3.6); all other modules are independent of these modifications.

The ModEM3DMT package is coarsely parallelized based on the distribution of forward modelling and sensitivity calculations on several processors. The parallel computation reduces both memory requirements and run times. The calculations are parallelized both over frequencies and the two orthogonal source field polarizations as each of them requires a separate forward calculation. Maximum parallelization, i.e. minimum computation time, is achieved by distributing the modelling problem on $2 \cdot N_p$ processors, where N_p is the number of periods used

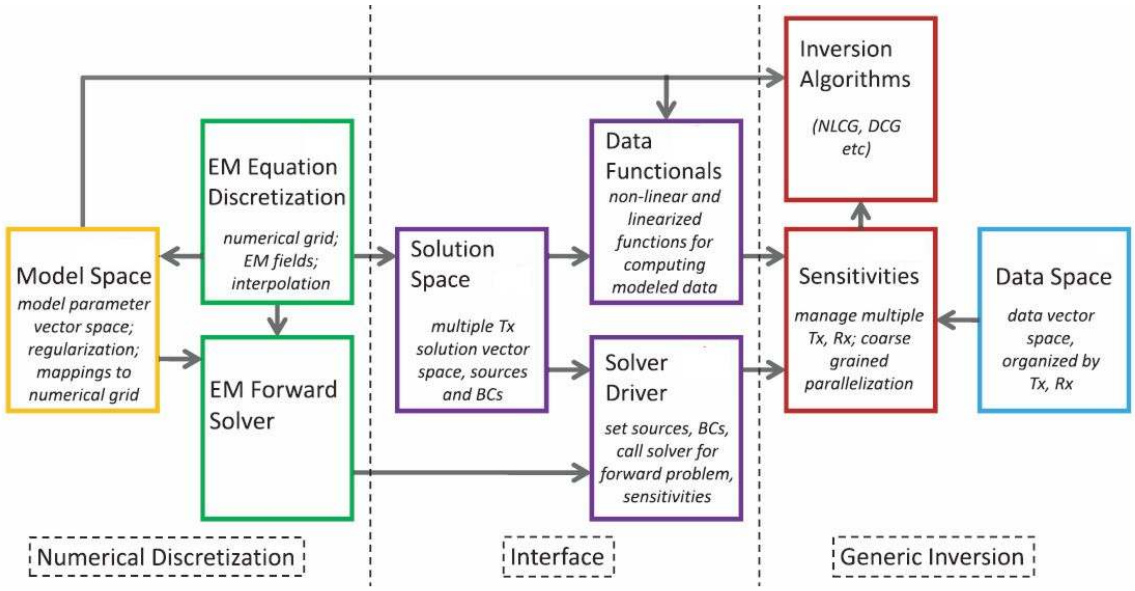

Figure 3.6: Schematic overview of the Modular Electromagnetic Inversion (ModEM) system. Boxes represent modules (or groups of modules in the actual implementation), with dependencies defined by arrows (modified from Egbert & Kelbert (2012)).

in forward calculation or inversion. Development and implementation of the parallelization of ModEM3DMT are described in Meqbel (2009).

3.2.1 Implementation of phase tensor and apparent resistivity & phase inversion

In the framework of this thesis, inversion of two new data types – the phase tensor (PT; Caldwell et al., 2004) and apparent resistivities & phases (RP) – was implemented into ModEM3DMT. As outlined in section 1.3, both data types provide advantages in the presence of galvanic distortion. PT data are always free of galvanic distortion (cf. (1.31), p. 9). In presence of static shift, downweighting of apparent resistivities vs. phases is a common procedure in 2D inversion to avoid static shift bias of the inversion results (e.g. Becken et al., 2011; Ritter et al., 2003; Tauber et al., 2003).

As described in the previous section, the integration of a new data type into ModEM requires modifications to the Data Functionals module (see interface layer in Fig. 3.6). First, the forward prediction and, secondly, the sensitivity calculation for the new data have to be implemented in order to account for the new data type.

The solution of the MT forward modelling problem is provided in form of the electric field $\mathbf{e}$ on the edges of the grid. The MT transfer functions at the observation points are estimated

from the solution of the electric fields and if required the model parameters by the function ψ

$$\mathbf{f}(\mathbf{m}) = \psi(\mathbf{e}(\mathbf{m}), \mathbf{m}). \tag{3.11}$$

The function ψ extracts (via interpolation and other mathematical basic functions) the corresponding values of electric and magnetic fields at the observation location to evaluate the model responses. Using (3.11) to rewrite the expression for the sensitivity matrix $\mathbf{J}$ (cf. (3.9)) yields

$$\mathbf{J} = \frac{\partial \mathbf{f}(\mathbf{m})}{\partial \mathbf{m}} = \frac{\partial \psi(\mathbf{e}(\mathbf{m}), \mathbf{m})}{\partial \mathbf{m}} = \frac{\partial \psi}{\partial \mathbf{e}} \frac{\partial \mathbf{e}}{\partial \mathbf{m}} + \frac{\partial \psi}{\partial \mathbf{m}} \tag{3.12}$$

or in matrix notation

$$\mathbf{J} = \mathbf{L}\mathbf{F} + \mathbf{Q}, \tag{3.13}$$

where

$$\mathbf{L} = \frac{\partial \psi}{\partial \mathbf{e}}, \quad \mathbf{F} = \frac{\partial \mathbf{e}}{\partial \mathbf{m}}, \quad \mathbf{Q} = \frac{\partial \psi}{\partial \mathbf{m}}. \tag{3.14}$$

$\mathbf{F}$ describes the dependency of the electric field on the model parameters, and $\mathbf{L}$ the dependency of the predicted data on the electric field. In 3D MT modelling, $\mathbf{Q}$ is zero, as the estimation of electric and magnetic fields at the observation points is not directly depending on the model parametrization. Hence, only $\mathbf{L}$ involves ψ and has to be implemented for the new data types.

Phase tensor (PT)

I implemented the inversion of PT data into ModEM3DMT in terms of tensor components Φ_{ij}. The PT (Φ) is derived from the impedance $\mathbf{Z} = \mathbf{X} + i\mathbf{Y}$ in terms of its real ($\mathbf{X}$) and imaginary ($\mathbf{Y}$) parts in a cartesian coordinate system (x_1, x_2, x_3):

$$\begin{pmatrix} \Phi_{11} & \Phi_{12} \\ \Phi_{21} & \Phi_{22} \end{pmatrix} = \frac{1}{\det \mathbf{X}} \begin{pmatrix} X_{22}Y_{11} - X_{12}Y_{21} & X_{22}Y_{12} - X_{12}Y_{22} \\ X_{11}Y_{21} - X_{21}Y_{11} & X_{11}Y_{22} - X_{21}Y_{12} \end{pmatrix}, \tag{3.15}$$

where $\det \mathbf{X} = X_{11}X_{22} - X_{21}X_{12}$ is the determinant of $\mathbf{X}$ (cf. sec. 1.2).

For inversion of PT, the term $\mathbf{L}$ in (3.13), i.e. the derivatives of the PT components with respect to the electric field have to be calculated. As $\Phi = \Phi(\mathbf{Z})$, the term $\mathbf{L}$ of the decomposition of the Jacobian (cf. (3.13)) can be split into

$$\mathbf{L}_\Phi = \frac{\partial \Phi}{\partial \mathbf{e}} = \frac{\partial \Phi}{\partial \mathbf{Z}} \frac{\partial \mathbf{Z}}{\partial \mathbf{e}} = \frac{\partial \Phi}{\partial \mathbf{X}} \frac{\partial \mathbf{X}}{\partial \mathbf{e}} + \frac{\partial \Phi}{\partial \mathbf{Y}} \frac{\partial \mathbf{Y}}{\partial \mathbf{e}}. \tag{3.16}$$

using the chain rule. To obtain $\mathbf{L}_\Phi$, I calculated the partial derivatives of the PT with respect

to the impedance tensor components $\frac{\partial \Phi_{ij}}{\partial Z_{ij}}$ and used the L-functionals of the impedances.

Each PT component Φ_{ij} depends on six of the eight impedance components. The derivatives $\frac{\partial \Phi_{ij}}{\partial X_{ij}}$ and $\frac{\partial \Phi_{ij}}{\partial Y_{ij}}$ are exemplarily given for the element Φ_{11} using the quotient rule:

$$
\begin{aligned}
\frac{\partial \Phi_{11}}{\partial X_{11}} &= \frac{1}{\det \mathbf{X}^2}(X_{22} \cdot (X_{22}Y_{11} - X_{12}Y_{21})) = \frac{1}{\det \mathbf{X}} X_{22}\Phi_{11} \\
\frac{\partial \Phi_{11}}{\partial X_{12}} &= \frac{1}{\det \mathbf{X}^2}(-Y_{21} \cdot \det \mathbf{X} - X_{21} \cdot (X_{22}Y_{11} - X_{12}Y_{21})) = -\frac{1}{\det \mathbf{X}}(Y_{21} + X_{21}\Phi_{11}) \\
\frac{\partial \Phi_{11}}{\partial X_{21}} &= \frac{1}{\det \mathbf{X}^2}(-X_{12} \cdot (X_{22}Y_{11} - X_{12}Y_{21})) = -\frac{1}{\det \mathbf{X}} X_{12}\Phi_{11} \\
\frac{\partial \Phi_{11}}{\partial X_{22}} &= \frac{1}{\det \mathbf{X}^2}(Y_{11} \cdot \det \mathbf{X} + X_{11} \cdot (X_{22}Y_{11} - X_{12}Y_{21})) = \frac{1}{\det \mathbf{X}}(Y_{11} + X_{11}\Phi_{11}) \\
\frac{\partial \Phi_{11}}{\partial Y_{11}} &= \frac{1}{\det \mathbf{X}^2} X_{22} \cdot \det \mathbf{X} = \frac{1}{\det \mathbf{X}} X_{22} \\
\frac{\partial \Phi_{11}}{\partial Y_{12}} &= 0 \\
\frac{\partial \Phi_{11}}{\partial Y_{21}} &= \frac{1}{\det \mathbf{X}^2}(-X_{12} \cdot \det \mathbf{X}) = -\frac{1}{\det \mathbf{X}} X_{12} \\
\frac{\partial \Phi_{11}}{\partial Y_{22}} &= 0
\end{aligned}
$$

The elements of $\mathbf{L}_\Phi$ for each PT component are obtained as linear combination of $\mathbf{L}$ of the six components of the impedance tensor involved with the partial derivatives as coefficients.

Note, the full PT contains four real valued components whereas the impedance tensor consists of four complex components. Within ModEM, complex data are represented as two vectors containing the real and imaginary part, respectively. The elements of $\mathbf{L}$ for complex data such as the impedance are of type complex. For impedances, the real and imaginary parts of the four complex $\mathbf{L}$-components contain the derivatives of real ($\mathbf{X}$) and imaginary ($\mathbf{Y}$) parts of the impedance, respectively. For data of the type real, such as PT, only the real part of $\mathbf{L}$ will be considered in operations including $\mathbf{J}$. Thus,

$$
\frac{\partial \Phi}{\partial \mathbf{e}} = \frac{\partial \Phi}{\partial \mathbf{X}} \Re \frac{\partial \mathbf{Z}}{\partial \mathbf{e}} + \frac{\partial \Phi}{\partial \mathbf{Y}} \Im \frac{\partial \mathbf{Z}}{\partial \mathbf{e}}. \tag{3.17}
$$

Apparent resistivity & phase (RP)

Apparent resistivities $\rho_a = \rho_a(\mathbf{Z})$ and phases $\phi = \phi(\mathbf{Z})$ are functions of the impedance tensor $\mathbf{Z} = \mathbf{X} + i\mathbf{Y}$ (see also sec. 1.2):

$$
\rho_{a,ij} = \frac{\mu_0}{\omega}|Z_{ij}|^2 = \frac{\mu_0}{\omega}(X_{ij}^2 + Y_{ij}^2) \tag{3.18}
$$

$$
\phi_{ij} = \arctan \frac{\Im(Z_{ij})}{\Re(Z_{ij})} = \arctan \frac{Y_{ij}}{X_{ij}}. \tag{3.19}
$$

In the following, indices i, j are omitted for clarity. Apparent resistivities and phases are a representation of the complex impedance data as amplitude and phase. Phases are linear quantities whereas apparent resistivities are usually considered on a logarithmic scale. Hence, I used $\ln(\rho_a)$ instead to yield a more linear behaviour of apparent resistivity data which is more similar to the phase behaviour.

$$\ln \rho_a = \ln(\frac{\mu_0}{\omega}) + \ln(X^2 + Y^2) \tag{3.20}$$

In addition, considering $\ln(\rho_a)$ instead of ρ_a provides advantages for data error settings and data weighting. This will be discussed in more detail in section 3.2.4.

Deriving **L**-components for apparent resistivities and phases, we can use the dependence of ρ_a and ϕ on **Z** using the chain rule

$$\mathbf{L}_\rho = \frac{\partial \ln \rho_a}{\partial \mathbf{e}} = \frac{\partial \ln \rho_a}{\partial \mathbf{Z}} \frac{\partial \mathbf{Z}}{\partial \mathbf{e}} = \frac{\partial \rho_a}{\partial \mathbf{X}} \frac{\partial \mathbf{X}}{\partial \mathbf{e}} + \frac{\partial \rho_a}{\partial \mathbf{Y}} \frac{\partial \mathbf{Y}}{\partial \mathbf{e}} \tag{3.21}$$

$$\mathbf{L}_\phi = \frac{\partial \phi}{\partial \mathbf{e}} = \frac{\partial \phi}{\partial \mathbf{Z}} \frac{\partial \mathbf{Z}}{\partial \mathbf{e}} = \frac{\partial \phi}{\partial \mathbf{X}} \frac{\partial \mathbf{X}}{\partial \mathbf{e}} + \frac{\partial \phi}{\partial \mathbf{Y}} \frac{\partial \mathbf{Y}}{\partial \mathbf{e}}. \tag{3.22}$$

Estimating the partial derivatives of ρ_a and ϕ with respect to real (X) and imaginary (Y) components of Z yields

$$\frac{\partial \ln \rho_a}{\partial Z} = \frac{1}{|Z|^2} \left(\frac{\partial \left(X^2 + Y^2\right)}{\partial X} + \frac{\partial \left(X^2 + Y^2\right)}{\partial Y} \right) = 2 \frac{X + Y}{|Z|^2} \tag{3.23}$$

for the logarithmic apparent resistivity and

$$\frac{\partial \phi}{\partial Z} = \frac{1}{1 + \left(\frac{Y}{X}\right)^2} \left(-\frac{Y}{X^2} + \frac{1}{X} \right) = \frac{X - Y}{X^2 + Y^2} = \frac{X - Y}{|Z|^2} \tag{3.24}$$

for the phase with $\frac{\partial \arctan(x)}{\partial x} = \frac{1}{1+x^2}$.

In terms of the complex **L**-functionals, equations (3.23) and (3.24) can be rewritten as

$$\mathbf{L}_\rho = \frac{\partial \ln \rho_a}{\partial \mathbf{Z}} \frac{\partial \mathbf{Z}}{\partial \mathbf{e}} = 2\Re \left(\frac{\mathbf{Z}^*}{|\mathbf{Z}|^2} \cdot \mathbf{L}_z \right) \tag{3.25}$$

$$\mathbf{L}_\phi = \frac{\partial \phi}{\partial \mathbf{Z}} \frac{\partial \mathbf{Z}}{\partial \mathbf{e}} = \Re \left(\frac{i\mathbf{Z}^*}{|\mathbf{Z}|^2} \cdot \mathbf{L}_z \right) \tag{3.26}$$

Forward and sensitivity calculation was implemented of the full tensor, i.e. eight apparent resistivity and phase components. For the diagonal components ($\rho_{a,xx}$, ϕ_{xx}, $\rho_{a,yy}$, ϕ_{yy}), however, both forward and **L**-component calculation require special treatment. In 1D and 2D situations, the diagonal elements of the impedance are zero both in real and imaginary parts. In these situations, the phase ϕ of the diagonal elements is undefined and $\log(\rho_a = 0) = -\infty$.

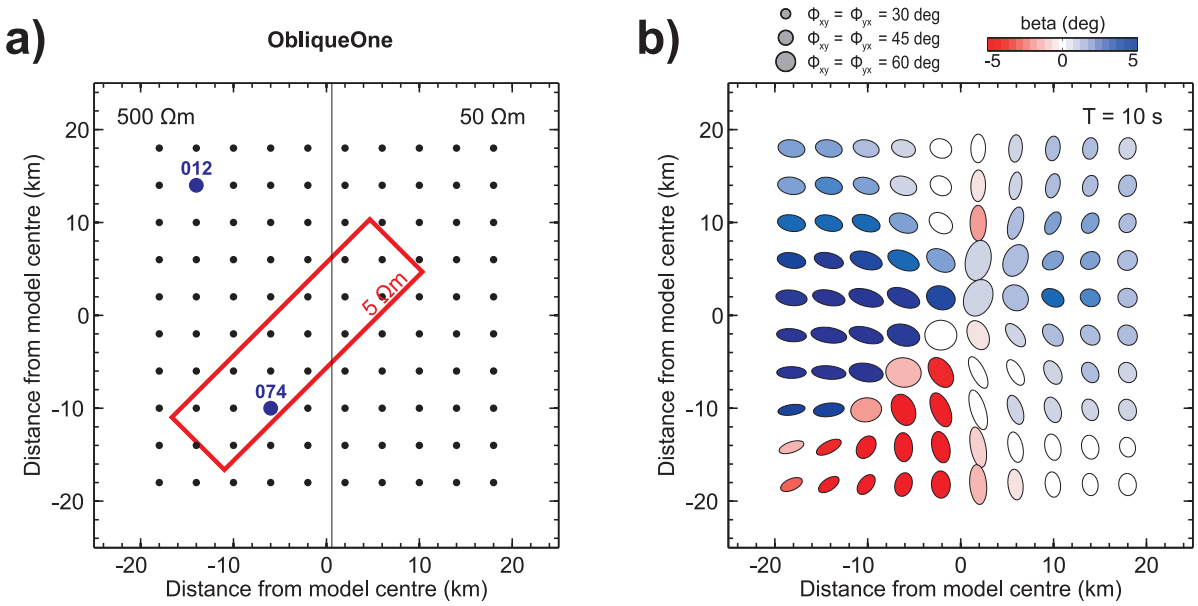

Figure 3.7: ObliqueOne 3D model and data set. **(a)** The main structural feature of the ObliqueOne model is a conductive 5 Ωm-block (red outline) of 30 km × 10 km × 9 km located with its top at 2.56 km depth in the central model domain. The major axis of the block is rotated 45° from the strike direction of the regional predominantly 2D resistivity structure consisting of two half-layers of 50 Ωm and 500 Ωm, respectively, between 0.1 km and 75.0 km depth. The top (< 0.1 km) and bottom (> 75 km) layers are set to 100 Ωm. forward data were obtained for a 10×10-site array (black dots) with a uniform site spacing of 4 km. Blue symbols indicate location of sites 012 and 074. **(b)** At periods > 1 s, the ObliqueOne data set exhibits 3D behaviour in wide parts of the array, indicated by PT beta-values deviating significantly from zero (blue and red colours).

Similarly, also the **L**-functionals with $|Z|$ in the denominator are undefined (see (3.24)). To avoid these complications, a floor value was applied to the diagonal impedances. Thus, initially the apparent resistivity and, in particular, the phase of these elements are biased by the minimum floor. With progress of inversion, however, this constraint becomes negligible. First inversion tests for synthetic data were successful. As appropriate choices for this floor and also data weighting have to be further tested, I only consider off-diagonal components of apparent resistivities and phases in the framework of this thesis.

3.2.2 3D ObliqueOne test model

The behaviour of 3D PT and RP inversion is illustrated using a synthetic data set generated with the 3D ObliqueOne model (Fig. 3.7a). The main feature of the ObliqueOne model is a conductive block ($10 \times 30 \times 9$ km^3, 5 Ωm) which strikes obliquely to a regional 2D structure (50 Ωm - 500 Ωm)). The logarithmic average of the regional 2D background structure is 158 Ωm. For forward modelling, the model structure was discretized by a 1 km × 1 km

mesh beneath the station array. In vertical direction, the thickness of the first layer is 20 m; subsequent layer thicknesses increase by a factor of 1.2. The oblique conductor is located in layers 19 to 26.

Phase tensor and impedance forward data were calculated for a 10 × 10-site array with 4 km site spacing, which covers the oblique conductor (OC). I used 16 logarithmically distributed periods between 0.01 s and 1,000 s. Prior to inversion, 3 % gaussian noise was added to the forward data. RP data were obtained from the noise-affected impedance data. The OC influences data between 0.1 s and 100 s. The strongest 3D effects are observed between 1 s and 100 s expressing in PT β values $> 3°$ in wide parts of the station array (Fig. 3.7b).

For 3D inversion of the ObliqueOne data sets I used a model grid with a horizontal discretization of 2 km × 2 km beneath the station array. The central domain of 21 × 21 cells is padded by 15 planes in all four horizontal directions, where cell sizes increase laterally by a factor of 1.3. The vertical discretization is the same as for the forward model. All inversions were started from homogeneous half-spaces using the starting model as prior model. Model covariance parameters $\alpha_x/\alpha_y/\alpha_z$ were initially set to 0.2 for all three directions.

3.2.3 Inversion of phase tensors

Data errors for PT inversion were defined relative to the absolute value of each PT component $|\Phi_{ij}|$. In addition, a constant error floor was applied to small PT values based on the properties of the PT in 1D and 2D situations. Above a 1D subsurface structure, i.e. a homogeneous or layered half-space, and in 2D situations when the coordinate system is aligned with the strike direction of the subsurface structure, the impedance tensor assumes an anti-diagonal form (Caldwell et al., 2004). Hence, also $\mathbf{X}^{-1}$ is anti-diagonal and the phase tensor in the rotated coordinate system has the diagonal form

$$\Phi^r = \begin{pmatrix} Y^r_{21}/X^r_{21} & 0 \\ 0 & Y^r_{12}/X^r_{12} \end{pmatrix} \tag{3.27}$$

The principal values of the phase tensor for 2D conductivity distribution are thus the tangents of the corresponding conventional impedance phases of the off-diagonal elements (cf. (1.17)). Based on this result, phase tensor error floors were defined as tangents of a constant angle ($\tan(\Delta\phi)$). For the following examples, I used data errors of 2 % of $|\Phi_{ij}|$ and a floor of $\tan(2°)$.

In a first step, I tested the influence of the prior model resistivity on the inversion outcome. PT inversion was started from a series of homogeneous half-space models between 10 Ωm and 1000 Ωm. The starting model was used as prior model.

The overall data fit in terms of RMS errors ranges between 1.50 and 1.02 for the inversion result of final iteration (Fig. 3.8a). The target RMS of 1.02 was only achieved for a prior model

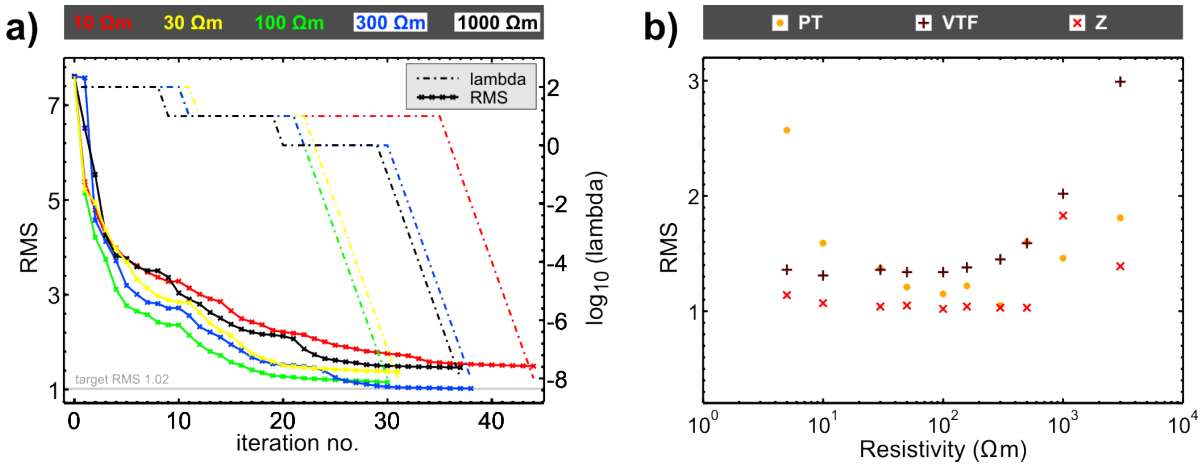

Figure 3.8: Convergence behaviour of 3D inversion for different prior models. **(a)** For 3D PT inversion, highest convergence rate and smallest final overall RMS values are achieved if prior model resistivities are close to the regional average resistivity. **(b)** Similar dependence of final RMS values on prior model resistivities is observed for VTF and Z inversion using the same inversion parameter settings.

resistivity of 300 Ωm. Higher final RMS values obtained for higher or lower prior resistivities are partially attributed to the inversion settings. The minimum RMS improvement required between two inversion iterations to continue (with the same trade-off parameter λ) was set to 0.02. If this value is reduced, e.g. to 0.001, PT inversion runs for a larger number of NLCG iterations and converges to the target RMS of 1.02 also for these prior models. However, a similar dependence of final RMS errors on prior model resistivities can be observed for impedance and VTF inversion using the same parameter setup (Fig. 3.8b). For all data types the lowest RMS values were achieved for prior model resistivities of 100 Ωm to 300 Ωm, i.e. close to the regional scale resistivity average of 158 Ωm. This behaviour indicates a general dependence of the inversion outcome on the prior model setup. This aspect of 3D inversion with ModEM will be discussed in more detail for the California MT array data set in section 3.4.3.

Closer inspection of the responses of the final inversion models (Fig. 3.9) shows that observed PT data are reproduced well over the entire frequency range. Shape and orientation of the PT ellipses as well as PT beta-estimates (dimensionality parameter, cf. sec. 1.2) are in very good agreement with the observed data. PT misfit values (lower panels in Figs 3.9a-c) distribute quite uniformly across the array, in particular for a prior model resistivities of 100 Ωm (Fig. 3.9b).

The corresponding final inversion models are displayed in Figure 3.10. All inversion results image both the 2D regional scale structure and the OC. PT data contain no direct information about absolute subsurface resistivities, but are only sensitive to variations of the resistivity structure. In general, the resistivity of the starting model serves as a pinpoint for the resistivity

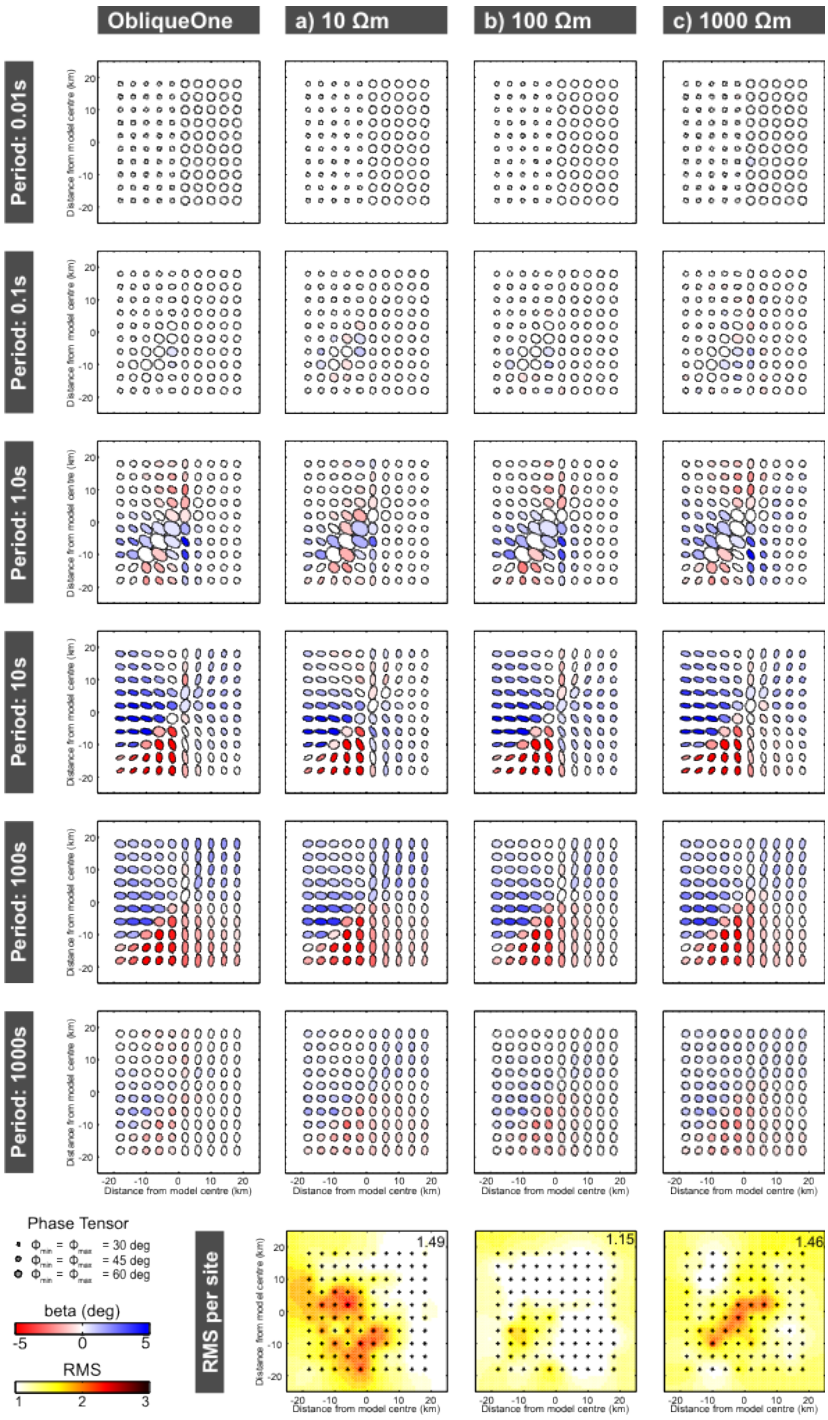

Figure 3.9: Comparison of ObliqueOne PT data (left column) and **(a)-(c)** final inversion responses for inversion runs with different prior models; lowermost panel shows RMS misfit values per site. PT data are reproduced over the entire period range similarly well in all inversion runs. Corresponding resistivity models are displayed in Figs 3.10a,c,e.

level of the subsurface image and biases the inversion result. This pinpointing effect of the starting model resistivity is enhanced in ModEM as the model regularization is based on a prior model, which forces the inversion algorithm to search for a solution close to the prior model (cf. (3.4)).

More detailed examination of the resistivity distribution for each of the final inversion models reveals that the bias affects particularly the regional scale structure, which extends beyond the station array. The location of larger-scale lateral variations represented by the contact plane of the two half-layers is well resolved independent of the prior model. Similarly, all results reproduce the magnitude of the resistivity contrast; the absolute resistivity values of the half-layers, however, depend on the prior model. Resistivities are underestimated for prior resistivities below the regional average of 158 Ωm and overestimated for higher prior model resistivities. In contrast, the absolute resistivity of the OC and adjacent areas is nearly independent of the prior model and close to the true value (5 Ωm) for all inversion models. The lateral extent of the OC is well constrained in the 3D PT inversion results independent of the prior resistivity (cf. profile slices in Fig. 3.10) as the OC is (i) horizontally fully covered by the station array and (ii) densely sampled by several sites both around and on top of the OC limiting maximum and minimum extent to the narrow space between these sites. These strict spatial limitations on the OC structure directly constrain the resistivity range of the subsurface in the vicinity of the OC. Hence, for small-scale structures within the site array, absolute resistivity levels can be constrained with PT inversion.

The depth location of vertical conductivity variations, e.g. upper and lower boundary of the OC, shows, however, a more significant dependence on the prior model as a consequence of the bias of the regional resistivity structure. Using prior resistivities below the regional average (10 - 100 Ωm, Figs 3.10a-c) for PT inversion, the OC is located at shallower depth than in the true model. For prior model resistivities above the regional average (300 Ωm and 1000 Ωm, Figs 3.10d-e) the image of the OC is moved to greater depth. The variability of the depth location of the OC reflects how the location of sensitivities within the model grid in inversion varies with the average model resistivity, i.e. on the penetration depth of the electromagnetic fields.

In addition to the depth variability, the image of the OC itself varies with the prior model resistivity. Forming a well-defined structure using 10 Ωm and 30 Ωm the image of the OC disaggregates into two features towards higher prior model resistivities (cf. profile slices in Fig. 3.10). These two features roughly describe the upper and lower edge of the OC. In between, resistivities are lower than the prior resistivity values indicating that these two conductive zones form a coherent structure. With increasing prior resistivities and hence increasing average resistivity of the inversion models the induction volume for a given period grows (skin effect). Since the model mesh is the same for all prior models, the induction volume comprises more cells towards higher prior model resistivities. In other words, the discretization of the investigated

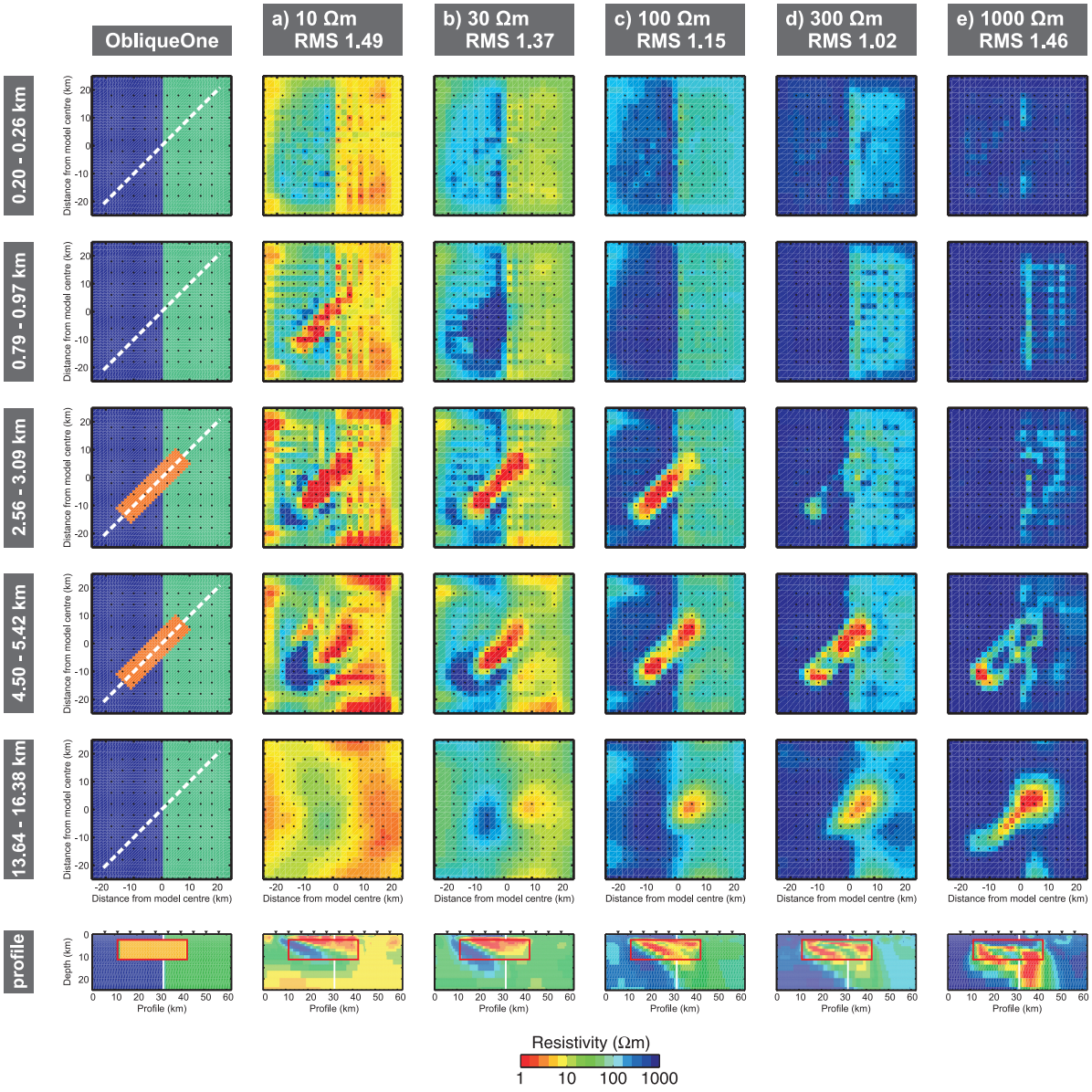

Figure 3.10: Resistivity models obtained from inversion of phase tensors (ObliqueOne data, cf. Fig. 3.7), displayed as horizontal slices at various depth and along a profile along the major axis of the oblique conductor (OC); the left column displays the original ObliqueOne model. **(a)-(e)** The dominant structures of the ObliqueOne model are resolved by all inversion results. The resistivity level and, hence, depth location of the the OC is biased by the resistivity of the prior model. Lateral conductivity variations, however, are similarly recovered in all results.

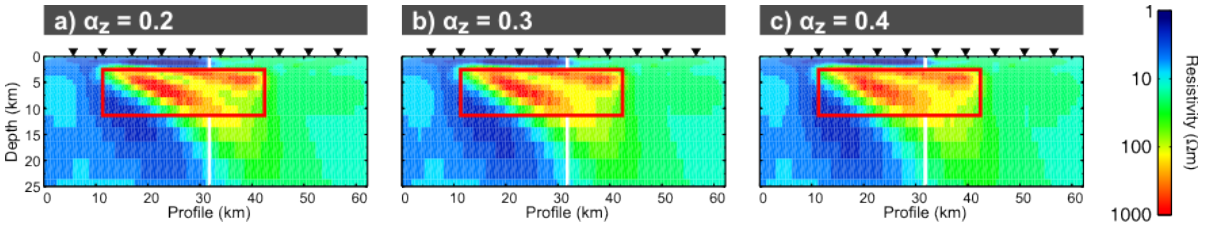

Figure 3.11: Influence of vertical smoothing on the outcome of PT inversion (prior model resistivity 100 Ωm). **(a)-(c)** The split of the image of the OC in PT inversion results using prior model resistivities of $\geq$ 100 Ωm reduces if smoothing in vertical direction (α_z) is increased ($\alpha_x = \alpha_y = 0.2$).

volume refines towards higher resistivities which effectively reduces the smoothness constraint. For the examples shown here, particularly the vertical continuity of the structures is reduced. The horizontal coherence of the OC is only little affected by the prior model as the horizontal mesh discretization (2 km $\times$ 2 km) is relatively coarse compared to the site spacing of 4 km. Applying higher smoothing in z-direction by increasing α_z, the split of the OC in PT inversion results is reduced (Figs 3.11a-c). Inversion of data which include information on absolute resistivities of the subsurface, e.g. impedances, is less dependent on the vertical regularization (not shown).

All in all, inversion of PT data is successful. As expected from the nature of PT data, the outcome of the inversion depends on the resistivity level of the prior model. Hence, it is essential to test a range of prior models. If structures are spatially well constrained by site layout and model parameter setup, PT inversion can recover the absolute resistivity of these features and surrounding regions. For large-scale structures extending beyond the station-covered area, most reliable inversion results are achieved providing a prior model with resistivities close to the regional average of the subsurface. Constraints on appropriate prior model resistivities can be obtained from RMS vs. prior resistivity distributions and inversion of other data types, which contain information about absolute resistivities, i.e. impedances and apparent resistivities.

3.2.4 Inversion of apparent resistivities and phases

Inversion of off-diagonal apparent resistivities & phases (RP) is illustrated with the 3D ObliqueOne data set (see sec. 3.2.2). In 3D inversion, RP data are treated as $\ln \rho_a$ and ϕ (deg). Subsequently, I set errors for apparent resistivity data in fractions of log10-decades (dec). For phases data errors are provided in degree. For the examples shown here, data errors are the same at all sites and constant over period.

Inversion of (log) apparent resistivities and phases combines two parameters with different information about the subsurface resistivity distribution. Whereas phases are particularly sensitive to variations of the subsurface resistivity structure, apparent resistivity data additionally

contain information about the absolute subsurface resistivities. Hence, the relative weight of apparent resistivities vs. phases affects the resolution of absolute subsurface resistivities.

ObliqueOne inversion results previously obtained from PT, VTF, and impedance inversion showed that the ObliqueOne structure is most accurately recovered for prior models close to the regional resistivity average (cf. Figs 3.8 and 3.10). A similar behaviour can be observed for RP inversion. In the following, however, I used a prior (and starting) model of 30 Ωm which is more conductive than the overall regional structure to better illustrate the contribution of apparent resistivities to the recovery of (absolute) subsurface resistivities and the influence of apparent resistivity vs. phase data weighting. Model mesh setup and smoothing parameters are the same as for phase tensor inversion tests described in the previous section. Phase data errors were initially set to 1°. Results for phase-only and RP inversion using apparent resistivity errors between 0.87 dec and 0.022 dec are summarized in Figure 3.12. Inverting only for phases the ObliqueOne structure is well recovered (Fig. 3.12a). As apparent resistivities are omitted, the inversion model is biased by the relatively conductive prior model. The overall subsurface resistivities are underestimated and the OC is located at shallower depth than in the true model, similar to the previously discussed PT results (cf. Fig. 3.10b). Integrating apparent resistivities into inversion the resistivity level of the final models gets closer to the original ObliqueOne structure as apparent resistivity errors are narrowed (Figs 3.12b-e). In addition, the shape of the OC becomes sharper and more coherent. Narrow (1°) error floors for phases are required to resolve a clear image of the subsurface structure if apparent resistivities are downweighted (Figs 3.12c-d).

Nearly all RP inversion achieved the target RMS of 1.05 (cf. Fig. 3.12). Higher RMS values are subject to the minimum required overall RMS improvement between two iterations set to 0.02 for each iteration step (see previous section). However, data misfits for both apparent resistivities and phases distribute uniformly between sites indicating that data are reproduced with similar quality over the entire array (lower panels in Fig. 3.12). The most balanced fit between apparent resistivities and phases is observed for errors of 0.22 dec and 1°. For smaller and larger ρ_a-errors apparent resistivities are overfit (blue and green colours) whereas phase misfits are systematically higher over the entire array (red colours). For each inversion result apparent resistivity misfits show a decrease across the station array from left to right, which is particularly pronounced for high ρ_a-errors, i.e. low weight on apparent resistivities (Figs 3.12c,f). In these cases, the resistivity of the left half-layer (500 Ωm) is significantly poorer recovered than the 50 Ωm-half-layer on the right, which is closer to the prior model resistivity of 30 Ωm. To sum up, the precision for resolving the absolute resistivity level is primarily determined by the relative weight of ρ_a vs. ϕ.

Finally, I tested the performance of the apparent resistivity and phase inversion in presence of static shift. To simulate static shift, ObliqueOne impedance data $\mathbf{Z}$ were distorted with a

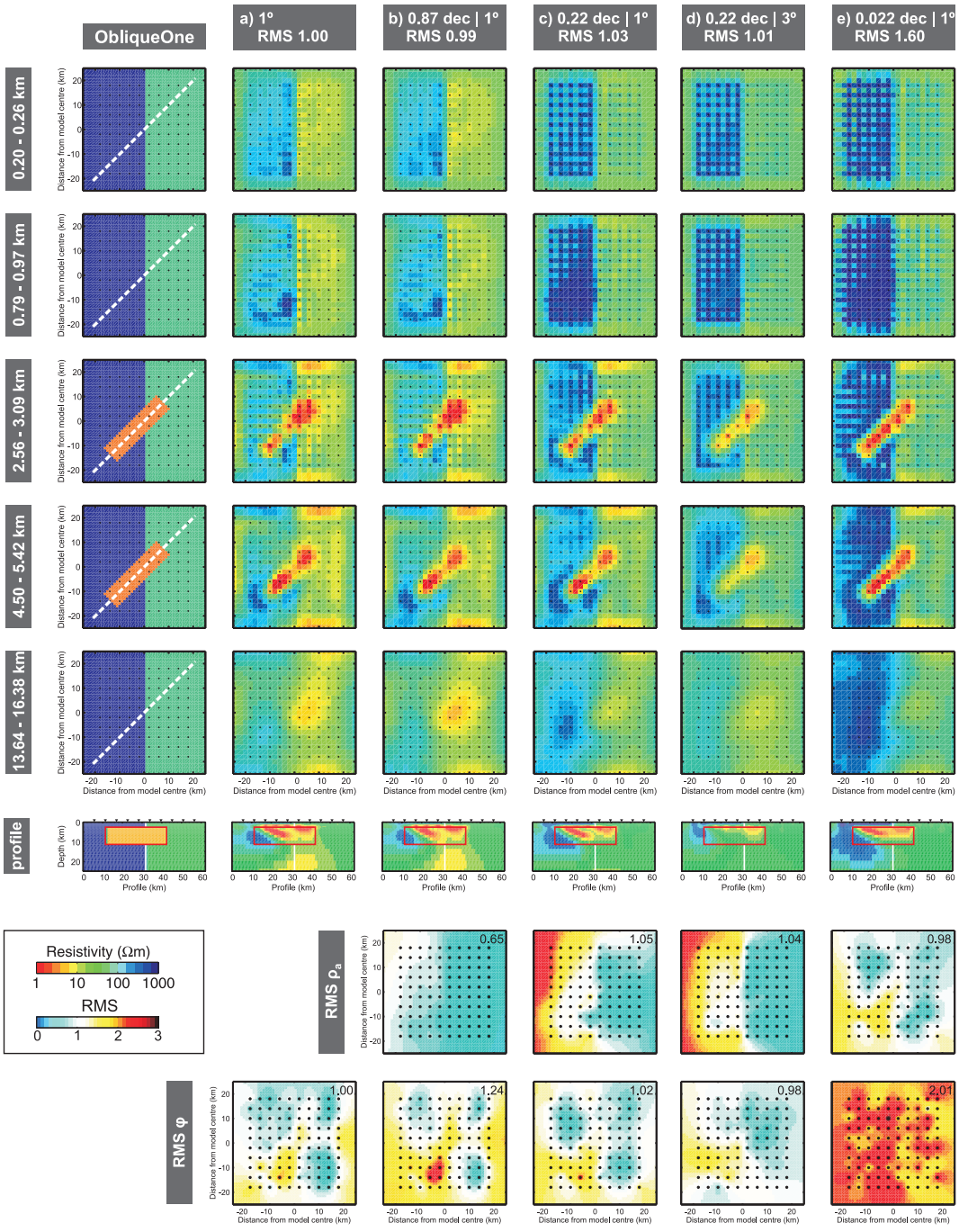

Figure 3.12: Resistivity models obtained from inversion of apparent resistivities & phases (RP) of the ObliqueOne data set (cf. Fig. 3.7), displayed as horizontal slices at various depth and along a profile along the major axis of the oblique conductor (OC); the left column displays the original ObliqueOne model. **(a)** Phase-only inversion recovers the ObliqueOne structure; model resistivities are biased by the prior model, similar to phase tensor inversion results (cf. Fig. 3.10b). **(b)-(e)** Integrating apparent resistivities constrains the subsurface resistivities as apparent resistivity error floors are narrowed. For large apparent resistivity errors, phase error settings determine the recovery of the ObliqueOne structure (cf. (c) and (d)).

diagonal distortion matrix $\mathbf{C}$:

$$\mathbf{C} = \begin{pmatrix} c_{xx} & 0 \\ 0 & c_{yy} \end{pmatrix}$$

and

$$\mathbf{Z}_{dist} = \mathbf{CZ}.$$

As $\mathbf{C}$ is diagonal, the impedance phase is free of distortion and only the amplitudes are scaled by c_{ii}, i.e. the apparent resistivities are shifted (cf. (1.28), sec. 1.3). This will be discussed in more detail in chapter 4. For the following examples, distortion parameters c_{xx} and c_{yy} are randomly distributed (Fig. 3.13). Apparent resistivities and phases were calculated from the distorted impedances $\mathbf{Z}_{dist}$.

The distorted ObliqueOne responses were inverted in terms of both impedances and apparent resistivities & phases. For both data types, starting and prior model is a 30 Ωm-half space and inversion parameters are the same as before. Data errors for impedances were set to 3 % of $|Z_{ij}|$ for the off-diagonal elements Z_{xy} and Z_{yx} and to 3% of $|Z_{xy} * Z_{yx}|^{1/2}$ for the diagonal elements Z_{xx} and Z_{yy}. Errors for apparent resistivities were set to 0.022 dec, 0.22 dec, and 0.87 dec; phase errors were 1° for all examples.

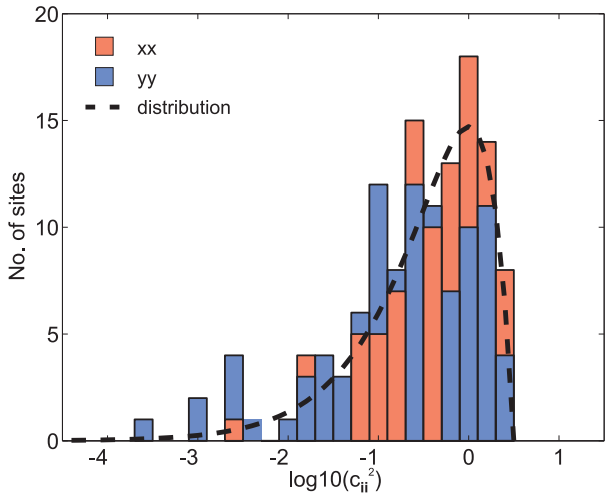

Figure 3.13: Statistical distribution of synthetic distortion parameters c_{xx} and c_{yy}. 100 sets distortion parameters c_{xx} and c_{yy} were estimated, so that the shift amplitudes of the apparent resistivity curves ($\log(c_{ii}^2)$) follow a modified Gamma distribution $\log(c_{ii}^2) \sim -\Gamma(k,\theta) + 0.5$ with shape $k = 2.0$ and scale $\theta = 2.0$, simulating a skewed shift distribution reported for real world data sets (e.g. Sasaki & Meju, 2006). A value of $\log(c_{ii}^2)$ = -1 indicates a downward shift of the corresponding apparent resistivity curve of one decade; values of 0 correspond to no shift. Distortion parameters c_{xx} and c_{yy} were randomly distributed to all 100 sites of the array.

Figure 3.14 compares the inversion results for all data sets. In the impedance inversion results (Figs 3.14a-b) the ObliqueOne structure is roughly resolved. 3D inversion introduces artificial conductive and resistive anomalies into the top layers of the model reaching from the surface down to about 1 km depth. This surface pattern can be understood as an attempt of the inversion algorithm to compensate for static shift within the model. The spatial extent of these surface anomalies is, however, above the inductive scale and has significant effects on the inductive subsurface response. As a consequence, the image of the regional scale structure is distorted. A similar picture is revealed when inverting RP data with narrow error bounds on apparent resistivities (Fig. 3.14c). Downweighting apparent resistivities by increasing their errors (Figs 3.14d-e), the ObliqueOne structure can be successfully recovered by RP inversion as the phases are undistorted. In addition, the near-surface structure of these inversion models is homogeneous as in the true model.

Inversion of distorted ObliqueOne data requires two to three times more NLCG iterations to converge than for undistorted impedances or apparent resistivities & phases and terminates with significantly higher overall RMS values. In order to compare the data fit quality between different types, I calculated RMS misfits for the final inversion result for off-diagonal phases assuming data errors of 1° (lower panel in Fig. 3.14). For impedance inversion and RP inversion using narrow apparent resistivity errors of 0.022 dec (Figs 3.14a-c) phase RMS misfits of 2.63 to 4.30 are relatively high on average. Using downweighted apparent resistivities (Figs 3.14d-e), average phase data misfits drop significantly to about 1.0. In addition, phase misfits for these examples distribute uniformly across the array. In contrast, RMS misfits for apparent resistivities calculated in a similarly normalized way exhibit a high variability from site to site for all results (not shown). However, no significant correlation between apparent resistivity misfit and shift amplitudes could be identified. Due to the coarse horizontal model discretization, artefacts of the upper 2 km are not independent between sites, but also affect responses at neighbouring sites and interact with deeper, more regional-scale structures.

Closer inspection of data fits for single sites illustrates the differing quality of subsurface recovery between the inversion results (Fig. 3.15). For the inversion result obtained with off-diagonal impedances, significant deviations between data and model responses become apparent when displayed as apparent resistivities and phases at sites 012 and 074 (Fig. 3.15a). The apparent resistivities, i.e. the impedance amplitudes are recovered at both sites. The distortion of the near-surface (cf. Fig. 3.14a), however, is not consistent with impedance phases. At period between 0.01 s to 10 s, the phase behaviour of the model response deviates significantly from the observed phase, in particular at site 074 where shifted ObliqueOne xy- and yx-apparent resistivities are separated by nearly two decades. Inverting RP data using narrow ρ_a-errors of 0.022 dec, which resulted in a similarly distorted near-surface structure (cf. Fig. 3.14c), reproduces both the distorted apparent resistivities (Fig. 3.15b) and phases. In this case, surface distortions related to the presence of the static shift are hidden from the

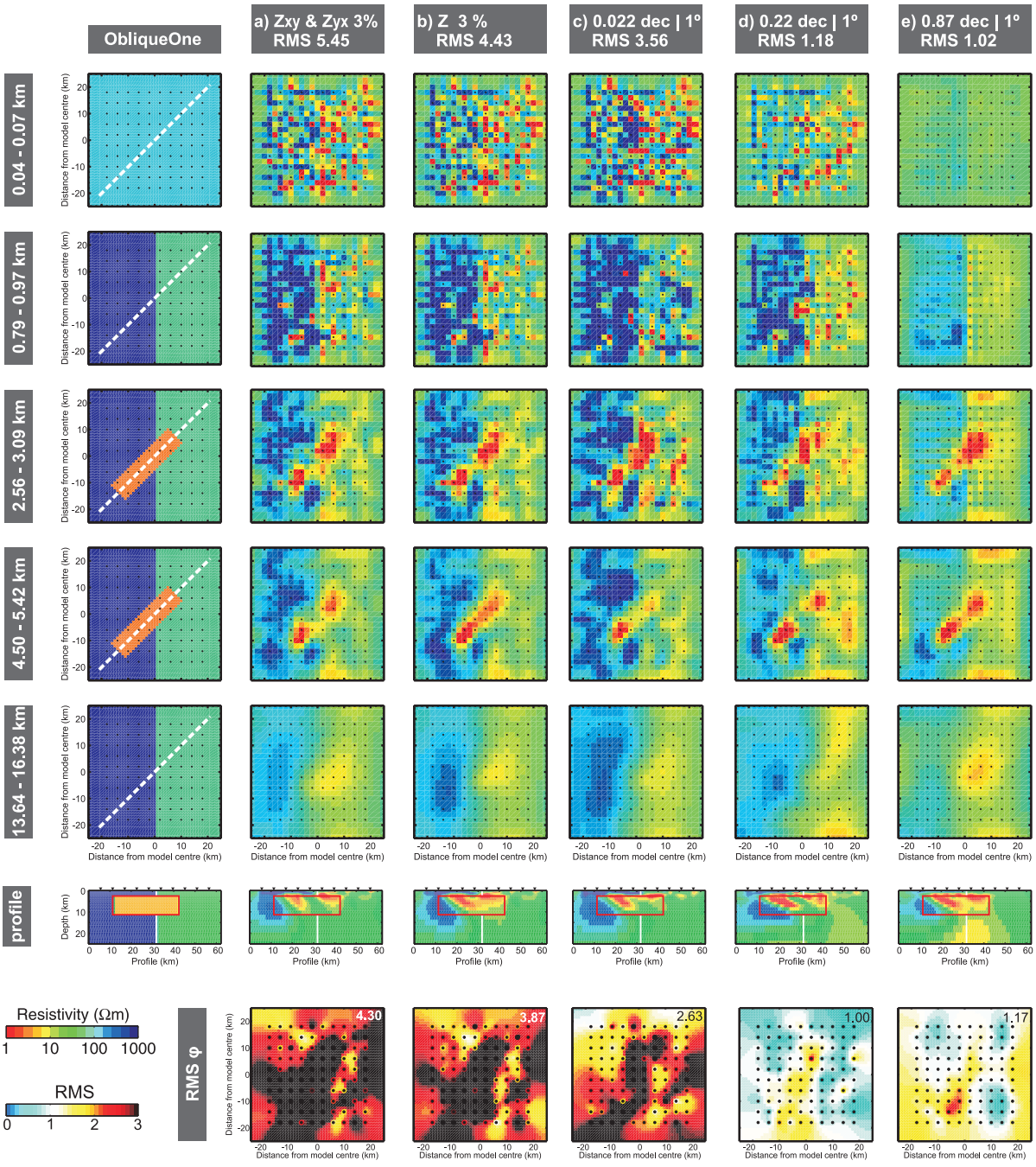

Figure 3.14: 3D resistivity models obtained from inversion of synthetically distorted ObliqueOne data (static shift). The upper panels display the original ObliqueOne model (left column) and inversion models for different data types and data error settings **((a)-(e))**. Note, first layer is located at shallower depth than in Fig. 3.12. The bottom panel shows RMS misfits for off-diagonal apparent phases (ϕ) at each site normalized to phase errors of 1° for comparison.

model responses. Using larger error bounds for apparent resistivities (0.87 dec, Fig. 3.15c), data fits for phases and the recovery of apparent resistivity curve shapes are excellent. At short periods, model responses for $\rho_{a,xy}$ and $\rho_{a,yx}$ lie within 0.1 decades at each site also where synthetic shift amplitudes for both components differ. At most sites, apparent resistivity curves lie within the error bounds. If shifted apparent resistivity curves are separated by more than twice the error level, however, inversion model responses lie outside this range. On average, the ρ_a-responses are at lower resistivity levels than the true curves as the prior model (30 Ωm) is more conductive than the regional resistivity average (158 Ωm).

All in all, apparent resistivity and phase inversion was successfully implemented. Even though only off-diagonal elements were used, the 3D ObliqueOne structure could be recovered successfully. In future, diagonal apparent resistivities and phases need to be included to improve the recovery of 3D structures. In presence of static shift, downweighting of apparent resistivities vs. phases is an efficient tool also for 3D inversion.

3.3 Setting up 3D inversion for the California MT array data set

A first step in setting up 3D inversion is the specification of the inversion coordinate system in which model discretization, site positions, and data are provided. ModEM3DMT employs a cartesian, right-handed coordinate system with z positive downwards. Data have to be rotated to align with the inversion coordinate system.

Initial 3D inversions of the field data from the California MT array (cf. sec. 3.1) tested two different coordinate orientations and were performed with a data subset comprising 73 sites providing almost uniform site coverage with average site spacing of 10 km (cf. Fig. 3.1).

In a first inversion setup, I used a coordinate system with x- and y-axis pointing towards geographic north and east, respectively (N00°-setup). The corresponding model grid consists of 77 × 77 × 57 cells in the two horizontal and the vertical directions, respectively. The inner part comprises a uniform mesh of 35 × 35 × 57 with an edge length of 4.0 km. On all four sides, the central domain is padded by 21 planes where cell sizes increase laterally by a factor of 1.3. The vertical thickness is 25 m for the first layer; subsequent layer thicknesses successively increase by a factor of 1.2. For all field data inversions, the bathymetry of the Pacific Ocean was included as a priori information. A resistivity of 0.3 Ωm was assigned to the ocean cells, and this model domain was kept fixed at all times during the inversion. Henceforth, definition of prior model resistivities refer to land cells only. Prior and starting models were always identical. Model smoothing (covariance parameters α_i) was set to 0.2 for all three spatial directions and for all layers.

I inverted all four impedance components and VTF. Measured data errors were discarded in favour of constant error floors. Data errors were set to 5 % and 3 % of $|Z_{ij}|$ for diagonal and off-diagonal impedance tensor elements, respectively, in combination with an error floor of 3 %

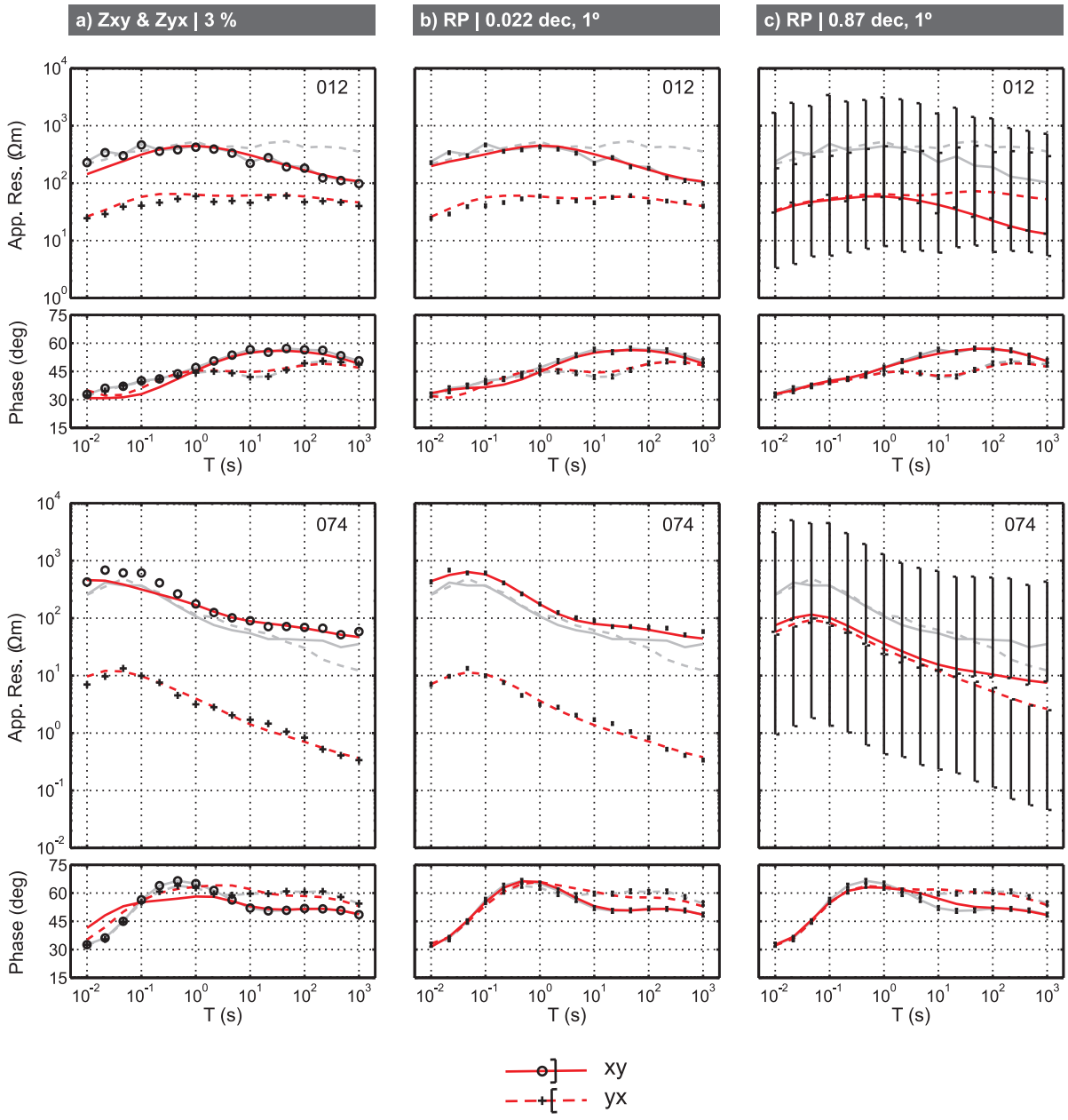

Figure 3.15: Comparison of data and inversion model responses (red lines) obtained for the shifted ObliqueOne data set (symbols) at sites 012 and 074 (see Fig. 3.7 for site locations); grey lines show original ObliqueOne forward responses. **(a)** Inverting impedances, near-surface distortions of the inversion model (cf. Fig. 3.14a) are inconsistent with impedance phases at periods < 10 s, whereas **(b)** for direct inversion of apparent resistivities (0.022 dec) and phases (1°) these distortions are hidden from the model response (cf. Fig. 3.14c). **(c)** When apparent resistivities are downweighted (0.87 dec) vs. phases (1°), inversion focuses on reproducing phase data; apparent resistivities are downward biased as the prior model is more conductive than the regional average resistivity (cf. Fig. 3.14e).

of $|Z_{xy} * Z_{yx}|^{1/2}$ for the diagonal elements. For VTF, I used a constant error of 0.02.

Joint inversion of impedances and VTF using a prior resistivity of 10 Ωm reveals subsurface changes from the prior model down to 80 km depth (Fig. 3.16a). The uppermost 10 km comprise a low resistive layer (< 10 Ωm) of varying thickness. At greater depth, the model is dominated by wide-stretching zones of uniformly high resistivities. On the Pacific side of the San Andreas fault (SAF) resistivities mostly exceed 500 Ωm reaching up to 2000 Ωm. Further inland, resistivities range between 100 Ωm and 500 Ωm. Separate inversions of impedances and VTF starting from land resistivities of 10 Ωm and 100 Ωm, respectively, reveal very similar images (Figs 3.16b-c).

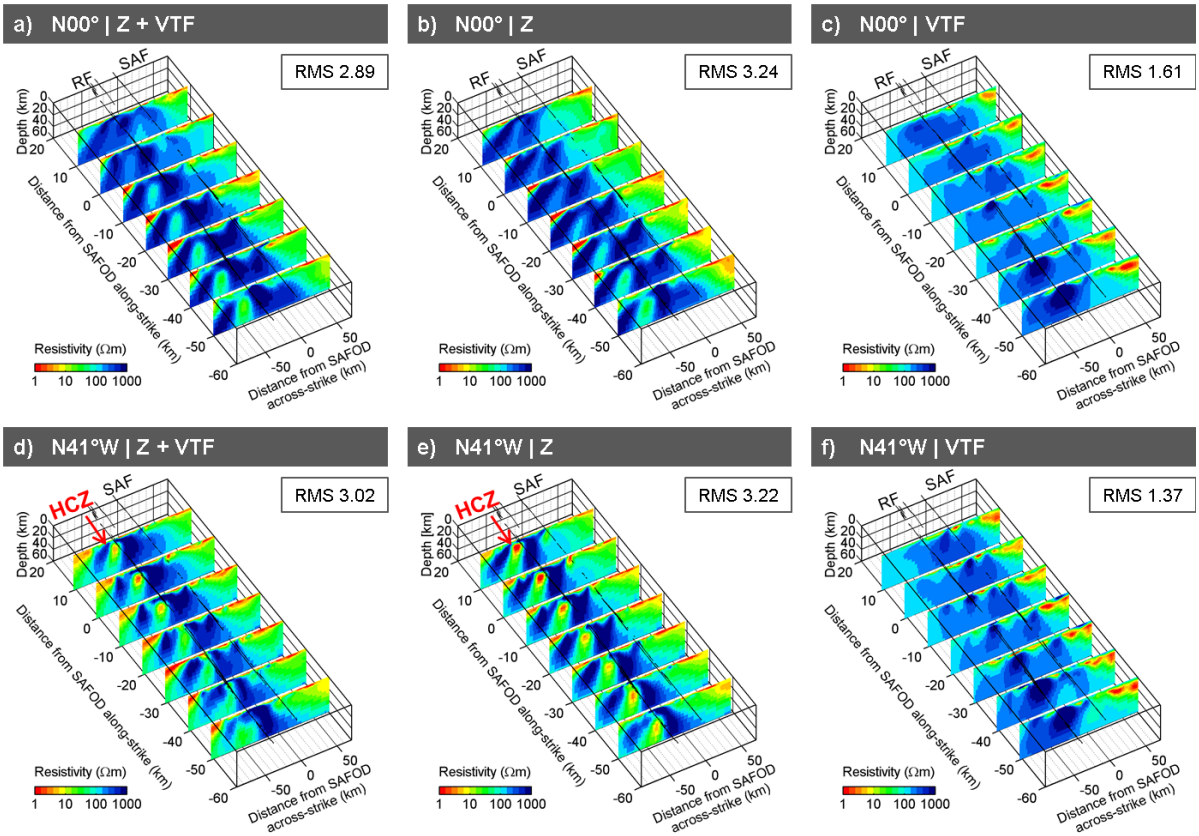

Figure 3.16: Resistivity image of the Parkfield region revealed by joint and individual inversion of impedance (Z) and VTF data for two inversion coordinate setups; **(a)-(c)** N00°-setup, **(d)-(f)** strike-aligned setup. Inversion models are displayed as slices along the seven profiles (cf. Fig. 3.1). Note, the HCZ is only recovered in the strike-aligned grid. RF Rinconada fault.

For a second 3D inversion setup, I defined the coordinate system aligned with the regional geo-electric and geologic strike direction of N41°W (cf. sec. 3.1), i.e. x now points to N41°W. Using again a horizontal subsurface discretization of 4 km × 4 km in the central domain, a smaller number of cells is required as the grid is aligned with the station array layout (cf.

Fig. 3.1). The new, strike-aligned model mesh comprises 20 × 40 × 57 cells in the central domain. On all four sides, the central domain is padded by 15 planes, where cell sizes increase laterally by a factor of 1.3. The vertical discretization is the same as for the first model mesh. As before, prior model resistivities were set to 10 Ωm and 100 Ωm for land cells. Bathymetry was included as a priori information and kept fixed at all stages during inversion (seawater resistivity 0.3 Ωm). Model covariance parameters α_i were set to 0.4, 0.2, and 0.3 for x-, y-, and z-direction, respectively. Impedance and VTF data were rotated to N41°W. Subsequently, data errors were recalculated for the rotated impedance data using the same settings as for the N00°-setup.

3D inversion models obtained for the strike-aligned setup (Figs 3.16d-f) exhibit a low resistive (< 10 Ωm) layer of varying thickness in the upper 10 km. At greater depth the inversion results recovered by joint impedance & VTF (Fig. 3.16d) and impedance-only inversion (Fig. 3.16e) image a highly conductive zone (HCZ, 1 - 10 Ωm) at about 15 - 25 km depth. The HCZ extends parallel to strike between the SAF and the coastline of the Pacific Ocean and is surrounded by highly resistive material of 500 Ωm to 2000 Ωm. In contrast, VTF-only inversion (Fig. 3.16f) shows a homogeneously resistive subsurface of 100 Ωm to 1000 Ωm below 10 km depth.

Final RMS values for both inversion coordinate systems are very similar and suggest equivalent data fits for both setups. Considering the subsurface models, however, only VTF inversion results agree for both runs (Figs 3.16c,f). In contrast, resistivity distributions imaged by inversion including impedance data significantly differ at depths > 10 km (Figs 3.16a-b,d-e). Whereas, final models of the N00°-setup image a homogeneous subsurface structure, strike-aligned results suggest the existence of a HCZ. Closer inspection of RMS distributions in frequency-space domain and for single components in the respective coordinate systems revealed no significant systematic misfit variations for either of the setups (not shown). However, when considering model responses of each model in both coordinate systems, i.e. rotating the response of NE-aligned results to N41°W and vice versa, significant discrepancies between the subsurface models become apparent (Fig. 3.17). Whereas both results are consistent with apparent resistivity and phase curves of the N00° coordinate system (Fig. 3.17a), only models including the HCZ explain both xy- and yx-components of the impedance data in the strike-aligned coordinate system. Responses of the homogeneous subsurface image recovered with the N00°-setup do not reproduce apparent resistivities and phases of the xy-component when rotated to strike (blue curve in Fig. 3.17b).

Previous independent line-by-line 2D inversion along the seven profiles by Becken et al. (2011) showed a deep subsurface structure including a HCZ, which is similar to the results in Fig. 3.16(e) (cf. Figure 2.7). The HCZ, located between the SAF and the coast at 20 - 30 km depth within the high-resistive zone was essential to fit 2D data along profiles ② to ⑥.

In order to get an impression of the consistency of the 2D results of Becken et al. (2011) with 3D inversion, I used the 2D inversion results to create a starting and prior model for 3D inversion. In both coordinate systems the 2D results were interpolated onto the 3D grids

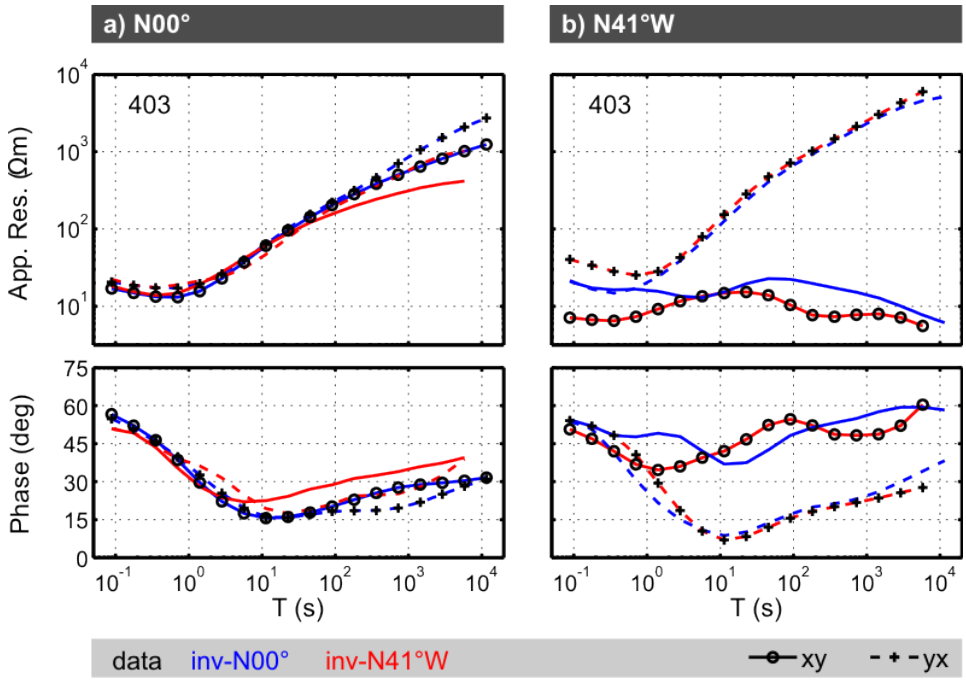

Figure 3.17: Comparison of observed data (symbols) and responses of impedance-only inversion results (lines) obtained in the geographic (inv-N00°, cf. Fig. 3.16b) and strike-aligned (inv-N41°W, cf. Fig. 3.16d) coordinate system.

for a depth range of 1 km to 80 km within the station array. Below 80 km a 50 Ωm half-space was added. Starting inversion of impedances and/or VTF from these prior models, the deep structure including the HCZ is retained in both coordinate systems, indicating that the 2D results are robust and generally valid in the 3D context. Significant changes between 2D and 3D models primarily occur in the upper 2 km close to site locations and represent local adjustments of the interpolated resistivity structure.

All in all, the results from 3D modelling suggest that a deep subsurface structure including a HCZ is consistent with the data set in both coordinate systems. When restarted from homogeneous prior models (including only bathymetry information) in the geographic coordinate system, 3D inversion reveals a very different subsurface structure. Modifications of the impedance-only inversion setup such as refining the model discretization and varying smoothing parameters did not result in any major changes for the deeper parts of the model in impedance inversion. Nevertheless, acceptable overall RMS misfits of 2.5 to 4.3 were reached for the model in Figure 3.16(b) and a series of other inversion runs (not shown). Hence, before continuing and discussing further details of 3D inversion of the California MT array data set, I investigate 3D inversion, in particular resolution for structures at depth > 10 km, with a complementary synthetic 3D data set.

3.4 3D inversion tests with a synthetic data set

3.4.1 The SYNPRK 3D model

In order to better demonstrate aspects of 3D inversion I generated a synthetic 3D data set. The SYNPRK model (Fig. 3.18a) comprises dominant structures of the survey area near Parkfield as revealed by 2D and (some of the) 3D inversion results: A highly conductive, 20 km wide and 25 km high zone (HCZ, 1 Ωm) with its top at 17 km depth is embedded in a background structure mimicking a highly resistive Pacific plate (2000 Ωm) and an intermediately resistive American plate (200 Ωm). The HCZ is located approximately 30 km southwest of the surface trace of the SAF. The top layers of the model comprise sedimentary material (3 Ωm) of varying thickness (2.2 - 6.8 km). The Pacific Ocean (0.3 Ωm) is included according to true bathymetry. Forward data were calculated with for a station distribution similar to the field data layout (Fig. 3.18a) and also for a regular site layout with profile distances of 10 km and an even site spacing of 2 km along the profiles. 3 % Gaussian noise was added to the synthetic data. For 3D forward modelling I used both ModEM3DMT and WinGLink (Mackie & Madden, 1993) to verify forward responses.

Figure 3.18(c) shows that the HCZ must extent along-strike for more than 500 km before it can be recovered with some certainty by 3D inversion. Recovering this structure is no problem though with 2D inversion using the algorithm of Rodi & Mackie (2001). With 2D inversion even blocks with shorter lateral extensions can be successfully recovered (Fig. 3.18c, lower panel). To be on the safe side, I used a HCZ extent of 1150 km for all subsequent 3D inversion tests.

3.4.2 Orientation of the coordinate system

First 3D impedance inversion results of the California MT array data set exhibited significant differences of the deep ($>$ 10 km) model structure depending on the orientation of the coordinate system (cf. sec. 3.3). In particular, inversion of impedance data in a strike-aligned coordinate system suggested the existence of a highly conductive zone (HCZ) at depth $>$ 10 km, whereas the HCZ was absent in results obtained for model and data alignment with geographic directions.

In a first test, I inverted the SYNPRK data set using both the north-east and the strike-aligned coordinate system analogue to the setups tested for the California MT array data set. 3D inversion of four-component impedance data (10 km x 10 km site spacing) using identical model parameters and data error settings as for the field data, I obtain analogue results (Figs 3.19a-b): 3D inversion images the low-resistive top layer similarly in both coordinate systems; for the deeper structures, however, the inversion results differ significantly. The HCZ of the SYNPRK model is recovered for the strike-aligned coordinate system whereas results

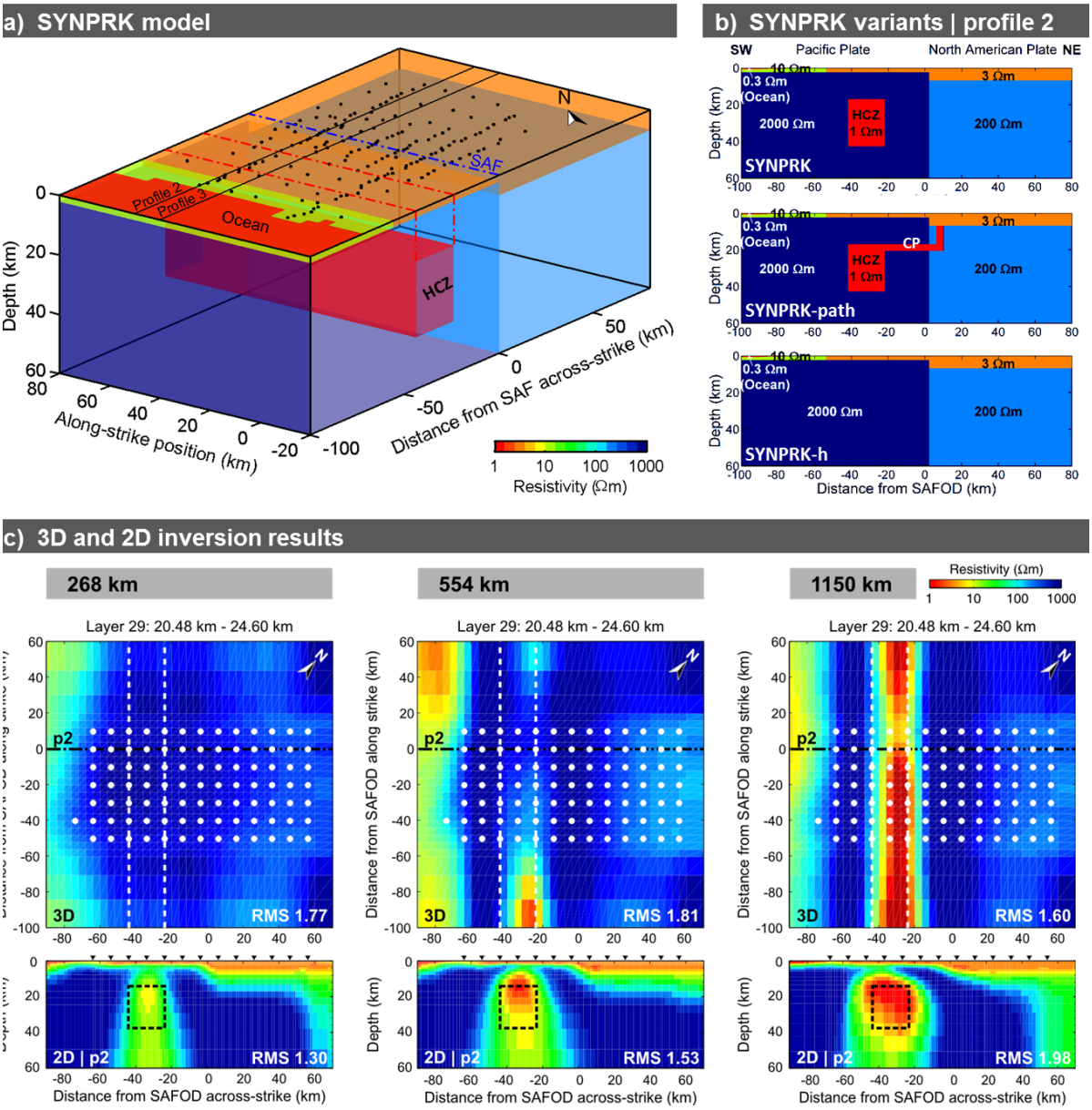

Figure 3.18: SYNPRK model. **(a)** The SYNPRK resistivity model includes the main structural features revealed by 2D and some of the 3D MT inversions. The highly conductive zone (HCZ) extends 1150 km along-strike; the Pacific Ocean is integrated according to true bathymetry. All other structures extend to the model edges. **(b)** Modifications of the SYNPRK model (upper panel) include a conductive path (CP) between the deep, conductive block and the upper-crustal San Andreas fault northwest of profile ③ (SYNPRK-path) and a homogeneous Pacific plate (SYNPRK-h), respectively. Synthetic 3D data sets generated with these models are used to demonstrate aspects of 3D inversion of the field data (see text). **(c)** 3D inversion tests (upper row) of the SYNPRK model for along-strike extents of the HCZ in the strike-aligned coordinate system (off-diagonal impedances, 3 % constant errors) show that the extent of the low resistive block must exceed 500 km to be recovered by 3D inversion with some certainty. However, 2D inversion (lower panels) along profile ② using a standard algorithm can reliably recover even shorter versions of the structure.

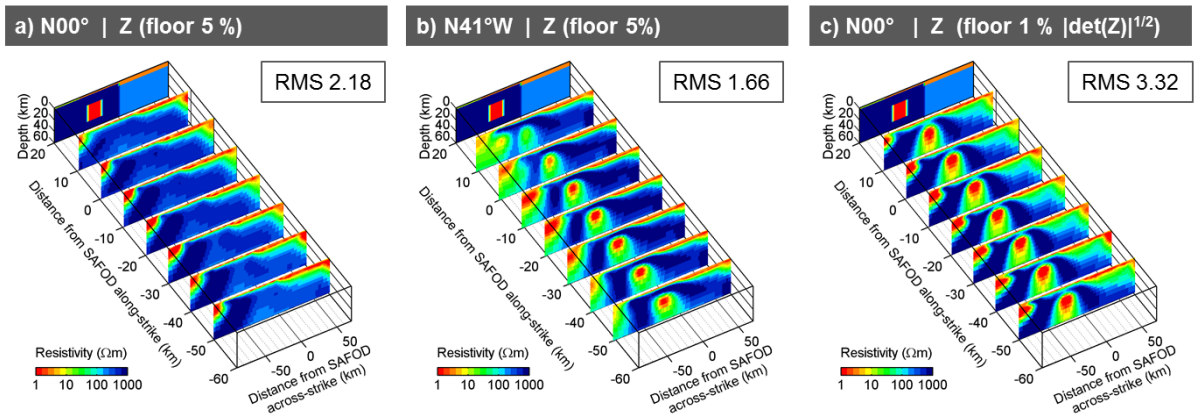

Figure 3.19: Resistivity distribution recovered by four component impedance inversion of the SYNPRK data set. For clarity, a profile slice through the original SYNPRK model is displayed in the background. **(a)** 3D inversion of SYNPRK impedance data (errors 3 % of $|Z_{ij}|$, diagonal elements floor 5 % of $|Z_{xy} * Z_{yx}|^{1/2}$) using a coordinate system aligned with geographic directions shows no significant structural variations in the deeper ($>$ 10 km) part of the model. **(b)** Recovering the deep SYNPRK structures including the HCZ is, however, no problem in the strike-aligned coordinate system. **(c)** Imaging the HCZ in the geographic coordinate system succeeds only if extremely narrow error bounds are applied to diagonal impedance elements ($\leq$ 1 % of $|\det(\mathbf{Z})|^{1/2}$).

obtained in the geographic coordinate system suggest a high-resistive, homogeneous deeper subsurface. Individual data misfits (RMS values) for all data components at each station for the geographic coordinate system reveal slightly increased Zxy and Zyx misfits at sites located above the HCZ along with a significant overall increase of impedance misfits towards the coastline (not shown). The consistent increase of data misfits towards the coastline appears to be due to lacking high-resistivity material in areas close to the coast and beneath the ocean. This will be examined more closely when discussing the influences of prior models on recovery of the SYNPRK structure in section 3.4.3.

In 3D, the 2 $\times$ 2 impedance tensor is fully occupied; electric and magnetic fields are elliptically polarized and non-orthogonal (Becken et al., 2008a). Within a complex 3D medium, the polarization directions of both fields and their relative orientation change laterally and with depth. The impedance tensor elements are calculated from electrical and magnetic fields measured at surface in an orthogonal coordinate system. Thus, each impedance tensor element is a mixed quantity of the anomalous tangential-electric (TE) and tangential-magnetic (TM) modes (Becken et al., 2008a). The contribution of each mode varies between sampling points of the impedance tensor, i.e. from site to site and with period. Hence, there is no unique coordinate system for the entire data set in which TE and TM mode contributions would optimally separate into individual impedance tensor components. In such strong 3D scenarios, the information of the subsurface is distributed over all tensor elements.

However, the SYNPRK model comprises predominantly 2D structures; the 3D nature of the

ocean and the finite along-strike extent of the HCZ constitute only weak 3D effects. In the pure 2D case, the TE and TM modes decouple and split up into E- and H-polarization, where electric and magnetic fields are polarized in directions of geo-electric strike and tangential to the earth's surface (e.g. Ward & Hohmann, 1987). Each polarization independently carries information about the resistivity distribution parallel to and along strike, respectively.

To examine the sensitivity of impedance and VTF data components to the HCZ in different coordinate systems, I removed the HCZ from the SYNPRK model (SYNPRK-h, cf. Fig. 3.18a) and compared forward responses of SYNPRK and SYNPRK-h model. In the NE coordinate system, the response of the HCZ is distributed between all components of the impedance tensor and both VTFs (Fig. 3.20a). If data are rotated to the geo-electric strike direction, the HCZ influences predominantly the Zxy and Ty components (Fig. 3.20b). All other components are only marginally affected because of the low current density – and therefore low sensitivity – perpendicular to strike within the surrounding highly resistive host.

When rotated to the predominant strike direction, the forward response of the SYNPRK-h model strongly deviates from the original SYNPRK data (Fig. 3.21b). Also an unacceptably high misfit of the inversion result obtained in the NE coordainate system (cf. Fig. 3.19a) becomes obvious. Considered in the NE coordinate system, however, the responses of the SYNPRK-h variant are close to the error bounds of the SYNPRK data (Fig. 3.21a). For a wide period range the two responses are undistinguishable within the error levels. Hence, 3D inversion with the above described data error settings only recovers the true subsurface structure with the HCZ, if the SYNPRK data set is rotated to the appropriate coordinate system (cf. Fig. 3.19a-b).

This finding is not only important for this particular synthetic data set, but has more general implications for 3D inversion, in particular for data sets which are dominated by regional 2D structures. The impedance tensor contains the same information independent of the coordinate system; no information is lost when rotating impedance data. Theoretically, data weighting can be provided in a way that data misfits and sensitivities have equivalent amplitudes in all coordinate systems. However, this requires the use of both data variances and data covariances, i.e. the full 4×4 covariance matrix for the impedance tensor. The inversion scheme of ModEM3DMT and other 3D codes (e.g. Siripunvaraporn et al., 2005), however, use only data variances (i.e. the diagonal elements of the error covariance matrix). Hence, data weighting using these 3D inversion appraoches depends on the coordinate system (cf. (3.5)). In 3D situations with a pronounced regional 2D structure, non-diagonal elements of the 4×4 impedance covariance minimize in a strike-aligend coordinate system where TE and TM mode maximally separate and dependencies between impedance tensor elements are minimal. Hence, rotation to strike allows for sensible data weighting in such situations.

In the NE coordinate system, the HCZ can only be resolved if much smaller data errors are used, in particular for the diagonal elements (e.g. a floor ≤ 1 % of $|\det(\mathbf{Z})|^{1/2}$, Fig. 3.19c). In

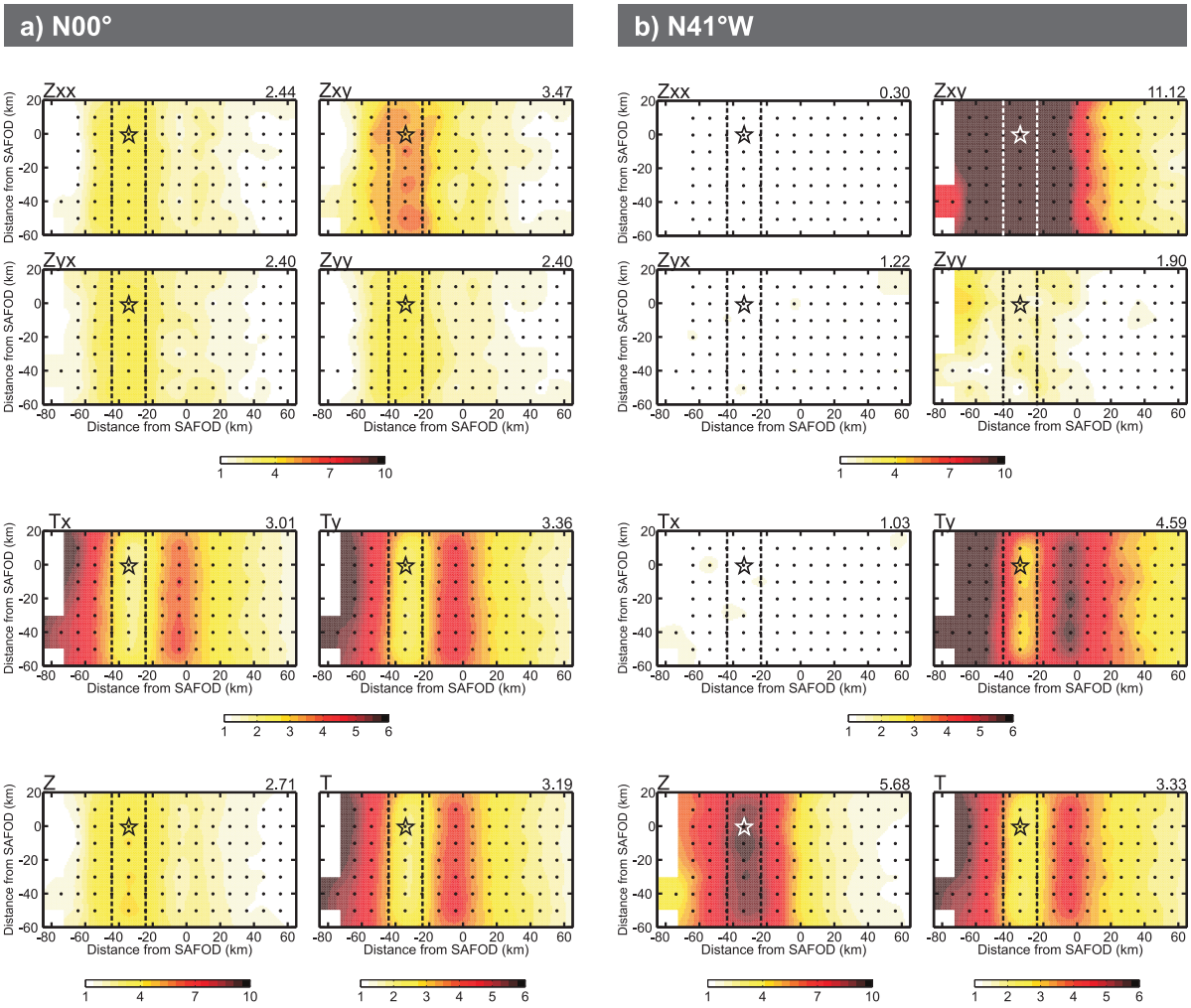

Figure 3.20: The influence of the HCZ of the SYNPRK model (cf. Fig. 3.18a) is reflected differently by the various data components depending on the orientation of the coordinate system. Differences between SYNPRK-h and SYNPRK responses are displayed as RMS misfits estimated for inversion error settings (see text). Dashed lines indicate HCZ edges projected to surface; data of site 2040 (asterisk) are displayed in Fig. 3.21. **(a)** In the geographic coordinate system RMS values are consistently above the noise floor at sites located above (Zxy & Zyx) and towards the edges of the conductor (Zxx, Zyy, and VTFs). **(b)** If data are rotated to geo-electric strike the influence of the HCZ is focused on Zxy and Ty.

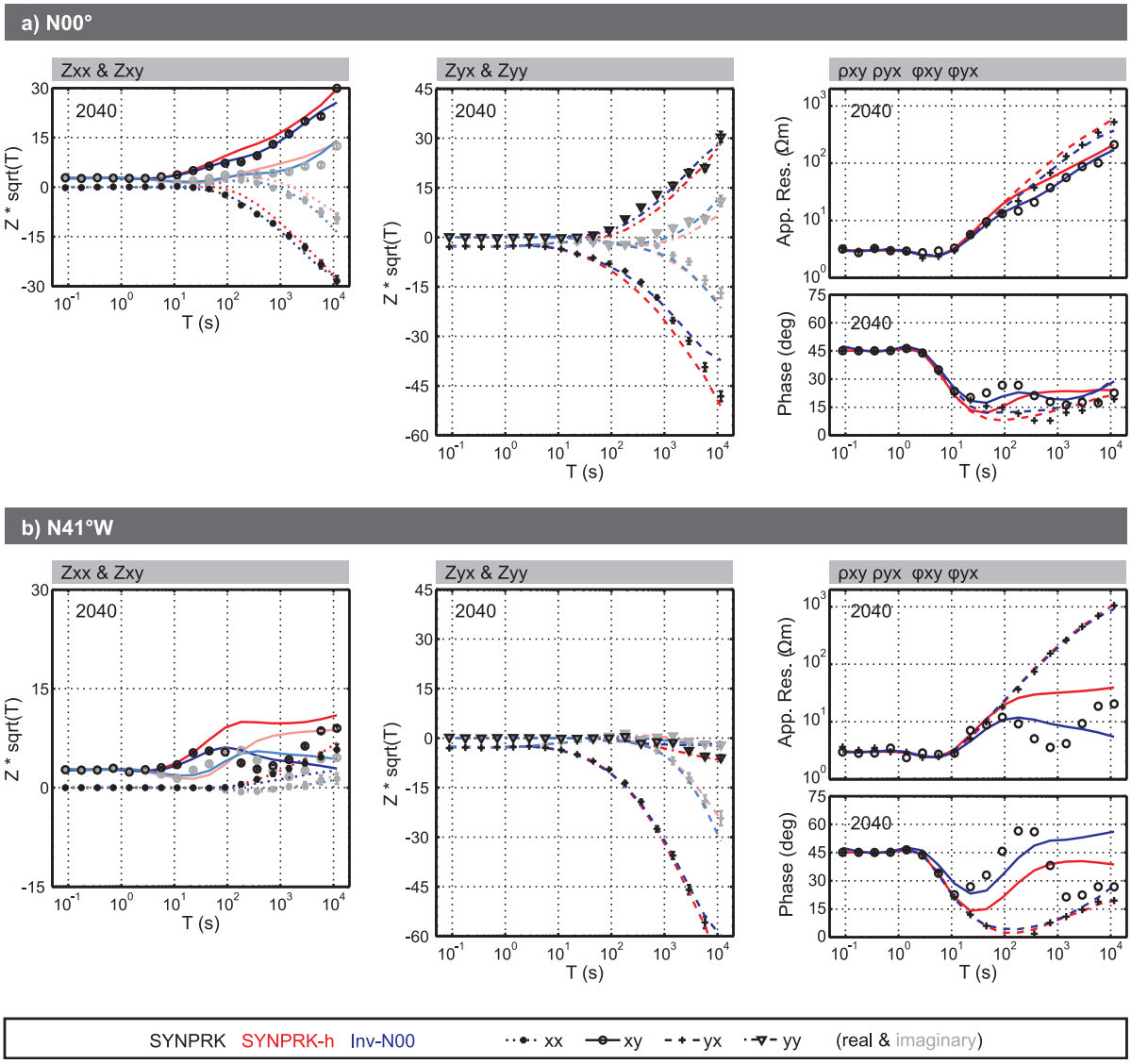

Figure 3.21: Responses of SYNPRK (symbols), SYNPRK-h (red lines) and a resistivity model obtained from inversion of SYNPRK data (NE coordinate system), in which the HCZ is not recovered (Inv-N00, blue lines, Fig. 3.19a); site 2040 is located above the HCZ (see Fig. 3.20). **(a)** In the geographic coordinate system the responses of the SYNPRK-h model and the inversion results do not significantly deviate from the error bounded original SYNPRK data. At most periods Zxx- and Zyy-responses are indistinguishable within the error levels. **(b)** In a coordinate system aligned with the predominant geo-electric strike direction, the information about the HCZ concentrates in the Zxy-component and the misfit of both the SYNPRK-h response and the rotated inversion response is clearly significant compared to the error bounds. Note, Zxy has very small amplitudes and error bars are smaller than the symbol sizes.

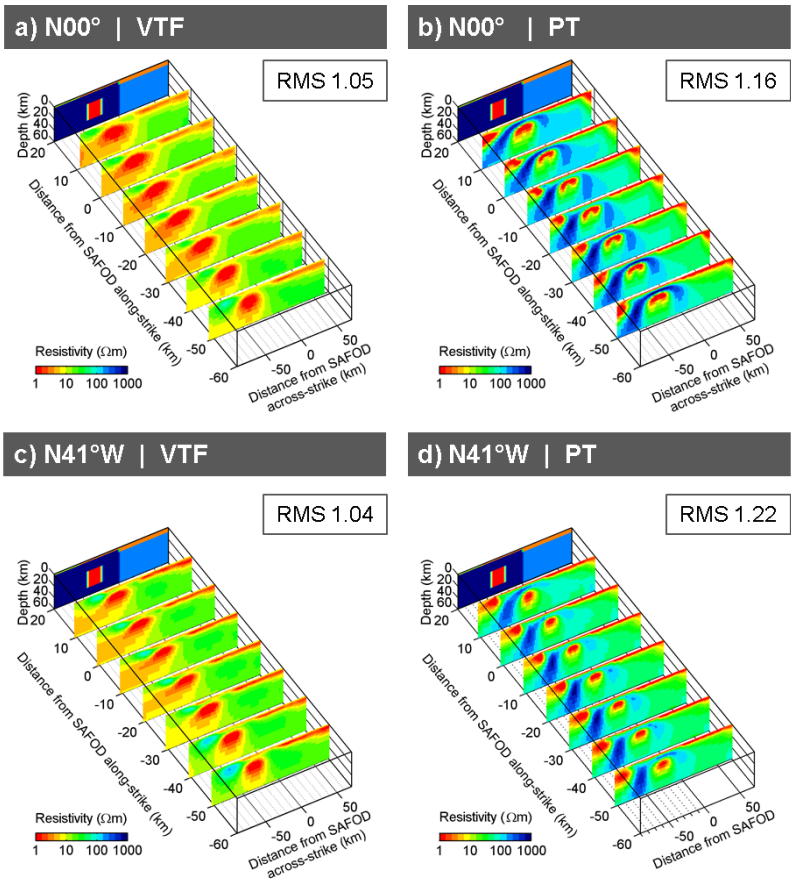

Figure 3.22: 3D inversion of VTF **(a),(c)** and **(b),(d)** PT data of the SYNPRK data set reveals the HCZ independent of the orientation of the inversion coordinate system for standard data error settings (VTF 0.02; PT 3 %, floor $\tan(2°)$).

practice, however, it is often not feasible to set Zxx and Zyy errors to such small values for the entire period range, because the diagonal components of field data at short periods and often suffer from poor signal-to-noise ratios, particularly in noisy environments. Defining large error bounds or using (large) statistically derived error bars, however, degrades the performance of 3D inversion. In these cases, the inversion algorithm has generally more freedom finding a model which still fits the data in a mathematically satisfying way (see also Newman et al. (2008)).

Intriguingly, inversion of VTF (Figs 3.22a,c) and PT (Figs 3.22b,d) data recovers the HCZ in both coordinate systems for data errors of 0.02 and 3 % (floor $\tan(2°)$), respectively, as well as a range of smaller and larger error bounds (not shown).

It is not completely clear yet, what causes the different behaviour of VTF and PT data. Most likely this is related to the sensitivity characteristics of these data types to subsurface structures

being different from that of impedance data. VTF and PT data are ratios of magnetic field components and impedance element products, respectively. Due to the normalization, PT and VTF do not comprise direct information about the absolute resistivity, but both data types are sensitive to variations of the subsurface resistivity structure. VTF amplitudes are directly proportional to the amplitude of subsurface conductivity contrasts. Similarly, deviations of PT tensors from a unity matrix describe the deviation of the resistivity structure from a homogeneous half-space. Hence, data-weights refer directly to the amount of information on structural variations contained in a data point. Using constant errors for all VTF data points in inversion as in the example of Figures 3.22(a) and (c), weight on VTF data indicating lateral conductivity changes such as the edges of the HCZ is effectively increased whereas low-amplitude data points in areas or period ranges referring to laterally more uniform regions are downweighted. In contrast, variations of the subsurface structure are reflected in impedance data as changes of the slope of the impedance vs. period curves. Impedance amplitudes are related to absolute subsurface resistivities.

Comparing model responses of SYNPRK and SYNPRK-h models for the two inversion setups reveals that the effect of the HCZ distributes differently to individual PT (Fig. 3.23) and VTF (Fig. 3.20) data components in both coordinate systems. Similar results were previously seen with impedance data (cf. Fig. 3.20). The overall RMS misfits including all components in both coordinate systems, however, are very similar for PT data, and even identical for VTF. The reason can be seen directly from the formula used for calculation of overall RMS values:

$$\mathrm{RMS} = \sqrt{\frac{1}{N}\sum_{i=1}^{N}\frac{(d_i^{obs} - d_i^{mod})^2}{e_i^2}}, \tag{3.28}$$

where d_i^{obs} and d_i^{mod} are observed and modelled data, respectively, and e_i represents the data errors for all N data points. For VTF, the same data errors $e_i = e$ were used for all data points so that (3.28) simplifies to

$$\mathrm{RMS} = \frac{1}{e\sqrt{N}}\sqrt{\sum_{j=1}^{N/2}(T_{x,j}^{obs} - T_{x,j}^{m})^2 + (T_{x,j}^{obs} - T_{x,j}^{m})^2}. \tag{3.29}$$

As the term $(T_{x,j}^{obs} - T_{x,j}^{m})^2 + (T_{x,j}^{obs} - T_{x,j}^{m})^2$ representing the length of the induction vector $(T_x \;\; T_y)$ is rotationally invariant, overall RMS values are identical in both coordinate systems.

In summary, a rotation of data (or model grid) to a predominant strike direction is not inherently required for 3D inversion if the full impedance, VTF, or PT data information is used as the nature of 3D modelling includes all strike directions. However, the above discussed

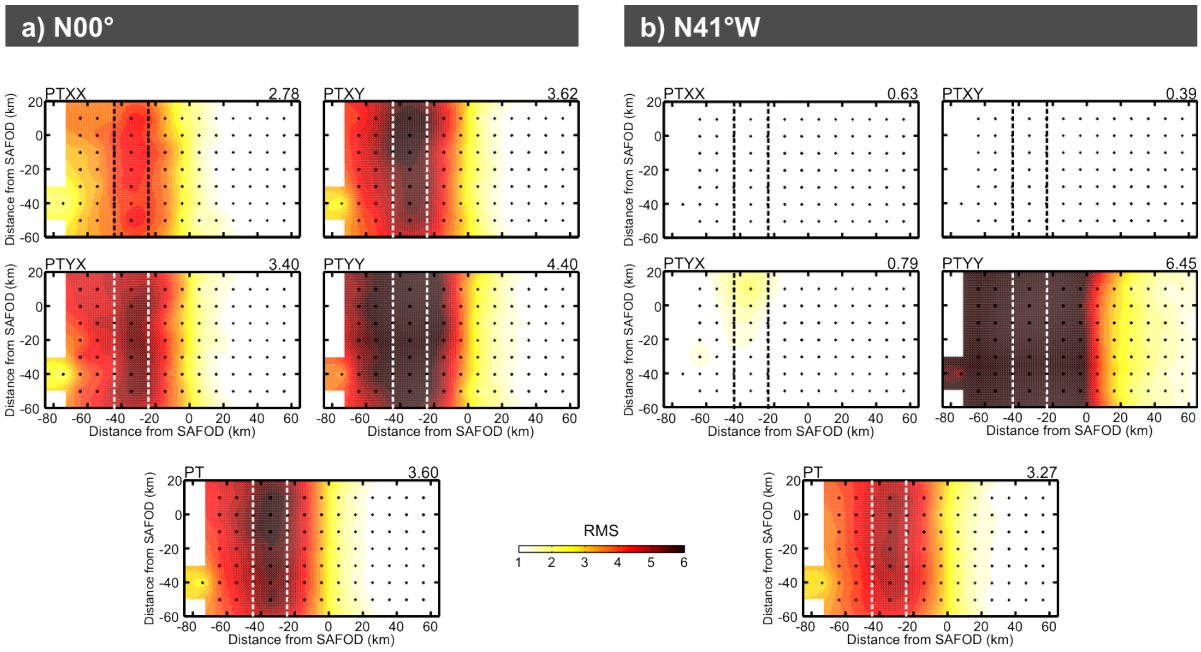

Figure 3.23: The HCZ (dashed outline) of the SYNPRK model (cf. Fig. 3.18a) is reflected differently by the various PT components depending on the orientation of the coordinate system. For the full PT tensor, however, the deviations of the model responses have similar amplitudes.

resolution tests showed that alignment of the inversion coordinate system with predominant regional structures can be a requirement to recover distinct structural details with 3D inversion. In particular, rotation of impedance data to strike facilitates a sensible setup of data weighting in inversion. Hence, further examination of 3D inversion with the SYNPRK data set only uses the strike-aligned coordinate system.

3.4.3 Model regularization

3D inversion tests described in this and subsequent sections for the SYNPRK data set (10 km x 10 km site spacing) were conducted in the strike-aligned coordinate system as this facilitates resolution of the SYNPRK resistivity structure (see sec. 3.4.2). The corresponding model mesh consists of 50 × 70 × 57 cells with a horizontal discretization of 4 km × 4 km in the central domain. Details of the model setup are described in section 3.3.

Solving the MT inverse problem requires a strong model parameter regularization, which limits the ability to detect abrupt resistivity changes. The inversion algorithm of ModEM3DMT penalizes smoothed deviations from a prior model as part of the model update search in the

following way:

$$(\mathbf{m_n} - \mathbf{m_0})^T {\mathbf{C_m}}^{-1} (\mathbf{m_n} - \mathbf{m_0}) \stackrel{!}{=} \text{min.},$$

where $\mathbf{m_n}$ is the current model at iteration n, $\mathbf{m_0}$ is the prior model, and $\mathbf{C}_m$ is the model covariance matrix describing the model smoothness constraint (cf. (3.4), p. 36). If no further information is given, ModEM3DMT assumes starting and prior model to be identical. Hence, all inversion results are based on – explicitly or implicitly – provided a priori information. Note, also using a homogeneous half-space as prior model imposes assumptions on the structure of the subsurface as inversion algorithm searches for a solution which has the smallest deviations from a homogeneous half-space. To obtain minimum structure inversion results homogeneous half-space models are assumed to provide reasonable a priori assumptions. For all inversions presented in the framework of this thesis, starting and prior model are the same. Model covariance or smoothing parameters ($\alpha_x/\alpha_y/\alpha_z$, cf. (3.8)) delineate minimum spatial scale lengths of subsurface resistivity variations in the inversion result model. As $\mathbf{C}_m$ is applied to the difference $\mathbf{m}_n - \mathbf{m}_0$, prior model properties and smoothing parameter settings are closely interrelated. In addition, appropriate settings for $\alpha_x/\alpha_y/\alpha_z$ depend on model mesh discretization with respect to subsurface structure scales and station distribution.

For the SYNPRK structure, the setup of model regularization by prior model resistivities and smoothing parameters affects significantly the resolution of the HCZ at depth. Figure 3.24 compares final inversion models for various setups of prior model resistivity structures and model smoothing. Initially, covariance parameters $\alpha_x/\alpha_y/\alpha_z$ were set to 0.4/0.2/0.3. When inverting off-diagonal impedances (3 % errors) using a homogeneous prior model resistivity of 10 Ωm (or below), 3D inversion successfully reveals the structures of the SYNPRK model (Fig. 3.24a). Using higher values, the HCZ is less clearly expressed (20 Ωm, Fig. 3.24b) and disappears for values of 50 Ωm (Fig. 3.24c) and above. However, the strongly differing and with respect to the deep HCZ structure inadequate inversion results are not reflected in the overall RMS values, which vary only between 1.52 and 1.60. This mystery is solved when misfit values are assessed in more detail (Figs 3.25a-b). For a background resistivity of 50 Ωm the missing HCZ leads to elevated Zxy misfits at sites located above the conductor. In contrast, the fit of the Zyx component is improved compared to the 10 Ωm result because higher prior model resistivities allow easier realization of the stark resistivity contrast between the Pacific plate (2000 Ωm) and the ocean (0.3 Ωm). Hence, the impedance component which is on average closer to the resistivity level of the prior model is better fit by inversion.

For PT inversion (3 %, min. tan(2°)) the prior model resistivity determines the overall resistivity level of the inversion result (Figs 3.24d-e, cf. Fig. 3.10). Similar to impedance results, the HCZ is only revealed using low-resistive prior models below 20 Ωm. When higher prior model resistivities are used (e.g. 50 Ωm, Fig. 3.24e) the HCZ is absent. In contrast

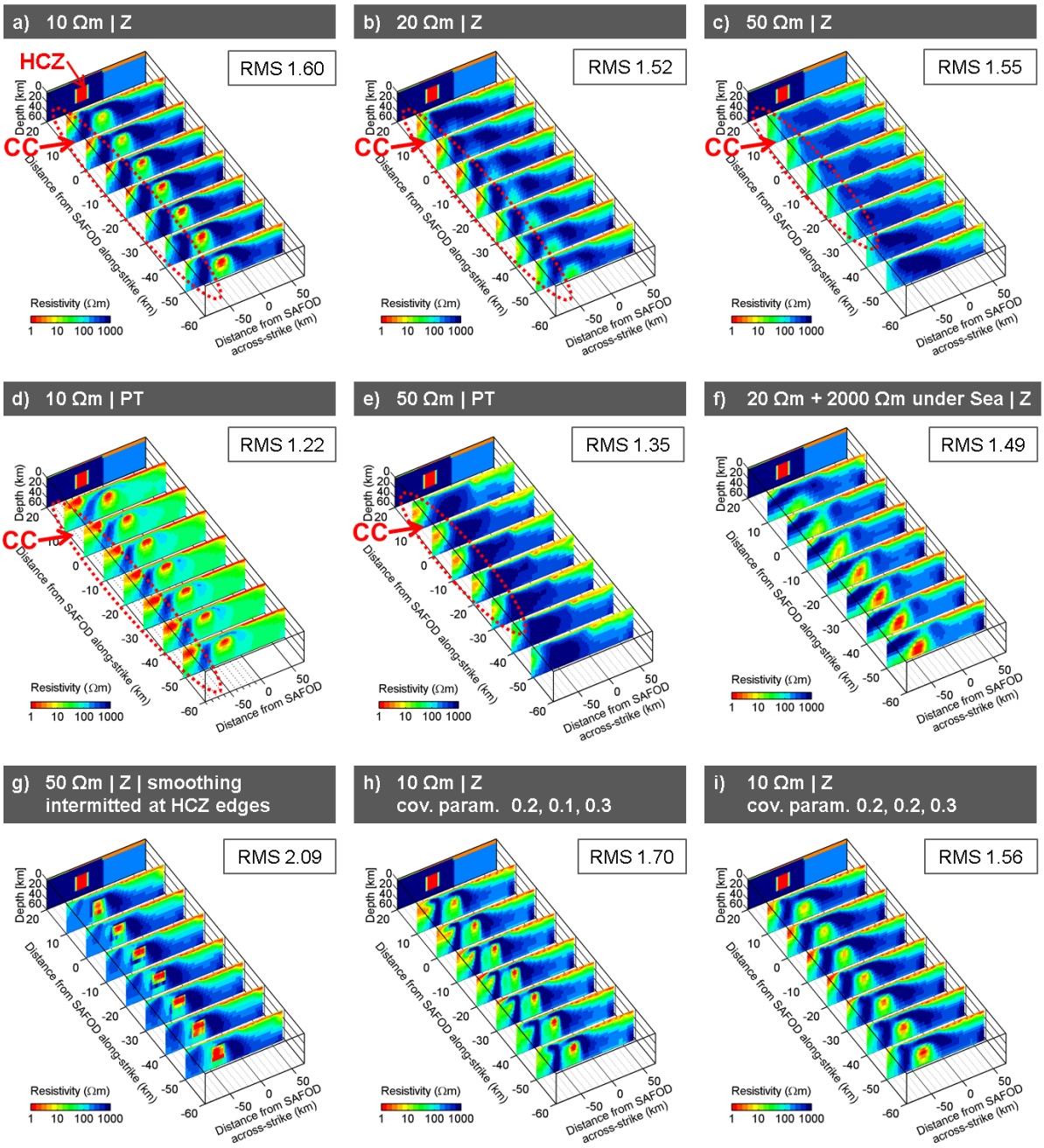

Figure 3.24: The outcome of 3D inversion of SYNPRK data set strongly depends on the setup of model regularization by prior model resistivities (a-f) and model covariance setup (g-i). The background slice at x = 20 km shows the SYNPRK model. **(a)-(e)** The HCZ disappears if initial background resistivities are set too high. Along the coastline, the inversion intends to construct the resistivity contrast between ocean and highly resistive subsurface by introducing artificial conductive zones (CC). **(f)** Using a priori information about high resistivities beneath the ocean (outside the displayed area) yields a continuous, resistive Pacific plate across the coastline and facilitates the recovery of the HCZ. **(g)** Model smoothness constraints suppress the recovery of the HCZ. With intermitted smoothing across the edges of the HCZ, inversion can recover the HCZ even for high a priori resistivities. **(h)-(i)** Applying lower smoothing results in a weaker expression of the deep subsurface structures. The 2D regional resistivity structures are best recovered for anisotropic covariance parameter setups (h).

to impedance results, the structural discrepancies for these higher prior model resistivities are reflected in significantly higher overall RMS error. In addition, site-by-site data fits vary significantly across the array.

In the vicinity of the coastline, a number of "additional" cells with high conductivity can be observed in all five models (labelled CC in Figs 3.24a-e). The high conductivity appears connected to the ocean (10 Ωm prior model) or as isolated features for the 20 Ωm and 50 Ωm prior models. Extent and intensity of these artificial conductors decrease with increasing a priori resistivity. Obviously, the inversion intends to construct the desired resistivity contrast between coast and the seafloor with the CC. In terms of finding a minimal model norm it is less costly to change some of the more conductive cells than a much larger volume of resistive cells, which would be necessary to recover the high-resistive Pacific plate of the SYNPRK model.

If a 2000 Ωm half-layer is included a priori beneath the ocean from -120 km across-strike distance from SAFOD towards the southwestern model edge (i.e. outside the displayed area), 3D inversion yields a continuous high-resistive Pacific plate across the coastline and now independent of the chosen prior model resistivities in the central part of the model (Fig. 3.24f). The respective Zxy misfits are distributed uniformly throughout the array and in both impedance components (Fig. 3.25c). In addition, the HCZ, which is bound to the smaller Zxy component, is resolved for slightly higher resistivity values.

Failure to recover the HCZ for prior model resistivities $>$ 20 Ωm is not only subject to the resistivity distribution of the prior model, but also attributed to the constraints imposed on minimum spatial scale length of conductivity variations by the setup of model smoothing ($\alpha_x/\alpha_y/\alpha_z = 0.4/0.2/0.3$). If smoothing is disabled across the edges of this zone, the inversion does recover the HCZ even when using a homogeneous 50 Ωm-background a priori (Fig. 3.24g). This approach represents only a weak constraint, as the inversion is still allowed to smooth across the domain boundaries.

Applying overall lower but continuous horizontal regularization does not recover the HCZ (not shown). Starting again with prior resistivities of 10 Ωm and using model covariance parameters of (0.2/0.1/0.3) does not improve resolution for the resistivity contrasts. Instead, the inversion produces a model showing less pronounced resistivity variations and slightly higher misfit values (Fig. 3.24h). Applying isotropic regularization yields an acceptable image of the deep structures (Fig. 3.24i). The conductivity of the strike-parallel HCZ is underestimated and lower than for smoothness constraints used for the initial inversions (cf. Fig. 3.24a). With anisotropic α-setup enforcing higher smoothing along strike the regional 2D structures are better resolved, but, in general, local 3D resistivity variations are suppressed.

Some of the SYNPRK inversion results show an asymmetric picture of the deeper resistivity structure (cf. Figs 3.24a,e). The strike of the bathymetric fabric of the Pacific Ocean is slightly oblique to the strike direction of the symmetric SYNPRK structure. The large scale distortion

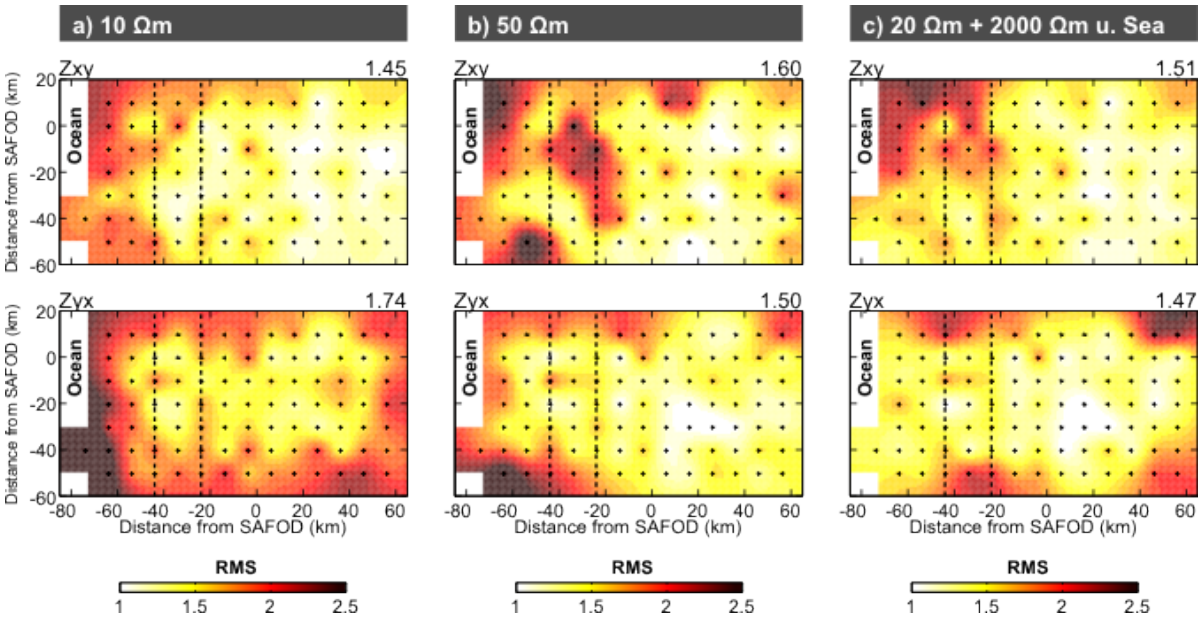

Figure 3.25: Systematic analysis of data misfits of SYNPRK inversion results in the frequency-space domain reveals large-scale structural deviations of 3D inversion results, which are not reflected in the overall final RMS value. **(a)-(b)** Misfit values increasing towards the ocean are related to insufficiently reproduced impedance splits for long periods and illustrate the poor recovery of the high resistivities of the Pacific plate extending beneath the ocean (cf. Figs 3.24a,c). **(c)** Impedance misfits are distributed uniformly if resistivities continue beneath the Pacific Ocean are imaged continuously across the coastline (cf. Fig. 3.24f). Elevated Zxy misfits at sites above the HCZ (dashed outline) in (b) and (c) point to the absence or underestimation of the HCZ.

of the electromagnetic fields, caused by the conductive ocean overlying an intermediately resistive subsurface, leads to a skewed resolution for the regional subsurface structures, although the ocean was always included as a priori information. Comparing forward responses obtained with ModEM and WinGLink (Mackie & Madden, 1993) for the SYNPRK model and a series of prior models I was able to exclude that this is related to the grid setup or other aspects of the forward calculation.

In summary, the outcome of 3D inversion strongly depends on the prior models. An inversion scheme which heavily penalizes deviations from a homogeneous prior model is prone to result in misleading 3D inversion results if strong conductivity contrasts are present in the subsurface.

3.4.4 Site distribution

In contrast to synthetic studies, the lateral subsurface coverage of real world measurements is usually non-uniform. For the California MT array, the spacing of the 169-site data set varies along the profiles between 10 km at the profile ends and between 4 - 2 km, where the lines cross the SAF (cf. Fig. 3.1).

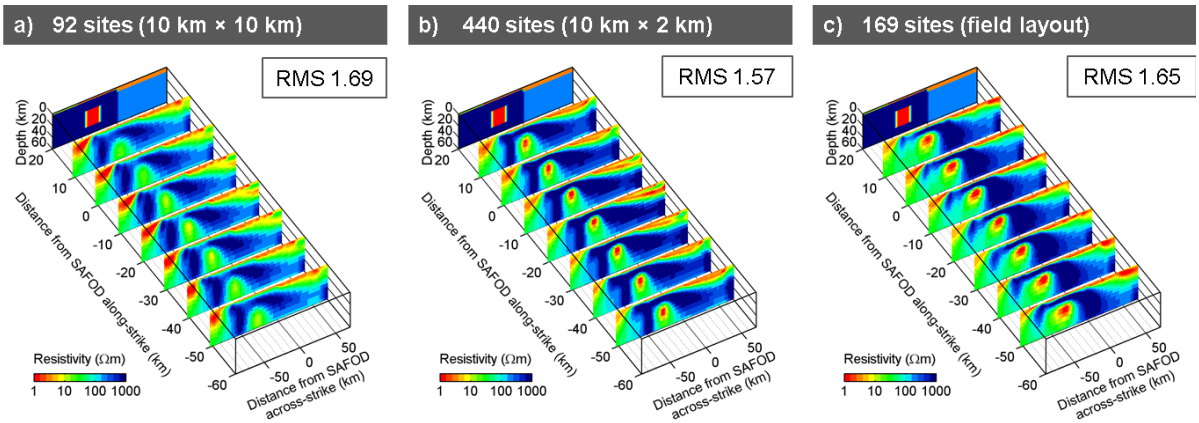

Figure 3.26: 3D resistivity models obtained from inversion of SYNPRK data sets using different site distributions. The background slice at x = 20 km shows the original SYNPRK model. **(a)-(b)** Uniform site spacing facilitates homogeneous recovery of the subsurface; **(c)** using the irregularly distributed site layout of the California data set, the high resistivities beneath the coastline are only poorly resolved.

To investigate the influence of the irregular station layout on the recovery of the SYNPRK structure I used a modified model grid suiting the 169-site data set. Horizontal cell sizes were refined to 2 km for the central part of the mesh (40 x 80 x 57), which increases the total number of model parameters to 70 x 110 x 57. The sizes of the horizontal padding planes were recalculated, again using a lateral increase factor of 1.3. Model covariance parameters were set to 0.4, 0.1, and 0.3 for x-, y-, and z-directions, respectively. In addition to the real California site distribution, SYNPRK-model configurations with 92 and 440 stations with uniform spacing of 10 km and 2 km along the profiles, respectively, were tested.

3D inversion of the off-diagonal impedances with constant errors of 3 % (Fig. 3.26) recovers the overall SYNPRK subsurface structure for all station layouts. Notable differences occur along the coastline, where resistive zones between the HCZ and the Pacific Ocean are more pronounced for the homogeneous site distributions. The comparably weak outcome of the low-resistive block for 92 sites (Fig. 3.26a) is related to the chosen regularization parameters, which are optimized for the shorter site distances along-profile of the 169-site data set. Increasing regularization in both horizontal directions results in similarly good results for the high-conductive zone (not shown).

In general, model smoothness constraints can accommodate partially the effects of differently varying site distances along the coordinate axes (440 and 92 sites). However, non-uniform site spacing along a single direction (169 sites, Fig. 3.26c) is a challenge for 3D inversion and can result in spurious variations of the regional conductivity structure. Inverting data on a coarser, but in return uniformly spaced data subset (92 sites) reveals the influence of irregular site-spacing.

3.4.5 Setup of data-weighting for single and joint data type inversion

Finally, the influence of different error setting for impedance components on the outcome of the inversion and tested joint inversion setups was examined.

Previously shown impedance data inversion results for the SYNPRK data set used data errors set individually for each impedance component proportional to its absolute value ($|Z_{ij}|$). Various authors applying 3D inversion to real world data sets suggested to use data errors relative to the mean of the complex off-diagonal impedances $|Z_{xy} * Z_{yx}|^{1/2}$ (e.g. Meqbel, 2009; Patro & Egbert, 2011). Setting impedance errors to 3 % of $|Z_{xy} * Z_{yx}|^{1/2}$ and using off-diagonal impedances, 3D inversion of the SYNPRK data set fails to retrieve any structural details below 10 km (Fig. 3.27a). The final overall RMS of 2.74 is slightly higher than before, but suggests an acceptable outcome of the inversion at first sight. Re-estimating the total RMS error for the final results using the initially applied errors of 3 % $|Z_{ij}|$ yields an overall final RMS value of 3.83, which is significantly higher than for previous inversion results (1.59 – 2.09, cf. Fig. 3.24). For the SYNPRK data using such averaged errors floors $\propto |Z_{xy} * Z_{yx}|^{1/2}$ downweights the important but smaller Zxy-component (cf. ocean effect Fig. 3.21b). The fairly high relative error floor for Zxy causes the HCZ to disappear. Setting error floors to 2 % for Zxy and to 5 % for Zyx to focus more on the structural information contained in the Zxy-component results in a better defined shape of the top of the HCZ (Fig. 3.27b) compared to results obtained with evenly scaled data errors (cf. Fig. 3.24a).

Inversion runs using only a reduced period range (T > 1s) terminate with relatively high RMS values (Fig. 3.27c). Closer inspection of the inversion model response reveals that the split of the impedance elements due to the ocean effect (cf. Fig. 3.21b) is not fully recovered. The Zyx responses are consistently smaller than the original SYNPRK data for the longest periods.

Adding VTFs, which are sensitive to lateral conductivity changes, to the inversion improves the resolution of coastal areas and the HCZ appears for prior models with resistivities of 50 Ωm (Figs 3.27d-e) or less. When inverting all four impedance components and the VTFs, the deep subsurface structures are not reproduced for such high a priori resistivities though yielding a significantly lower overall RMS (Fig. 3.27f). As the SYNPRK model is dominated by regional 2D structures and the coordinate system is aligned with the (2D) geo-electric strike, the diagonal impedance components and the strike-parallel Tx-component are small. Thus, relative data errors of these components are large and disguise model discrepancies and their expression in poor data fits as they reduce overall RMS misfits. Similar to the impedance results, combining PT or apparent resistivity & phase (RP) data with the strike-parallel VTF-component Ty (Figs 3.27g-h) improves the resolution of the HCZ compared to the outcomes of PT-only (Fig. 3.22d) or RP-only (Fig. 3.27i) inversion, respectively.

In summary, integrating VTFs improves the resolution of lateral conductivity variations

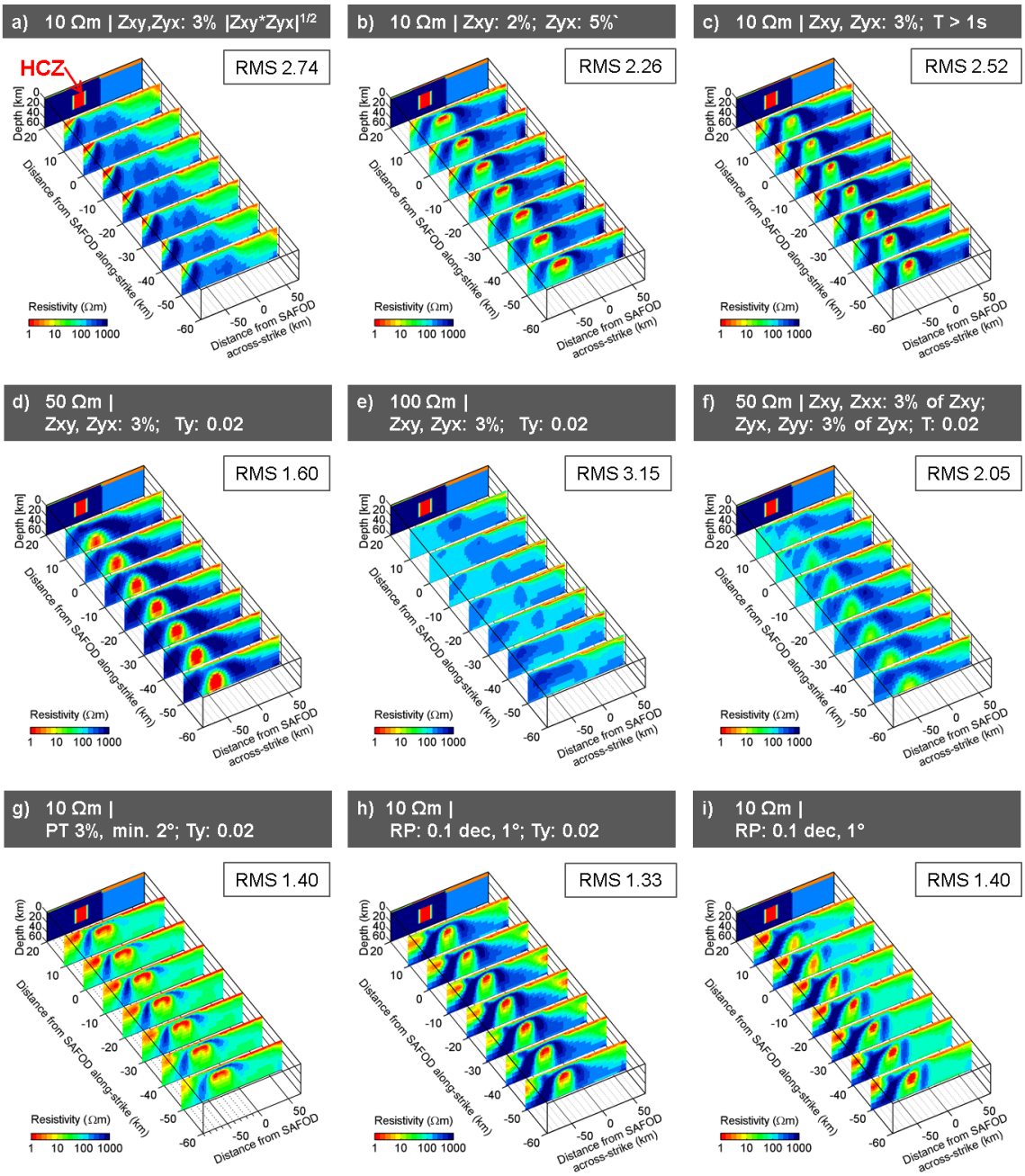

Figure 3.27: 3D inversion of synthetic data (SYNRPK model) using different impedance weighting schemes as well as joint inversion approaches. The background slice at x = 20 km shows the SYNPRK model. **(a)** Averaging impedance error floors downweights the smaller Zxy component and the HCZ bound to Zxy is not revealed; **(b)** use of small relative error floors for Zxy, in return, clarifies the shape of the top of the HCZ. **(c)** Using only long period data > 1 s is sufficient to resolve the SYNPRK structures. **(d)-(e)** Inverting impedances jointly with VTFs reproduces high resistivities in coastal areas and the HCZ for prior model resistivities of 50 Ωm. **(f)** However, using all four impedances + VTFs fails to recover the predominantly 2D resistivity structure of the SYNPRK model. **(g)-(i)** Joint inversion of PT + VTFs or RP + VTFs improves the spatial resolution of the HCZ as well as high resistivities of the Pacific plate compared to PT-only (cf. Fig. 3.22d) or RP-only (i) inversion, similar to observations for impedance data in (d).

significantly compared to results obtained only with impedance-derived quantities. Moreover, it is essential to set error floors individually and according to the importance of a particular transfer function component, as the driving forces behind the inversion is minimizing the overall misfit. It is not fully clear how to optimize weighting of individual impedance data components in general, as they often differ considerably in their absolute values.

3.5 Inversion of the California MT array data

For 3D inversion, a rotation of data and model grid to a predominant strike direction is not inherently required if the full impedance tensor or VTF information is used. Initial 3D inversions of the field data, however, exhibited strongly differing subsurface images and data fit qualities for strike-aligned and north-east coordinate setups, respectively (see sec. 3.3). Subsequently discussed inversion and resolution tests for the SYNPRK data showed that alignment of the model grid with predominant (2D) structures can be a requirement to recover distinct structures with 3D inversion (sec. 3.4). Therefore, closer investigation of the field data from California in the following uses data and model rotated into the predominant regional geologic strike direction of N41°W (Page et al., 1998) for inversion. This strike direction is consistent with the tensor decomposition analysis of Becken et al. (2011).

I used two data sets with different site layouts (cf. Fig. 3.1) with 169 and 73 sites. The 169 sites are distributed along seven profiles with a line spacing of approximately 10 km and variable site spacing along the lines ranging from 2 km in the central part across the SAF, increasing to 10 km towards the profile ends. Inversion of the SYNPRK data revealed that uniform site coverage facilitates a better (more homogeneous) reconstruction of the deeper subsurface (cf. sec. 3.4.4). Therefore a series of inversion tests were conducted with a subset of 73 sites providing more uniform site spacing of ∼10 km in both horizontal directions. Details on frequency layout and site selection for the data sets are described in section 3.1. Discretization of the subsurface was based on the 4 km × 4 km (73 sites) and 2 km × 2 km (169 sites) model meshes described for previous studies in the strike-aligned coordinate system (see sections 3.3 and 3.4.4). Following the results of the SYNPRK study, I applied higher model smoothness constraints along-strike. Model covariance parameters $\alpha_x/\alpha_y/\alpha_z$ were set to 0.4/0.2/0.3 and 0.4/0.1/0.3 for the 4 km × 4 km and 2 km × 2 km grids, respectively. For all inversions, bathymetry (sea water resistivity 0.3 Ωm) was provided as a priori information and kept fixed.

To get an impression how individual components of the data contribute to the overall resistivity image of the survey area, I inverted individual data components separately and successively added further components and sites to the inversion.

3.5.1 Inversion of single components

At first, I inverted each off-diagonal impedance tensor component (Zxy, Zyx) and the VTF components (Tx & Ty) separately using the 73-site subset. The model mesh was based on a 4 km × 4 km discretization and background resistivities of 10 Ωm (all) and 50 Ωm (only Tx & Ty). As the impedances were rotated to the regional strike direction, inverting only Zxy or Zyx is similar to a 2D TE- or TM-mode-only inversion. Data errors were set to 3 % of $|Z_{ij}|$ for impedances and 0.02 for VTF.

The 3D inversion results obtained from the impedance components (Figs 3.28a-b) show two contradictory, but somehow complementary pictures of the subsurface. When inverting the Zxy component (Fig. 3.28a), the major subsurface feature is a highly conductive zone (HCZ) at depth extending parallel to the SAF. The shape of the top of the structure varies along-strike and the body is connected to the surface by a conductive channel beneath profiles ② and ③. Inversion of Zyx (Fig. 3.28b), however, yields high (500 - 3000 Ωm) resistivity values which are far off from the prior model for large parts of the central mesh. These high-resistivity zones are required by the data, as the inversion scheme strongly penalizes deviations from the prior model. The contradictory results of Zxy and Zyx inversions resemble the strong split of the impedance tensor components into TE- and TM-mode in rotated coordinates aligned with the regional geo-electric strike direction (cf. Figs 3.3a and 3.17b). In this setting, Zyx data are insensitive to the HCZ (cf. Fig. 3.20b).

Inversion of VTFs reveals a relatively conductive deeper subsurface using prior model resistivities of 10 Ωm (Fig. 3.28c). The zones of higher conductivity beneath the coastline (CC) seem to be an artefact of the minimum structure inversion trying to avoid vast zones of high resistivities beneath the ocean. Similar observations were made for the SYNPRK data set, where the inversion aimed to construct the resistivity contrast between a highly resistive subsurface and the ocean by introducing artificial conductive zones along the coastline (cf. Figs 3.24a-e). Further inland, the HCZ can be traced through all profiles at depth. The HCZ is oriented slightly oblique to regional strike and is located further inland compared to the Zxy inversion model (Fig. 3.28a). Beneath the southern profiles ⑦ to ④ this zone is clearly delimited; towards the northern profiles ③ to ① it merges with the coastal conductor (CC). In the southeastern part of the model, resistivities between the HCZ and the CC are very high. Induction arrows in this part of the array have a strong off-profile component indicating higher resistivity material located towards the southeast and outside the survey array. In general, it is difficult to resolve absolute resistivity levels with VTFs and hence, inversion results depend more on the resistivity level of the prior model. In the VTF-only inversion model for the California data set obtained with 10 Ωm, the sedimentary cover is similar to the one revealed by inversion of impedances, suggesting that an a priori model resistivity of 10 Ωm is a reasonable assumption for the shallow resistivity structure. For deeper parts, however, 2D and Zyx inversion results

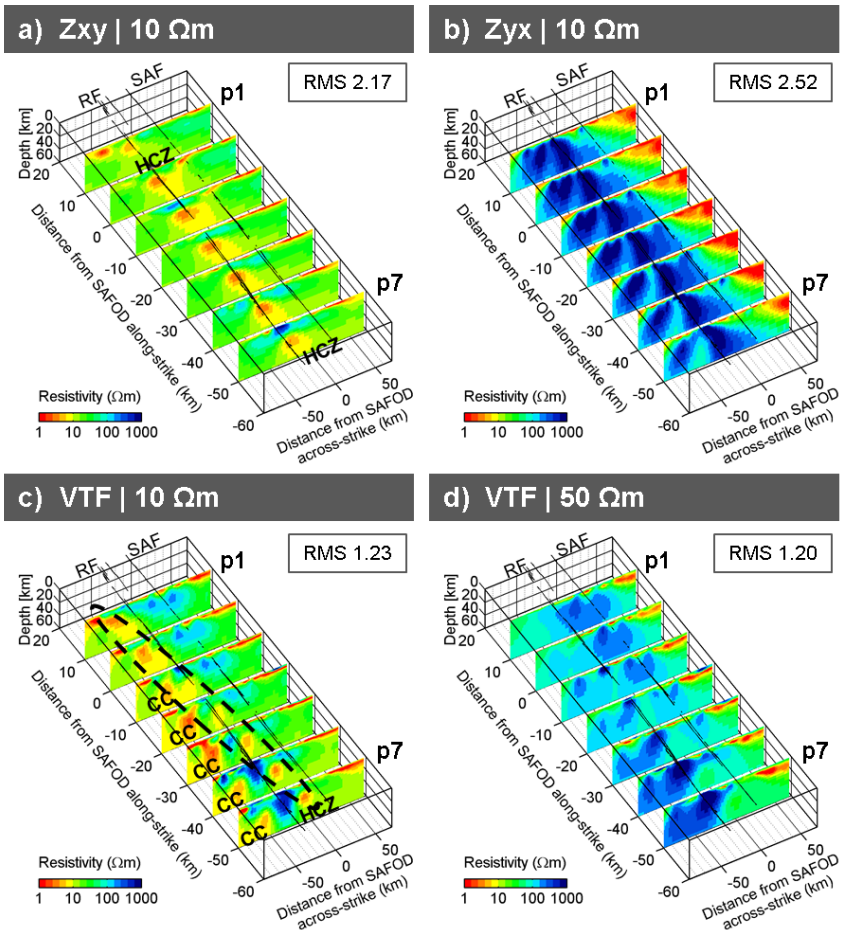

Figure 3.28: Separate 3D inversion of each off-diagonal impedance component and VTFs show contradictory, but somehow complementary pictures of the subsurface. **(a)** Whereas Zxy inversion recovers the HCZ, **(b)** results inverting Zyx yield extended zones of high resistivities at depth, to accommodate for the strong split of impedance tensor components in TE- and TM-mode.
(c)-(d) For VTFs, the resistivity level of the prior model substantially influences the outcome of 3D inversion. Using 10 Ωm, zones of high conductivity (CC) appear beneath the coastline (cf. Figs 3.24a-e), whereas for 50 Ωm the final inversion model is overall resistive.
RF Rinconada fault.

suggest higher resistivities.

Setting prior model resistivities to 50 Ωm, inversion of VTFs resolves a deep structure consisting of high resistivities (500 - 1000 Ωm), which complies with the Zyx result. It seems surprising that the HCZ does not appear in the VTF-inversion, as VTFs are particularly sensitive to lateral conductivity contrasts. Forward modelling tests revealed that the very conductive sedimentary cover has a strong shielding effect, and the HCZ influences the VTFs only at periods > 50 s. In the survey area, the saline water of the Pacific Ocean and thick, low-resistive sediments of the San Joaquin valley are two large-scale, predominantly 2D regional conductors, in contrast to the much higher-resistive subsurface. These lateral contrasts have a significant, far-reaching effect on the profile-parallel VTF component (Ty) at intermediate to long periods (> 50 s). This can be best demonstrated if VTFs are presented as induction vectors (Fig. 3.29). In the Wiese convention, the induction vectors point away from the regional conductors in the east and west. Induction vector amplitudes decrease with increasing distance from the boundaries and both effects cancel out in the middle. The Ty-contribution of the HCZ (dashed red line in Fig. 3.29) is relatively small and oppositely directed. Effectively,

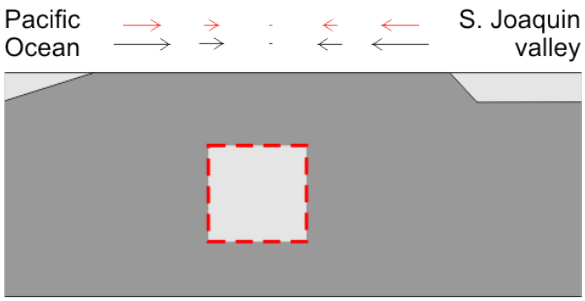

Figure 3.29: Ocean and sediments of the San Joaquin valley dominate VTF behaviour across strike (Ty). Induction vectors are in the Wiese convention. A conductor (dashed red outline) at depth between Pacific Ocean and San Joaquin valley causes oppositely directed induction vector amplitudes which leads to more rapidly decreasing total induction vectors (red arrows). An equivalent induction vector behaviour can be achieved with overall lower resistivity between the ocean and the San Joaquin valley (black arrows, cf. Fig. 3.28d).

this leads to induction vector amplitudes decreasing more rapidly when moving away from the conductivity contrasts (red arrows in Fig. 3.29). In this simplified case, the same behaviour of induction vectors can be produced if the isolated HCZ is replaced with an overall lower resistivity contrast between the coast and the San Joaquin valley.

This is exactly what happens in the 3D VTF-only inversion which exhibits reduced bulk resistivity values at depth (light blue colours in Fig. 3.28d) compared to the Zyx-result (dark blue colours in Fig. 3.28b). The solution in Figure 3.28(d) is preferred by the inversion because the final model is smoother and requires smaller deviations from the prior model than the "true" structure including a HCZ and higher surrounding resistivities. For the simple SYNPRK model in Figure 3.18, VTF-only inversion is able to recover the HCZ at its proper location for prior models up to 50 Ωm. For the California data set, however, HCZ images are generally weaker than for the SYNPRK results (cf. Fig. 3.24) and suggest a lower overall conductance for this structure. In addition, the lateral variability of the sedimentary cover and topography have a much stronger impact on the VTF data over a wide period range. This will be discussed in section 3.5.2. Overall, the influence of the HCZ on VTF is feeble.

3.5.2 Influence of regional structures on VTF responses

Previous results from VTF-only inversion of the California data set suggested a significant influence of conductive (0.3 Ωm - 30 Ωm) surface structures (< 10 km depth) such as the saline water of the Pacific Ocean towards southeast and the variable sedimentary overburden in the survey area, respectively, on the recovery of the deeper subsurface (cf. Fig. 3.28c). These surface conductors lower the penetration depth of the electromagnetic fields (skin effect) and dominate VTF reponses over a wide period range. In the following, I illustrate the effect of seawater and lateral variations of sediment thickness with 3D forward modelling.

Pacific Ocean

The far-reaching influence of the Pacific Ocean on VTF data is expressed in induction arrows pointing away from the coastline (Wiese convention) for most parts of the array at periods

> 1000 s (cf. Fig. 3.4). For inversion of California and SYNPRK data discussed within this work bathymetry was included in the prior models where water depths exceed 0.05 km.

3D grids for modelling of the California data set were discretized using horizontal cell dimensions of 4 km × 4 km and 2 km × 2 km in the central part of the mesh. VTF forward responses for both meshes using a land (or background) resistivity of 100 Ωm agree for most sites over a wide period range (red and blue arrows in Fig. 3.30a). Significant differences between the two model responses are limited to sites located directly at the coast and periods < 50 s and result from differing discretization of the coastal bathymetry between the two meshes (Fig. 3.30b).

Comparing forward responses with field data reveals discrepancies of induction arrow directions at low periods (11.3 s) in areas where the coastline is curvy and bathymetry is shallow (yellow shaded zones in Fig. 3.30a). At periods >100 s, VTF strike directions coincide for synthetic and observed VTF data (cf. Fig. 3.4) and underline the significant influence of the ocean on VTF data in California. Faster decay of observed VTF amplitudes away from the coast is caused by the conductive sediments of the San Joaquin valley (see below).

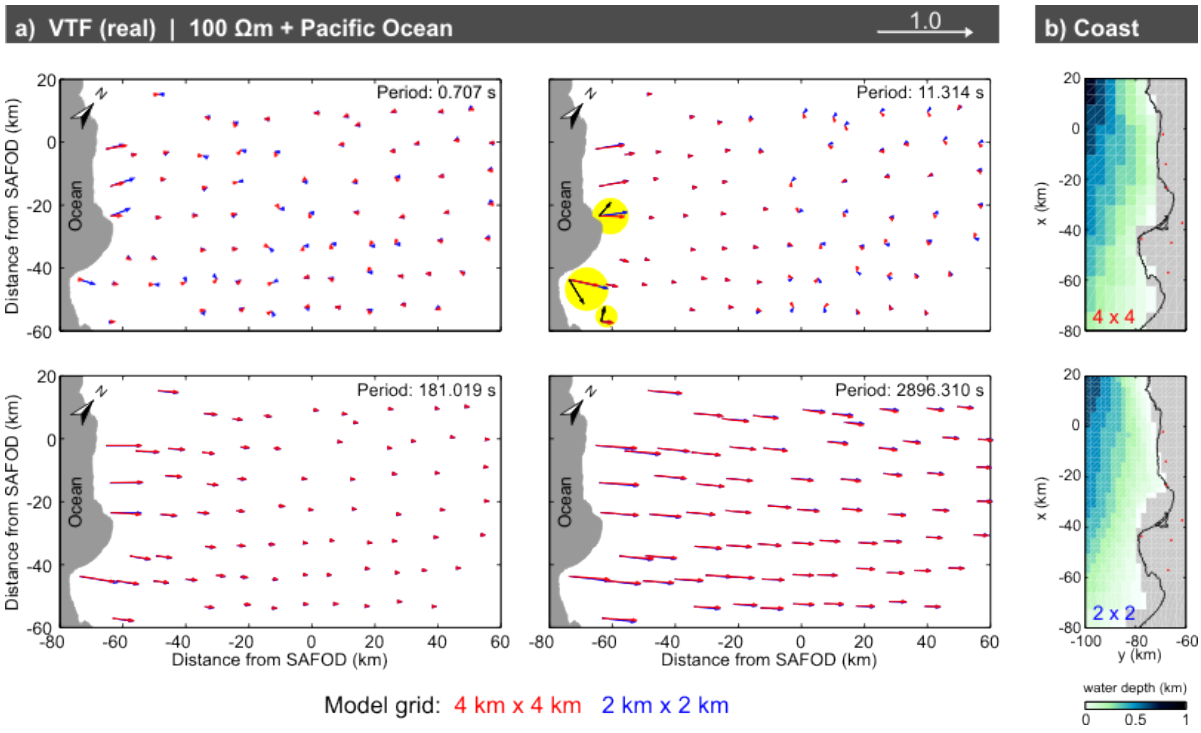

Figure 3.30: Influence of the Pacific Ocean on VTF responses. **(a)** VTF forward responses (Wiese convention) of a 100 Ωm half-space including bathymetry obtained with 2 km × 2 km (red) and 4 km × 4 km (blue) horizontal discretization, respectively, agree at most sites and periods. Differences between model responses and observed VTFs (black arrows) in coastal areas at short periods (11.3 s, yellow shaded zones) indicate the limited accuracy of discrete models. **(b)** Coastal bathymetry for 4 km × 4 km (upper panel) and 2 km × 2 km (lower panel) model grids.

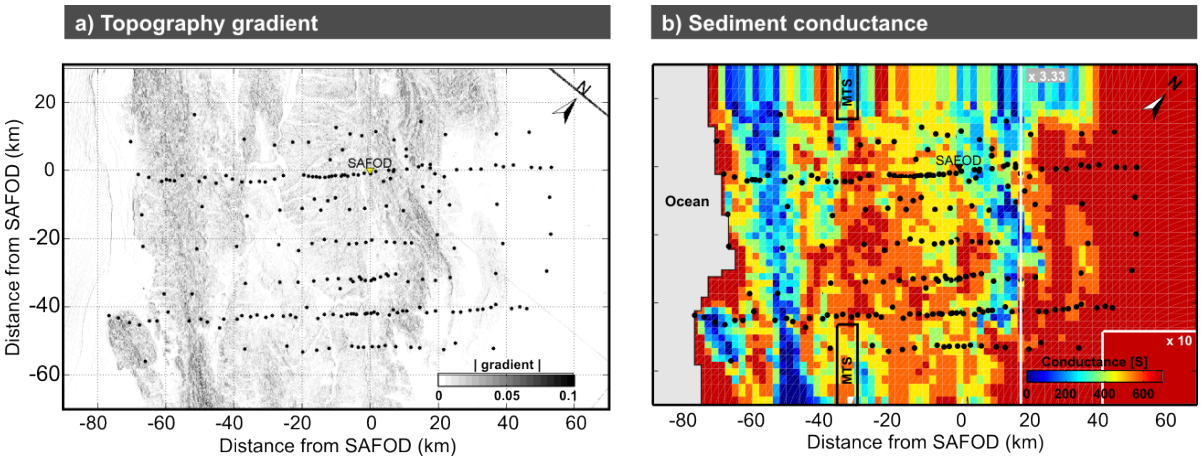

Figure 3.31: Simulation of lateral variations of surface conductors based on topography. **(a)** Across-strike (SW-NE) topography gradients estimated from elevation data of the U.S. Coastal Relief Model (3' resolution) provided by NOAA National Geophysical Data Center. **(b)** Sediment conductance values of the SimSed model estimated from topography gradients ((a), see text). For the SimSed-m variant, conductance values in the San Joaquin valley were increased by factors of 3.33 and 10 (white outlines). Black solid lines mark areas where model resistivities were replaced with 500 Ωm down to 6.77 km depth to account for mountain ranges (MTS) with significant along-strike topography gradients.

Sedimentary overburden

Whereas detailed bathymetry data are available for the survey area with high lateral resolution, sediment thickness is usually inferred as secondary information from seismic, magnetic or gravity measurements and mostly along single profiles only (e.g. Hole et al., 2006; McPhee, 2004); direct observation of sediment thickness (and electrical conductivity) is limited to single points, e.g. in the SAFOD drillhole (Hickman et al., 2007).

Thus, for 3D forward modelling I simulated the sedimentary overburden in the survey area using topography gradients as proxy. I assume highest accumulation of sediments where topography is flat and, in return, thin sedimentary cover where slopes are steep. As topographic features in the survey area run predominantly parallel to geologic and geo-electrical strike (cf. Fig. 3.1), I only consider across-strike (SW-NE) topography gradients (Fig. 3.31a). Horizontal resolution is 0.1 km.

I assume a linear relationship between topography gradient g and sediment thickness h for gradients $|g| < 0.66 \cdot |g|_{max}$, where $|g|_{max}$ is the maximum absolute gradient in the survey area. Gradients $|g| \geq 0.66 \cdot |g|_{max}$ were assigned to zero (minimum) sediment thickness. Subsequently, gradient values $0 \leq |g| < 0.66 \cdot |g|_{max}$ were linearly scaled so that gradients $g = 0$ in the San Joaquin valley match sediment thicknesses of 7 km as observed in inversion results.

For 3D forward modelling of the simulated sediments (SimSed) I used the $70 \times 110 \times 57$ grid with horizontal cell sizes of 2 km $\times$ 2 km in the survey area. As horizontal discretization is much

coarser than the spatial resolution of topography data (0.1 km × 0.1 km), median sediment heights were estimated for each model mesh column. Resistivities of the SimSed model were set to 200 Ωm and 0.3 Ωm for the background and the Pacific Ocean, respectively. For the sediments, I assumed a constant sediment resistivity (ρ_{sed}) of 10 Ωm for the entire survey area as a first guess. Hence, the sediment conductance $G = 1/\rho_{sed} \cdot h$ is directly proportional to the topography gradient. Conductance values range between 0 S and 700 S (Fig. 3.31b).

VTF responses of the SimSed model (Fig. 3.32b) are quite similar to the observed induction arrows at periods of 45 s to 10,000 s (Fig. 3.32a). At long periods (2,896 s), VTFs are dominated by the high conductivities of the ocean. Both direction and amplitude of the field data are well reproduced by the SimSed data up to 60 km away from the coast. At shorter periods (45 s, 362 s), induction vectors of calculated and observed data align in most parts of the array. However, SimSed responses underestimate measured VTF amplitudes in this period range.

Previously shown 3D and 2D MT inversion results suggest extremely low sediment resistivities in the San Joaquin Valley. Hence, I rescaled conductance values in this area by factors of 3.33 and 10, respectively (white outlines in Fig. 3.31b). In addition, I removed sediments and inserted two resistive blocks (500 Ωm) where topography exhibits significant along-strike gradients (black outlines in Fig. 3.31b). Responses (Fig. 3.32c) of the modified SimSed model (SimSed-m) show better agreement of modelled and measured VTF amplitudes at sites in and close to the San Joaquin valley for all periods. Furthermore, localized features such as the rotation of VTFs to directions parallel to strike in the southwestern part of the survey area are reflected by the SimSed-m responses.

All in all, the general behaviour of observed VTF can be reproduced well by this simple approximation of the sedimentary cover and the ocean. The results suggest that VTFs are significantly influenced by these surface conductors over a wide period range.

3.5.3 Further single and joint inversion results

In the following, impedance components were successively combined for inversion of the California data set. I inverted the off-diagonal impedances for all periods and diagonal impedances where the absolute value of the phase tensor beta criterion – as an indicator for 3D strucutres – exceeds 1° (cf. Fig. 3.2c). Impedance errors were defined per tensor row and set to 3 % of |Zxy| for Zxx and Zxy and 3 % of |Zyx| for Zyx and Zyy. In addition, a 5 % error floor was applied to the main diagonal elements to provide meaningful error bounds where they exceed the off-diagonal element of the respective row. This error definition is a compromise between optimizing data fit and the particularities of this data set: (i) to include as many data points as possible, in particular where both diagonal impedances exhibit 3D properties, (ii) to ensure Zyy is taken into account even if amplitudes are small compared to the other tensor components, and (iii) to impose as small relative errors as possible to ensure that variations in the

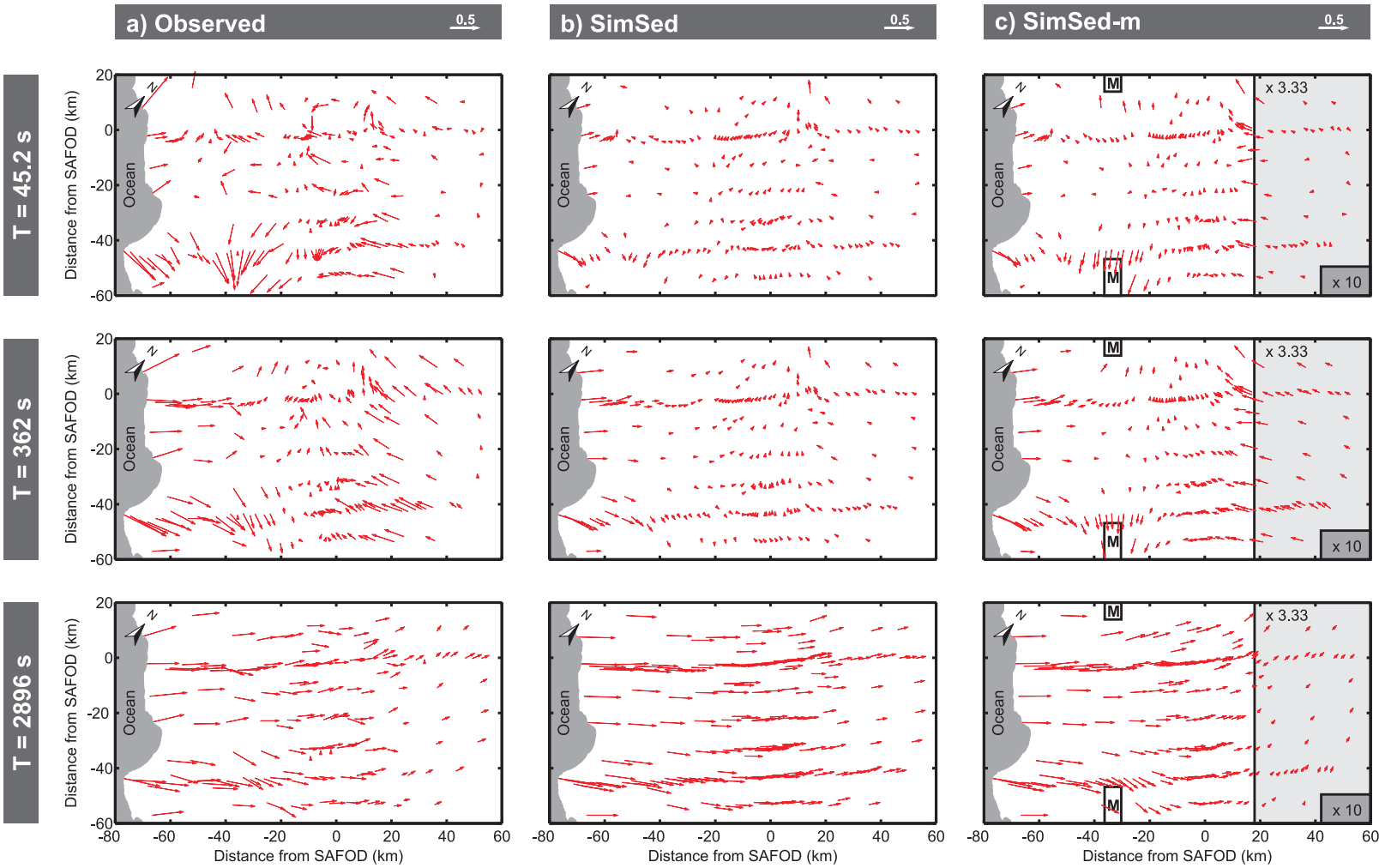

Figure 3.32: Influence of conductive surface structures on long-period VTF data of the California MT array. **(a)** Observed VTF data. **(b)** Calculated responses of the SimSed model (Fig. 3.31) simulating the sedimentary cover and the Pacific Ocean above a homogeneous half-space exhibit a directional behaviour similar to the observed VTF in wide parts of the array. **(c)** The amplitude behaviour are reproduced better if sediment conductances are increased in the San Joaquin valley by factors of 3.33 and 10 (shaded areas) and resistive blocks (M) are inserted where mountain ranges flank the survey area (SimSed-m, cf. Fig. 3.31b).

transfer function curves are reflected by the inversion. In addition, I used apparent resistivities & phases (RP) with errors equivalent to 0.22 decades (dec) and 2°, respectively, as well as PT data (4 % of $|\Phi_{ij}|$, floor: tan(2°)), and VTFs (0.02). All inversions were started with prior model grids comprising the Pacific Ocean and a uniform background resistivity of 10 Ωm.

The results obtained with 73 and 169 sites are summarized in Figure 3.33. In general, all inversions reveal structural variations up to 60 km depth, being compatible with the 2D results (cf. Fig. 2.7). At depths > 10 km, all inversion models image a SAF-parallel HCZ embedded in a high-resistive background. Intensity and location of this zone depend on the site distribution, inverted data types, data-weighting and a priori information (high resistivities beneath the ocean). Along-strike the HCZ continues beyond the southeastern edge of the station array at depths > 20 km in most inversion results, whereas it usually stops at the northwestern edge.

Using the 73-site subset (Figs 3.33a-f), 3D inversion is dominated by regional 2D resistivity structures, particularly if only off-diagonal impedances (Fig. 3.33a) or apparent resistivities & phases are used (Fig. 3.33b). If the diagonal impedance components (Figs 3.33c-d) are included, the shape of the HCZ does not change much but the conductivity of the structure varies along strike. Higher conductivity is found beneath the northwestern profiles, which decreases towards southeast. Beneath profiles ② and ③, a subvertical conductive zone (C) is revealed close to the SAF which extends downwards to about 10 km. PT inversion using the same model covariance parameter setup recovers the major features of the subsurface structure including the HCZ (not shown). The high resistivities of the Pacific Plate, however, were much better recovered if laterally isotropic smoothing ($\alpha_x = \alpha_y = 0.3$) was used (Fig. 3.33e). Alternatively, joint inversion of PT and VTF improves the recovery of high resistivities at depth and particularly in the coastal area (Fig. 3.33f).

Using four-component impedance data at 169 sites, the low-resistive zone appears narrower (Fig. 3.33g) than for 73 sites, especially if VTFs are included (Fig. 3.33h). This could be due to poorer resolution for high resistivities along the coast related to the irregular site distribution (cf. Fig. 3.26). By adding a 1000 Ωm half-layer (thickness: 60 km) a priori beneath the ocean extending from y = - 120 km to the southeastern model boundary facilitates recovery of high resistivities across the coastline (Fig. 3.33i). Moreover, the width of the low-resistive zone is now similar to the 73-site inversion results (cf. Fig. 3.24i). For the joint impedance + VTF inversion model (Fig. 3.33h) impedance misfits are slightly higher at sites on top of the HCZ. Starting a VTF-only inversion from the impedance-only result displayed in Figure 3.33(h), returns a model which is mostly unchanged showing slightly reduced conductivity values at depth (not shown). The overall VTF data misfits are slightly higher than for a VTF-only inversion. Closer inspection reveals significantly higher VTF misfits at a small number of sites, where impedances appear to be affected by static shift. In conclusion, a HCZ at depth is compatible with the VTF data but not necessarily required.

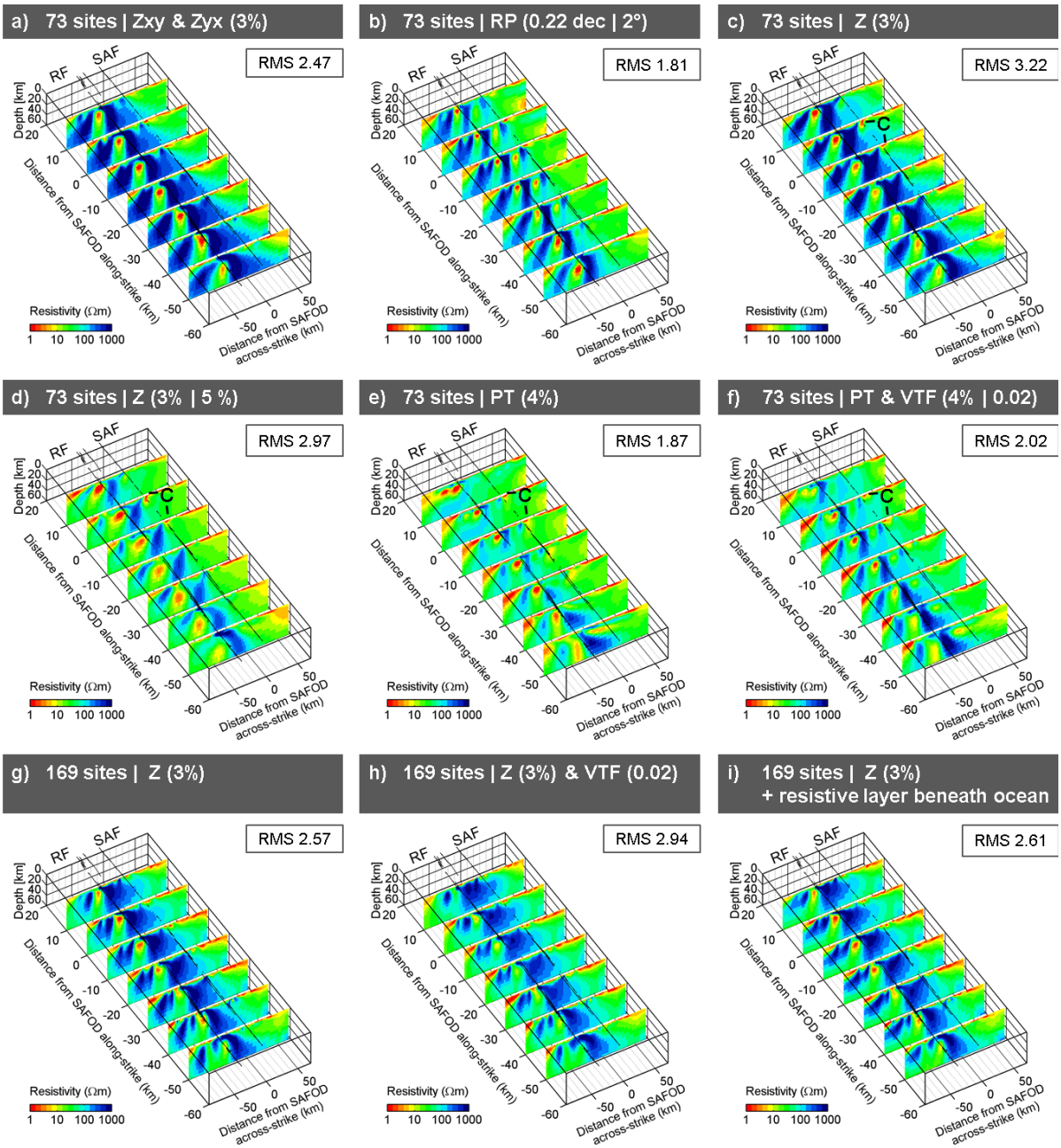

Figure 3.33: 3D resistivity models obtained from California MT data with two site layouts (cf. Fig. 3.1) and different data types. All inversions recover similar major subsurface features, showing a SAF-parallel highly conductive zone (HCZ) embedded in a high resistive Pacific Plate. **(a)-(f)** 73 sites; **(g)-(i)** 169 sites. **(a)-(b)** With a coarse, but uniform site coverage 3D inversion homogeneously recovers the 2D regional resistivity structure, in particular if only **(a)** off-diagonal impedances or **(b)** RP data are used. **(c)-(d)** To depict 3D along-strike variations of the conductivity structure, i.e. the subvertical conductive zone (C) close to the SAF beneath profiles ② and ③, the full impedance tensor is required. Putting more weight on the Zxy- and Zxx-components intensifies the appearance of the HCZ (d). **(e)** Inversion of PT data recovered the HCZ and also the surrounding high resistive zones if isotropic regularization ($\alpha_i = 0.3$) is used. **(f)** Joint inversion of PT and VTF improves the resolution of high resistivities in the coastal area. **(g)-(i)** For the denser, but irregularly spaced 169-site data set, high resistivities beneath the coast are less pronounced and the HCZ appears to be narrower. Including a highly resistive layer beneath the ocean a priori ((i), outside displayed area) improves recovery of central model domain structures and, in particular, the HCZ.

The upper 250 m of the models obtained with impedance or joint impedance + VTF inversion exhibit a highly variable, small-scale resistivity pattern, by which the 3D inversion compensates for small amounts of static shift and more complex galvanic distortion. This "geological noise" is effective for large parts of the data set, but apparent resistivities of xy- and yx-components between neighbouring sites vary typically only within half a decade at the shortest periods. Figure 3.34(b) suggests that the inversion is successful in compensating galvanic distortion even at more severely affected sites (red curve).

Closer inspection of the inversion models, however, reveals that distortion of impedances affects the resistivity structure directly beneath MT stations to several kilometres depth, e.g. at site 408 (Figs 3.34a,c-e). But put in perspective to the overall survey volume, the features can still be regarded as local. For the joint impedance + VTF inversion in Fig. 3.34(e) impedances are fitted only at long periods (blue curve in Fig. 3.34b), because VTF data, which are free of galvanic distortion, work against the appearance of inductive-scale artefacts. Impedance-only inversion results in a significantly better fit. Transferring the structure beneath site 408 from Figure 3.34(d) to the joint impedance + VTF inversion model results in an improved fit for the apparent resistivities (impedance amplitudes) at the expense of significantly altered VTFs at 408 and neighbouring sites. Joint inversion of impedances + VTFs is therefore more robust in presence of galvanic distortion. Additionally, a fine discretization of inversion models helps in this respect. Similarly, downweighting apparent resistivities vs. phases in RP inversion, reduces subsurface artefacts related to severe galvanic distortion. Inverting PT and/or VTF data which are free of galvanic distortion yields a continuous surface conductor (Fig. 3.34a).

As stated before, the 3D subsurface images largely match the 2D inversion results (cf. Fig. 2.7). A prominent difference is the absence of a conductive path (CP) between the HCZ at depth and the SAF beneath the northwestern profiles ① to ③ in the 3D inversion models. This connection between conductors at depth and the seismogenic SAF was interpreted as pathways for fluids and played an important role in the geologic interpretation of the MT results (Becken et al., 2011). The CP appeared, however, for 3D Zxy-only inversion (cf. Fig. 3.28a). Putting more weight on xy- and xx- than on yx- and yy-impedances by adjusting the error floors to 3 % and 5 %, respectively, or using a denser site spacing (169 sites, Figs 3.33g-i) did not significantly change the subsurface structure in this respect.

In order to get an impression of the consistence of the 2D results of Becken et al. (2011) with 3D inversion, I used the 2D inversion results to create starting and prior models for 3D inversion. 2D results were interpolated onto the 2 km × 2 km 3D grid for a depth range of 1 - 80 km within the station array. The outer parts of the 2D resistivity structure were continued as 2D boundaries in the horizontal directions parallel and perpendicular to strike as well as vertically for layers 1 to 14 (< 1 km). Below 80 km a 50 Ωm half-space was used.

The outcome of joint impedance + VTF 3D inversion (Fig. 3.35) which started from the

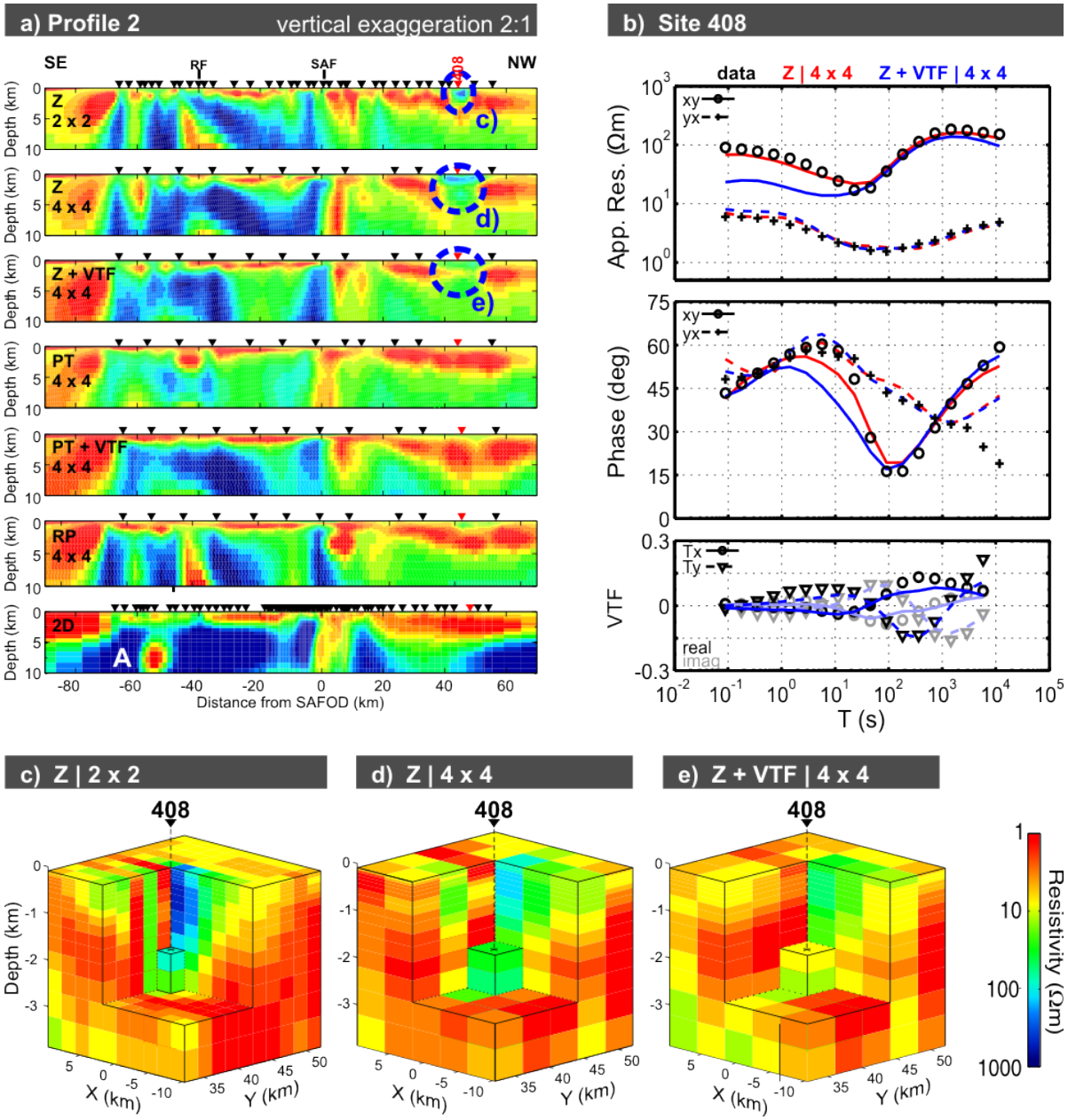

Figure 3.34: Near-surface structure along profile ② for various inversion models. **(a)** The overall resolution of the resistivity structure within the upper 10 km is very similar for various 3D inversion setups and compatible with the 2D result. Differences occur for isolated (3D) features (A) or where 3D inversion introduces features (dashed blue outlines) compensating for galvanic distortion at site 408 **(b)**. The extent and efficiency of these structures depends on the model discretization and the inverted quantities. **(c)** The 2 km x 2 km discretization (169 sites) and the applied regularization allow for both small-scale structures and high resistivity contrasts. **(d)** For the 4 km x 4 km grid (73 sites, impedances) a similar compensation of galvanic distortion provokes a significant inductive response. **(e)** In joint impedance + VTF inversion (4 km x 4 km grid, 73 sites), VTFs work against artefacts related to galvanic distortion; impedances are fitted only at long periods, as can be seen in **(b)**.

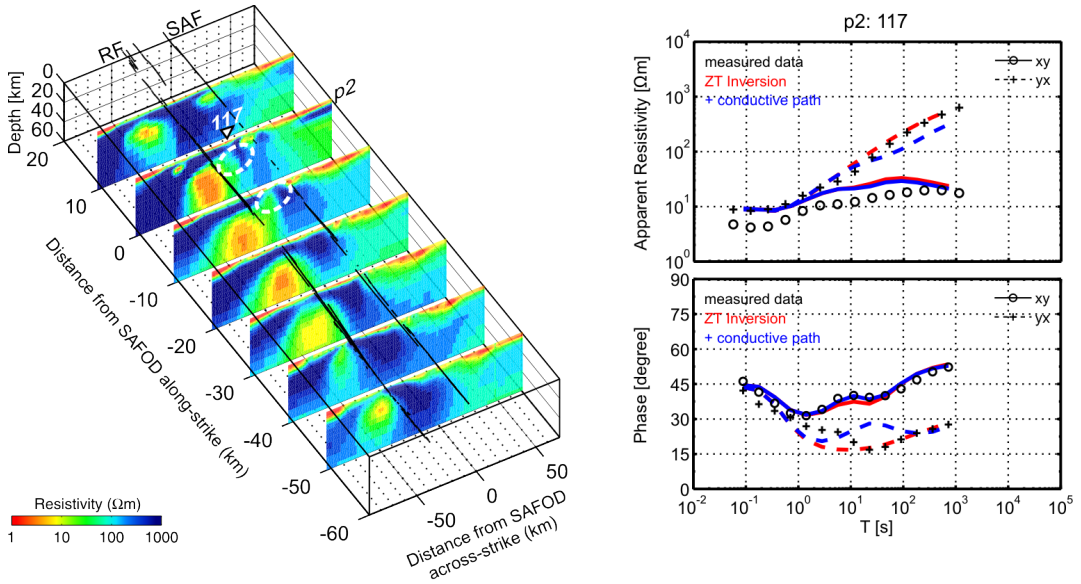

Figure 3.35: 3D resistivity structures obtained from inversion of the California data using 2D inversion models as a priori information. 3D inversion attenuates the conductive channel beneath profiles ② and ③ (white dashed outlines). Model responses in this area exhibit systematic deviations from the data at periods of 1 - 10 s (red curve, right panel). Restoring the link in the final 3D inversion model has an effect on the yx-component between 10 s - 100 s (blue curve, right panel). The response of the conductive link, however, appears to be part of the general discrepancy between data and inversion responses at shorter periods.

interpolated 2D inversion models shows that the 2D results are robust and generally valid in the 3D context. The overall RMS of 3.40 is acceptable considering that due to the much coarser 3D grid the shallow subsurface could only be roughly approximated when creating the starting model and, more importantly, because data misfits do not reveal systematic variations in the frequency-space domain. Changes between 2D and 3D models primarily occur in the upper 2 km close to site locations. These changes represent local adjustments of the interpolated resistivity structure and near-surface structural features accounting for galvanic distortion. In 2D inversion, static shift was addressed by setting high error floors to the TE-mode apparent resistivities and using a fine horizontal discretization to allow TM-mode static shifts to be accounted for within the 2D inversion models (cf. Becken et al., 2008b, 2011).

Intriguingly, the conductive channel, which links the HCZ at depth with the surface in the 2D models, was attenuated by 3D inversion and partly replaced with higher resistivities (white dashed outline, profiles ② – ③). At sites located on profile ② in the vicinity of the SAF a systematic deviation of 3D inversion responses from the measured yx-impedance phases can be observed for periods between 1 s and 10 s. Restoring the link manually in the final 3D inversion model shows a significant effect on the yx-component of the apparent resistivity and phase data between 10 s and 100 s (Fig. 3.35, right panel). The response of the conductive

path, however, appears to be consumed by a general discrepancy between data and inversion responses at shorter periods. This indicates that the conductive link may be consistent with the data but not required by 3D inversion.

Two possible explanations for the general absence of the conductive path in the 3D inversion results come to mind: (i) the CP is an artefact introduced by limitations of 2D inversion or (ii) 3D inversion cannot resolve this structure. This issue will be discussed in detail in the next section.

3.5.4 Resolution studies

Along-strike extent of HCZ

The along-strike extent of the deep HCZ is depicted similarly in the 3D inversion results of the California data set. The HCZ is continued beyond the southeastern (SE) edge of the station array at depths > 20 km, whereas it stops at the northwestern (NW) edge (Fig. 3.36). In a series of forward modelling tests based on the inversion result presented in Figure 3.33(i), I investigated the resolution of the HCZ structure outside the California MT array.

Towards NW, the low resistivities of the HCZ (< 10 Ωm) terminate close to the northwesternmost station at ∼10 km distance from profile ① (Figs 3.36a-c). Further along-strike beyond the array resistivity values of 30 Ωm to 50 Ωm exceed the prior model resistivities (10 Ωm) (Fig. 3.36). However, adjacent model regions comprise even higher resistivities (100 - 300 Ωm) and suggest that the HCZ continues further NW. Setting HCZ along-strike model resistivities (zone A in Fig. 3.36a) to higher (100 Ωm) or lower (5 Ωm) values at depth between 6.78 km and 20.48 km does not significantly alter the model responses. Hence, towards NW the along-strike extent of the HCZ is not constrained by the data.

Beyond the SE edge of the station array, extended zones of low resistivities (0.5 - 10 Ωm) appear at depth of 8 km to 40 km extending 150 km along-strike SE of profile ⑦ (hatched area in Figs 3.36a-c). In the inversion models, these zones are usually connected to the HCZ at depths > 20 km. Extension of the connection towards shallower depth (14.18 km) as outlined by feature B (Fig. 3.36b) is similarly compatible with the data.

To investigate the influence of the conductive structures beyond profile ⑦, I increased resistivities in zone C (20.48 - 51.15 km depth) to 100 Ωm. These modifications significantly change model responses for periods > 10 s at stations located above the HCZ and towards the coast on profiles ⑦ to ③ and result in significantly larger data misfits. In particular, phase maxima of the xy-component in the period of 70 s to 700 s related to the HCZ are up to 7° lower. High conductivities in zone C must extend at least 40 km beyond profile ⑦ to yield a reasonable fit of the xy-phases.

The broad shape of zone C suggests that the HCZ may become wider outside the station array. To test if a continuation with uniform across-strike extent could also explain the data,

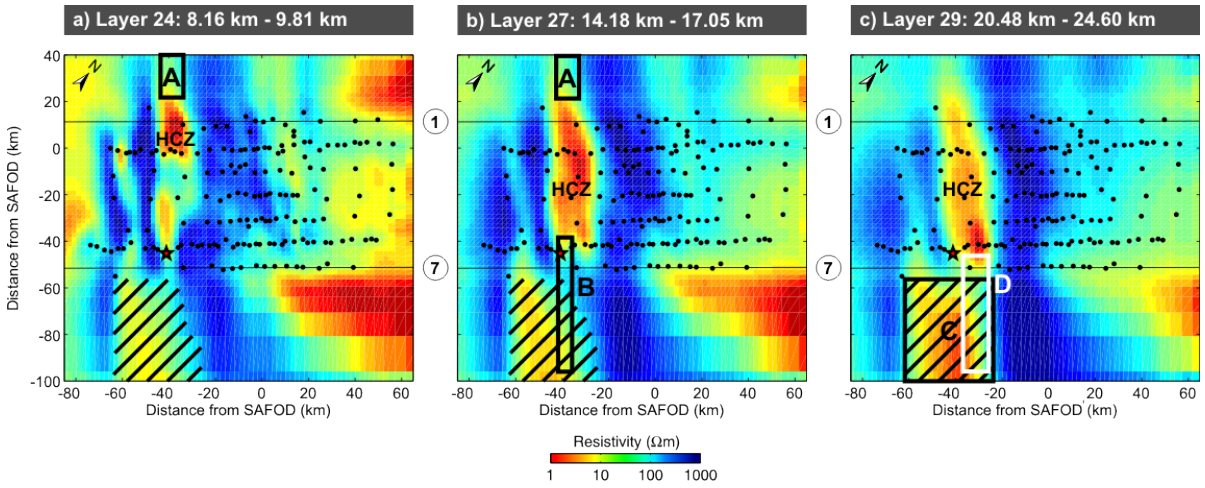

Figure 3.36: Illustration of 3D forward modelling tests investigating the along-strike extent of the HCZ based on the 3D inversion result displayed in Fig. 3.33(i). Zones A - D outline areas were model resistivities were modified (see text). Note, zone C extends 100 km further southeast outside the displayed area. The shape of extended zones of low resistivities in the southern survey area (hatched area) is closely related to site 503 (asterisk).

I replaced zone C with resistivities of 100 Ωm and extended the HCZ as it appears beneath profile ⑥ at depth of 20.48 km to 42.60 km (feature D in Fig. 3.36b, 10 Ωm). This model variant produces equivalent MT responses at most sites. Substantial differences are limited to site 503 (asterisk in Figs 3.36) and suggest that the broad appearance of high conductivities SE of profile ⑦ is an artefact related to this site. Similar to the previous test, Zxy data require the conductor (D) to continue at least 40 km beyond the station array.

In summary, the minimum along-strike extent of the HCZ can be constrained to 100 km between the NW edge of the survey area to 40 km beyond profile ⑦ towards the SE.

Conductive path between HCZ and SAF

In the following, I investigate the recovery of a conductive path (CP) between HCZ and the SAF in 3D and 2D inversion. I used the SYNPRK-path model, where the HCZ was connected to the sediments for 530 km and 20 km northwest of profile ③, respectively (Fig. 3.18). Comparison of SYNPRK-path and SYNPRK model responses reveals that sensitivity to the conductive path (CP) is limited to the vicinity of the SAF for VTFs and off-diagonal impedances, while the xx- and yy-impedances are affected over a much larger area.

Along profile ②, impedance phase changes (up to 15°) from the SYNPRK response are observed for the off-diagonal components at periods of 10 s and 3000 s in the area where the CP reaches surface (Fig. 3.37a). Whereas yx-phases exhibit larger differences if the CP is limited to 20 km beneath profiles ③ to ②, xy-phases are particularly altered by the 530 km-

long CP extending to the NW edge of the HCZ as Zxy is dominated by currents parallel to strike. With respect to the entire data set, deviations of the SYNPRK-path data from the SYNPRK responses are larger for the 530 km-long CP.

Inversion results of the California data which lack the CP exhibit systematic misfits between data and model responses along profile ② (Fig. 3.37b). The misfit patterns between observed and modelled data are similar to the differences between SYNPRK-path and SYNPRK responses (arrows in Figs 3.37a-b). This suggests that a CP linking the HCZ to the surface is present in the subsurface but this feature is not resolved by 3D inversion.

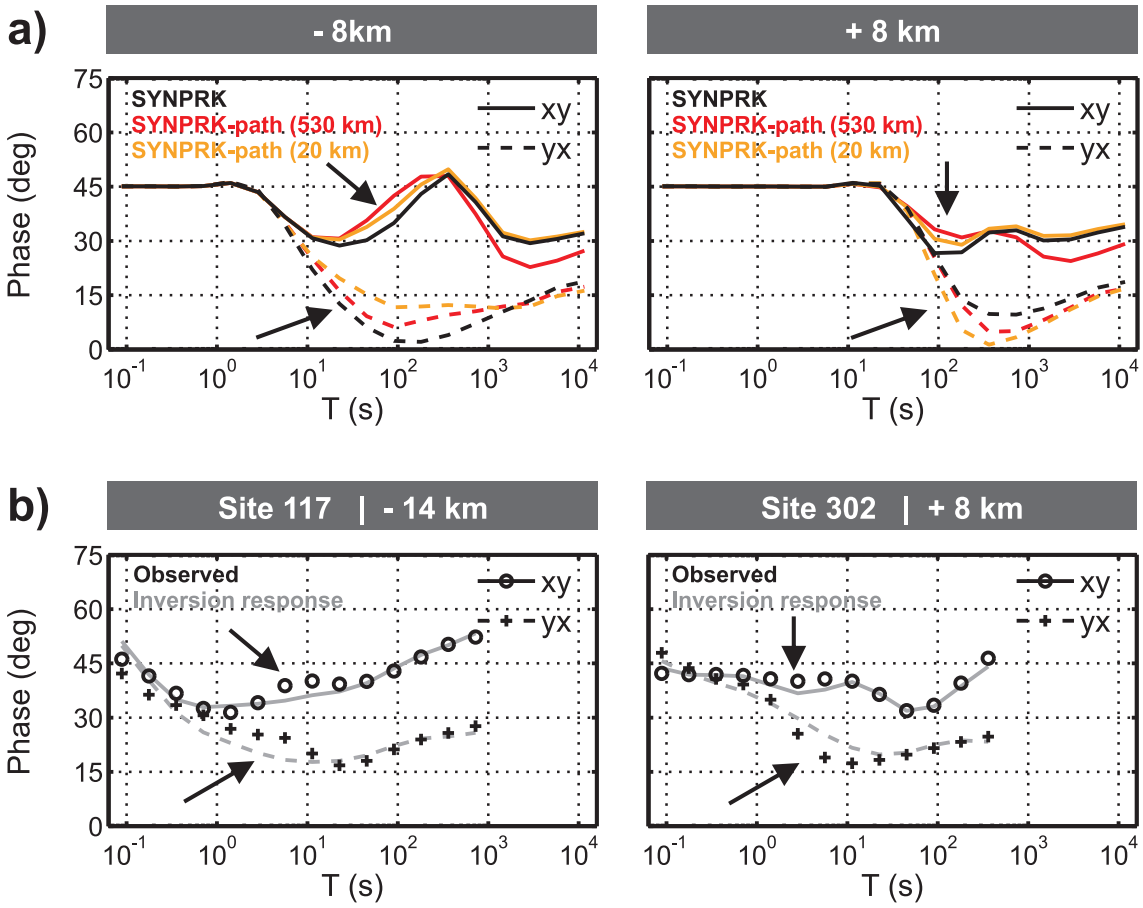

Figure 3.37: Conductive path (CP) between HCZ and SAF? **(a)** Comparison of SYNPRK-path and SYNPRK phase responses along profile ② at ±8 km distance from where the CP reaches surface. The influence of the CP is expressed in systematic phase changes from the SYNPRK response on either side of the CP-outcrop (indicated by arrows). **(b)** For the field data, phase misfit patterns between observed data and inversion model responses at sites located along profile ② on both sides of the point where the CP reaches surface in the 2D results are similar to the differences between SYNPRK-path and SYNPRK responses (arrows, cf. (a)). This behaviour suggests that the misfit is related to the absence of the conductive path in the inversion results.

To investigate this, I tested 3D inversion with the SYNPRK-path data sets (CP 530 km and 20 km) using both a homogeneous (10 km × 10 km) and the irregular 169-site field station layout. Model setups are the same as previously described for the California MT array and the SYNPRK-inversions (sec. 3.4). The results are summarized in Figure 3.38.

Similar to the measured data, full impedance inversion (10 km × 10 km) recovers an isolated deep conductor (Fig. 3.38a, HCZ), whereas Zxy-only inversion reveals a link between the deep HCZ and the sediments (Fig. 3.38b). Misfit distributions over the array do not reveal systematic variations which would correlate with the SYNPRK-path sensitivity distribution. Instead, data misfits are dominated by incomplete reproduction of the coastal resistivity contrast, which was already described for the SYNPRK model (cf. Figs 3.24 and 3.25). However, visual comparison of apparent resistivity and phase curves reveals small systematic phase misfits at sites near the SAF similar to the misfits observed for the California MT array (cf. Fig. 3.37b). Inverting PT data shows a clear image of the CP (Fig. 3.38c). For this example, model covariance parameters were set to 0.3 for both horizontal directions. Using the same smoothing setup as for impedance inversion (0.4/0.2/0.3) the connection between HCZ and surface is only weakly expressed in the inversion result (not shown). In return, setting model smoothing parameters to 0.3/0.3/0.3 for impedance inversion impairs the overall recovery of the regional scale SYNPRK-path model. For the California field data set, I also observed general improvements of PT inversion with isotropic covariance settings (cf. Fig. 3.33e).

Finally, downweighting the Zyx and Zyy components in impedance inversion reduces the influence of the ocean effect on the inversion result and enables resolution for the conductive path (Fig. 3.38d). Adding VTFs to the inversion improves the shape of the conductive link (Fig. 3.38e). For all impedance inversion results, a pronounced conductor at depth appears in the coastal area. Such a structure was also observed for the SYNPRK inversion models (cf. Figs 3.24 and 3.27). However, this coastal conductor is more intensely expressed in the SYNPRK-path results and incorporation of VTFs does not suppress this artificial feature. Removing the conductor, I find the diagonal impedances most severely affected as their amplitudes are reduced at long periods. This suggests that a conductivity contrast in the coastal area is an alternative way to explain the SYNPRK-path data, at least the xx- and partly the yy-impedances. The influence of the coastal structure on the image of the SYNPRK-path structure becomes particularly apparent, if the 169-site field data layout is used. This setup provides increased site density close to the SAF above the conductive link of the SYNPRK-path model; the coastal area, however, is less densely sampled. Inversion results of these data on a 2 km x 2 km model grid image an extremely low-resistive (30 Ωm) deeper subsurface compared to the 2000 Ωm Pacific Plate of the SYNPRK-path model, in particular along the coastline (Fig. 3.38f). The conductive path is not resolved but the HCZ is connected to the sedimentary layer directly above. Similar difficulties resolving the highly resistive Pacific Plate along the coast were observed for inversion of the SYNPRK data using the 169-site layout (cf. Fig. 3.26c).

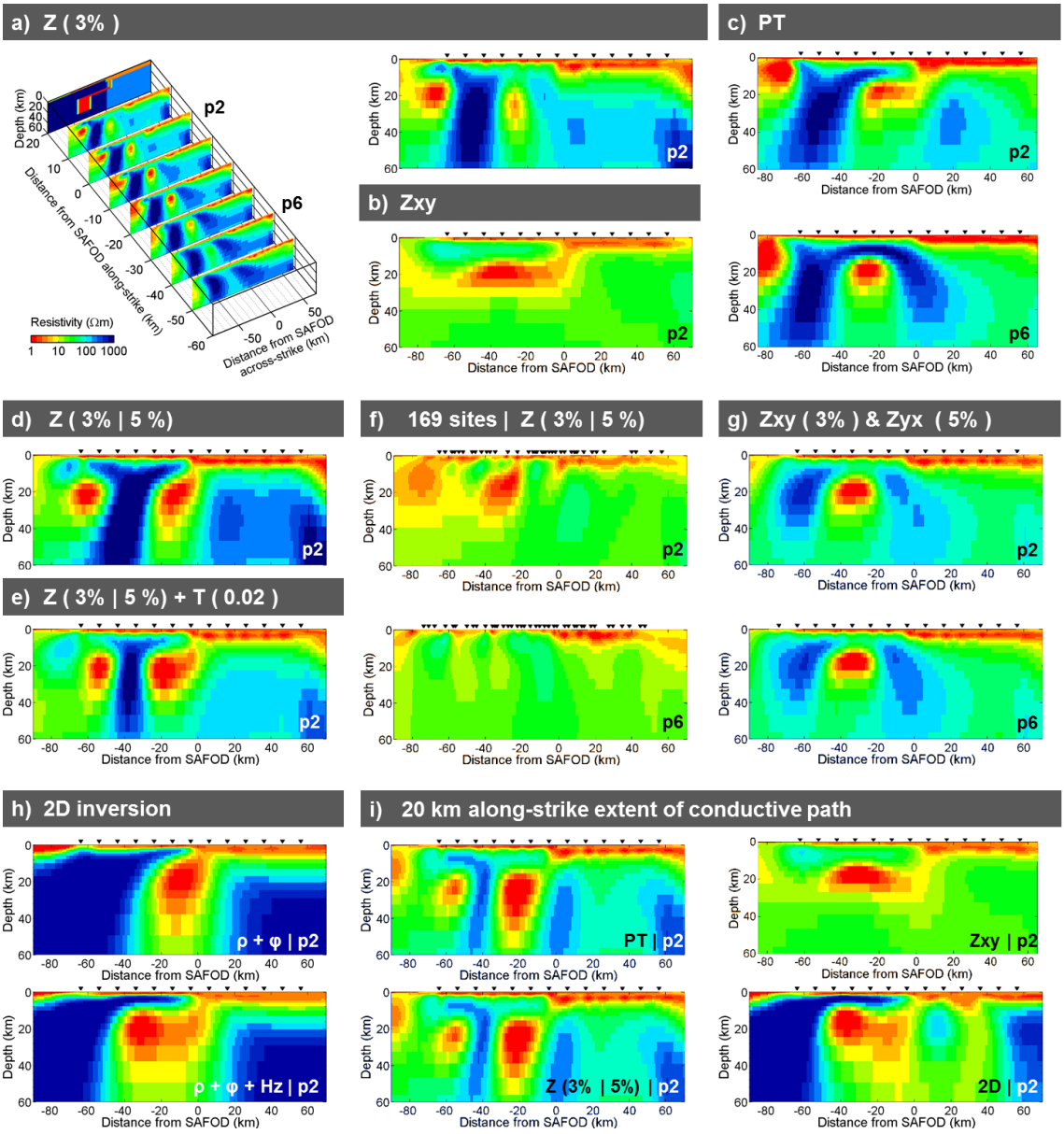

Figure 3.38: Resistivity models obtained from 3D and 2D inversion results of SYNPRK-path data sets (cf. Fig. 3.18) along selected profile lines for CP extents of 530 km (a-h) and 20 km (i). **(a)** Full impedance using same error floors as for the California data set reveals an isolated HCZ; **(b)** Zxy-only and **(c)** PT inversion, on the other hand, recovers the conductive path (CP). **(d)-(e)** In 3D inversion, the CP can only be recovered if the full impedance tensor is used and error bounds for Zxx and Zxy (3 %) are smaller than for Zyx and Zyy (5 %). **(f)-(g)** Inversion using the irregular 169-site field layout, however, fails to recover the CP. Similarly, off-diagonal impedance 3D inversion is not able to resolve the 3D conductive path (g). **(h)** However, 2D inversion immediately recovers the conductive path. Note the similar influence of VTFs on the shape of the conductive path in 2D and 3D (d, e) inversion. **(i)** If the CP extends only 20 km along strike, both 3D PT and impedance inversion fail to recover this structure (left column). The CP is, however, depicted by 3D Zxy-only and 2D inversion (right column).

In contrast to the SYNPRK inversion, however, the conductivity of the deep HCZ varies along-strike and the HCZ is only clearly imaged in the area beneath profiles ① to ③ where it is connected to surface. In regions, where the link is only weakly expressed or not present at all, the station layout does not influence the conductivity distribution along the deep conductor (cf. Fig. 3.27). This would suggest that the apparently poor resolution to subsurface structures of the 169-site data set is mostly an artefact caused by combination of the SYNPRK-path structure and the particular site layout.

The artificial coastal structures are reduced when discarding the diagonal impedance components, inverting only Zxy and Zyx (10 km × 10 km site layout); however, the conductive path, however, is not resolved (Fig. 3.38g). Surprisingly, 2D inversion of the SYNPRK-path data set along profile ② with the same site configuration immediately recovers the CP for standard inversion settings and error floors (Fig. 3.38h). Note the similar effect of VTFs on the shape of the conductive link in 2D (Fig. 3.38h) and 3D (Figs 3.38d-e) inversion models. Compared to the 2D inversion results of the measured California data the connection suggested in the results for the SYNPRK-path data (CP 530 km) is more conductive. In addition, the CP image in the 3D inversion results of Zxy data has a larger along-strike extent than observed for the field data (cf. Fig. 3.28a).

I finally used the SYNPRK-path data set generated with the CP extent limited to 20 km beneath profiles ③ to ②. For this scenario, the conductive link is not reliably recovered with 3D PT or four-component impedance inversion (Fig. 3.38i, left column). A hint to this structure in the 3D result is a slightly reduced background resistivity beneath the SAF for the northern profiles. In order to reveal reasonable model structures at the coast, Zyx data had to be downweighted. However, Zyx is the component which is most sensitive to the 20 km-long CP (cf. Fig. 3.37a). In 3D, the short CP variant is only recovered when inverting separately for the Zxy-component. However, recovering this short CP variant is no problem with 2D inversion (Hz, TM, TE), even though I had to exclude yx-phases close to 0° in the period range between 50 s and 500 s which are most indicative for the CP (cf. Fig. 3.37a). If yx-phases between 0° and 5° are not masked, 2D inversion fails to converge and introduces misleading artificial structures beneath affected sites. In contrast to 3D inversion results 2D models successfully image the highly resistive Pacific Plate extending beneath ocean, which facilitates the resolution of the conductive path. 2D inversion uses a model regularization which only penalizes lateral and vertical variations of model resistivities but does not penalize against a prior model. The use of prior models in ModEM3DMT suppresses these far-reaching but homogeneous structures and impedes the resolution of the CP (cf. Fig. 3.38f).

In summary, 3D inversion of the full impedance tensor can only resolve the conductive link if it is (i) very pronounced with resistivity of 1 Ωm and extending along-strike for at least 150 km and (ii) the impedance components affected by the ocean effect (mainly Zyx) are downweighted. In all other tests, only hints of its existence are revealed indirectly, e.g.

expressed in a slightly weaker resistive barrier near the inland edge of the HCZ, along-strike variation of the conductivity of the HCZ or the presence of a boosted artificial coastal conductor. Such hints are only recognized and interpreted correctly if the true underlying structure is known. Examining the data fit site by site, the misfit caused by the absence of the CP in SYNPRK-path inversion results is minor compared to the general data fit quality. Hence, no pronounced systematic misfit is observed for the models without a conductive path. However, using Zxy-only and 2D inversion the CP can be imaged for both 530 km and 20 km along-strike extent.

Considering the 3D and 2D inversion results obtained for the California MT array (cf. Figs 3.28a, 3.33, 2.7), I find a dependence of CP recovery on the setup of the inverted data which is similar to the SYNPRK-path results, in particular for the CP with limited along-strike extent (20 km, cf. Fig. 3.38i), where the CP was recovered for 3D Zxy- and 2D inverison but not if the full impedance tensor was used. These findings support the existence of a conductive path between the HCZ to the SAF in the Parkfield region. Furthermore, the results indicate that such a conductive path structure does not extend much further NW than the MT station array as full impedance inversions of the California data did not resolve the conductive link directly. However, the field data do not constrain the along-strike extent of this conductive path in NW direction. For inversion of four component impedance data, the most explicit hint to such a structure is given in several of the 73-site inversion results (Figs 3.33c-f), where a subvertical conductor appeared close to the SAF beneath profiles ② and ③ at the location where the conductive path reaches surface in 2D inversion results. In addition, 3D inversion using the 2D inversion model as a priori information confirmed, that the 2D inversion results are consistent with the 3D data set. Removal of the path during inversion is mostly caused by model smoothing and results in a systematic misfit for the yx-impedance component in the vicinity of the SAF on profile ②.

3.5.5 Preferred 3D model

Comparing the 3D inversion results of the California data set and considering the results of the SYNPRK and SYNPRK-path model studies, I chose the inversion result of Figure 3.33(i) as preferred model (PRK-3D). The inversion is based on impedances from 169 sites and includes a priori high resistivities beneath the Pacific Ocean; the VTF data are not used. Figure 3.39 shows the PRK-3D inversion result at four horizontal slices. The upper 250 m of the model exhibit a highly variable, small-scale resistivity pattern (Fig. 3.39a), which is how 3D inversion compensates for small amounts of galvanic distortion. The surficial features appear stretched along the SAF-parallel axis since higher model smoothness was enforced in this direction.

At mid-range depths ($<$ 10 km, Figs 3.39b-c), the 3D resistivity structure is dominated by a conductive (0.1 - 5 Ωm) sequence with a thickness of approximately 2 km in most parts of

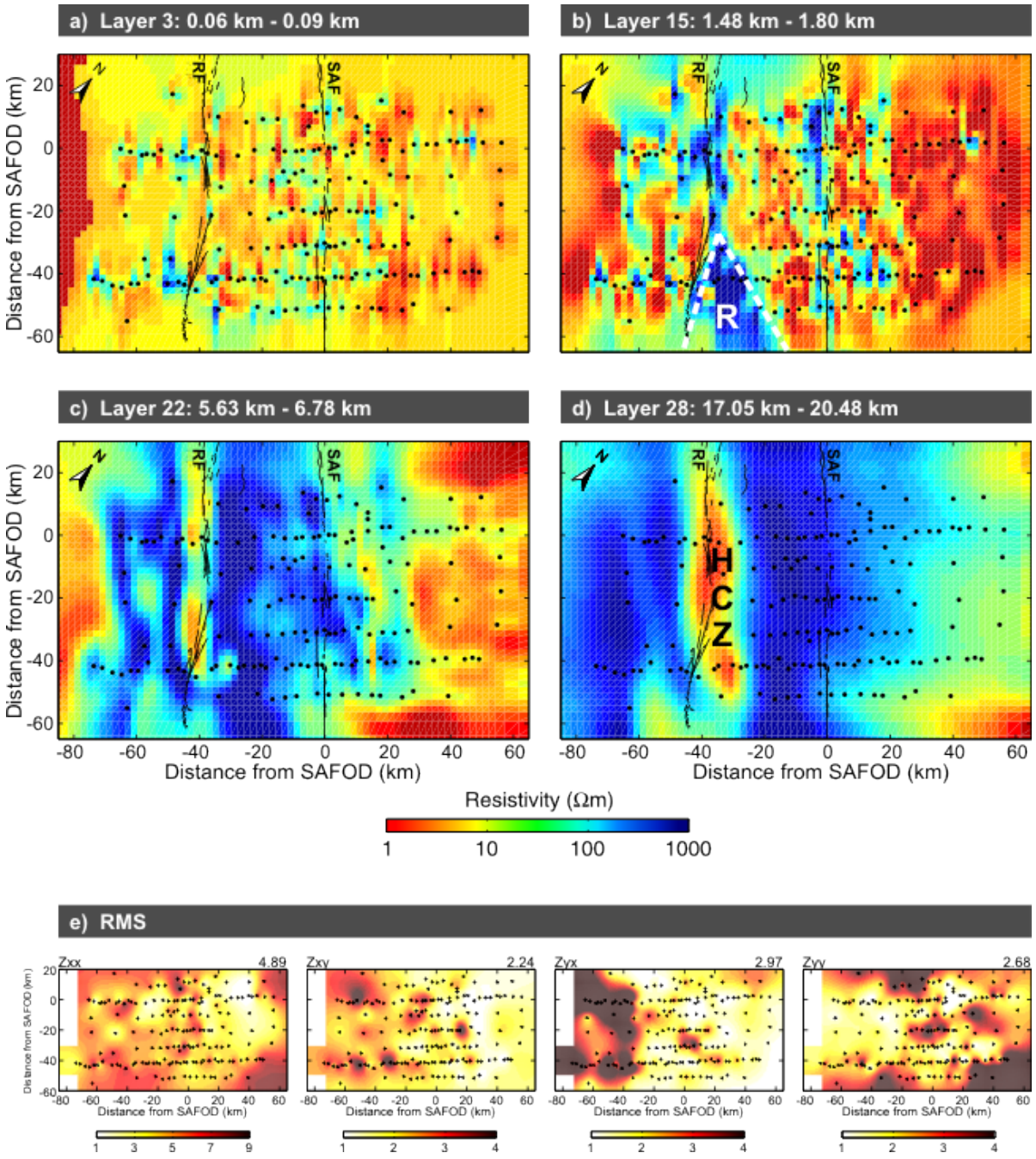

Figure 3.39: (a)-(d) Preferred 3D inversion model PRK-3D (cf. Fig. 3.33i) displayed as horizontal slices at various depths; RF Rinconada fault **(e)** PRK-3D data misfits for all inverted components. **(a)** Variable, small-scale structures in the top layers illustrate how 3D inversion accounts for galvanic distortion in the model structure. **(b)-(c)** The thickness of the low-resistive sedimentary cover varies between 2 km on the Pacific side of the SAF and 9 km at the northwestern profile ends. The resistive wedge (R) at 1 - 4 km depth in the southwestern survey area is important to fit VTF data in this region. **(d)** At depths > 10 km a zone of high conductivities (HCZ) extends parallel to the regional strike direction. **(e)** Misfit distributions for the PRK-3D response show a uniform data fit.

the array and up to 5 - 9 km in the San Joaquin valley. In areas close to the coast and along the surface traces of the San Andreas and Rinconada faults the conductive layer thins out and zones of high resistivities ($\sim$ 1000 Ωm) reach close to surface. At mid-crustal levels (approx. 10 - 20 km, Fig. 3.39d), the model shows resistive structures (200 - 2000 Ωm) extending from the coast to the SAF. A 10 - 20 km wide region west of the SAF appears as conductive (1 - 10 Ωm); this zone (HCZ) extends parallel to the SAF with its top located between 9 km and 17 km depth.

Throughout the array, the data fit is of similarly good quality, yielding an overall RMS of 2.61. Investigation of the misfit values in the frequency-space domain revealed usually smooth and homogeneous distribution for most components (Fig. 3.39e). However, I still observe a moderate increase of misfit values towards the ocean and long periods for impedance components which are sensitive to the high resistivities of the Pacific Plate (Zyx, Zxx; cf. Fig. 3.25).

3.6 Comparison of 3D and 2D results

3D and 2D inversion results of the measured data are displayed in Figures 3.33, 3.34, 3.39, and 2.7. Direct comparisons of selected profile traces can be found in Figure 3.40.

In the upper 10 km, 3D and 2D inversion results depict very similar resistivity structures. Along the seven profile traces, the lateral variations of the conductive sedimentary cover agree remarkably well, although larger site distances and a much coarser subsurface discretization were used for 3D modelling (Fig. 3.34a). Structural differences in this depth range are small-scale, occurring for some isolated (3D) resistivity features (labelled A in Figs 3.34a and 3.40a) or where measurements are severely affected by galvanic distortion (Fig. 3.34a, dashed blue outline).

At depths below 10 km, the subsurface images of 3D and 2D models are in principle consistent (Figs 2.7, 3.33f, 3.40). They reveal a SAF-parallel HCZ embedded in a high-resistive background and the absolute resistivity levels are very similar. Other characteristics of these structures, in particular of the HCZ, are unexpectedly different (see below).

The HCZ appears consistently with its southwestern edge located at about 40 km west of the SAF beneath profiles ① - ⑥ (Fig. 3.33f). For 2D inversion, the depth to the top of the HCZ is a very robust and well-defined feature (15 - 20 km, Becken et al., 2011). In 3D inversion, on the other hand, this zone appears at slightly shallower depth (9 - 17 km) and surficial structures are often more conductive (Fig. 3.40). This suggests that resistivities of 3D models in this region are biased towards low values by the chosen background resistivity of the prior model (cf. Fig. 3.24). Unfortunately though, using higher a priori resistivities for the 3D inversion impedes resolution for the HCZ.

The HCZ in the 3D inversions exhibits a similar across-strike extent of 10 - 15 km beneath

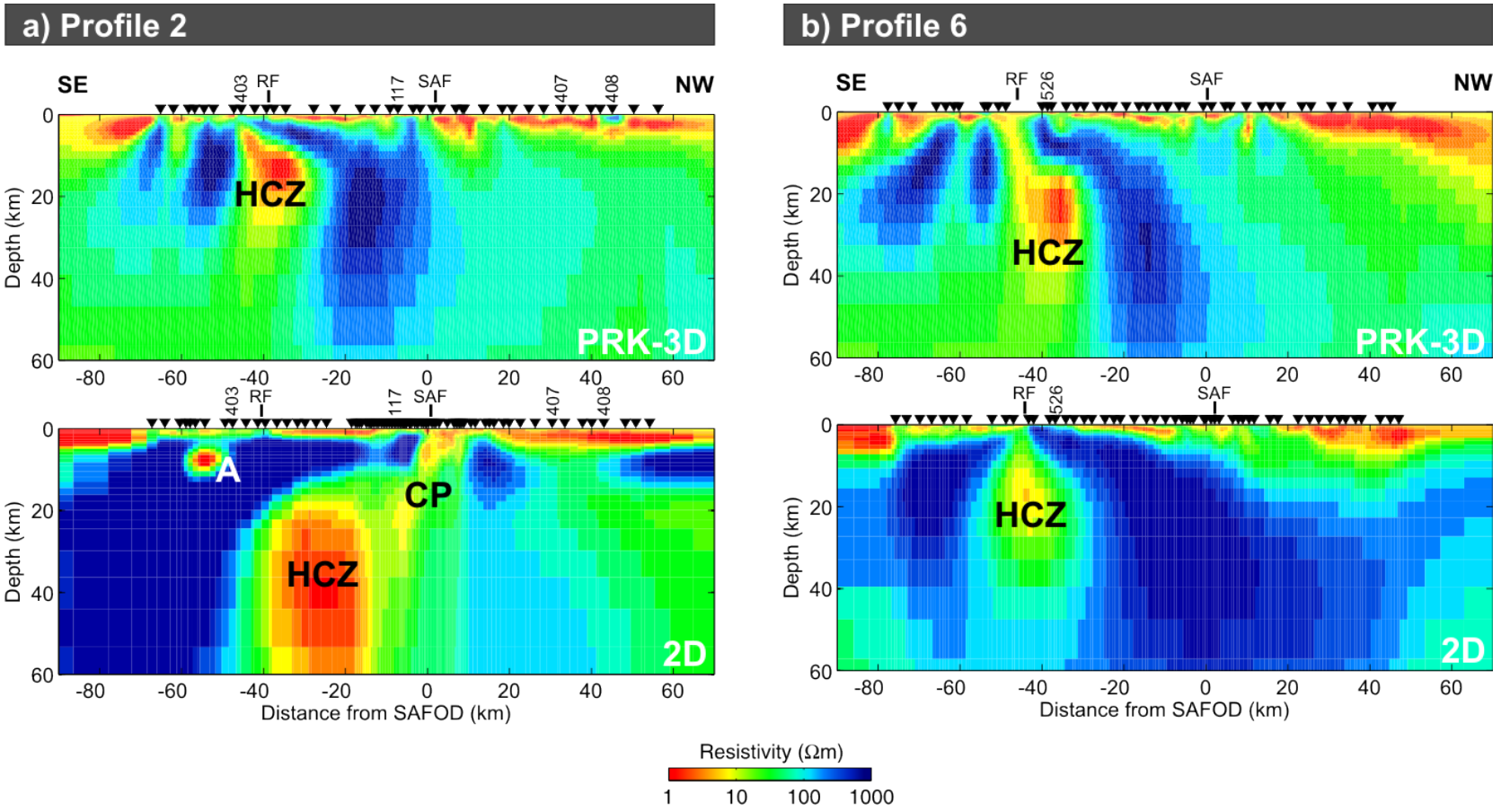

Figure 3.40: Comparison of PRK-3D (cf. Fig. 3.33i) and 2D (Becken et al., 2011) resistivity models along profiles ② and ⑥. 3D and 2D inversion results are in general consistent, in particular for the upper 10 km where differences are only small-scale, e.g. feature A beneath profile ②. **(a)** The HCZ is systematically narrower in 3D inversion results, which is most pronounced beneath profile ②. Moreover, the conductive path (CP) connecting the HCZ to the SAF is not resolved in 3D inversion. **(b)** Along profile ⑥, 3D and 2D results are very similar for the entire depth range. 3D responses, however, explain the data in this area significantly better than the 2D result as the 3D model integrates significant off-profile structures in the upper 4 km (cf. Fig. 3.39b).

all profiles at approximately 15 - 20 km depth (Fig. 3.39d). 2D inversion imaged this zone as wider (20 - 35 km; profiles ① - ⑤, ⑦) and more variable in both horizontal and depth extent. For 3D, along-strike variability is suppressed, as a relatively strong smoothing is applied. If a lower regularization is applied parallel to the SAF, however, the deep structures are generally feebler expressed, but along-strike variations are not more pronounced (cf. Fig. 3.24h). This is consistent with the synthetic studies as I observed similarly narrower low-resistive zones for the SYNPRK data when compared to 2D results (cf. Fig. 3.18c). The overall conductance of the HCZ is lower for the 3D results.

Differences in the deep resistivity structure of 3D and 2D results are most pronounced beneath profile ② (Fig. 3.40a). Here, the cross-sectional area of the HCZ differs significantly. The conductive path (CP), which links the HCZ with the seismogenic SAF in the 2D results cannot be resolved in 3D directly (see sec. 3.5.4, Fig. 3.38). The depiction of a CP in Zxy-only results (cf. Fig. 3.28a), however, supports the existence of such a link at least beneath profiles ② and ③. Further northwest, the presence of a link remains unclear. The absence of the CP in the 3D results causes small, but systematic deviations of the yx-impedance phases for periods of 1 - 10 s (Fig. 3.41b; cf. Figs 3.35, 3.37b) in this area. In general, 3D and 2D data fits are of similar quality along profile ② (Figs 3.41a-c).

Beneath profile ⑥, images of both shallow and deep resistivity structures are very similar for 3D and 2D inversion models (Fig. 3.40b); even width and conductance of the HCZ are nearly identical. Becken et al. (2011, supplementary) indicated that the inverted quantities in this profile section were not entirely consistent with the 2D assumptions and, hence, the geometry of the HCZ in the 2D result might be biased by 3D effects in the data. In this region, 3D inversion reveals a highly resistive zone (labelled R in Fig. 3.39b) at 1 - 4 km depth beneath the surface trace of the Rinconada fault, which widens towards the southeast. forward modelling tests show, that this resistive wedge is very important to fit the impedances and particularly the VTFs, which have a strong off-profile component in this area (see also sec. 3.5.2). Consequently, 3D inversion can explain the measured data along profile ⑥ significantly better (Fig. 3.41d).

In 2D modelling, the HCZ virtually extends "infinitely" along-strike. In the 3D models, the HCZ is continued beyond the southeastern edge of the station array at depths > 20 km, whereas it stops at the northwestern edge (Fig. 3.39d). This skewed image of the HCZ could reflect the influence of the strike direction of the bathymetric fabric of the Pacific Ocean, which is oblique to the regional strike direction of the survey area (cf. Figs 3.24, 3.18c). forward modelling tests based on the PRK-3D model suggest a minimum HCZ extension of 40 km beyond profile ⑦ (see sec. 3.5.4). The extent towards NW is not resolved but a NW continuation would be compatible with the data. The overall minimum along-strike extent of the HCZ measures about 100 km.

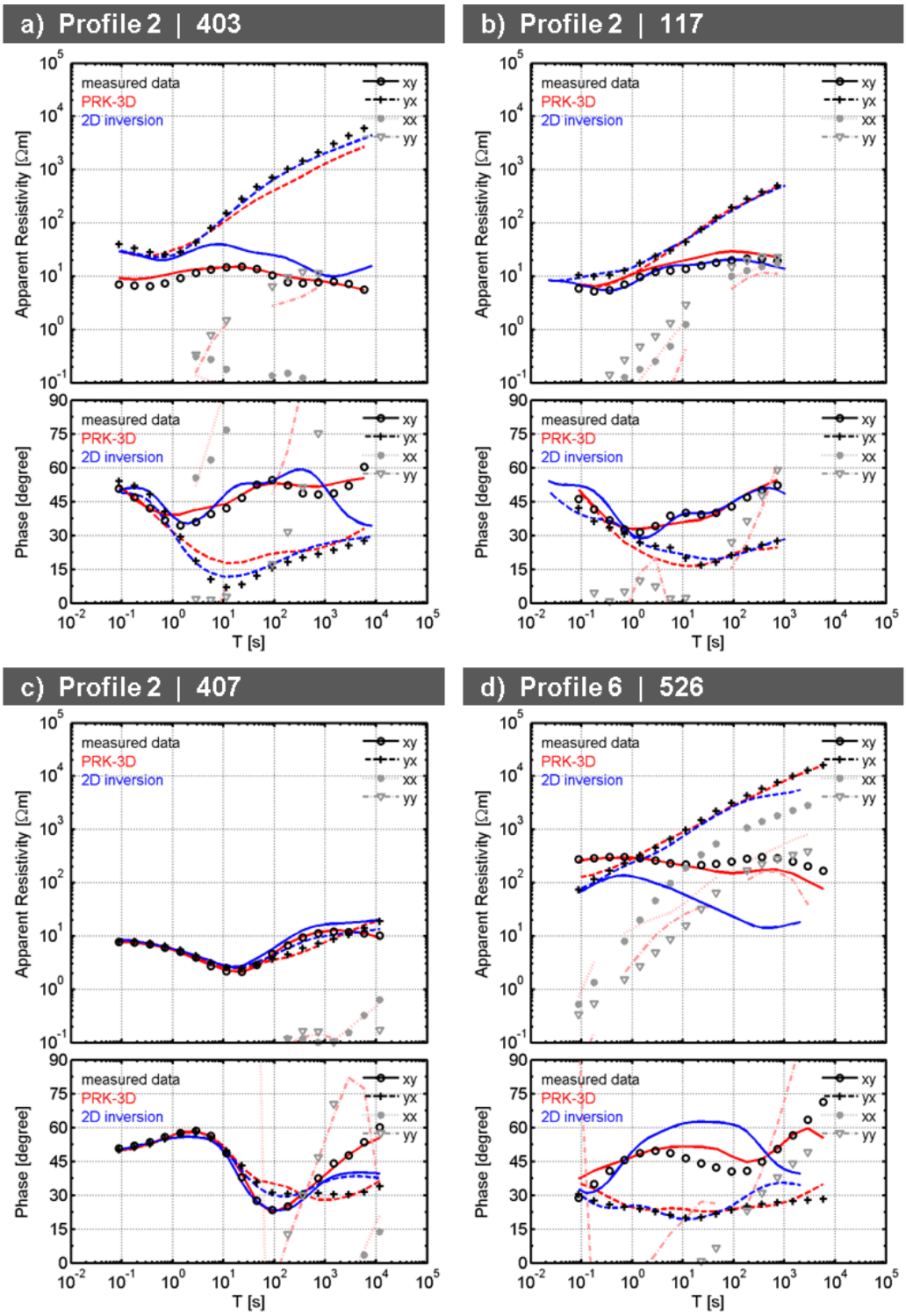

Figure 3.41: Comparison of PRK-3D and 2D model responses at sites along profiles ② **(a)-(c)** and ⑥ **(d)**. Site locations are marked in Fig. 3.40.

3.7 Discussion

3D MT inversion including two new data types was systematically tested with a large real-world and a complementary synthetic data set. The inversion results were robust with respect to existence, size and position of regional scale conductivity structures. At the same time, unexpected obstacles and pitfalls were revealed.

The outcome of 3D inversion is not always independent of the coordinate system, even if the full impedance tensor is used. For both the California and the SYNPRK data sets the extended highly conductive zones at depth could only be resolved with standard data error settings if data and model grid were rotated to the dominant strike direction of the SAF fault system. In presence of a 2D regional background structure with large conductivity contrasts, reliable and meaningful 3D impedance inversion models can only be recovered in a coordinate system where tangential-electric and tangential-magnetic modes maximally separate. The influence of the inversion coordinate system is significantly less expressed for VTF and PT data which are normalized quantities and particularly sensitive to variations of subsurface conductivities. In order to use the full MT data, however, detailed strike-analysis of the data set and rotation of the data, are essential pre-processing steps for 3D inversion.

A second major factor with significant influence on the outcome of 3D MT inversion is the setup of the model regularization. The ModEM3DMT inversion package and many other codes search for a result with the smallest possible distance from a prior model, i.e. the existence of an a priori model is inevitable. The distance of the true subsurface structure from the prior model in resistivity space prejudices the resistivity structure of the inversion result. In presence of extended zones with strongly contrasting average resistivities, like in the SYNPRK model, this approach is prone to introduce artificial and misleading structures while substantial 2D and 3D structures are considerably compromised or suppressed. Already intermediate background resistivity values for the prior or starting models caused the 3D inversion to "loose" the HCZ because the overall structure would have been too "far away" from the prior model. Instead, a false resistivity contrast appeared beneath the coastline. In general, a model regularization which is independent of a prior model would be desirable.

Alternatively and if available, a priori information, particularly on a regional scale, even if outside the station area, helps recovering structures in the central parts of the survey area. Inclusion of high-resistive half-layers beneath the ocean facilitated the resolution of the structure of the SYNPRK model, particularly the recovery of the HCZ, and improved the data fit.

Optimal smoothing parameters for the model mesh are strongly interconnected with the station distribution and a suitable model discretization, particularly for irregular site distributions. Besides, parameter settings are also related to the inverted data type(s). If these parameters are not set appropriately, structural variations can be lost, over- or underestimated. I argue that 3D inversion of regional MT data is incomplete as long as these parameters are not rig-

orously and systematically tested. The best 3D inversion results can usually be achieved with uniform station grids. If a pronounced regional 2D conductivity structure exists, anisotropic model regularization enforcing a higher smoothness parallel to the strike axis can help resolving the regional structure more independent of the site distribution. However, this is a trade-off between resolution of 2D and 3D structures as high regularization will tend to suppress (3D) along-strike variations. In presence of regional 2D structures, data and inversion model grid should be aligned with the regional geo-electric strike direction. If the station distribution is not uniform but strongly varying in x- and y-directions (e.g. for irregularly spaced profile data), recovery of the subsurface structures can be seriously impaired. To analyse possible influence of the site layout I suggest to use data subsets with more uniform station distribution and to compare these results to those for irregularly site spacing.

Very important controls for 3D inversion are sensible data weighting schemes, taking relative sizes of components into account. Where amplitudes of individual impedance components significantly differ, data weighting schemes based on impedance tensor averages can lead to erroneous models, as they effectively cause a downweighting of the smaller component(s) and information contained in these data may be lost. Additionally, the inversion of single data components can provide instructive insights into the contribution of particular components to the overall inversion result and can help identifying structures which are not or only poorly resolved by standard inversions using all components.

For a comprehensive and reliable 3D inversion, the full impedance tensor is required. I found heavily distorted, weakened or missing structures when using only the off-diagonal impedances. For the SYNPRK-path model, inversion of off-diagonal impedances only revealed the 2D regional structure and some 3D features. The 3D conductive path (CP) could only be reliably revealed if the full impedance tensor was used. With real-world data, the use of the diagonal impedance elements is somewhat limited. In 1D or 2D environments, diagonal impedances are usually very small (coordinate system aligned with strike) and, for real data, often have poor signal-to-noise ratios. Inclusion of these data points typically requires high error floors and can degrade the performance of 3D inversion. For the presented real-world data set, integrating diagonal impedances only if they are large, i.e. proper "3D data points", yielded consistently better results. Inverting VTFs jointly with impedances improves the resolution of lateral conductivity contrasts. In particular, VTFs can help to clarify the subsurface structure beyond the station-covered area and to obtain a more consistent picture of the central survey area.

Moderate galvanic distortion of the impedance data does not seriously affect the recovery of the deep and regional structure; however, the appearance of small-scale features and near-surface structures can be significantly biased. The extent of these distortions depends on the model setup (discretization and smoothing) and the data types which are used in inversion. For a rough discretization, 3D impedance inversion may transfer galvanic distortion of the data into an inductive-scale feature in the model. Using a finer horizontal discretization and/or

adding VTFs to the data set, which are not affected by galvanic distortion, likely produces a more reliable picture of the near-surface. To circumvent the problem of galvanic distortion, I implemented inversion of apparent resistivities & phases (RP) and distortion-free phase tensors (PT) into ModEM3DMT. For RP inversion, the effects of moderate galvanic distortion in terms of static shift could be successfully reduced in inversion of both synthetic and field data by giving greatest weight to the phases. Results presented in the framework of this thesis used only off-diagonal RP components, which limits the applicability to 3D subsurface situations. Recently obtained results integrating also diagonal apparent resistivities and phases showed promising results reducing the influence of static shift and recovering also complex 3D situations at the same time. Additionally or alternatively, 3D inversion of PT data effectively minimized the influence of (complex) galvanic distortion on the upper 10 km of the field data inversion models, particularly in combination with a VTF inversion. However, both VTF and PT data are mostly sensitive to relative conductivity variations but cannot reliably recover the absolute conductivity level of the subsurface structure. Hence, the setup of an appropriate prior model is even more important for PT and VTF inversion.

For a meaningful evaluation of the inversion results, a systematic assessment of misfits for each data component and their variations in the frequency-space domain is essential. While the minimization of the overall RMS is one of the driving forces of 3D inversion, results of both synthetic and field data inversions illustrated that the total RMS is not a reliable quantity for the judgement of an inversion outcome. Models with similarly good RMS values showed significantly differing and partly erroneous and misleading pictures of the subsurface. For the SYNPRK data set, the differing quality of the inversion results could only be revealed if data misfits were analysed separately for all inverted data components. Systematic assessment of individual misfits is particularly efficient for the detection of large-scale structural inconsistencies.

Moreover systematic differences in data fit quality and differing misfit levels between single components can hint at more general challenges for the 3D inversion approach. For both the California and the SYNPRK data, the systematic increase of long-period yx-impedance misfits towards the coastline hinted at an insufficient reproduction of extended zones of high resistivities in the 3D inversion models, which impaired and partly inhibited depiction of the HCZ at depth. If a particular component can only be insufficiently fit, also structural information contained in other components may be attenuated or even lost. In these cases, downweighting of consistently poorer fitted data, e.g. yx-impedances of the SYNPRK data set, can improve resolution of structural information contained in other data types or components.

If handled properly 3D inversion of large real-world data sets can be successful and meaningful. The extensive MT data from California could be inverted with excellent fits for most parts of the data. The conductivity models reveal structural variations down to about 60 km depth which are largely consistent with the 2D inversion results.

The 3D modelling results also provided new insights into structures in the southern part

of the survey area, where strong 3D effects are present in the data. Extended 3D structures appear in the upper 5 km and, contrary to the 2D results, the HCZ is imaged with continuous across-strike extent. In this region the data fit of the 3D model is significantly better than for 2D. In general, the HCZ is narrower in the 3D models and appears at shallower depth compared to 2D results. 2D and 3D inversion tests with synthetic (SYNPRK) data indicate that 3D inversion tends to depict structures at systematically shallower depth levels than their true locations, in particular if prior and starting models with low resistivities are used. forward modelling suggests that the HCZ extends for at least 40 km beyond the southernmost profile ⑦. Towards the northwest the along-strike extent remains unclear; data neither require nor exclude a continuation beyond the survey array.

The conductive path between the deep low-resistive zone and the upper crustal SAF, which was a robust feature in 2D modelling of the northern profiles ② and ③, could not directly be resolved with 3D inversion. Its presence, however, helps to explain data in this area. Systematic tests with synthetic data (SYNPRK-path) indicate that the strong model regularization required in 3D inversion inhibits the appearance of this feature. While the conductive path is very important and interesting for the interpretation of this data set, it is only a minor structural detail within 3D inversion. Much larger challenges for the 3D inversion scheme are the required wide range of resistivities and the strong conductivity contrasts.

Overall, the results of the synthetic studies and, in particular, inversion of the California data set suggest that 2D and 3D inversion techniques should be used complementarily to permit a comprehensive interpretation of a data set. 3D inversion is usable for interpretation of large real-world data sets and exhibits clear advantages over 2D inversion approaches in complex subsurface situations. However, 2D inversion provides still more options and control about the resolution of small-scale structures, as well as other aspects which have not been discussed here, e.g. the handling of static shift and the integration of detailed topography and bathymetry as a much finer discretization of the subsurface can be realized.

In conclusion, 3D inversion is a useful, if still computationally demanding, tool for inversion of large real-world data sets. However, even for full 3D inversion thorough analysis of dimensionality and strike behaviour of the data set is advisable. In presence of a pronounced geo-electric strike direction, a rotation of data and model grid should be considered. If the coordinate system is not aligned with a dominant strike direction, the outcome of 3D inversion can be erroneous and misleading. If the inversion scheme heavily penalizes deviations from a prior model the setup of the prior model has to be handled carefully and a range of prior models should be tested. In presence of strong conductivity contrasts model regularization based on a prior model is prone to produce misleading models. As 3D magnetotelluric inversion is strongly ill-posed, inversion parameters have a significant influence on the inversion outcome and should be systematically investigated. Appropriate choices for model and data parameters are interrelated and specific for each data set. In general, a horizontally uniform

coverage of the subsurface facilitates consistent resolution of the subsurface. Irregular site coverage can evoke a distorted picture of the subsurface. A sensible data-weighting scheme is essential to recover the full information of all inverted components. Systematic assessment of misfit variations in the frequency-space domain is an efficient tool for detection of systematic or large-scale structural deficits of the 3D inversion result. Galvanic distortion can significantly impair 3D inversion models and can result in spurious structures at depth. Inversion of the phase tensor or apparent resistivity and phase data is a valuable asset to tackle this problem. Moreover, the advantages of both 3D and 2D inversion should be used complementarily to render a comprehensive interpretation of the entire data set.

4 Modelling static shift in magnetotellurics

Static shift in MT sounding data, i.e. a frequency-independent shifting of amplitude log-apparent-resistivity versus period curves relative to regional values is a common problem in MT exploration (e.g. Jones, 1988; Jiracek, 1990; Berdichevsky et al., 1989). If not considered properly, the effect on MT inversion can be immense and will typically result in erroneous subsurface models and interpretations.

Static shift is the expression of galvanic distortion of the observed electric fields due to the presence of local, small-scale conductivity discontinuities below the resolution scale of the MT experiment (cf. sec. 1.3).

The general description of galvanic distortion by a real 2×2 tensor $\mathbf{C}$, which relates the observed impedance $\mathbf{Z}$ to the regional impedance $\mathbf{Z}_r$: $\mathbf{Z} = \mathbf{C} \cdot \mathbf{Z}_r$ ((1.27), p. 8), can be split up into two parts:

$$\mathbf{Z} = \begin{pmatrix} c_{xx}Z^r_{xx} + c_{xy}Z^r_{yx} & c_{xx}Z^r_{xy} + c_{xy}Z^r_{yy} \\ c_{yy}Z^r_{yx} + c_{yx}Z^r_{xx} & c_{yy}Z^r_{yy} + c_{yx}Z^r_{xy} \end{pmatrix} \tag{4.1}$$

$$= \begin{pmatrix} c_{xx} & 0 \\ 0 & c_{yy} \end{pmatrix} \begin{pmatrix} Z^r_{xx} & Z^r_{xy} \\ Z^r_{yx} & Z^r_{yy} \end{pmatrix} + \begin{pmatrix} 0 & c_{xy} \\ c_{yx} & 0 \end{pmatrix} \begin{pmatrix} Z^r_{xx} & Z^r_{xy} \\ Z^r_{yx} & Z^r_{yy} \end{pmatrix}. \tag{4.2}$$

The first term in (4.2) describes the frequency-independent, linear scaling of the impedance amplitudes due to the presence of the galvanic scatterer which results in static shift of the corresponding apparent resistivity curves. The second term describes the mixing of two regional impedance elements of the same column in the observed impedance component. As a consequence, the frequency behaviour of the observed impedance component, i.e. apparent resistivity and phase curve shape, differs from that of the regional components (see also Jones, 2011).

The relative contribution of the first and the second term of (4.2) depends on the geometry of the galvanic scatterer and the relative sizes of the impedance components. In the special case that the main axes of the anomaly are aligned with the coordinate axes or measurements are taken at a point of symmetry of the anomaly c_{xy} and c_{yx} are zero and the second term vanishes. In very extreme cases, where the electric field components are deflected by 90°, the first term would vanish.

As outlined in section 1.3, in 2D and 1D situations, the diagonal elements of $\mathbf{Z}_r$ vanish.

Hence,

$$\mathbf{Z}^{\mathrm{1D/2D}} = \begin{pmatrix} c_{xy} Z^r_{yx} & c_{xx} Z^r_{xy} \\ c_{yy} Z^r_{yx} & c_{yx} Z^r_{xy} \end{pmatrix}. \tag{4.3}$$

As only the observed off-diagonal impedance elements are required for interpretation, the second term of (4.2) can be neglected. In 1D and 2D situations, galvanic distortion off-diagonal impedance components manifests exclusively as static shift of the apparent resistivity curves (cf. (1.30), p. 9).

The degree of curve-distortion in 3D situations mainly depends on the relative sizes of the mixing impedance elements, i.e. on the particular regional subsurface structure. Also in 3D situations, amplitudes of the diagonal impedance elements Z_{xx} and Z_{yy} are often small in relation to those of the off-diagonal components Z_{xy} and Z_{yx} so that Z_{xx} and Z_{yy} will be more severely distorted. In return, the frequency behaviour of the regional off-diagonal impedances Z^r_{xy} and Z^r_{yx} can be assumed to be better preserved in the corresponding observed off-diagonal elements where 3D effects of the subsurface are not extreme.

Here, I focus on the static shift part of the galvanic distortion problem, i.e. only the first term of (4.2) will be considered. This approximation is appropriate to describe distorted off-diagonal impedance components for 1D and 2D situations as well as for moderate 3D subsurface situations and low to intermediate degree of galvanic distortion. Full consideration of the galvanic distortion problem in 3D in terms of a four-component distortion tensor is beyond the scope of this thesis.

Static shift can vary strongly from site to site and is related to the heterogeneity of the near surface. Galvanic scatterers are usually assumed to be randomly distributed in the subsurface. Such structures result, for instance, from weathering of surface rocks and exhalative hydrothermal alteration as well as from transported overburden, i.e. deposits laid down by wind, water, and volcanic eruptions (Sasaki & Meju, 2006). As the size of these inhomogeneities is usually much smaller than the site spacing static shift is independent between different measurement points in the sense that it originates from independent scatterers. However, the type of scattering structures and thus the shift amplitudes within a survey area can be biased by surface geology. Re-analyzing data from several collocated MT and TEM surveys, Sasaki & Meju (2006) find good support for normal distribution of static shift. However, these distributions are often skewed and have non-zero means, depending on the geological environment. For example, bias of static shift can be partially attributed to the selection of MT site locations. Most likely, sites will be preferentially located where site set-up is physically least demanding, e.g. in sandy patches or depressions, so that a considerable number of sites might be located in the vicinity of similar heterogeneities common to the survey area.

Setup of inversion model parameters such as discretization and regularization is usually op-

timized for the resolution of inductive scale subsurface structures, which are the targets of MT exploration. For example, minimum mesh cell dimensions are chosen depending on site spacing and expected minimum skin depths specific for the survey area and the observed period range. However, this is usually above the scale of galvanic scatterers. As a consequence, the purely galvanic responses of small-scale near-surface conductivity variations are mistaken for responses of some larger, inductive-scale feature. In the inversion model, the subsurface structure will be distorted on a large scale. Thus, in presence of significant near-surface heterogeneities, this straight-forward approach will usually result in erroneous and misleading subsurface models not only for the surface layers but down to regional scale depths.

Figure 4.1 exemplarily illustrates the impact of static shift on 2D inversion results. The 2D synthetic model (Fig. 4.1a) comprises two neighbouring blocks of 10 Ωm and 1000 Ωm, respectively, which are embedded in a 1D layered half-space (block-block-layered, BBL). Using periods between 0.001 s and 1,000 s and standard inversion settings (10 % errors for ρ_a and 1.5° for ϕ) the subsurface structure is well resolved inverting the TM, TE, and Hz data of all 50 sites along the profile (Fig. 4.1b). If randomly distributed downward-biased static shift is added to two thirds of the sites, the result is an erroneous and misleading model (Fig. 4.1c). Structures are distorted from surface (cf. right panels in Figs 4.1a-c) to more than 5 km depth. The BBL structure is depicted clearer using high error floors (500 %) for TE-mode apparent resistivities (Fig. 4.1d). Results improve further when the model mesh in the vicinity of MT stations is refined (Fig. 4.1e). In this case, 2D inversion is allowed to insert small-scale near-surface structures which compensate significant amounts of TM-mode static shift (right panels in Fig. 4.1e).

In a previously discussed synthetic 3D example (ObliqueOne, Fig. 3.14, p. 53) in which distorted four-component impedance data were inverted revealed similar deep-reaching distortion of the model structures. A very rough and incoherent pattern of resistivities was observed in the upper layers, which can be interpreted as an attempt of the inversion to account for static shift within the model structure. However, the influence static shift is not limited to these surface layers but affects the inversion model down to regional scale depth ranges. In the example, the top of the oblique conductor and the surrounding background structure at 2.5 km depth, which is clearly resolved under normal circumstances, appears blurred. Only the very deep structure below 5 km depth is well resolved.

In the California MT array only a small number of sites are obviously affected by static shift and more complex galvanic distortion. 3D inversion results of the data set in the vicinity of site 408, however, illustrate how significantly galvanic distortion at a single site can bias the 3D inversion results of a wide region (cf. Fig. 3.34, p. 86).

Effective strategies for handling galvanically distorted MT data have been developed mainly for 2D data interpretation and fall into two major categories. The first group of methods aims at solving the problem within the inversion process. In a direct approach, data are interpreted

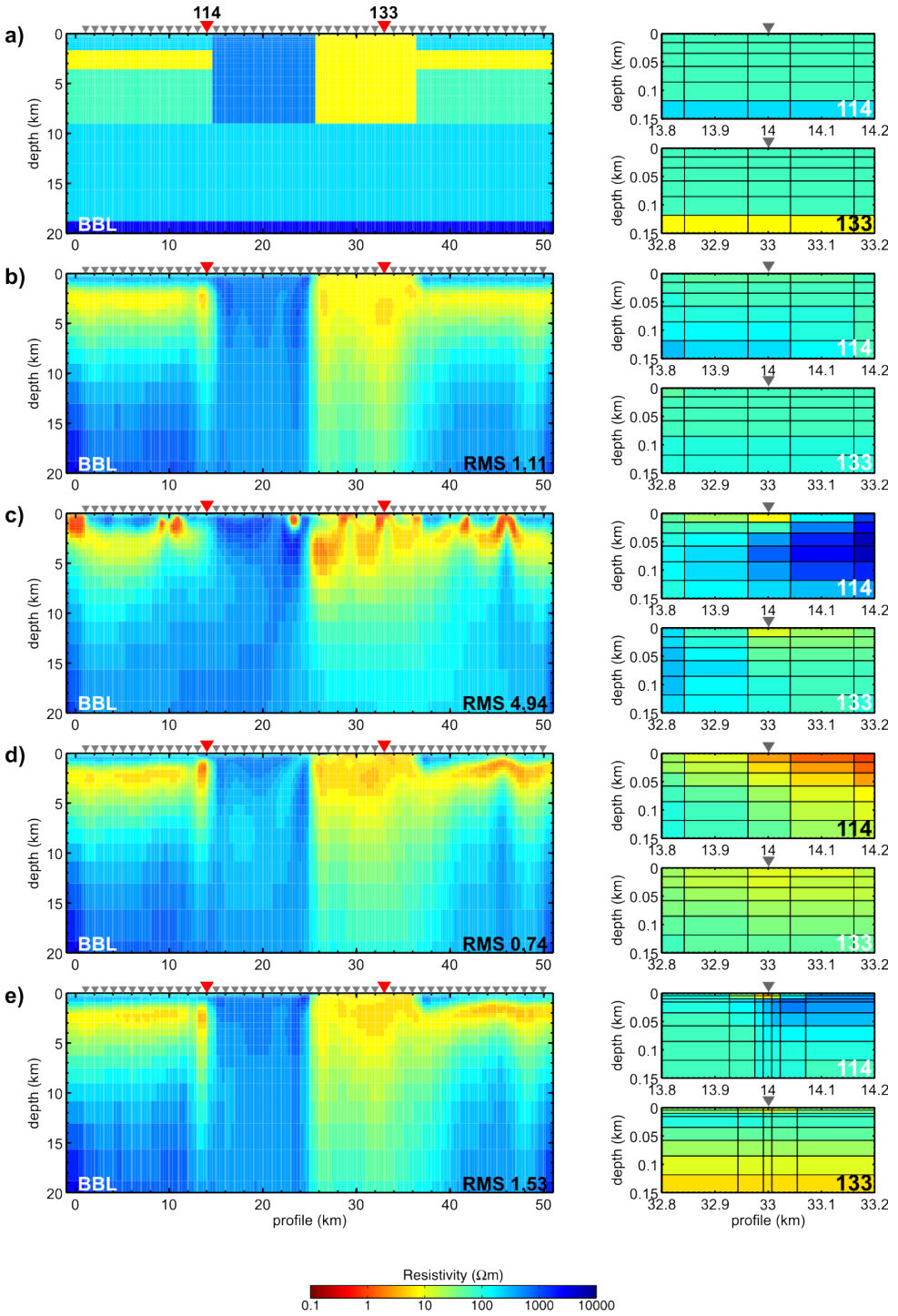

Figure 4.1: Effect of static shift on 2D MT inversion. **(a)** 2D BBL model. **(b)-(e)** Inversion results of TM- and TE-mode data for (b) original BBL FWD data (3 % Gaussian noise, 10 % error for ρ_a and 1.5° for phases) and (c-e) BBL responses compromised with downward-biased static shift. Pane views on the right show surface structures beneath sites 114 and 133, respectively. (c) error settings as in (b); (d-e) TE apparent resistivity errors increased to 500 %; for (e) model mesh was refined (cf. pane view).

by a joint inversion for subsurface conductivity and static shift parameters (deGroot-Hedlin, 1991, 1995; Sasaki, 2004; Sasaki & Meju, 2006). Other workers downweight shift-affected apparent resistivity data by assigning high error floors to these components (e.g. Becken et al., 2008b; Ritter et al., 2003; Tauber et al., 2003) or/and explicitly assume that inversion solves for the distortion problem by adding compensating structures to the surface layers if a fine discretization is used (e.g. Becken et al., 2008b; Farquharson & Craven, 2009; Newman et al., 2008; Xiao et al., 2010; Patro & Egbert, 2011).

A second major strategy aims at estimating galvanic distortion of the measured data prior to interpretation by modelling and inversion. Since the distortion matrix $\mathbf{C}$ is unknown, the equation system (1.27) is underdetermined and additional assumptions or constraints are required. Partial remedies for 2D surveys are based on tensor decomposition methods (e.g. Bahr, 1988; Groom & Bailey, 1989; McNeice & Jones, 2001; Becken & Burkhardt, 2004; Bibby et al., 2005), spatial filtering of measured data (e.g. Torres-Verdín & Bostick, 1992), statistical interpolation methods (Tournerie et al., 2007), correction for static shifts using complementary transient electromagnetic measurements (e.g. Sternberg et al., 1988) or vertical magnetic transfer functions (Ledo & Gab, 2002), or a priori constraints on the subsurface structure (Jones, 1988).

In the following, a class of 2D and 3D substitute model structures for galvanic scatterers is presented and a new approach to identify static shift prior to inversion is discussed. All 2D forward (FWD) modelling and inversion calculations were performed using WinGLink (Rodi & Mackie, 2001); for 3D modelling the ModEM package (Egbert & Kelbert, 2012) was used.

4.1 Substitute structures for static shift

A fairly widespread idea of a galvanic scatterer is that of an isolated, small-scale conductivity inhomogeneity located directly beneath a measurement site. The image of such a "well-shaped" inhomogeneity is useful when transferring the static shift problem to subsurface modelling, where static shift can be reproduced by such conceptional near-surface structures substituting the real world galvanic scatterer.

The predominantly used finite difference method rectangular grids limit modelling of true scattering structures by the way in which electric fields are computed. Most 2D and 3D MT codes use point values of the electric fields at the location of the MT site to estimate model responses whereas in practice the electric fields are measured as voltage differences between two points which are usually 50 to 100 m apart. Hence, aspects such as possible conductivity interfaces between the ends of an electrode pair cannot be taken into account.

4.1.1 2D modelling

In 2D subsurface models all structural features and conductivity interfaces extend infinitely along one common strike direction (x); the strike or main axis of near-surface inhomogeneities is always aligned with the subsurface structure and the coordinate system. Hence, any conductivity inhomogeneity of dimension below the inductive scale will only produce a scaling of the electric field component parallel to profile (E_y); the amplitude of the along-strike component E_x as well as the direction of both components will remain unaffected. Thus, simulation of galvanic distortion is limited to reproducing static shift for the Z_{yx}-component (TM-mode) by 2D forward modelling.

For an illustration of the impact of such substitute structures, a 1D layered half-space (LH) model was used as regional reference model (Fig. 4.2). TE and TM-mode apparent resistivities and phases were calculated for 22 periods between 0.001 s and 1000 s. As the LH model is 1D, the responses are the same for both modes and at all sites along the profile. The right panel of Figure 4.2 exemplarily displays the FWD response of the LH model at site 124 (red triangle) in the centre of the profile.

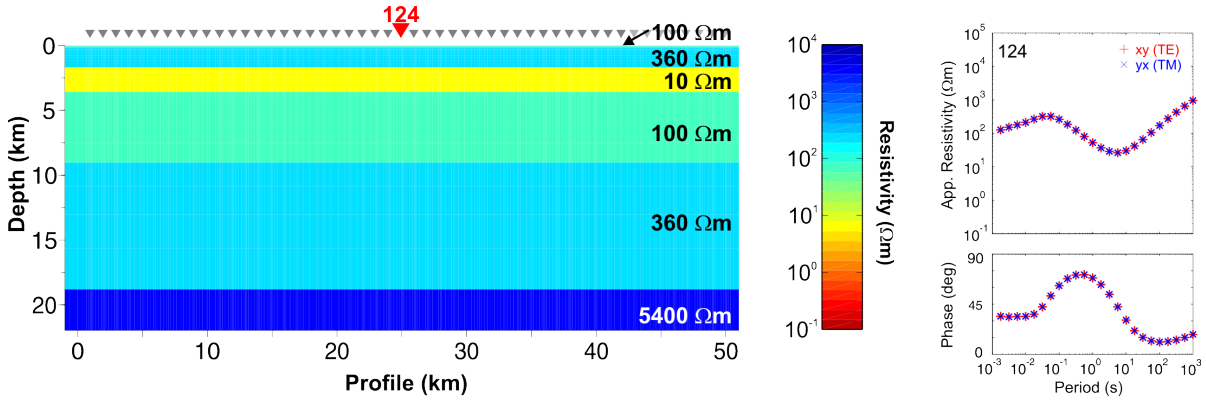

Figure 4.2: A 1D layered half-space model (LH, left panel) is used as regional background structure for 2D FWD simulation of substitute structures for galvanic scatterers beneath site 124 (red triangle). The right panel shows the LH MT response at that site.

At surface, the LH model comprises a 107 m thick layer of 100 Ωm. In the following, a class of conceptional conductive (10 Ωm, Fig. 4.3) and resistive (10^4Ωm, Fig. 4.4) subsurface anomalies was added to the conductivity model just below the surface at site 124. The 2D FWD responses of the disturbed models (lines) are displayed together with the original 1D LH response (symbols) in the right panels of Figures 4.3 and 4.4.

As outlined in section 1.3, conductive anomalies generally produce downward shifts of the apparent resistivity curves (Figs 4.3a-c). The simplest concept of a substitute structure is that of a homogeneous block which is located directly beneath a measuring site. Figure 4.3(a)

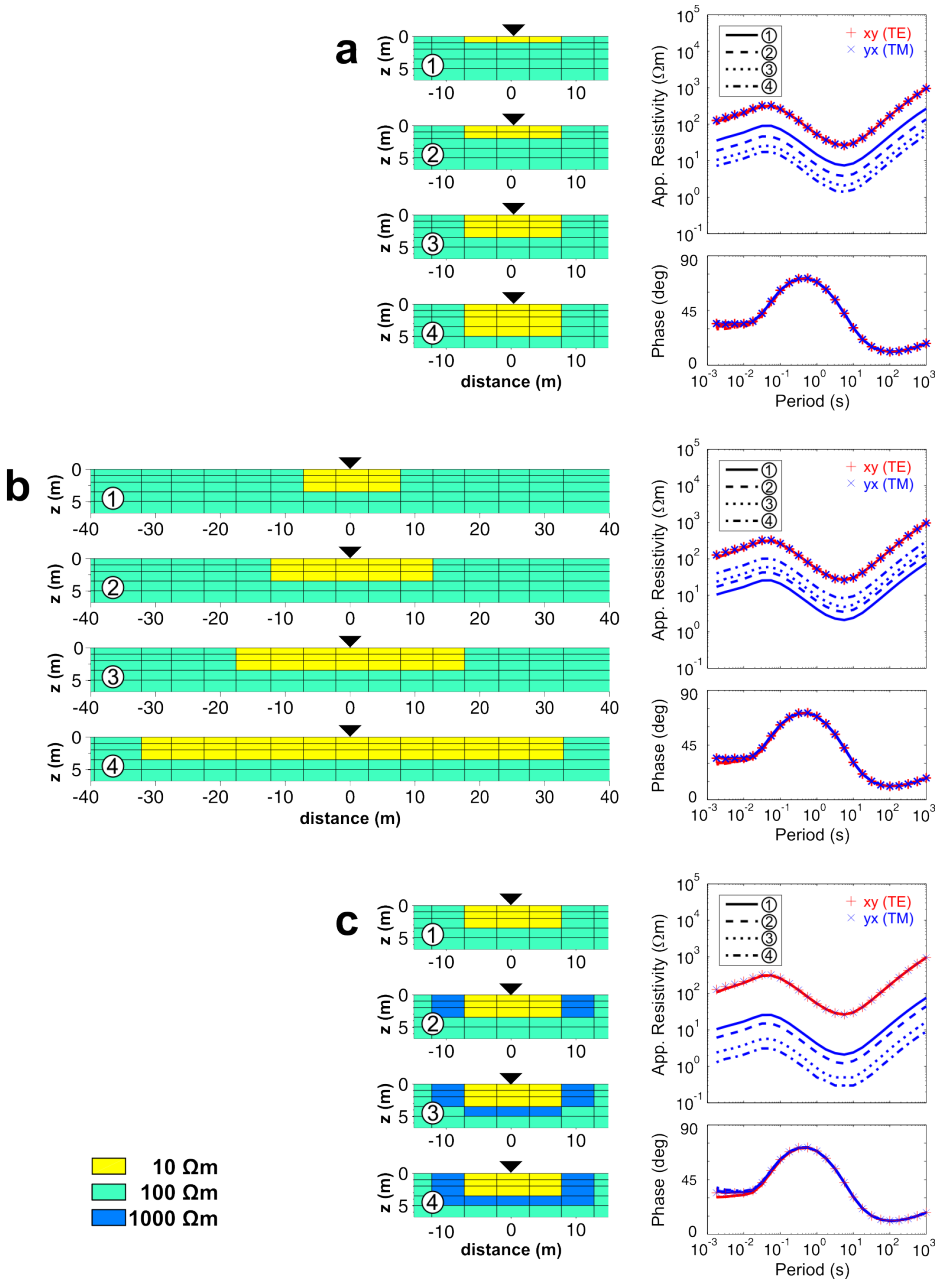

Figure 4.3: Conceptional conductive (10 Ωm) surface anomalies (left panels) added to the LH model beneath site 124 (cf. Fig. 4.2). Right panels compare 2D FWD responses of the disturbed LH models (lines) to the original LH response (symbols). As anomalies are more conductive than the LH surface layer TM apparent resistivities are shifted downwards. The shift amplitude depends on the dimension of the anomalous strucutre. **(a)** Shift increases with block thickness, i.e. with the size of xz-faces of the anomaly. **(b)** With increasing block width, the static shift effect becomes smaller as the lateral resistivity contrast which is responsible for the distortion of the electrical field moves away from the site location.**(c)** Enhancing the conductivity contrast by padding the conductor with resistive (1000 Ωm) cells TM downward shift is increased. Structures of this type can be observed in inversion models below static shift affected sites when static shift is not taken into account during inversion.

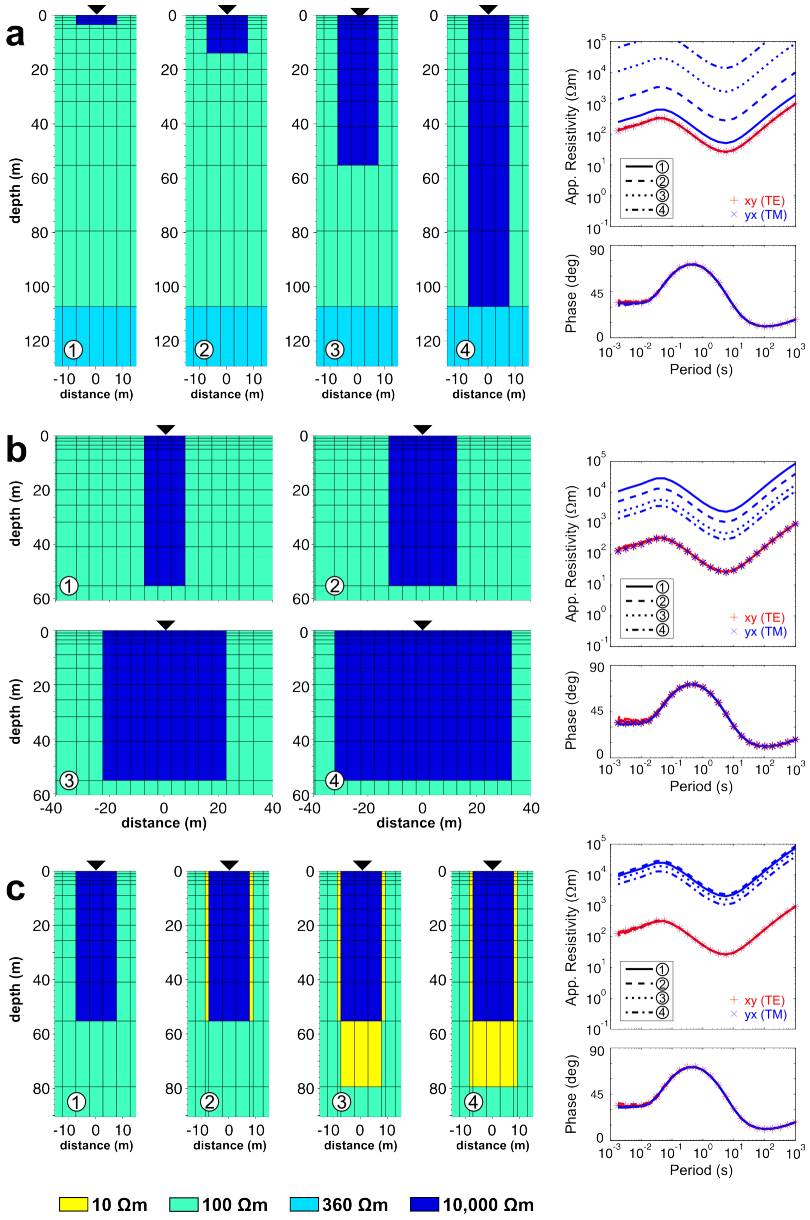

Figure 4.4: Conceptional resistive (1000 Ωm) surface anomalies (left panels) added to the LH model beneath site 124 (cf. Fig. 4.2). Right panels compare 2D FWD responses of the disturbed LH models (lines) to the original LH response (symbols). As anomalies are more resistive than the LH surface layer TM apparent resistivities are shifted upwards. The dependence of shift amplitudes on the anomaly dimensions is analogue to the conductive anomalies (cf. Fig. 4.3). (a) Shift increases with block thickness. (b) With increasing block width, the static shift effect becomes smaller as the lateral resistivity contrast which is responsible for the distortion of the electrical field moves away from the site location. (c) Padding the resistive block with a thin column of conductive (10 Ωm) cells has only minor impact on the amplitude of the static shift, different from the results in Figure 4.3c. As the additional conductive horizontal padding cells must be very small and narrow to prevent inductive effects, the outer and inner boundary of the double-layer structure are at nearly the same distance from the MT station and the two opposite effects from outer and enhanced inner edge cancel out.

presents the influence of a 15 m wide 10 Ωm-conductor with thickness varying from 1 m to 5 m. The shift amplitude increases with the block thickness as the size of the lateral anomaly boundaries (xz-faces) become larger and more charges can accumulate.

In a second test, the thickness was kept fixed at 3 m and the lateral dimensions of the 10 Ωm-block were altered between 15 m and 65 m (Fig. 4.3b). With increasing block width, the static shift effect becomes smaller as the lateral resistivity contrast which is responsible for the distortion of the electrical field moves away from the site location. Finally, the conductivity contrast was enhanced by padding the conductor with resistive (10^3 Ωm) cells. Consequently, TM downward shift is increased (Fig. 4.3c).

When the anomalous structure is resistive, TM apparent resistivity curves are shifted upwards (Figs 4.4a-c). Resistive substitute structures have to be larger than conductive ones to produce the same shift amplitudes. As penetration depth (skin depth; cf. (1.13), p. 3) of the electromagnetic fields increases with resistivity, field density decreases and, hence, the accumulation of charges at the anomaly boundaries beneath the site is lower.

Analogue to the conductive substitute structures, a homogeneous but now highly resistive block (10^4 Ωm) with a width of 15 m and varying thicknesses between 5 m and 110 m beneath the site results in upward shift of the TM-mode (Fig. 4.4a). Static shift increases with increasing vertical block dimensions. In Figure 4.4(b) the lateral extent of the 10^4 Ωm-block was altered between 15 m and 65 m for a fixed thickness of 55 m. As seen for the 10 Ωm-block, the static shift effect becomes smaller with increasing block width as the resistivity contrast distorting the electrical field moves away from the site location. Padding the resistive block with a thin column of conductive (10 Ωm) cells has only minor impact on the amplitude of the static shift (Fig. 4.4c).

The substitute structures presented here produce significant downwards and upwards directed shift of the TM apparent resistivity curves. At the same time, TE resistivity curves and phase curves of both TM and TE-modes are mostly unaffected.

For each type of substitute structure the amount of static shift which can be reproduced is limited: Increasing the vertical dimensions or conductivity values, the structure is becoming effectively inductive at some point. Most of the structures shown here are below the inductive scale; however for the largest variants of all examples slight deviations of the phase curves at the shortest periods can be observed which indicate that the inductive threshold is reached. Considering the tests in Figures 4.3(a) and 4.4(a) this threshold is in the range of 10 % of the skin depth of the shortest period (0.001 s), which is 50 m for 10 Ωm and 1.58 km for 10^4 Ωm (cf. (1.13), p. 3). Thus, in particular, the conductive substitute structures producing downward shift have to be very small in order to not inductively affect the subsurface response.

Why are these considerations important? A widely used strategy to tackle static shift in (2D) MT inversion is to explicitly assume that inversion solves for the static shift problem by adding small compensatory structures to the surface layers, which do not interfere with

the resolution of the regional subsurface structure. In other words, the inversion is expected to insert substitute features such as the examples shown above into the subsurface model. Substantial amounts of static shift can be compensated in this way. However, the results of the FWD modelling tests also show that a necessary prerequisite for this approach is a very fine horizontal and vertical discretization beneath a station in relation to the minimum inductive scale length.

4.1.2 3D modelling

For forward modelling of substitute structures for static shift in 3D, the 3D ObliqueOne model was used as regional reference model (Fig. 4.5). The main structural feature is a 10 km × 30 km × 8 km block of 5 Ωm which cuts obliquely through two resistive half-layers (50 Ωm, 500 Ωm). For a detailed description of model structure and FWD data see section 3.2.2.

At surface, the ObliqueOne model comprises a 107 m thick layer of 100 Ωm. In the following, conceptional subsurface anomalies were added into this surface layer of the conductivity model just below site 074, where the 3D character of the model response is most pronounced and all four impedance components exhibit significant amplitudes. For FWD modelling of the modified ObliqueOne model, a nested modelling approach was used. The nested grid is centred at site 074 and provides a very fine discretization of the anomalous region. Horizontal cell dimensions start at 2 m × 2 m for the central cell and increase laterally by a factor of 1.5. The vertical discretization is adopted from the original model. The topmost 107 m were refined from 4 to 11 layers providing a minimum layer thickness of 2 m at surface increasing downwards by a factor of 1.3. In total, the nested grid consists 45 × 45 × 24 cells comprising a volume of 19 km × 19 km × 2.12 km.

In a first step, I inserted box shaped symmetric resistivity anomalies (right column in Fig. 4.6) into the ObliqueOne model surface layers which are horizontally centred at site 074 (cf. Fig. 4.5). Conductive (10 Ωm, A-C in Fig. 4.6) and resistive (1000 Ωm, D) subsurface anomalies cause apparent resistivity curves of all four components to be down- and upward shifted, respectively. As seen from the 2D results, shift amplitudes increase with vertical extent of the inhomogeneity (A, B; cf. Figs 4.3a, 4.4a). If boxes have the same extent in x- and y-direction (A, B, D), apparent resistivity curves of all four components are shifted by the same amount. For feature C, however, horizontal dimensions of the anomalous structure differ. Here, the two horizontal electric field components E_x and E_y are scaled differently, resulting in distinct amounts of static shift for Z_{xx} & Z_{xy} related to E_x and Z_{yx} & Z_{yy} related to E_y, respectively. Note, changing the anomaly dimension along only one horizontal axis influences both horizontal electric field components and, thus, shift amplitudes for all four components (cf. B and C). Feature C has larger y-dimension than B, while x-extents are the same. Apparent resistivity responses above C exhibit lower shift amplitudes for E_y-related components compared to B as

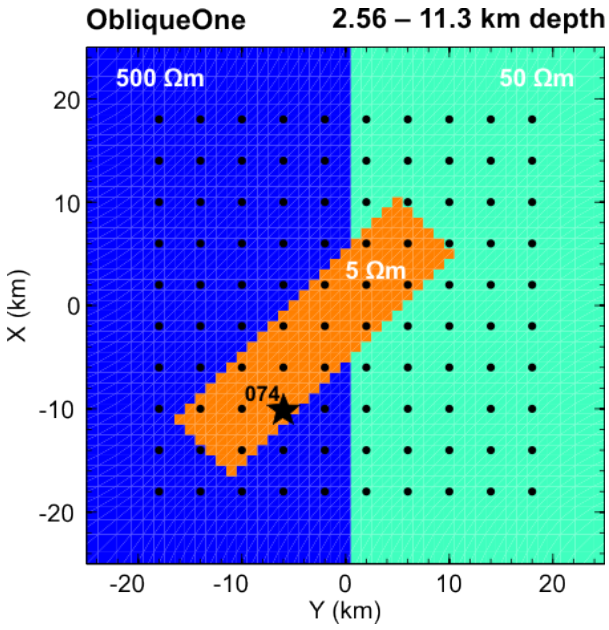

Figure 4.5: Horizontal slice through 3D ObliqueOne model at 2.56 km depth illustrating the main structural features. The ObliqueOne model provides the regional structure for illustration of the impact of 3D near-surface inhomogeneities at site 074 (asterisk).

perpendicular xz-faces of the anomaly moved further away (cf. Fig. 4.3a). In contrast, shift of components derived from E_x are larger than for box B as the area of the yz-faces was increased (cf. Fig. 4.3b).

For subsurface anomalies which are non-symmetric or not aligned with the modelling and measurement coordinate system, the distortion of the electric field is not only expressed as static shift but the observed impedance elements are a mixture of two of the regional impedance elements (Fig. 4.7). All three structures in Figure 4.7 produce significant downward shift of the off-diagonal apparent resistivities. In addition, slight changes of the apparent resistivity and phase curve shape can be observed for these two components at periods above 10 s at which the diagonal elements become significant. For the diagonal components deviations from pure static shift are more pronounced. For periods < 1 s, the station response reflects the 1D and 2D regional near-surface structure above the 3D oblique conductor (< 2.56 km) and the regional diagonal impedance elements are very small compared to the off-diagonal components. Hence, in this period range the observed diagonal impedances Z_{xx} and Z_{yy} are dominated by the regional off-diagonal elements Z^r_{yx} and Z^r_{xy}, respectively. Considering all four components, the most significant deviation from pure static shift is produced by the drop-shaped inhomogeneity A, which has lowest symmetry with respect to the measurement site.

In summary, static shift can be generated with 3D FWD modelling using a similar principle as for 2D. Again, substitute structures for galvanic scatterers have to be very small with respect to the minimum inductive scale-length to prevent significant inductive contributions to the model response.

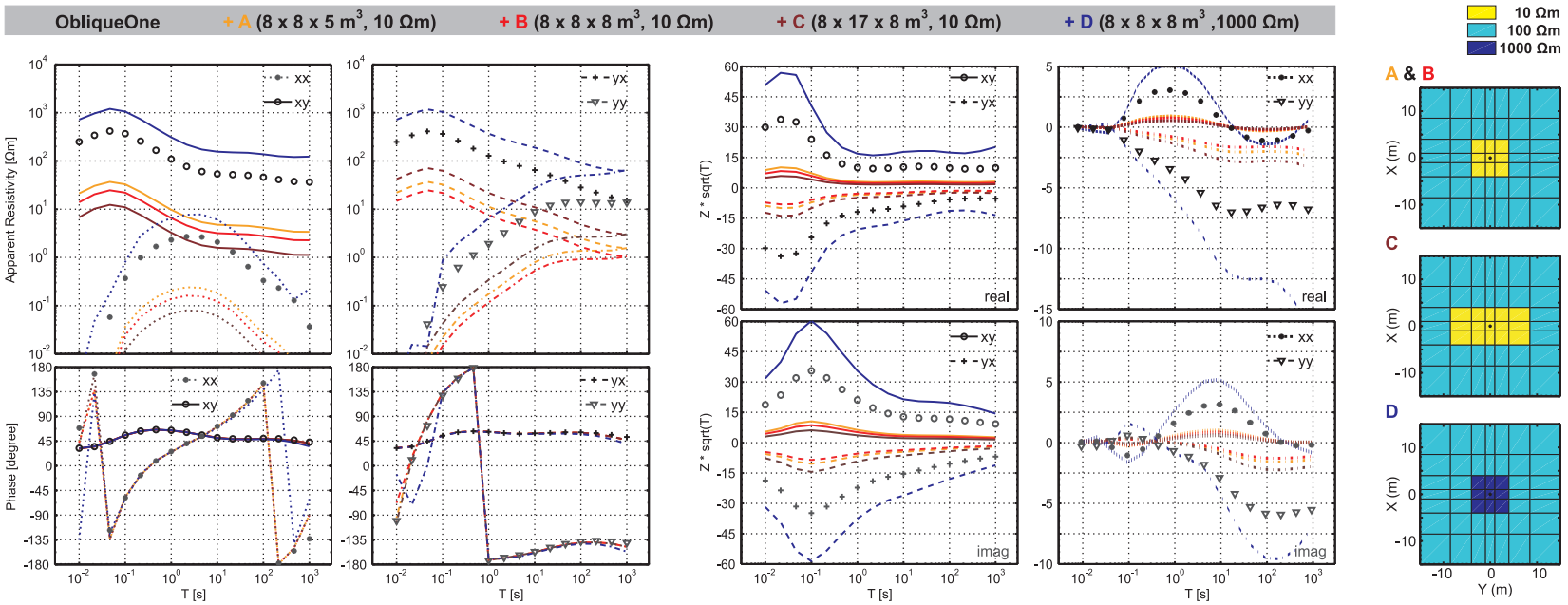

Figure 4.6: Effect of 3D box-shaped near-surface anomalies (right column) on MT responses above a 3D subsurface structure (left). Conductive (10 Ωm, A-C) and resistive (1000 Ωm, D) inhomogeneities centred at site 074 (ObliqueOne model, cf. Fig. 4.5) scale impedance FWD responses (central panels) and cause apparent resistivity curves (top left panels) to be up- and downward shifted from the original response (symbols).

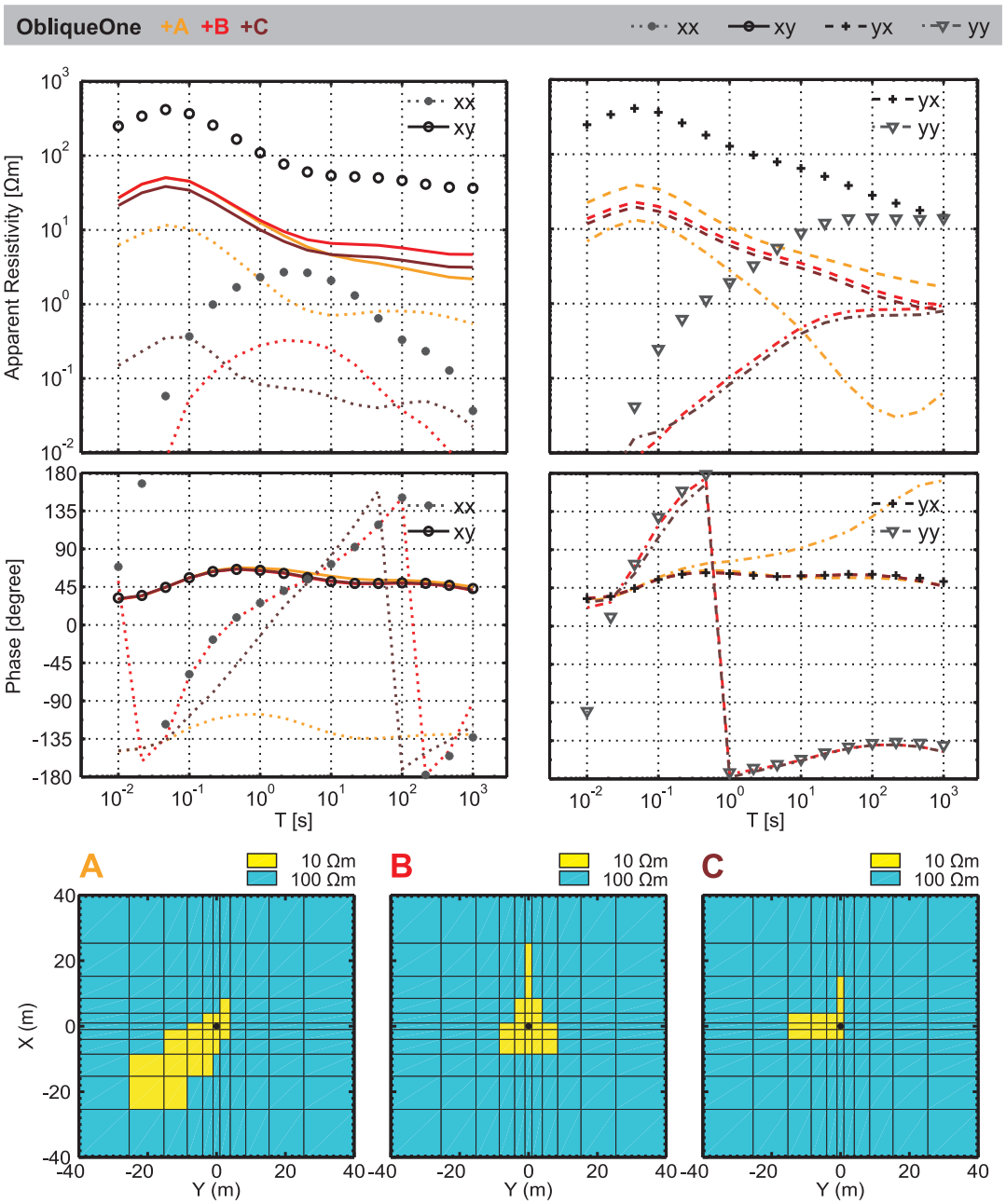

Figure 4.7: Influence of complex shaped 3D inhomogeneities (lower panel) on 3D ObliqueOne responses (upper panel). Structures A - C (height 12 m) were inserted into the ObliqueOne model at site 074 (cf. Fig. 4.5). Observed responses (lines) are mixed quantities of the regional impedances (symbols). At periods < 10 s diagonal impedance elements are dominated by larger off-diagonal elements, in particular for feature A which exhibits lowest symmetry with respect to x- and y-axes. For the off-diagonal components influence of the corresponding diagonal elements and, thus, deviation of distortion from static impedance scaling is visible at periods > 100 s.

4.2 AIDE – Automatized identification and estimation of static shift

If data only differ by various amounts of static shift, log-log plots of apparent resistivity curves agree in shape but are vertically offset. Based on this distinct curve shape behaviour I developed the automatized scheme AIDE to identify apparent resistivity curve pairs as *shifted* or *non-specific pairs* and subsequently estimate static shift values for the first class of pairs.

Given an observed local apparent resistivity curve $\rho_{ij}^{\mathrm{loc}}(\omega_k)$ and a corresponding reference curve $\rho_{ij}^{\mathrm{ref}}(\omega_k)$ estimated at N_k discrete frequencies ω_k, I define the distance $\Delta_{ij}(\omega_k)$ of these curves

$$\Delta_{ij}(\omega_k) := \log_{10}(\rho_{ij}^{\mathrm{loc}}(\omega_k)) - \log_{10}(\rho_{ij}^{\mathrm{ref}}(\omega_k)). \tag{4.4}$$

In the following, indices i, j indicating components x, y will be omitted for clarity. In general, the frequency behaviour of ρ^{loc} and ρ^{ref} differs and $\Delta(\omega_k)$ varies with ω_k.

In the static shift case ρ^{loc} and ρ^{ref} are related by the frequency-independent galvanic distortion parameter c (cf. first term in (4.2))

$$\rho^{\mathrm{loc}} = c^2 \cdot \rho^{\mathrm{ref}}. \tag{4.5}$$

Thus,

$$c^2 = \frac{\rho^{\mathrm{loc}}}{\rho^{\mathrm{ref}}} \qquad \text{or} \qquad \log_{10}(c^2) = \log_{10}(\rho^{\mathrm{loc}}) - \log_{10}(\rho^{\mathrm{ref}}) \tag{4.6}$$

and with (4.4)

$$\Delta(\omega_k) = \log_{10}(c^2) = const. \tag{4.7}$$

Hence, Δ is independent of frequency and represents the vertical offset of the local log-apparent-resistivity curve from the reference curve in decades. In the following, Δ is referred to as shift amplitude or shift value. The galvanic distortion parameter c can be directly taken from Δ.

In summary, *non-specific* and *shifted* curve pairs can be discriminated by the distribution of $\Delta(\omega_k)$, which is of broad shape for the *non-specific* class, whereas Δ-estimates of the *shifted pairs* class exhibit a δ-type distribution peaking at a distinct value of $\Delta = \log_{10}(c^2)$. Figure 4.8 illustrates the above described considerations.

In practical cases, in particular for measured data, shifted curve pairs will only approximately satisfy (4.5). Thus, $\Delta(\omega_k)$-estimates will scatter around the theoretical value $\log_{10}(c^2)$. A *shifted pair* is identified if the distribution of the distance estimates is *close* to a δ-distribution, i.e. exhibits a *significant* peak, which exceeds a critical threshold.

In the AIDE scheme, the distribution of $\Delta(\omega_k)$ estimates is determined using discrete interval

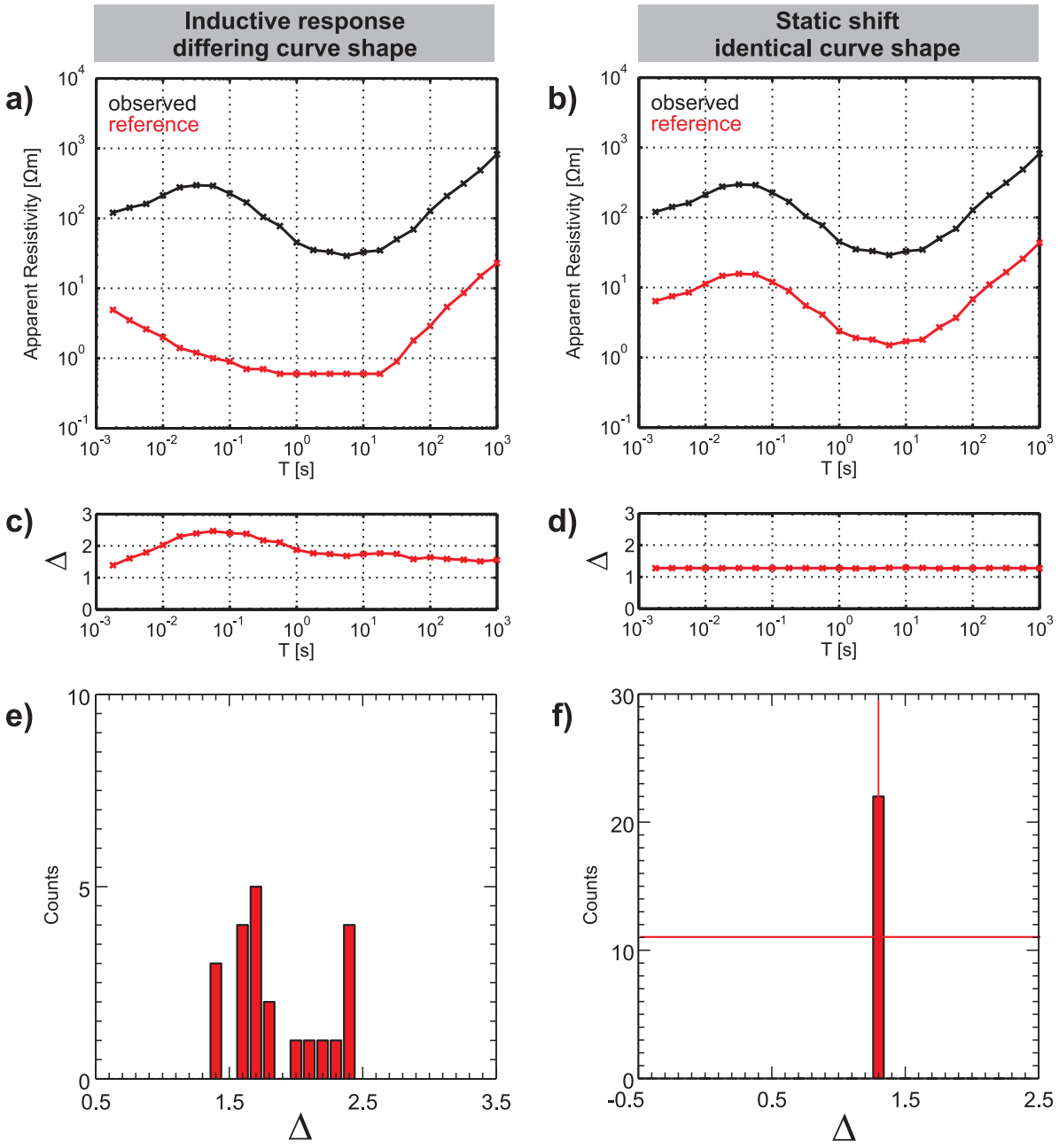

Figure 4.8: Identification of static shift. In the general case when curve shapes of locally observed (black) and reference (red) apparent resistivities differ **(a)**, $\Delta(\omega_k)$-estimates **(c)** vary with frequency scattering over a broad range **(e)**. In contrast, in the case of static shift apparent resistivity curves **(b)** are of similar shape and their vertical distance **(d)** is constant over frequency so that the distribution of $\Delta(\omega_k)$ peaks at a distinct value **(f)**.

intervals I_a of equal interval width w

$$I_a = -0.5\left[(A-1)+aw \quad (A-1)-aw\right]. \qquad a = 1...A = 2n+1, \;\; n \in \mathbb{N} \tag{4.8}$$

N_a is the number of Δ estimates in the interval I_a. The central interval

$$I_{(A-1)/2} = [-b/2 \;\; b/2]$$

is always centred around zero. The distribution of $\Delta(\omega_k)$ is defined to exhibit a significant peak if it comprises at least one interval in which N_a exceeds the threshold $N_a > tN_k$:

$$\Sigma = \left\{ I_a | N_a > tN_k^{\mathrm{loc}} \right\} \qquad \text{and} \qquad \Sigma \neq \{\}\,, \tag{4.9}$$

where t is the threshold level ($0 \leq t \leq 1$). The subset $\Sigma = \{I_s\}$, $s = 1...S$ comprises the *significant intervals* I_s. If $\Sigma \neq \{\}$ the curve pair is classified as shifted and the peak value $\bar{\Delta}$ is estimated as weighted mean from the set of significant intervals Σ

$$\bar{\Delta} = \frac{1}{\sum_{s=1}^{S} N_s} \sum_{s=1}^{S} N_s I_s^c, \tag{4.10}$$

where $I_s^c = -0.5[(A-1)+(a-1)b]$ is the centre of I_s. Subsequently, the local resistivity curve is assigned to be shifted by $\bar{\Delta}$ from the reference curve

$$\log_{10}(\rho^{\mathrm{loc}}) = \log_{10}(\rho^{\mathrm{ref}}) + \bar{\Delta} \tag{4.11}$$

and the average galvanic distortion parameter $\bar{c}$ is estimated:

$$\bar{c} = 10^{0.5\bar{\Delta}}. \tag{4.12}$$

The procedure described above uses one single apparent resistivity reference curve. Similarly, using multiple reference curves $\{\rho^{\mathrm{ref1}}, \rho^{\mathrm{ref2}}, ...\}$ yields $\{\Delta_1(\omega_{k1}), \Delta_2(\omega_{k2}), ...\}$. For the estimation of $\bar{\Delta}$ and $\bar{c}$ in this case, I consider the joint distribution $\{\Delta_1(\omega_{k1}), \Delta_2(\omega_{k2}), ...\}$ and similarly follow (4.8) to (4.12).

Table 4.1 summarizes parameters available in the AIDE software. Required input parameters are the interval width w to set up the discretization of the distribution of $\Delta(\omega_k)$ (cf. (4.8)) and the threshold level t which determines the significant peak amplitude of the Δ-distribution relative to the total number of Δ-estimates (cf. (4.9)). Using reference data which were not obtained at the local site, the search radius r outlines the maximum distance from the local site within which reference data are considered. Optionally, the frequency range can be restricted to $\omega_{min} \leq \omega \leq \omega_{max}$. N_{min} defines the minimum number of $\Delta(\omega_k)$-estimates which

are required for calculation of $\bar{\Delta}$.

Table 4.1: Overview of AIDE parameters.

Parameter		required	optional
w	interval width	x	
t	threshold level	x	
r	search radius		x
$\omega_{min}, \omega_{max}$	minimum and maximum frequency		x
N_{min}	minimum number of $\Delta(\omega_k)$-estimates		x

To yield meaningful $\bar{\Delta}$- and $\bar{c}$-estimates reference apparent resistivity data are required to be sufficiently close to the undistorted subsurface response at the local site. Using multiple reference curves, each reference curve can be affected by a different amount of shift but shift amplitudes have to sum up to zero for the entire reference data set. If only one reference is used, however, the apparent resistivity curve has to be free of static shift.

Practical examples for reference data include MT measurements from close-by sites, transient electromagnetic (TEM) measurements, or MT model responses obtained with inversion of distortion-free data (e.g. phase tensors or vertical magnetic transfer functions) or (down-weighted) apparent resistivities & phases. Within the scope of this thesis, I used MT responses obtained in the vicinity of the local site as reference data for the AIDE scheme. Sections 4.3 and 4.4 present the application of this method to synthetic data sets and field data from the California MT array, respectively.

4.3 Using spatial coherence of data to correct for static shift

MT data reflect the conductivity distribution of the subsurface below and in the vicinity of the observation point. In MT surveys, data are often sampled in a way that the induction volumes of neighbouring sites overlap for large parts of the investigated period range to ensure a consistent coverage of the subsurface. As a consequence, measurements at neighbouring or close-by sites are partially redundant. In combination with the spatial uniformity of the source fields (cf. section 1.1), such densely sampled MT data are spatially coherent. The degree of spatial coherence, i.e. the similarity of the data of near-by sites and the radius in which data are "similar", depends on the wave length of lateral subsurface structure variations in the survey area. Maximum spatial coherence would be given by a true 1D subsurface, where data are identical at all survey points.

In contrast, the near-surface inhomogeneities causing static shift are localized and affect sites individually. The distribution of inhomogeneities can usually be assumed independent between sites and randomly distributed in the survey area.

Hence, apparent resistivity curves within a radius r around an observation point can be used as reference data in the AIDE algorithm to identify and estimate static shift at a local site (see sec. 4.2). As neighbouring sites are used as reference data, the method is henceforth referred to as AIDE-N method.

4.3.1 Testing AIDE parameters and influence of statistical properties of static shift values

To test how AIDE-N parameters and statistical properties of static shift distributions in the survey area influence identification and estimation of static shift I used a synthetic 1D layered half-space model (LH, cf. Fig. 4.2) which provides ideal spatial coherence.

LH responses were calculated for 50 profile sites and 22 periods between 0.001 s and 1,000 s. 2.5 % Gaussian noise was added to the apparent resistivities and phases. Above a 1D subsurface structure undistorted xy- and yx-apparent resistivities are identical. In presence of static shift, apparent resistivity curves can be offset as the two components can be affected by different amounts of distortion. In the following, I exemplarily consider the xy-component and the corresponding shift value $\Delta_{xy} = \log_{10}(c_{xx}^2)$.

Static shift of the LH data set was simulated with three sets of synthetic shift values representing different assumptions and findings concerning the statistical distribution of shift values (Fig. 4.9). Shift amplitudes of sets N1 and N2 follow a normal distribution with a standard deviation of 1 and mean values of 0 and -0.5, respectively. Joint subsurface resistivity and static shift inversion algorithms are usually based on a zero-sum and/or Gaussian distribution for the static shift parameters assuming that a set of shift amplitude will appear as a (zero-mean) random perturbation for a large number of sparsely distributed MT sites (e.g. deGroot-Hedlin, 1991; Ogawa & Uchida, 1996; Sasaki, 2004; Sasaki & Meju, 2006). However, it is questionable whether such assumptions are valid in practice as Sasaki & Meju (2006) find that shift values are systematically biased within a survey area so that the mean deviates from zero and/or the distribution is non-symmetric. To simulate this finding shift values of set G obey a modified gamma distribution $\Delta_{xy} \sim -\Gamma(k, \theta) + 0.5$ with shape $k = 2.0$ and scale $\theta = 2.0$. Expected and mean value of set G are -0.5, the maximum of the distribution is located at 0. For all sets, shift values were distributed randomly along the profile to 34 out of 50 sites ($\approx$ 66 %).

I applied the AIDE-N method to each of the three shifted LH data sets using 27 combinations of the parameters search radius r (1.5 km, 2.5 km, 3.5 km) – corresponding to 2, 4, and 6 reference sites, respectively – interval width w (0.1, 0.2, 0.3), and threshold level t (0.1, 0.2, 0.3). The resulting $\bar{\Delta}_{xy}$-estimates are summarized in Figure 4.10. The top row of each panel displays the original shift value.

Visual comparision of $\bar{\Delta}_{xy}$-estimates in Figure 4.10 suggests similarly good recovery of shift for all three shift sets independent of their statistical properties. Along large parts of the

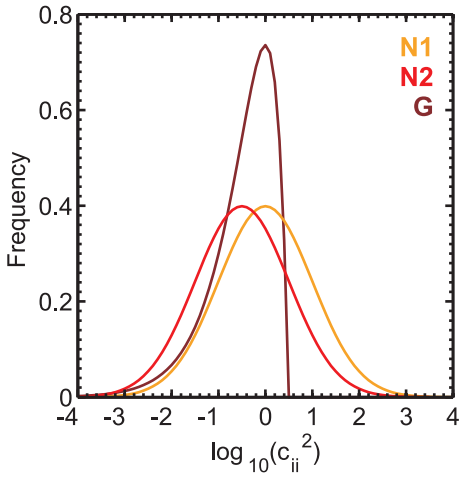

Figure 4.9: Distribution of synthetic static shift values. Sets N1 and N2 follow a normal distribution with a standard deviation of 1 and mean values of 0 and -0.5, respectively. Shift values of set G obey a modified gamma distribution $\Delta \sim -\Gamma(k,\theta) + 0.5$ with shape $k = 2.0$ and scale $\theta = 2.0$, simulating a skewed shift distribution reported for real world data sets (e.g. Sasaki & Meju, 2006).

profile estimation of static shift amplitudes is in good agreement with the originally applied shift values. At most sites (columns in Fig. 4.10) shift estimates close to the original value could be retrieved for a broad range of parameter settings (rows). Investigating $\bar{\Delta}_{xy}$-estimates for the different shift sets in more detail reveals a slight bias of results for distributions N2 and G which have a non-zero mean (Fig. 4.11).

Closer inspection of shift estimates in Figure 4.10 for each parameter combination (row) reveals that shift recovery depends on the along-profile distribution of static shift. Where shift was assigned to only a few sites, e.g. around site 114, neighbouring sites provide a good reference to the true resistivity level of the subsurface. Hence, the original shift amplitude can be precisely recovered. Moreover, shift estimates in these regions depend only weakly on the parameter settings (nearly constant colour per column beneath sites 112 - 116). In areas where shift rate is high, i.e. nearly all sites are affected by significant amounts of shift (e.g. sites 120 - 125, 135 - 145), the variability of the estimates for different AIDE parameter combinations is much higher at each site.

In the following, I examine the influence of each AIDE parameter r, w, and t in more detail. The search radius r corresponds to the number of reference sites. For increasing values of r the quality of shift estimates improves as $\bar{\Delta}_{xy}$-estimates are based on an increasing number of reference sites and are, thus, more representative for the true shift value. For the LH data examples in Figure 4.10, this effect is particularly obvious for the radius increase from $r = 1.5$ km (max. 2 references) to $r = 2.5$ km (max. 4 references) (cf. Fig. 4.11).

The interval width w describes the discretization of the $\Delta_{xy}(\omega_k)$-distribution and mainly determines the precision of the localization of peaks within the distribution and consequently the quality of the shift amplitude $\bar{\Delta}_{xy}$. For the LH data set, the influence of w is most clearly expressed for a search radius of 1.5 km. Now, only the two direct neighbours of each site are used as reference data. At sites where these neighbours are free of static shift, e.g. at 114,

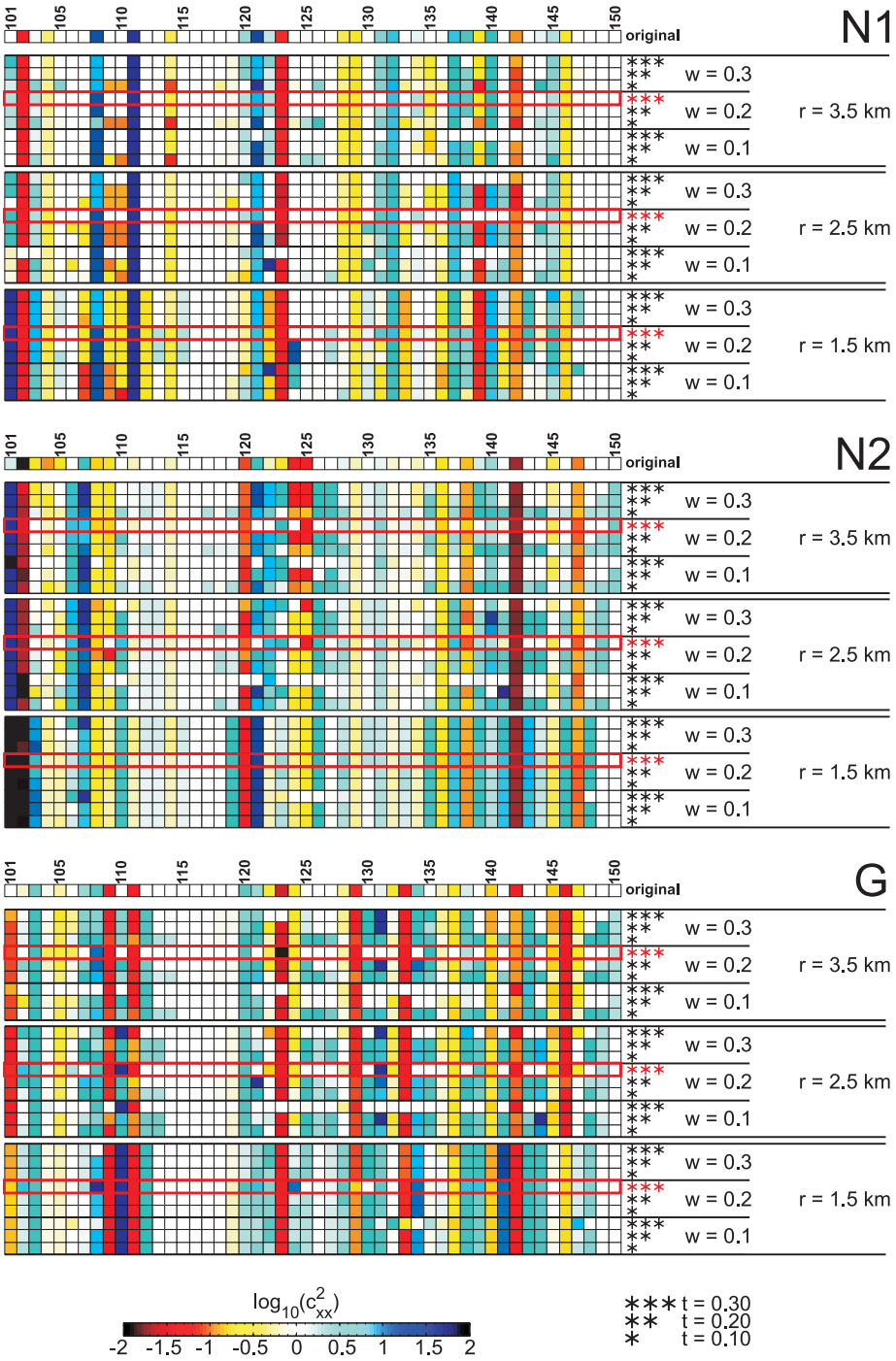

Figure 4.10: Colour-coded AIDE-N shift value estimates for 1D LH data (cf. Fig 4.2) compromised with three different sets of randomly distributed static shift (N1, N2, and G, cf. Fig. 4.9). Horizontal sequence of sites corresponds to profile location; site distance is 1 km. Original shift values are displayed in the top rows. Each panel row shows the shift estimates for a particular combination of the AIDE-N parameters radius r, interval width w, and threshold level t as indicated on the right. Distribution of shift estimates in red outlined rows is taken for comparison with the respective original N1, N2, and G distributions in Fig. 4.11.

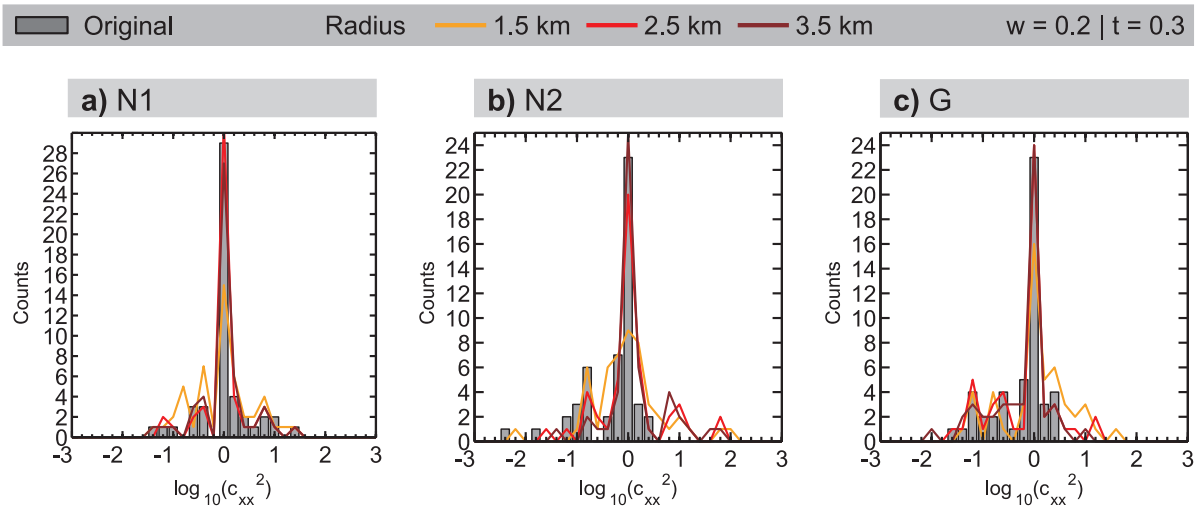

Figure 4.11: Comparison of distributions of original shift values (bars) and AIDE-N estimates (lines) for the LH data set (cf. red outlines in Fig. 4.10). Recovery of the overall shift distribution for each set improves with increasing search radius, i.e. increasing number of reference sites. AIDE-N estimates for sets N2 and G are systematically more symmetric around zero than the original distributions, which is related to the zero-mean assumption for shift values of the reference data.

129, and 140, all $\Delta_{xy}(\omega_k)$-estimates fall into the same interval. In this case, the $\Delta_{xy}(\omega_k)$-distribution comprises only one significant interval and $\bar{\Delta}_{xy}$ is identical to the central value of this interval (cf. (4.10)). The narrower the intervals are defined, the better can the true shift amplitude be approximated by $\bar{\Delta}_{xy}$.

The threshold level t was introduced as similarity measure between locally observed and reference data. In 1D, data are identical at all sites and a second implication of t becomes apparent. As all N_k $\Delta^i_{xy}(\omega_k)$-estimates obtained from a particular reference curve $\rho^{\mathrm{ref,i}}$ are identical and the same period layout is used at each site of the data set, we can similarly consider each reference site to contribute one estimate Δ^i_{xy} to the distribution $\{\Delta^1_{xy}, \Delta^2_{xy}, ...\}$. The number of Δ-estimates N_Δ is equivalent to the number of reference sites N_r.

If reference data are affected by the same amount of shift or are undistorted, shift estimates Δ^i_{xy} for all sites are located in the same interval. This interval will always be identified as significant as $N_\Delta \geq t \cdot N_k = t \cdot N_k$ for all $t = 0...1$ (cf. (4.9)). However, if the surrounding sites are affected by significantly differing amounts of shift, Δ-estimates for the reference sites end up in N_r different intervals in the most extreme case. Significant intervals in the distribution of Δ^i_{xy} will only be identified if $t < 1/N_r$, although taken separately each single pair (ρ^{loc}, $\rho^{\mathrm{ref,i}}$) will be identified as shifted pair for all t. Hence, t also represents an upper limit to the scattering of shift values in the reference data set.

For the LH example (Fig. 4.10), $\bar{\Delta}_{xy}$-estimates for $r = 1.5$ km ($N_r = 2$) are virtually independent of t as $t < 1/N_r$ for all tested threshold levels ($t = 0.1, 0.2, 0.3$). Where estimates

vary with t, this is related to the Gaussian noise added to the data set. For larger search radii (r = 2.5 km, 3.5 km), the variability of shift value estimates with t is higher as more (N_r = 4, 6) reference sites are included and, hence, the minimum Δ_{xy}-counts per interval decreases to 1/4 = 0.25 and 1/6 = 0.17, respectively. For t = 0.1, all intervals containing $\Delta_{xy}(\omega_k)$-estimates exceed the critical threshold and are consequently identified as significant. Using higher threshold levels (t = 0.3, 0.2), only intervals which comprise shift estimates from at least two of the four or six reference sites are significant. Thus, the subset of significant intervals and subsequently $\bar{\Delta}_{xy}$ vary for different threshold settings.

Moreover, the influences of search radius, interval with and threshold level are interrelated. In particular, the interval width w influences the interval counts and, thus, the range of meaningful threshold levels t.

4.3.2 2D subsurface structure

In more practical cases, when the subsurface structure is 2D (or 3D, see section 4.3.3), subsurface responses vary from site to site. In this case, the search radius r represents a compromise between (i) the attempt to include many sites to provide a solid base for estimation of the static shift parameters and (ii) the aim to consider only relevant reference sites, which are sufficiently similar to the local site. Thus, r is a representation of the assumed horizontal wave length of subsurface structures.

A 2D subsurface situation was simulated with the 2D BBL model which consists of the previously discussed LH model and two adjacent blocks (10 Ωm, 1000 Ωm) in the central profile area (cf. Fig. 4.1). FWD data were calculated for the 50-site profile and 22 periods (0.001 - 1,000 s) in the same way as for the LH data set (see previous section). Synthetic shift values following set G (cf. Fig. 4.9) were applied independently to both TE and TM-mode apparent resistivities at 66 % of the 50 stations (TE: 34, TM: 33).

Shift amplitudes for TE and TM-mode data were estimated with the AIDE-N scheme using the same parameter combinations as for the LH data set (r = 1.5 km, 2.5 km, 3.5 km; w = 0.1, 0.2, 0.3; t = 0.1, 0.2, 0.3) and results are summarized in Figure 4.12. The overall recovery of the static shift values along the profile is good for both modes and compatible with the recovery rate for the LH data set (cf. Fig. 4.10). In most regions above the 2D BBL structure curves of (one or more) sites within the search radius are similar enough to be classified as shifted pairs.

Shift recovery rate at each site varies along profile and with AIDE parameter settings. Towards the profile ends, where the BBL model is dominated by the 1D LH structure, shift amplitudes at single sites (columns) are very similar for all 27 parameters combinations. In contrast, close to the edges of the two blocks $\bar{\Delta}_{ij}$-estimates exhibit clearly higher variability per site. In this 2D area curve shapes vary significantly from site to site.

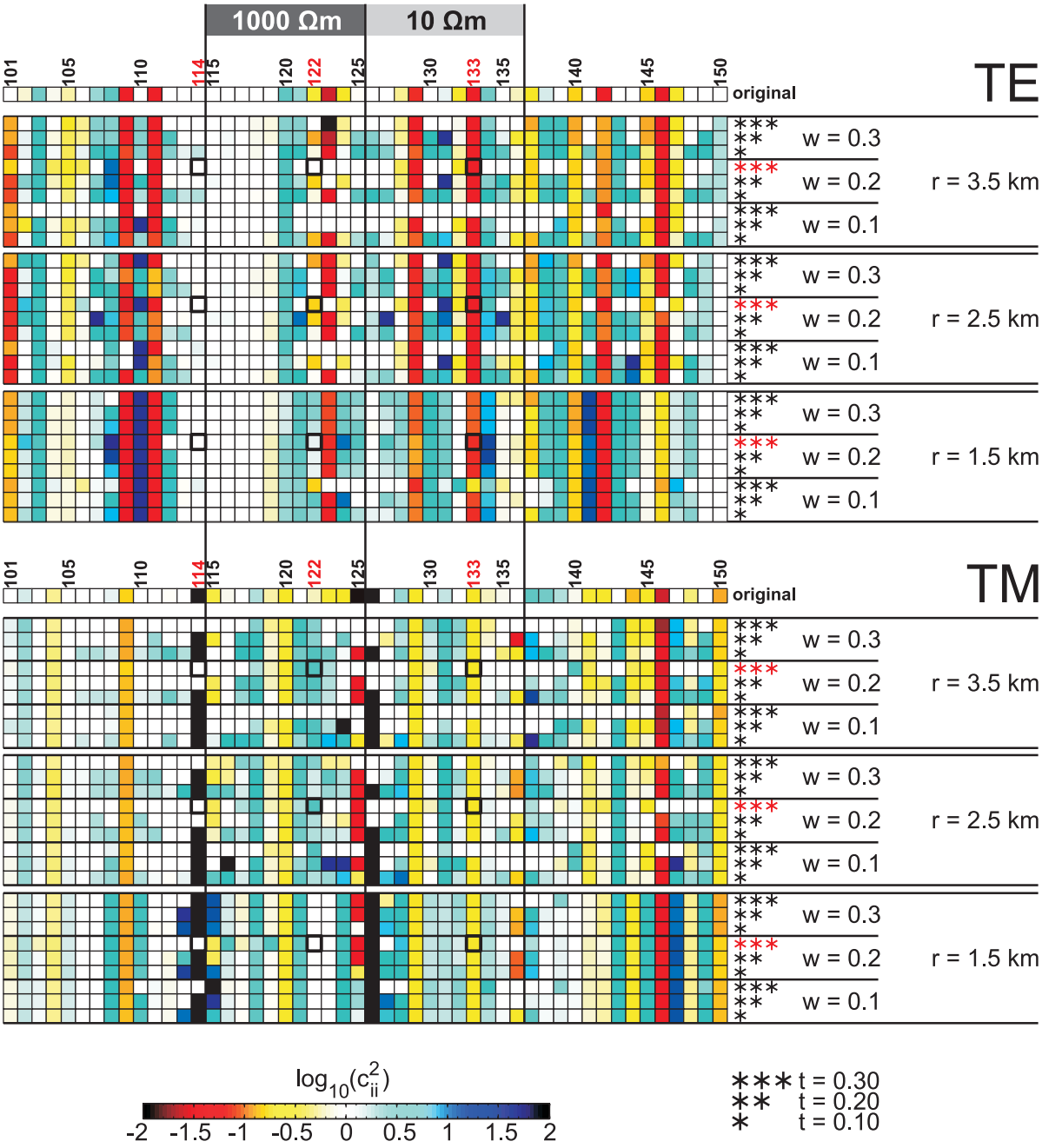

Figure 4.12: AIDE-N shift estimates for synthetically shifted TE and TM data of the 2D BBL model (cf. Fig. 4.1). Original shift values (top row) follow set G (cf. Fig. 4.9); shift rate is 66 % for both modes. $\Delta_{ij}(\omega_k)$-distributions for selected parameter combinations at sites 114, 122, and 133 (black outline) are displayed in Figure 4.13.

Moreover, in the vicinity of the block boundaries TE-mode shift values are systematically better and more reliably recovered than TM-mode estimates. This finding can be explained by the different spatial behaviour of TE and TM-mode subsurface responses. At vertical 2D conductivity contrasts, electromagnetic field components of the TE-mode (E_x, B_y) vary smoothly across a lateral conductivity contrast and TE-mode apparent resistivities change gradually from site to site. In contrast, the field component constituting the TM-mode (E_y, B_x) are discontinuous at such surfaces. Hence, TM-mode transfer functions change very rapidly across the block edges and apparent resistivity curves of neighbouring stations exhibit lower similarity than for the TE-mode. However, moving away from such a lateral conductivity interfaces the influence of this contrast on the TM-mode data decays faster than for the TE-mode.

The different spatial behaviour of TE- and TM-mode data is reflected in the distribution of $\Delta_{ij}(\omega_k)$-estimates in the central profile area (Fig. 4.13). For sites located very close to the edge of a 2D block $\Delta_{xy}(\omega_k)$-distributions (TE) exhibit one (upper panel in Fig. 4.13a) or several pronounced peak(s) depending on the shift distribution in the reference data set. In contrast, $\Delta_{yx}(\omega_k)$-estimates are distributed over a broader, but coherent range so that interval counts are lower on average (lower panel in Fig. 4.13a). TM-shift at site 114 is not recognized by the AIDE scheme for any of the search-radii, although the reference sites are free of static shift and provide a reliable reference to the true subsurface resistivity level. Further away from the block boundaries, $\Delta_{yx}(\omega_k)$-distributions (TM) exhibit clearer peaks than the TE $\Delta_{xy}(\omega_k)$-results (Figs 4.13b-c). At the same distance from the block boundaries, the shape of the $\Delta_{xy}(\omega_k)$-distribution is stronger affected by the resistivity interface above the resistive (1000 Ωm) than the conductive (10 Ωm) block due to the different skin depths (cf. Figs 4.13b-c).

I also tried to improve shift amplitudes iteratively. In step one of this process, apparent resistivities were corrected for all sites with $\bar{\Delta}_{ij}$-estimates obtained for one particular set of AIDE parameters as shown in Figure 4.12. In step two, these corrected apparent resistivity curves which are assumed to be closer to the true apparent resistivity curve level were subsequently used to obtain the new $\bar{\Delta}_{ij}$-estimates (second iteration), etc. When applying this scheme to the BBL data set for up to three iterations (Fig. 4.14), significant improvements of the cumulated $\bar{\Delta}_{ij}$-estimates can be observed in regions, where a subset of shift amplitudes was successfully identified already in the first iteration (e.g. 120 - 125 (TE), $r = 3.5$ km). However, where shift estimates of the first iteration are biased over several sites, this bias manifests or even increases for subsequent iterations (101 - 103 (TE)).

In summary, in 2D situations, the quality of shift recovery depends more significantly on the appropriate choice of the search radius r than in 1D. Where r is too large, reference data include a range of apparent resistivity curve shapes and $\Delta_{ij}(\omega_k)$-distributions are of broad shape. However, if the search radius is too narrow, estimates are biased towards the immediate site neighbours. As TM and TE apparent resistivities change with different spatial rates, parameter settings have to be tuned individually for both modes.

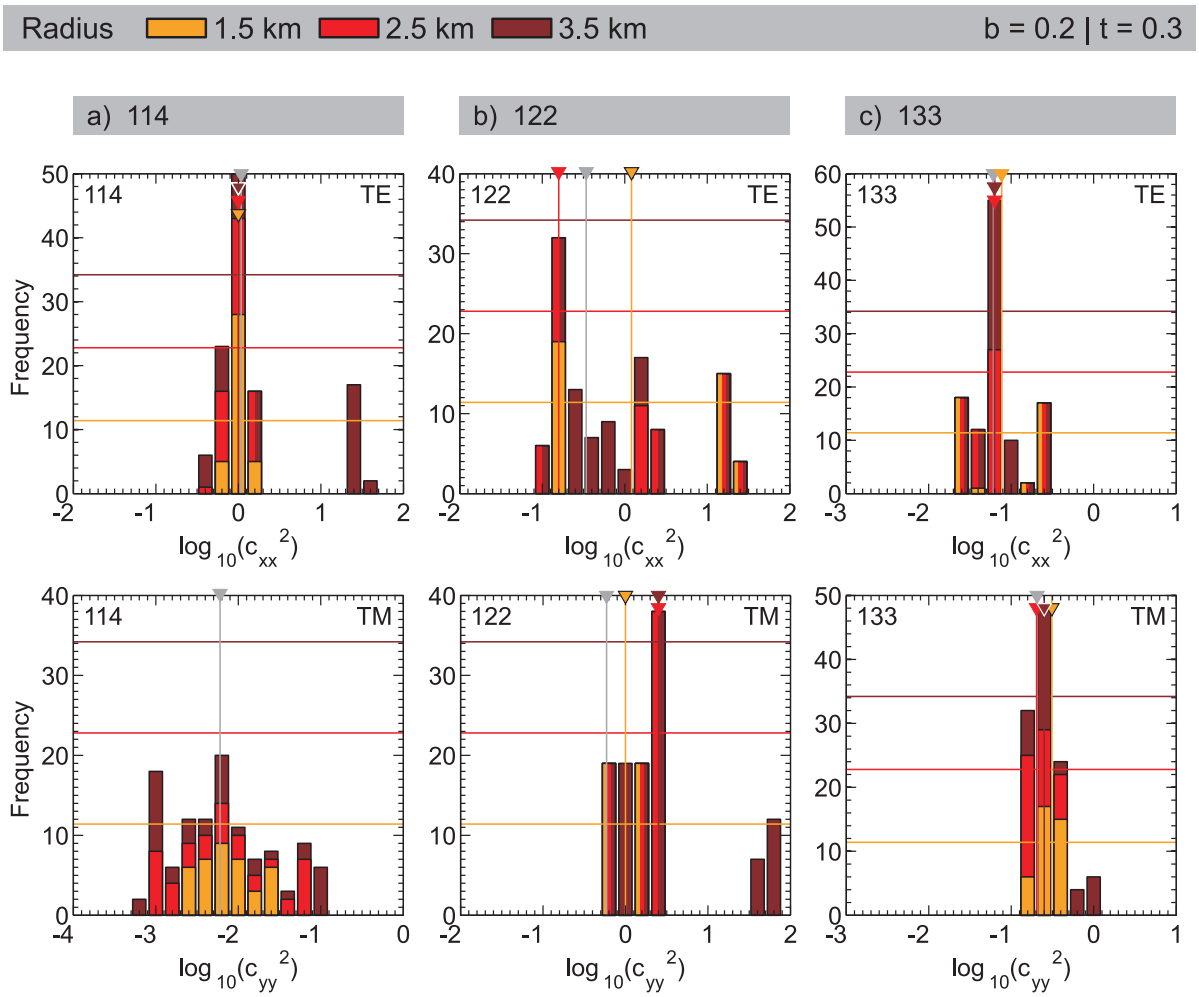

Figure 4.13: $\Delta_{ij}(\omega_k)$-estimate distributions for three sites of the 2D BBL data set at various distances from lateral subsurface conductivity contrasts (see Fig. 4.12 for site locations). Grey lines and triangles indicate the originally applied shift value; if shift was identified, coloured vertical lines and triangles mark $\bar{\Delta}_{ij}$ for the respective search radius. Horizontal lines indicate threshold levels. Distributions with broad shape indicate significant variations of apparent resistivity curve shapes within the reference data set due to 2D subsurface structures. For TE- and TM-mode data, strongest influences of the BBL block-structures manifest at different distances from the block edges (see text).

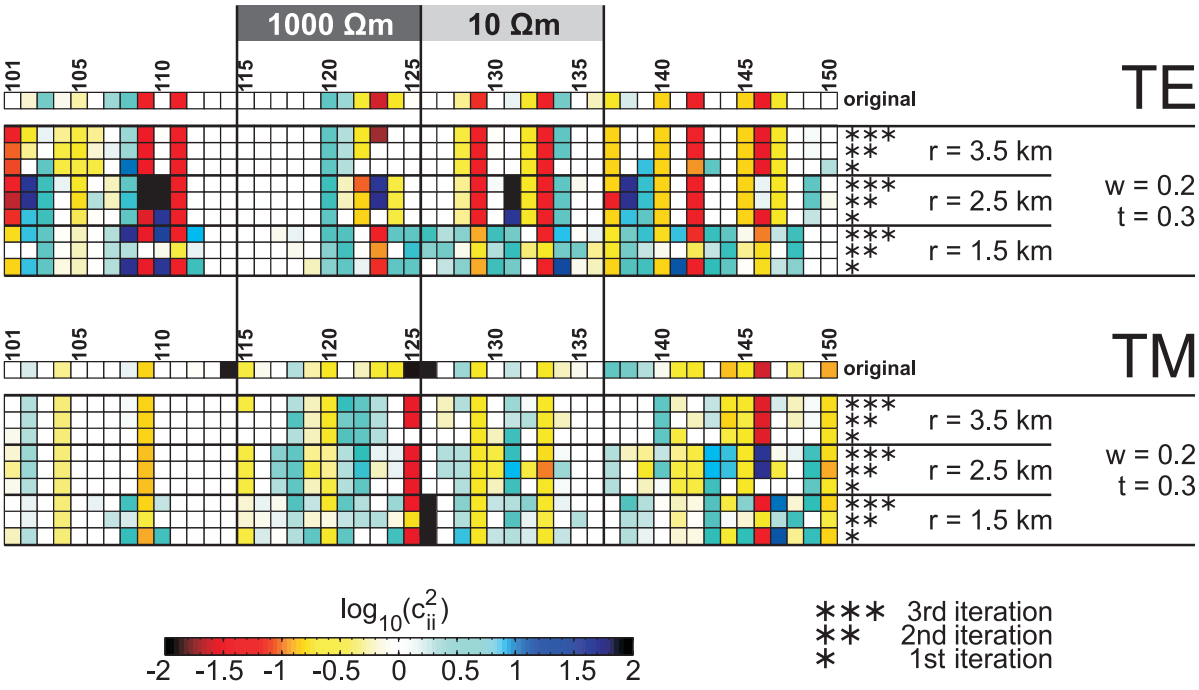

Figure 4.14: Cumulated shift estimates for iterative application of AIDE-N method to the BBL data set. Between each AIDE-N iteration, apparent resistivity data were corrected with the $\bar{\Delta}_{ij}$-estimates of the previous iteration.

4.3.3 3D subsurface structure

For simulation of a 3D subsurface, I used the ObliqueOne model (Fig. 4.15) which served as background structure for the 3D FWD modelling of galvanic distortion (cf. sec. 4.1.2). A detailed model description is given in section 3.2.2. The ObliqueOne data set comprises 10 × 10 sites with uniform site spacing of 4 km and 16 periods between 0.001 s and 1,000 s. 3 % Gaussian noise was added to the impedances prior to calculating apparent resistivities and phases. In order to generate static shift, the same shift amplitudes were applied to ρ_{xx} & ρ_{xy} and ρ_{yx} & ρ_{yy}, respectively, corresponding to the assumption of a diagonal distortion matrix (cf. first term in (4.2), p. 105). Shift values Δ_{ij} follow set G (cf. Fig. 4.9) and were distributed randomly over all 100 sites.

The AIDE-N scheme was applied to all four apparent resistivity components independently. I used search radii of 4.5 km and 8.5 km corresponding to 4 and 12 reference sites, respectively; interval width ($w = 0.1, 0.2, 0.3$), and threshold level ($t = 0.1, 0.2, 0.3$) settings are the same as for the previously discussed 1D and 2D examples. The results are summarized in Figure 4.16.

Visual inspection of the resulting AIDE-N shift estimates (Fig. 4.16) reveals dissimilar shift recovery quality for all four components. Most obviously, shift estimates for the off-diagonal

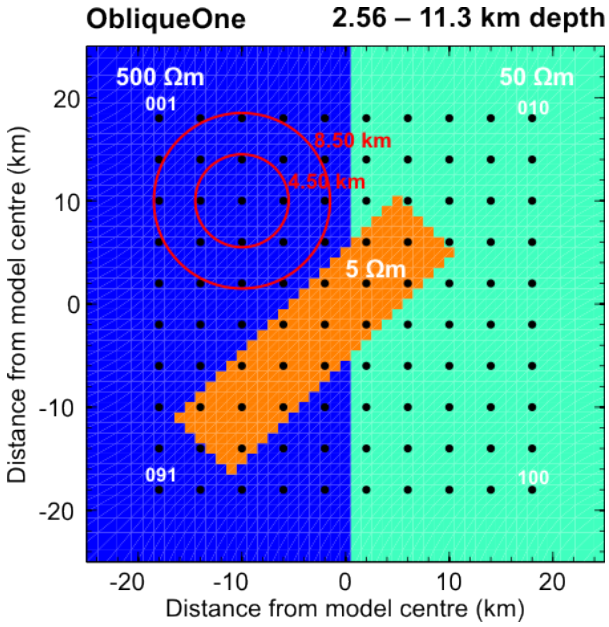

Figure 4.15: Main structural features of ObliqueOne model. Red circles illustrate the distribution of reference sites for search-radii of 4.5 km and 8.5 km, respectively.

components ρ_{xy} and ρ_{yx} show a significantly higher agreement with the originally applied shift values than those for the diagonal components ρ_{xx} and ρ_{yy}. This outcome reflects the different spatial coherence length of individual impedance components which is, in general, larger for the off-diagonal than for the diagonal components. Close to 3D subsurface features, ρ_{xx} and ρ_{yy} change significantly over short distances which impedes the identification of shifted curve pairs. In addition, where subsurface is dominated by 1D or 2D structures impedance amplitudes are very small and unstable. Hence, only few ρ_{xx}- and ρ_{yy}-curves were identified as shifted from the set of reference data, in particular for the larger search radius (8.5 km) Independent of the search radius, the recovered $\bar{\Delta}_{ij}$-amplitudes still agree reasonably well for ρ_{xx}; however, estimates for ρ_{yy} are poor (see below).

Overall, estimates of $\bar{\Delta}_{xx}$ and $\bar{\Delta}_{xy}$, referring to $\log_{10}(c_{xx}^2)$, excel the results obtained for $\bar{\Delta}_{yx}$ and $\bar{\Delta}_{yy}$ ($\log_{10}(c_{yy}^2)$). The regional structure of the ObliqueOne model represented by the two half-layers is 2D. At long periods, Z_{xy}-data are dominated by the regional 2D TE-mode background response and similarly Z_{yx} by the TM-mode. As seen for the 2D BBL data set, the different spatial behaviour of the two modes across lateral conductivity variations leads to different success rates of shift identification (cf. Fig. 4.12). As a consequence, when expanding the search radius from 4.5 km to 8.5 km shift recovery significantly decreases for ρ_{yx} whereas quality for ρ_{xy} is nearly preserved. The different behaviour of the electric field components across the interface of the regional-scale half-layers affects also the shift recovery for the diagonal components.

The results in Figure 4.16 reveal interrelation of interval width w with threshold level settings with respect to shift recovery. Most obviously, w and t determine the shift identification rate,

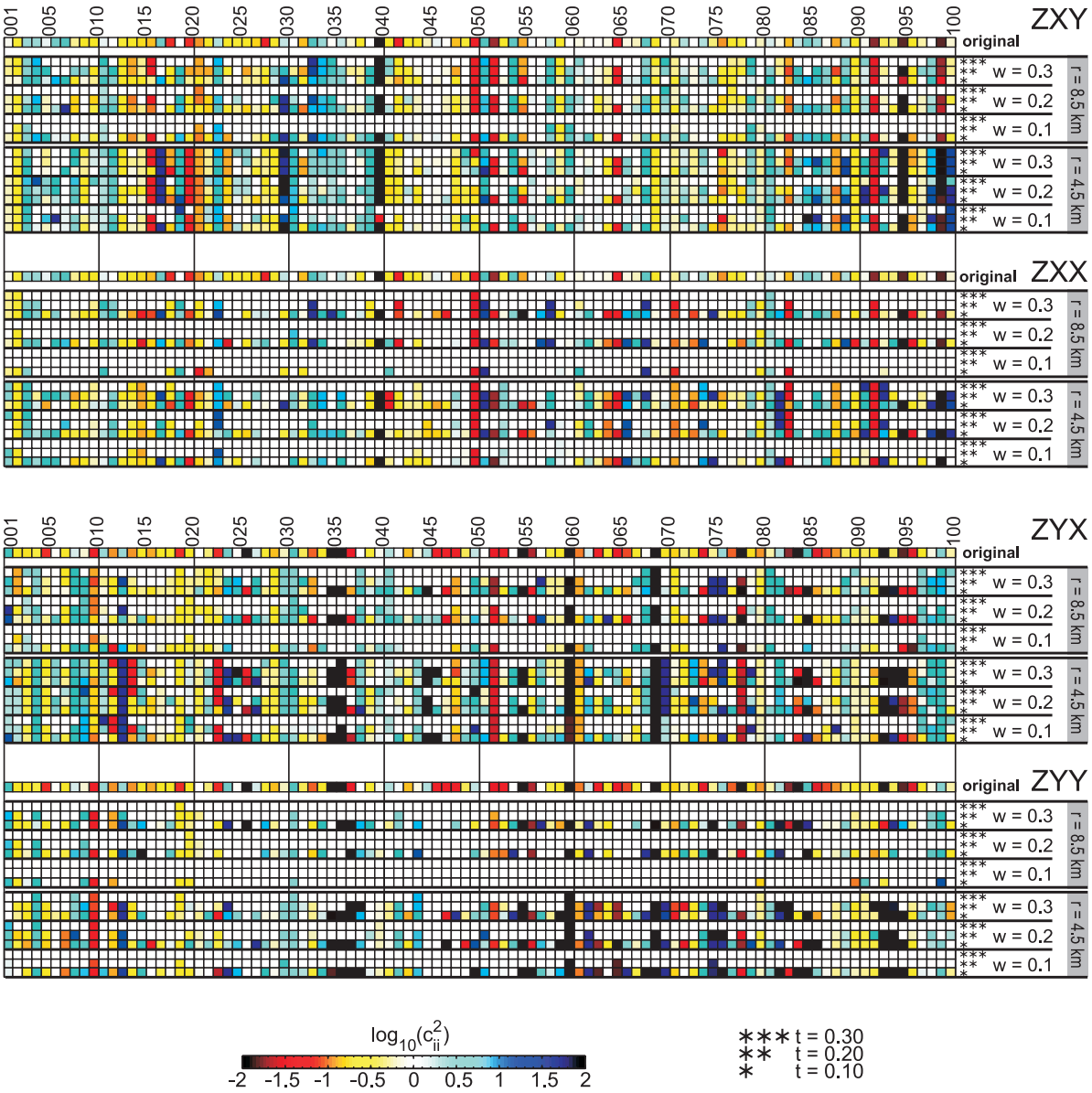

Figure 4.16: Application of AIDE-N method to the shifted 3D ObliqueOne data set (see Fig. 4.15 for site locations). Quality of shift recovery differs between all four components. Higher spatial coherence of off-diagonal apparent resistivities in comparison to the diagonal components leads to higher quality of shift estimates. The overall better shift recovery for xx- and xy-components compared to the yx- and yy-results is related to the 2D background structure of the ObliqueOne model (cf. Fig. 4.12).

i.e. the detection of significant peaks in the $\Delta_{ij}(\omega_k)$-distributions. For increasing interval width w, interval counts increase and more intervals will be identified as significant when using a constant threshold level. Similarly, a larger number of local sites is classified as shifted if interval width is constant and the threshold level is lowered. Similar observations were made in previous tests with 1D and 2D data sets (cf. Figs 4.10, 4.12). For the 3D ObliqueOne example, however, the influences of w and t are more pronounced. Curves of the reference data set are less similar to the local site as the subsurface structure is 3D and, more importantly, the horizontal sampling of lateral subsurface changes is less dense when compared to the sampling of the 2D blocks for the BBL model (cf. Figs 4.15 and 4.1). In particular, static shift of the diagonal components is only recognized for small threshold levels. Δ-estimates for these components are distributed over a wider range and result in lower interval counts than for the off-diagonal elements when using the same interval widths. Where curves were finally identified as shifted the amplitude of $\bar{\Delta}_{ij}$ depends only weakly on w and t.

Finally, the influence of the threshold level is also related to the size of the search radius, i.e. the amount of reference data which is used to estimate the shift values. For increasing search radius, the average similarity of the apparent resistivity curves of the reference and local data reduces. Consequently, $\Delta_{ij}(\omega_k)$-distributions widen and show less pronounced peaks. Hence, a lower threshold level is required to yield a comparable rate of shift recovery.

In summary, recovering static shift in 3D with the AIDE-N method is feasible. For off-diagonal components, identification rates were high and shift amplitude estimation were successfully recovered. Results for diagonal elements suffer from lower spatial coherence of these components. However, when assuming that galvanic distortion is limited to static shift $\bar{\Delta}_{ij}$-estimates obtained from off-diagonal elements can be used for correction of the corresponding diagonal impedances.

4.4 Application to the California MT array

In the California MT array, very few obvious signs of galvanic distortion are observed. At short periods (0.1 - 10 s), off-diagonal apparent resistivities usually differ less than half a decade between components and from site to site. In addition, apparent resistivity curves vary smoothly along-profile in densely sampled areas. Main diagonal elements are usually small at short periods and amplitudes increase towards longer periods. At a few sites, the main diagonal impedances are large at short periods and curves appear intriguingly similar to the corresponding off-diagonal element. However, such clear indications of significant galvanic distortion are limited to few sites (see sec. 3.1; cf. Fig. 3.34).

The 169-site data set of the California MT array is characterised by a variable site spacing of $\sim$2 km in the central parts across the San Andreas fault increasing to about 10 km towards the profile ends (see also sec. 3.1). Hence, the number of references for each local site varies

significantly across the array for constant AIDE-N search radius r (upper panels in Fig. 4.17). Using $r = 5.0$ km reference data can only be found for sites in the densely sampled areas towards the centre of the array (Fig. 4.17a); in the more sparsely sampled areas, search radii have to exceed 10 km (Figs 4.17b-c).

To identify static shift in the California MT array, I applied the AIDE-N scheme with interval width $w = 0.2$, threshold level $t = 0.3$, and three different search radii ($r = 5.0$ km, 12.5 km, 20.0 km). I used the full period range (0.088 - 11,585 s) and required a minimum of $N_{min} = 10$ $\Delta_{ij}(\omega_k)$-estimates at each site. Shift estimates were obtained individually for each of the four impedance components and are displayed in Figure 4.17.

Shift identification rates strongly vary with the search radius and differ between the four components. In general, with increasing search radius, less curves are identified as shifted. In particular, for the diagonal components significantly fewer (12.5 km) or even no (20.0 km) curves were identified as shifted, similar to the previously discussed 3D ObliqueOne data set (cf. Fig. 4.16). Using $r = 5.0$ km, however, shift identification rates for all four components are comparable. Visual inspection of the California MT data confirmed that apparent resistivity curves usually appear similar within ∼5 km and ∼10 km distance from the local site for diagonal and off-diagonal elements, respectively.

Shift estimate amplitudes range mostly between ±0.5 decades for all components independently of the search radius. Where diagonal components were classified as shifted ($r = 5.0$ km), $\bar{\Delta}_{ij}$-amplitudes often match those estimated for the off-diagonal element that is related to the same distortion parameter c_{ii} (solid outlines in Fig. 4.17a). However, shift amplitudes for a particular component and site obtained with different search radii often disagree (Figs 4.17a-b). $\bar{\Delta}_{ij}$-values estimated with $r = 12.5$ km are based on a significantly higher number of reference sites and are assumed to represent a better approximation of the true distortion. Where estimates for $r = 5.0$ km originate from only 1 reference, apparent resistivities of these two sites simply "exchange" their relative shifts. Visual inspection suggests that original and shifted curves obtained for $r = 12.5$ km correspond well to the average resistivity level of close-by sites for both off-diagonal components. Only at few sites obvious misidentifications were discovered.

In regions where the AIDE-N scheme ($r = 12.5$ km) identified high rates of static shift in the array (features A - F in Fig. 4.17b), 3D inversion models of the California data set show significant distortion of surface (< 10 km) structures (A - F in Fig. 4.18a). Where AIDE-N results suggest high shift amplitudes at one or few spatially isolated sites the relative bias of the inversion model resistivities directly beneath the station from the surrounding resistivities corresponds to the sign of shift amplitude (A, B, F in Figs 4.17b and 4.18a). At site 408 (A), for instance, upwards shift of more than a decade was identified for the xy-component and the model structure directly beneath this site is particularly resistive. However, a direct correlation of shift amplitudes and model resistivity structure is not possible, as static shift often results in more complicated model distortions, in particular if the model mesh is coarse (cf. Figs 3.34c-e and 4.1c-d.

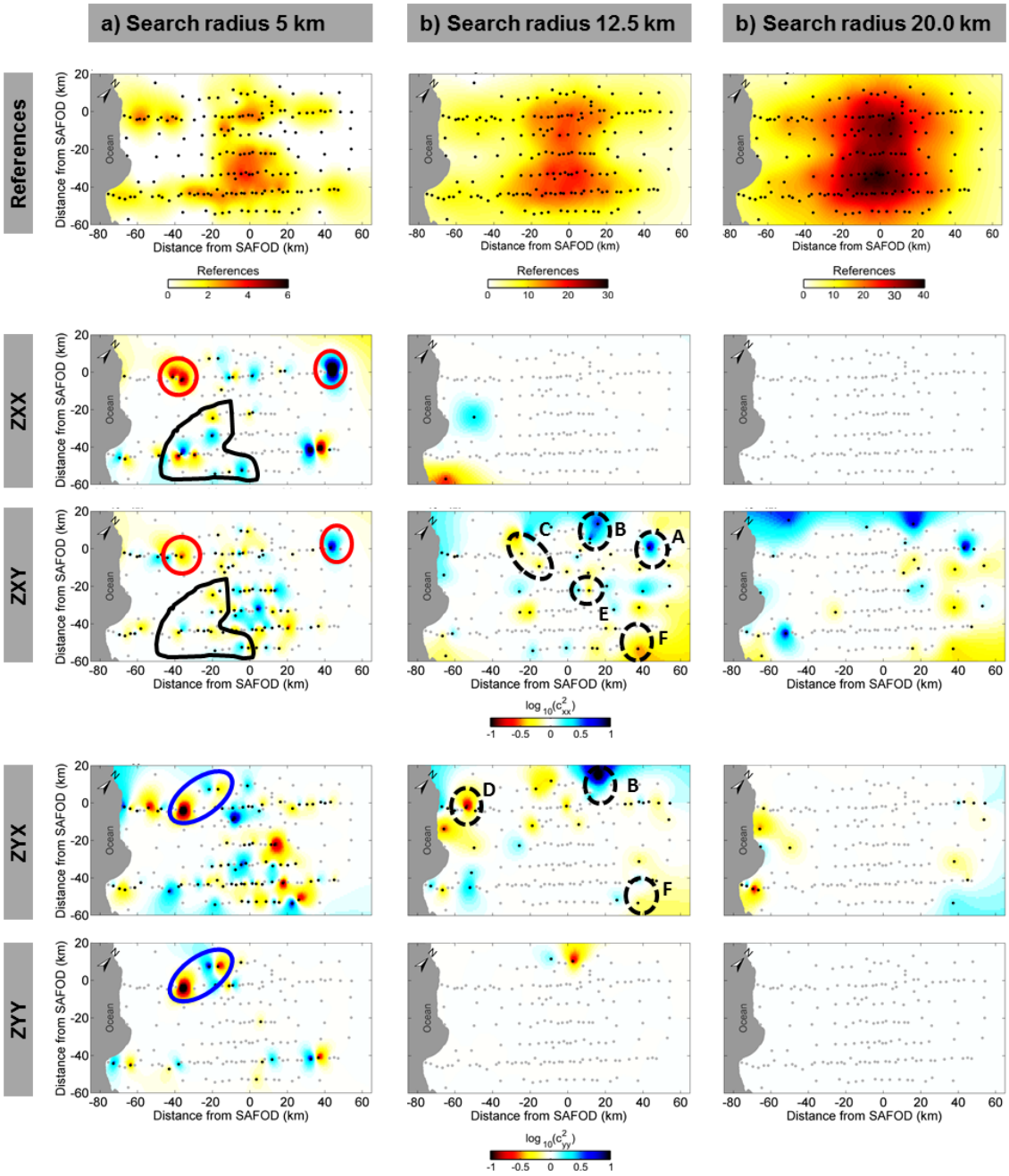

Figure 4.17: Distribution of reference sites (upper row) and AIDE-N shift estimates for the California MT array data set for three different search radii (**(a)-(c)**); $w = 0.2$, $t = 0.3$. For increasing search radius less sites are classified as shifted as curve-similarity decreases. Using a search radius of 5.0 km (a), shift estimates $\bar{\Delta}_{ij}$ obtained from either off-diagonal or main diagonal element (Zxx & Zxy, Zyx & Zyy) are in good agreement (solid oulines in (a)). For $r = 12.5$ km (b), high shift amplitudes and/or presence extended shift clusters (dashed outlines, A-F) corresponds to regions where 3D inversion models of the California data set show significant near-surface distortion (see Fig. 4.18a).

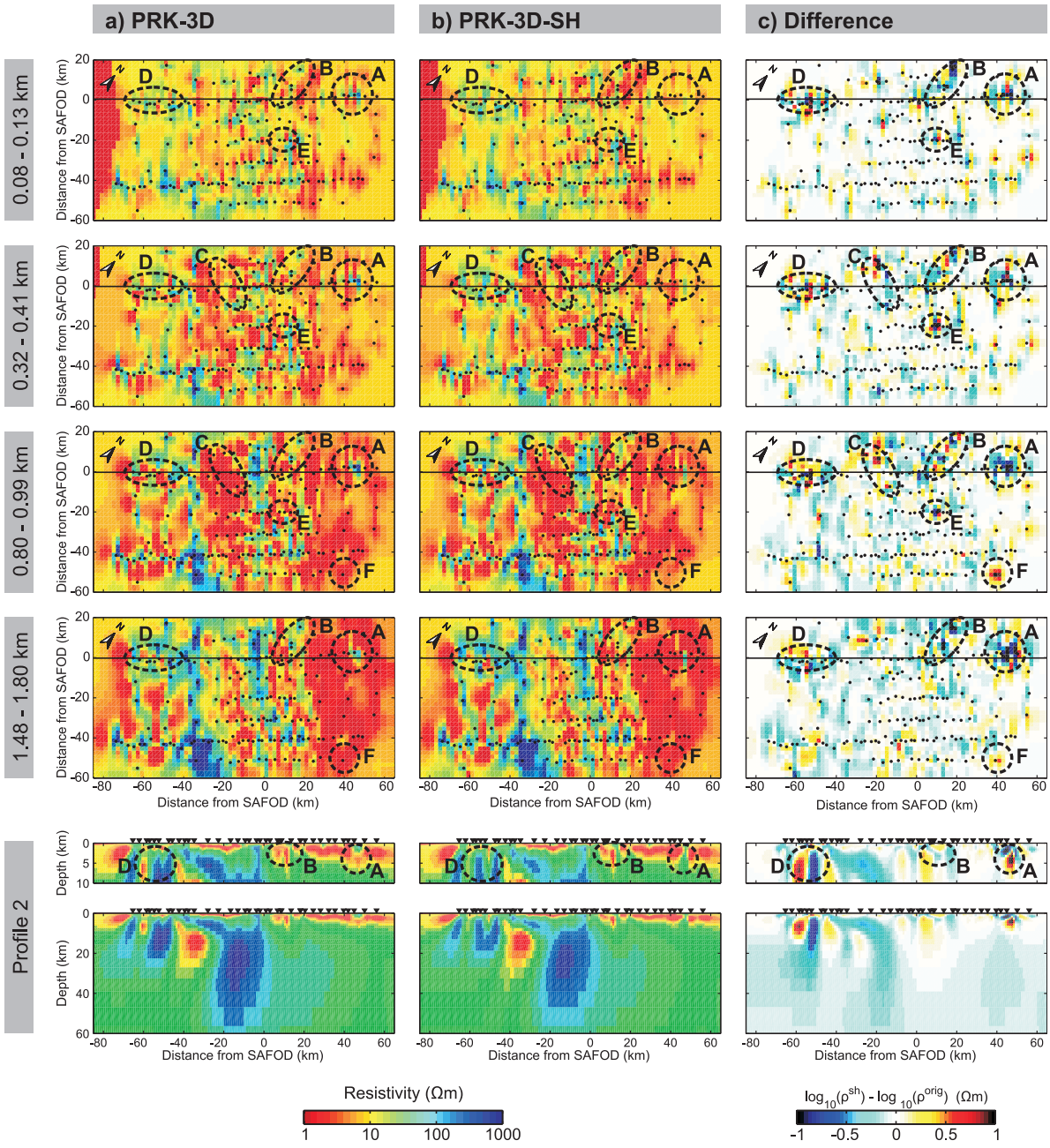

Figure 4.18: Comparison of 3D inversion results for 169-site California data set obtained with **(a)** original (PRK-3D) and **(b)** shift-corrected data (PRK-3D-SH). **(c)** Logarithmic difference between models PRK-3D-SH and PRK-3D; blue colours indicate that the PRK-3D model is more resistive, red colours that it is more conductive than the PRK-3D-SH model. Significant deviations of the new inversion result from the preferred model are mainly restricted to the top 5 km and occur predominantly where data were significantly shifted (features A-F, cf. Fig. 4.17).

Finally, I used the shift estimates obtained for the 12.5 km search radius to correct the impedance data of the California MT array for 3D inversion. To be consistent with the assumption of static shift diagonal components were corrected with the $\bar{c}_{ii}$ estimates obtained from the off-diagonal elements. Subsequently, impedance data were inverted using the same error settings and inversion setup as for the preferred PRK-3D result (see sec. 3.5.5).

Overall, the 3D inversion model obtained with the corrected data set (PRK-3D-SH, Fig. 4.18b) is very similar to the PRK-3D result (Fig. 4.18a), in particular at depths > 10 km. Significant differences occur in the vicinity of sites at which notable shift amplitudes were identified and are limited to the uppermost 2 km to 8 km (labelled A-F in Figs 4.18a-c). In both horizontal directions, features A - F extend over several cells around the shift-corrected sites and illustrate that presence of static shift leads to distortions of surface model structures over large areas.

In regions A, B, and F the structure of the PRK-3D-SH model appears smoother than the PRK-3D result. In particular, the extremely high and low resistivities within feature A which were previously identified as artefacts (cf. Fig. 3.34) were reduced. In region D, where substantial amounts of shift were assigned to a large number of sites, structural differences between the two inversion models extend to more than 10 km depth. However, several sites exhibit signs of more complex galvanic distortion. Model structures in this area and depth range are not well constrained by the data set in general (cf. Fig. 3.34).

The overall misfit of the PRK-3D-SH model (RMS 2.89) is slightly higher than for the original PRK-3D results (RMS 2.61). Closer inspection of PRK-3D-SH inversion responses at each site reveals that data fits of off-diagonal impedance elements as well as long period (T > 10 s) diagonal components are equivalent for both results (Fig. 4.19). Where static shift corrections were small corrections (< 0.5 decades) and data exhibit no obvious signs of severe galvanic distortion also the diagonal elements are similarly well recovered (654, upper panels in Figs 4.19a-b). In presence of more severe galvanic distortion, the diagonal elements are only poorly recovered at periods < 10 s (e.g. site 408, Fig. 4.19b). Surprisingly, I achieved diagonal impedance fits which are compatible with the PRK-3D results for the entire period range if only the off-diagonal impedance elements were corrected for static shift (not shown), although this setup is inconsistent with the assumption of static shift. For these results, the shallow surface structures are imaged slightly differently from the previous setup.

In summary, the AIDE-N method successfully identified sites, where visual inspection of apparent resistivity curves provided indications for the presence of static shift or even more complex galvanic distortion. The estimation of shift amplitudes was satisfying towards the densely sampled central parts of the array where a large number of close-by reference sites was available. Correcting California MT data for static shift prior to 3D inversion, the near-surface structure of resistivity appeared smoother in shift-affected regions. If a large number of sites are more severely distorted, however, estimation of the full four-component distortion matrix should be considered to correct data consistently and obtain reliable subsurface models.

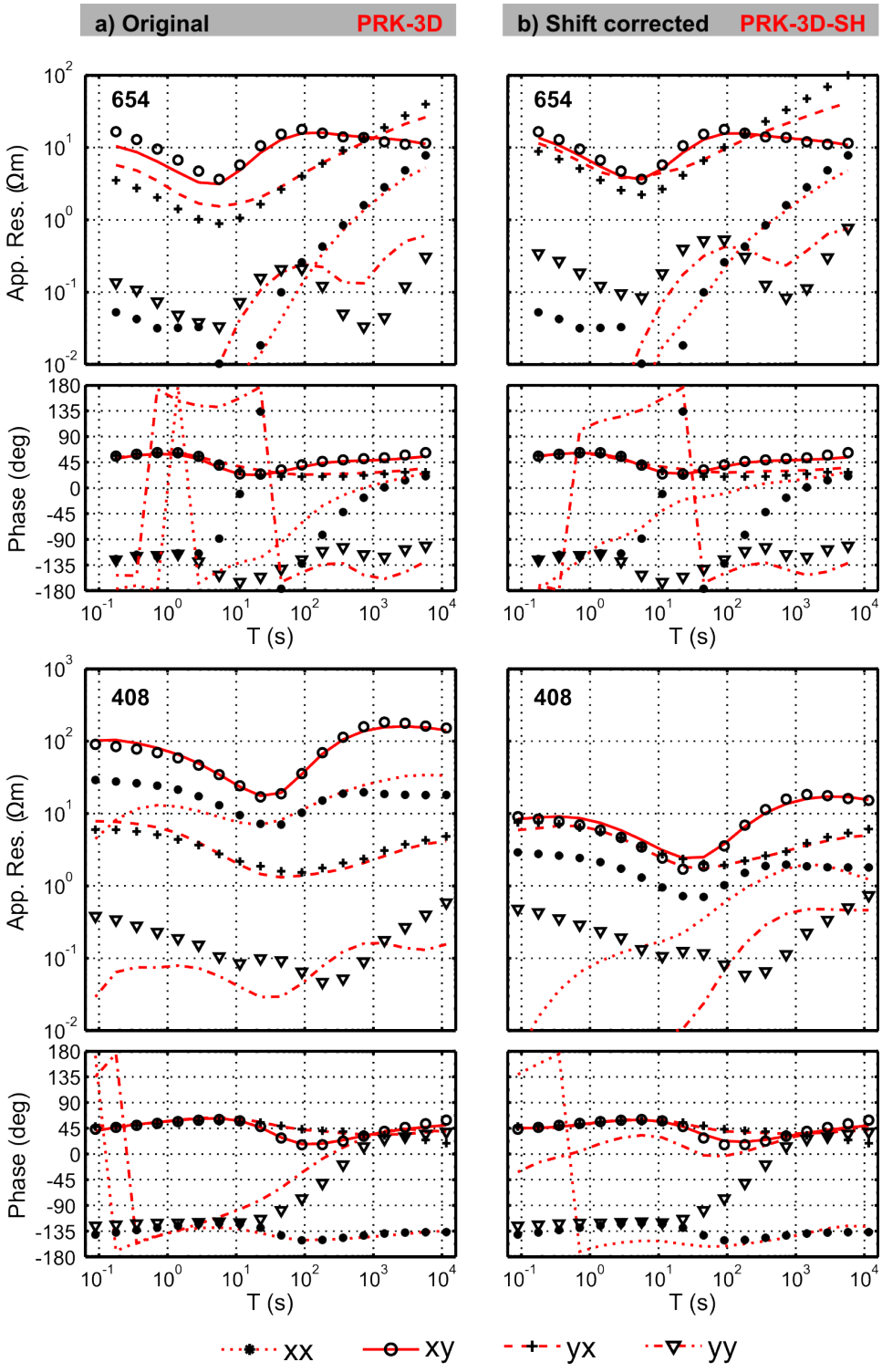

Figure 4.19: Original **(a)** and shift-corrected **(b)** data (symbols) of the California data set and corresponding inversion responses (lines). Sites 654 and 408 are located in zones E and A, respectively (cf. Figs 4.17b, 4.18).

4.5 Discussion

Using 2D and 3D FWD modelling, I was able to simulate down- and upward static shift of apparent resistivities of several decades using conceptual substitute structures for galvanic scatterers. Such structures have to be very small, usually < 10 % of the minimum skin depth, to avoid significant inductive influences on the subsurface response. Thus, when using inversion approaches which assume that static shift is accomodated within the resistivity model by small-scale near-surface structures, model discretization has to be very fine in the vicinity of sites. Otherwise, large-scale artefacts can appear which impair the resolution of the regional conductivity structure. Smoothing routinely applied in minimum structure inversions does not allow for the sharp conductivity contrasts required to produce sensible static shifts.

The newly developed scheme for automatic identification and estimation of static shift (AIDE) was used with close-by MT measurements as reference data (AIDE-N). In tests with synthetic data sets and the California MT array, shift identification and shift amplitude recovery proved successful for 1D to 3D subsurface situations. In general, optimal parameter settings have to be identified individually for each data set and depend most importantly on the dimensionality of subsurface structures, horizontal sampling density of lateral conductivity variations, i.e. MT survey setup, and the statistical properties of shift distribution within the array. In case shift rate is low, shift amplitude estimates can be improved by applying the AIDE-N scheme repeatedly.

In 2D and 3D situations, a suitable search radius, i.e. identification of the coherence scale-length of the survey data, is the most important parameter. Optimal choices are distinct for each of the two (2D) or four (3D) apparent resistivity components as their spatial behaviour is different. In particular, diagonal impedance element amplitudes (3D) change considerably over much shorter distances than the off-diagonal elements. Therefore, successful recovery of diagonal element static shift requires narrow search radii and dense site spacing. In general, absolute shift amplitudes can only be estimated correctly if the neighbouring sites provide a reliable reference. The search radius outlines the trade-off between the aim to include only meaningful – close-by and similar – data and the need for a sufficiently large reference set to avoid bias.

Application of the AIDE-N scheme to the 3D California MT array data set successfully identified subregions of the site array which are affected by static shift and more complex galvanic distortion. Clusters of high shift amplitudes correlate with regions where visual inspection of observed data suggested shift and where near-surface structures of 3D inversion models appear distorted. Shift amplitude estimation was difficult due to the variable site spacing; in densely sampled areas shift values showed good agreement with regional average resistivity levels. 3D inversion of shift-corrected data yielded usually smoother images of the near-surface resistivity structure, particularly where isolated sites were identified as shifted.

In summary, AIDE-N is a useful method for localization of static shift and more severe galvanic distortion for 1D to 3D data sets. Estimation of shift amplitudes is feasible where survey setup provides a reasonable reference data set. Moreover, the AIDE scheme can be combined with other types of reference data such as TEM soundings or responses of inversion models obtained with undistorted data, e.g. phase tensors or vertical magnetic transfer functions.

In case of frequent and severe galvanic distortion, however, more ingenious approaches to data handling are required for 3D inversion to ensure a reliable interpretation of MT data. As pointed out previously, the diagonal impedance components are the most severely biased by galvanic distortion. The inclusion of the diagonal components, however, is the basis for 3D inversion and this additional gain of information is the main advantage over a 2D interpretation. This problem of 3D MT inversion has so far experienced little attention. Several authors estimated full distortion matrices to eliminate distortion prior to inversion (e.g. Heise et al., 2008, 2010; Hill et al., 2009). However, a fundamental problem of this approach is that the equations which describe the effects of galvanic distortion on the impedance tensor are underdetermined. Distortion removal has to be based assumptions that may not be correct and, hence, bears the risk of resulting in inconsistent (inversion) data sets. To tackle complex galvanic distortion comprehensively in 3D situations, I suggest considering the frequency-independent galvanic distortion parameters as four additional unknowns at each site that have to be solved for during the inversion. A similar approach was suggested for 2D by deGroot-Hedlin (1995). Recently, Avdeeva et al. (2012) reported on first experiences of using such a joint inversion strategy and showed promising results. Retrieving distortion parameters within the 3D inversion process promises to be superior to conventional strategies as (i) this approach ensures that the recovered impedance is physically meaningful, (ii) no assumptions and limitations concerning the dimensionality of the subsurface conductivity structure or the galvanic scatterer (cf. Sasaki, 2004; Sasaki & Meju, 2006) are imposed, and (iii) model meshes are kept at practical dimensions.

5 Summary

Three-dimensional (3D) magnetotelluric (MT) inversion of a MT array data set from central California comprising 250+ sites resulted in new insights into the 3D resistivity distribution of the survey area. But at the same time, unexpected issues and pitfalls of application of 3D MT inversion to real-world data sets were revealed. The most significant findings are summarized below.

3D MT inversion

3D MT inversion was systematically tested with respect to model and data setup using the California MT array data and complementary synthetic data sets. In general, optimal inversion parameter settings are specific to the particular data set. However, I could identify crucial parameters which need to be carefully examined to render a comprehensive inversion result as they can interfere with and compromise the recovery of significant regional-scale structures.

Inversion coordinate system. The outcome of 3D inversion is not always independent of the inversion coordinate system even if the full impedance tensor is used. In presence of dominant regional 2D resistivity structures 3D inversion can fail to recover significant large-scale structures of predominantly 2D character. A massive, high-conductive zone (HCZ) extending 100 km or more parallel to strike could only be reliably recovered if data and model grid were aligned with geo-electric strike, in particular for impedance inversion. Strike and dimensionality analyses are essential pre-processing steps for 3D MT inversion and interpretation. Alignment of inversion setup with strike should be considered in the presence of a pronounced geo-electric strike direction.

A priori model. In a number of 3D MT inversion schemes model regularization is based on an a priori model (e.g., Egbert & Kelbert, 2012; Siripunvaraporn et al., 2005), i.e. a priori information is inevitable. The prior model predetermines the average resistivity of the inversion result and, more importantly, can interfere with the large-scale subsurface image, in particular where large conductivity contrasts are present. For the presented data sets, changes of prior model resistivities in the order of few tens of Ωm decided on the recovery of the HCZ at depth. Closer inspection of initial inversion RMS errors can help to constrain appropriate prior model resistivities.

Data weighting. Appropriate data weighting is important to fully exploit the structural information of each inverted data component. To resolve the full 3D structure of the impedance tensor inclusion of the diagonal components is essential. In particular, in presence of large conductivity contrasts data weighting schemes taking relative impedance element sizes into account are required. If subsurface structures are dominated by predominant 2D structures, impedance weighting is facilitated when data are aligned with strike and coupling between components is at its lowest.

Data fit appraisal. For a large number of inversion results similar overall RMS values were obtained although the resistivity models showed significantly differing images of the subsurface. A (low) overall RMS value can disguise significant differences in recovery of data subsets both between various inversion results and within a single data set. Systematic assessment of data fits in the frequency-space domain for each component proved to be an essential and efficient tool to uncover such large-scale structural discrepancies between inversion results and to understand their relation to inversion and/or data setup.

Galvanic distortion

If not considered properly, the effect of galvanic distortion on (3D) MT inversion can be immense and will typically result in erroneous subsurface models. To tackle the problem, I implemented inversion for apparent resistivity & phase and phase tensor data into ModEM3DMT (Egbert & Kelbert, 2012) and developed an automatic static shift estimation scheme (AIDE).

Apparent resistivity & phase inversion. Downweighting apparent resistivities vs. phases is a well-established approach to reduce influence of galvanic distortion on 2D MT inversion results. Here, this approach was applied for the first time to 3D inversion. California and synthetic results showed good results where galvanic distortion is moderate and expressed predominantly as static shift.

Phase tensor inversion. The inversion for distortion-free phase tensor (PT) data, resulted in significantly smoother near-surface structures in the 3D inversion models for the California data set. A challenge, however, is the setup of appropriate starting and prior models as PT data do not contain direct information on absolute subsurface resistivities.

Removal of static shift (AIDE). A newly developed tool based on spatial coherence of densely-sampled MT data which is expressed in similarity of apparent resistivity curves between sites was used to identify and remove randomly distributed galvanic distortion. For the California MT array this approach reduced artificial near-surface structures.

Geo-electric structures in central California

3D inversion and FWD modelling results of the California MT array data set were in general consistent with the 2D results of Becken et al. (2008b, 2011) and could provide new insights into subsurface structures at both shallow and great depth.

Southeastern survey area. In the southeastern part of the survey area, where strong 3D effects are present in the data, extended 3D structures were imaged in the upper 5 km and contrary to the 2D results, the HCZ (20 - 40 km depth) was imaged with continuous along-strike extent beneath the entire survey array. In this area 3D models explain the observed data consistently better than the 2D results.

Deep high-conductive zone. The along-strike extent of the deep high-conductive zone could be constrained with 3D inversion and FWD modelling to measure at least 100 km. Results suggest that the HCZ continues at least 40 km beyond the southeastern edge of the survey array. Towards the northwest, the extent is not resolved by the existing MT data.

Conductive fluid path? The conductive path between the deep HCZ and the SAF was and is an important feature for the interpretation of the data set. Becken et al. (2011) inferred a pathway for fluids from mantle-depth into the SAF system to exist in the northwestern survey area where the SAF exhibits creep. In 3D inversion, such a 3D conductive link was only imaged directly for particular impedance data components but not when inverting for the full impedance tensor or other data types. However, site-by-site inspection of observed and modelled data as well as 3D and 2D FWD modelling and inversion tests with a synthetic model strongly suggest the presence of such a structure.

3D MT interpretation now and into the future

3D MT inversion is already a very useful tool for interpreting large real-world data sets if handled carefully. With expected further advances in computational facilities 3D inversion will become less time-consuming and available to a larger group of MT practitioners. However, it will take some more time until we reach the same level of understanding of 3D inversion with respect to inversion strategies and model uncertainties which we have obtained with 2D modelling and inversion over the past 30 or so years since the first 2D MT codes became available and initiated the transition from 1D to 2D interpretation. While progressing, the experience and knowledge we have already gained should be used in exploiting the advantages of both 3D and 2D inversion.

The 3D MT interpretation approach holds great promise by overcoming the simplifications necessary to force the 3D nature of the real world into 2D models. Future development of 3D MT inversion should, in my opinion, address following aspects: The use of a **model regularization** which is independent of an a priori model. Penalizing only the model roughness, for instance, complies with "Occams razor" while avoiding prior assumptions on average subsurface resistivities. The consideration of **data covariances** within the inversion to account for dependencies between data points. I expect that this reduces the influence of the inversion coordinate system on the inversion outcome and facilitates to transfer the information contained in the various magnetotelluric data components into a comprehensive subsurface image. Further development of strategies to tackle complex **galvanic distortion** comprehensively in 3D situations. This includes new approaches for starting model setup for phase tensor inversion with respect to the conductivity levels, e.g. integration of a priori information from impedance and/or VTF inversion. To fully exploit the capacity of 3D MT data sets for imaging subsurface structures, joint inversion schemes which solve simultaneously for the subsurface conductivity structure and for distortion parameters appear particularly promising.

Bibliography

Argus, D. F. & Gordon, R. G., 2001. Present tectonic motion across the Coast Ranges and San Andreas fault system in central California, *Geol. Soc. Am. Bull.*, **113**(12), 1580–1592.

Argus, D. F. & Heflin, M. B., 1995. Plate Motion and Crustal Deformation Estimated With Geodetic Data From the Global Positioning System, *Geophys. Res. Lett.*, **22**(15), 1973–1976.

Árnason, K., Eysteinsson, H., & Hersir, G. P., 2010. Joint 1D inversion of TEM and MT data and 3D inversion of MT data in the Hengill area, SW Iceland, *Geothermics*, **39**(1), 13–34.

Atwater, T. & Molnar, P., 1973. Relative motion of the Pacific and North American plates deduced from sea-floor spreading in the Atlantic, Indian, and South Pacific Oceans, in *Proceedings of the Conference on Tectonic Problems of the San Andreas fault system*, pp. 136–148.

Atwater, T. & Stock, J., 1998. Pacific-North America Plate Tectonics of the Neogene Southwestern United States: An Update, *Int. Geol. Rev.*, **40**(5).

Avdeev, D. & Avdeeva, A., 2009. 3D magnetotelluric inversion using a limited-memory quasi-Newton optimization, *Geophysics*, **74**, F45–F57.

Avdeeva, A., Moorkamp, M., & Avdeev, D., 2012. Three-dimensional joint inversion of magnetotelluric impedance tensor data and full distortion matrix, in *21st Workshop on Electromagnetic Induction, Darwin (Australia)*.

Bahr, K., 1988. Interpretation of the magnetotelluric impedance tensor: regional induction and local telluric distortion, *J. Geophys.*, **62**, 119–127.

Bahr, K., 1991. Geological noise in magnetotelluric data: a classification of distortion types, *Phys. Earth Planet. In.*, **66**, 24–38.

Bakun, W. H. & Lindh, A. G., 1985. The Parkfield, California, Earthquake Prediction Experiment, *Science*, **229**(4714), 619–624.

Bakun, W. H. & McEvilly, T. V., 1984. Recurrence Models and Parkfield, California, Earthquakes, *J. Geophys. Res.*, **89**(B5), 3051–3058.

Becken, M. & Burkhardt, H., 2004. An ellipticity criterion in magnetotelluric tensor analysis, *Geophys. J. Int.*, **159**(1), 69–82.

Becken, M. & Ritter, O., 2012. Magnetotelluric Studies at the San Andreas Fault Zone: Implications for the Role of Fluids, *Surv. Geophys.*, **33**, 65–105.

Becken, M., Ritter, O., & Burkhardt, H., 2008a. Mode separation of magnetotelluric responses in three-dimensional environments, *Geophys. J. Int.*, **172**, 67–86.

Becken, M., Ritter, O., Park, S. K., Bedrosian, P. A., Weckmann, U., & Weber, M., 2008b. A deep crustal fluid channel into the San Andreas Fault system near Parkfield, California, *Geophys. J. Int.*, **173**(2), 718–732.

Becken, M., Ritter, O., Bedrosian, P. A., & Weckmann, U., 2011. Correlation between deep fluids, tremor and creep along the central San Andreas fault, *Nature*, **480**, 87–90.

Berdichevsky, M. N., Vanyan, L. L., & Dmitriev, V. I., 1989. Methods used in the U.S.S.R. to reduce near-surface inhomogeneity effects on deep magnetotelluric sounding, *Phys. Earth Planet. In.*, **53**(3-4), 194–206.

Bertrand, E. A., Caldwell, T. G., Hill, G. J., Wallin, E. L., Bennie, S. L., Cozens, N., Onacha, S. A., Ryan, G. A., Walter, C., Zaino, A., & Wameyo, P., 2012a. Magnetotelluric imaging of upper-crustal convection plumes beneath the Taupo Volcanic Zone, New Zealand, *Geophys. Res. Lett.*, **39**, L02304.

Bertrand, E. A., Unsworth, M. J., Chiang, C.-W., Chen, C.-S., Chen, C.-C., Wu, F. T., Türkoğlu, E., Hsu, H.-L., & Hill, G. J., 2012b. Magnetotelluric imaging beneath the Taiwan orogen: An arc-continent collision, *J. Geophys. Res.*, **117**, B01402.

Bibby, H. M., Caldwell, T. G., & Brown, C., 2005. Determinable and non-determinable parameters of galvanic distortion in magnetotellurics, *Geophys. J. Int.*, **163**(3), 915–930.

Bird, P., 2003. An updated digital model of plate boundaries, *Geochem. Geophys. Geosyst.*, **4**(3).

Bunge, H.-P. & Grand, S. P., 2000. Mesozoic plate-motion history below the northeast Pacific Ocean from seismic images of the subducted Farallon slab, *Nature*, **405**, 337–340.

Burford, R. O. & Harsh, P. W., 1980. Slip on the San Andreas fault in central California from alinement array surveys, *B. Seismol. Soc. Am.*, **70**(4), 1233–1261.

Bürgmann, R. & Dresen, G., 2008. Rheology of the Lower Crust and Upper Mantle: Evidenve from Rock, Mechanics, Geodesy, and Field Observations, *Annu. Rev. Earth Pl. Sc.*, **36**, 531–567.

Byerlee, J., 1990. Friction, overpressure and fault normal compression, *Geophys. Res. Lett.*, **17**(12), 2109–2112.

Cagniard, L., 1953. Basic theory of the magneto-telluric method of geophysical prospecting, *Geophysics*, **18**(3), 605–635.

Caldwell, T. G., Bibby, H. M., & Brown, C., 2004. The magnetotelluric phase tensor, *Geophys. J. Int.*, **158**(2), 457–469.

Chave, A. & Smith, J. T., 1994. On electric and magnetic galvanic distortion tensor decompositions, *J. Geophys. Res.*, **99**(B3), 4669–4682.

Cumming, W. & Mackie, R., 2010. Resistivity Imaging of Geothermal Resources Using 1D, 2D and 3D MT Inversion and TDEM Static Shift Correction Illustrated by a Glass Mountain Case History, in *Proceedings World Geothermal Congress 2010, Bali, Indonesia*.

deGroot-Hedlin, C., 1991. Removal of static shift in two dimensions by regularized inversion, *Geophysics*, **56**(12), 2102–2106.

deGroot-Hedlin, C., 1995. Inversion for regional 2-D resistivity structure in the presence of galvanic scatterers, *Geophys. J. Int.*, **122**, 877–888.

DeMets, C., Gordon, R. G., Argus, D. F., & Stein, S., 1990. Current plate motions, *Geophys. J. Int.*, **101**, 425–478.

Dickinson, W. R., 1997. Tectonic implications of Cenozoic volcanism in coastal California, *Geol. Soc. Am. Bull.*, **109**(8), 936–954.

Dickinson, W. R. & Snyder, W. S., 1979a. Geometry of subducted slabs related to San Andreas Transform, *J. Geol.*, **87**, 609–627.

Dickinson, W. R. & Snyder, W. S., 1979b. Geometry of Triple Junctions related to San Andreas Transform, *J. Geophys. Res.*, **84**(B2), 561–572.

Dubrovine, P. V. & Tarduno, J. A., 2008. A revised kinematic model for the relative motion between Pacific oceanic plates and North America since the Late Cretaceous, *J. Geophys. Res.*, **113**, B12101.

Egbert, G. D., 1997. Robust multiple-station magnetotelluric data processing, *Geophys. J. Int.*, **130**(2), 475–496.

Egbert, G. D. & Booker, J. R., 1986. Robust estimation of geomagnetic transfer functions, *Geophys. J. R. astr. Soc.*, **87**, 173–194.

Egbert, G. D. & Kelbert, A., 2012. Computational recipes for electromagnetic inverse problems, *Geophys. J. Int.*, **189**(1), 251–267.

Ellsworth, W. L., 1990. Earthquake History 1769 – 1989, in *The San Andreas fault system, California: U.S. Geological Survey Professional Paper*, vol. 1515, pp. 153–187, U.S. Geological Survey.

Engebretson, D. C. & Cox, A., 1984. Relative Motions Between Oceanic Plates of the Pacific Basin, *J. Geophys. Res.*, **89**(B12), 10291–10310.

Farquharson, C., Oldenburg, D., Haber, E., & Shekhtman, R., 2002. An algorithm for the three-dimensional inversion of magnetotelluric data, in *Proceedings of the 72nd Annual International Meeting, SEG, Expanded Abstracts*, pp. 649–652.

Farquharson, C. G. & Craven, J. A., 2009. Three-dimensional inversion of magnetotelluric data for mineral exploration: An example from the McArthur River uranium deposit, Saskatchewan, Canada, *J. Appl. Geophys.*, **68**(4), 450–458.

Fulton, P. M. & Saffer, D. M., 2009. Potential role of mantle-derived fluids in weakening the San Andreas Fault, *J. Geophys. Res.*, **114**(B7), 1–15.

Ghosh, A., Vidale, J. E., Peng, Z., Creager, K. C., & Houston, H., 2009. Complex nonvolcanic tremor near Parkfield, California, triggered by the great 2004 Sumatra earthquake, *J. Geophys. Res.*, **114**, B00A15.

Gordon, R. G. & Jurdy, D. M., 1986. Cenozoic Global Plate Motions, *J. Geophys. Res.*, **91**(B12), 12389–12406.

Groom, R. W. & Bahr, K., 1992. Corrections for near surface effects: Decomposition of the magnetotelluric impedance tensor and scaling correction for regional resistivities: a tutorial, *Surv. Geophys.*, **13**, 341–379.

Groom, R. W. & Bailey, R. C., 1989. Decomposition of Magnetotelluric Impedance Tensors in the Presence of Local Three-Dimensional Galvanic Distortion, *J. Geophys. Res.*, **94**(B2), 1913–1925.

Guéguen, Y. & Palciauskas, V., 1994. *Introduction to the Physics of Rocks*, Princeton University Press.

Han, N., Nam, M. J., Kim, H. J., Song, Y., & Suh, J. H., 2009. A comparison of accuracy and computation time of three-dimensional magnetotelluric modelling algorithms, *J. Geophys. Eng.*, **6**(2), 136–145.

He, Z., Hu, Z., Luo, W., & Wang, C., 2010. Mapping reservoirs based on resistivity and induced polarization derived from continuous 3D magnetotelluric profiling: Case study from Qaidam basin, China, *Geophysics*, **75**, F25–F33.

Heise, W., Caldwell, T. G., Bibby, H. M., & Bannister, S. C., 2008. Three-dimensional modelling of magnetotelluric data from the Rotokawa geothermal field, Taupo Volcanic Zone, New Zealand, *Geophys. J. Int.*, **173**(2), 740–750.

Heise, W., Caldwell, G., T., M., B. H., & Bennie, S. L., 2010. Three-dimensional electrical resistivity image of magma beneath an active continental rift, Taupo Volcanic Zone, New Zealand, *Geophys. Res. Lett.*, **37**, L10301.

Hickman, S., Zoback, M., & Ellsworth, W., 2004. Introduction to special section: Preparing for the San Andreas Fault Observatory at Depth, *Geophys. Res. Lett.*, **31**(12), 10–13.

Hickman, S., Zoback, M., Ellsworth, W., Boness, N., Malin, P., Roeckner, S., & Thurber, C., 2007. Strucutre and Properties of the San Andreas Fault in Central California: Recent Results from the SAFOD Experiment, *Scientific Drilling Special Issue No. 1*, pp. 29–32.

Hill, D. P., Eaton, J. P., & Jones, L. M., 1990. Seismicity, 1980-86, in *The San Andreas fault system, California: U.S. Geological Survey Professional Paper*, vol. 1515, pp. 115–151, U.S. Geological Survey.

Hill, G. J., Caldwell, T. G., Heise, W., Chertkoff, D. G., Bibby, H. M., Burgess, M. K., Cull, J. P., & Cas, R. A. F., 2009. Distribution of melt beneath Mount St Helens and Mount Adams inferred from magnetotelluric data, *Nature Geosci.*, **2**(11), 785–789.

Hole, J. A., Ryberg, T., Fuis, G. S., Bleibinhaus, F., & Sharma, A. K., 2006. Structure of the San Andreas fault zone at SAFOD from a seismic refraction survey, *Geophys. Res. Lett.*, **33**(7), 2–5.

Hubbert, M. K. & Rubey, W. W., 1959. Role of fluid pressure in mechanics of overthrust faulting, *B. Seismol. Soc. Am.*, **70**, 116–166.

Ingham, M. R., Bibby, H. M., Heise, W., Jones, K. A., Cairns, P., Dravitzki, S., Bennie, S. L., Caldwell, T. G., & Ogawa, Y., 2009. A magnetotelluric study of Mount Ruapehu volcano, New Zealand, *Geophys. Res. Lett.*, **179**, 887–904.

Irwin, W. P., 1990. Geology and plate-tectonic development, in *The San Andreas fault system, California: U.S. Geological Survey Professional Paper*, vol. 1515, pp. 61–80, U.S. Geological Survey.

Irwin, W. P. & Barnes, I., 1975. Effect of geologic structure and metamorphic fluids on seismic behavior of the San Andreas fault system in central and northern California, *Geology*, **3**(12), 713–716.

Jiracek, G. R., 1990. Near-surface and topographic distortions in electromagnetic inductions, *Surv. Geophys.*, **11**, 163–203.

Jiracek, G. R., Gonzalez, V. M., Caldwell, T. G., Wannamaker, P. E., & Kilb, D., 2007. Seismogenic, electrically conductive, and fluid zones at continental plate boundaries in New Zealand, Himalaya, and California, USA, in *A continental plate boundary: tectonics at South Island, New Zealand Geophysical Monogaph Series AGU*, vol. 153, pp. 347–369, eds Okaya, D., Stern, T., & Davey, F.

Johnson, P. A. & McEvilly, T. V., 1995. Parkfield seismicity : Fluid-driven ?, *J. Geophys. Res.*, **100**(B7), 937–950.

Jones, A., 2011. Three-dimensional galvanic distortion of three-dimensional regional conductivity structures: Comment on Three-dimensional joint inversion for magnetotelluric resistivity and static shift distributions in complex media by Yutaka Sasaki and Max A. Meju, *J. Geophys. Res.*, **116**, B12104.

Jones, A. G., 1988. Stafic shift of magnetotelluric data and its removal in a sedimentary basin environment, *Geophysics*, **53**(7), 967–978.

Kaufmann, A. A., 1985. Distribution of alternating electrical charges in a conducting medium, *Geophys. Prospect.*, **33**, 171–184.

Kelbert, A., Egbert, G. D., & deGroot Hedlin, C., 2012. Crust and upper mantle electrical conductivity beneath the Yellowstone Hotspot Track, *Geology*, **40**(5), 447–450.

Kennedy, B. M., Kharaka, Y. K., Evans, W. C., Ellwood, A., DePaolo, D. J., Thordsen, J., G., A., & Mariner, R. H., 1997. Mantle Fluids in the San Andreas Fault System, California, *Science*, **278**(5341), 1278–1281.

Langbein, J., Borcherdt, R., Dreger, D., Fletcher, J., Hardebeck, J. L., Hellweg, M., Ji, C., Johnston, M., Murray, J. R., Nadeau, R., Rymer, M. J., & Treiman, J. A., 2005. Preliminary Report on the 28 September 2004 M 6.0 Parkfield, California Earthquake, *Seismol. Res. Lett.*, **76**(6), 10–26.

Lawson, A. C., 1895. Sketch of the geology of the San Francisco peninsula, in *U.S. Geological Survey Annual Report*, vol. 15, pp. 439–473, U.S. Geological Survey.

Ledo, J. & Gab, A., 2002. Static shift levelling using geomagnetic transfer functions, *Earth Planets Space*, **54**(1), 493–498.

Lisowski, M. & Prescott, W. H., 1981. Short-range distance measurements along the San Andreas fault system in central California, 1975 to 1979, *B. Seismol. Soc. Am.*, **71**(5), 1607–1624.

Liu, L., Spasojević, S., & Gurnis, M., 2008. Reconstructing Farallon Plate Subduction Beneath North America Back to the Late Cretaceous, *Science*, **322**, 934–938.

Mackie, R. L. & Madden, T. R., 1993. Three-dimensional magnetotelluric inversion using conjugate gradients, *Geophys. J. Int.*, **115**, 215–229.

Mackie, R. L., Rodi, W., & Watts, M. D., 2001. 3-D magnetotelluric inversion for resource exploration, in *Proceedings of the 71st Annual International Meeting, SEG, Expanded Abstracts*, pp. 1501–1504.

Matthews, V. I., 1976. Correlation of Pinnacles and Neenach Volcanic Formations and their bearing on San Andreas fault problem, *Am. Assoc. Petrol. Geol. Bull.*, **60**, 2128–2141.

McCrory, P. A., Wilson, D. S., & Stanley, R. G., 2009. Continuing evolution of the Pacific-Juan de Fuca-North America slab window system – A trench-ridge-transform example from the Pacific Rim, *Tectonophysics*, **464**, 30–42.

McNeice, G. W. & Jones, A., 2001. Multisite, multifrequency tensor decomposition of magnetotelluric data, *Geophysics*, **66**(1), 158–173.

McPhee, D. K., 2004. Crustal structure across the San Andreas Fault at the SAFOD site from potential field and geologic studies, *Geophys. Res. Lett.*, **31**(12), 10–13.

Menvielle, M., 1988. Effects of crustal conductivity heterogeneities on the electromagnetic field, *Surv. Geophys.*, **9**, 319–348.

Meqbel, N., 2009. *The electrical conductivity structure of the Dead Sea Basin derived from 2D and 3D inversion of magnetotelluric data*, Ph.D. thesis, Free University Berlin.

Minster, J. B. & Jordan, T. H., 1987. Vector Constraints on Western U.S. Deformation from Space Geodesy, Neotectonics, and Plate Motions, *J. Geophys. Res.*, **92**(B10), 4798–4804.

Moore, D. E. & Rymer, M. J., 2007. Talc-bearing serpentinite and the creeping section of the San Andreas fault., *Nature*, **448**(7155), 795–7.

Nadeau, R. M. & Dolenc, D., 2005. Nonvolcanic tremors deep beneath the San Andreas Fault., *Science*, **307**(5708), 389.

Nadeau, R. M. & Guilhem, A., 2009. Nonvolcanic Tremor Evolution and the San Simeon and Parkfield, California, Earthquakes, *Science*, **325**, 191–193.

Newman, G. A. & Alumbaugh, D. L., 1997. Three-dimensional massively parallel electromagnetic inversion-I. Theory, *Geophys. J. Int.*, **128**(2), 345–354.

Newman, G. A. & Alumbaugh, D. L., 2000. Three-dimensional magnetotelluric inversion using non-linear conjugate gradients, *Geophys. J. Int.*, **140**(2), 410–424.

Newman, G. A., Gasperikova, E., Hoversten, G. M., & Wannamaker, P. E., 2008. Three-dimensional magnetotelluric characterization of the Coso geothermal field, *Geothermics*, **37**, 369–399.

Nicholson, C., Sorlien, C. C., Atwater, T., Crowell, J. C., & Luyendyk, B. C., 1994. Microplate Capture, rotation of the western Transverse Ranges, and initiation of the San Andreas transform as low-angle fault system, *Geology*, **22**, 491–495.

Ogawa, Y. & Uchida, T., 1996. A two-dimensional magnetotelluric inversion assuming Gaussian static shift, *Geophys. J. Int.*, **126**(1), 69–76.

Olsen, K. B., Day, S. M., Minster, J. B., Cui, Y., Chourasia, A., Faerman, M., Moore, R., Maechling, P., & Jordan, T., 2006. Strong shaking in Los Angeles expected from southern San Andreas earthquake, *Geophys. Res. Lett.*, **33**.

Page, B. M., Thompson, G. A., & Coleman, R. G., 1998. Late Cenozoic tectonics of the central and southern Coast Ranges of California, *Geol. Soc. Am. Bull.*, **110**(7), 846–876.

Parkinson, W. D., 1959. Directions of Rapid Geomagnetic Fluctuations, *Geophys. J. Roy. Ast. Soc.*, **2**(1), 1–14.

Patro, P. K. & Egbert, G. D., 2008. Regional conductivity structure of Cascadia: Preliminary results from 3D inversion of USArray transportable array magnetotelluric data, *Geophys. Res. Lett.*, **35**(20), 1–5.

Patro, P. K. & Egbert, G. D., 2011. Application of 3-D inversion to magnetotelluric profile data from the Deccan Volcanic Province of Western India, *Phys. Earth Planet. In.*, **187**, 33–46.

Peng, Z., Vidale, J. E., Creager, K. C., Rubinstein, J. L., Gomberg, J., & Bodin, P., 2008. Strong tremor near Parkfield, CA, excited by the 2002 Denali Fault earthquake, *Geophys. Res. Lett.*, **35**, L23305.

Peng, Z., Vidale, J. E., Wech, A. G., Nadeau, R. M., & Creager, K. C., 2009. Remote triggering of tremor along the San Andreas Fault in central California, *J. Geophys. Res.*, **114**, B00A06.

Pili, É., Kennedy, B. M., Conrad, M. E., & Gratier, J.-P., 2010. Isotopic evidence for the infiltration of mantle and metamorphic CO2-H2O fluids from below in faulted rocks from the San Andreas Fault system, *Chem. Geol.*, **281**(3-4), 242–252.

Powell, R. E. & Weldon, R. J. I., 1992. Evolution of the San Andreas fault, *Annu. Rev. Earth Planet. Sci.*, **20**, 431–468.

Price, A. T., 1973. The theory of geomagnetic induction, *Phys. Earth Planet. In.*, **7**, 227–233.

Rice, J. R., 1992. Fault Stress States, Pore Pressure Distributions, and the Weakness of the San Andreas Fault, in *Fault Mechanics and Transport Properties of Rocks*, vol. 1487, pp. 475–503, eds Evans, B. & Wong, T.-F., Academic Press, San Diego.

Ritter, O., Junge, A., & Dawes, G., 1998. New equipment and processing for magnetotelluric remote reference observations, *Geophys. J. Int.*, **132**(3), 535–548.

Ritter, O., Weckmann, U., Vietor, T., & Haak, V., 2003. A magnetotelluric study of the Damara Belt in Namibia 1. Regional scale conductivity anomalies, *Phys. Earth Planet. In.*, **138**(2), 71–90.

Rodi, W. & Mackie, R. L., 2001. Nonlinear conjugate gradients algorithm for 2-D magnetotelluric inversion, *Geophysics*, **66**, 174–187.

Ryberg, T., Haberland, C., Fuis, G. S., Ellsworth, W. L., & Shelly, D. R., 2010. Locating non-volcanic tremor along the San Andreas Fault using a multiple array source imaging technique, *Geophys. J. Int.*, **183**(3), 1485–1500.

Sasaki, Y., 2001. Full 3-D inversion of electromagnetic data on PC, *J. Appl. Geophys.*, **46**(1), 45–54.

Sasaki, Y., 2004. Three-dimensional inversion of static-shifted magnetotelluric data, *Earth Planets Space*, **56**, 239–248.

Sasaki, Y. & Meju, M. A., 2006. Three-dimensional joint inversion for magnetotelluric resistivity and static shift distributions in complex media, *J. Geophys. Res.*, **111**(B5), 1–11.

Sass, J. H., Williams, C. F., Lachenbruch, A. H., Galanis, S. P. J., & Grubb, F. V., 1997. Thermal regime of the San Andreas fault near Parkfield, *J. Geophys. Res.*, **102**(B12), 27575–27585.

Schellart, W. P., Stegman, D. R., Farrington, R. J., Freeman, J., & Moresi, L., 2010. Cenozoic Tectonics of Western North America Controlled by Evolving Width of Farallon Slab, *Science*, **329**, 316–319.

Schleicher, A. M., van der Pluijm, B. A., & Warr, L. N., 2010. Nanocoatings of clay and creep of the San Andreas fault at Parkfield, California, *Geology*, **38**(7), 667–670.

Schmucker, U., 1987. Substitute conductors for electromagnetic response estimates, *Pure Appl. Geophys.*, **125**(2/3), 341–367.

Scholz, C. H., 2002. *The mechanics of earthquakes and faulting*, Cambridge University Press, 2nd edn.

Segall, P. & Harris, R., 1987. Earthquake Deformation Cycle on the San Andreas Fault Near Parkfield, California, *J. Geophys. Res.*, **92**(B10), 10511–10525.

Shelly, D. R., 2010. Migrating tremors illuminate complex deformation beneath the seismogenic San Andreas fault., *Nature*, **463**(7281), 648–52.

Shelly, D. R. & Hardebeck, J. L., 2010. Precise tremor source locations and amplitude variations along the lower-crustal central San Andreas Fault, *Geophys. Res. Lett.*, **37**(14), 1–5.

Shelly, D. R., Ellsworth, W. L., Ryberg, T., Haberland, C., Fuis, G. S., Murphy, J., Nadeau, R. M., & Bürgmann, R., 2009. Precise location of San Andreas Fault tremors near Cholame, California using seismometer clusters: Slip on the deep extension of the fault?, *Geophys. Res. Lett.*, **36**(1).

Sieh, K. E. & Jahn, R. H., 1984. Holocene activity of the San Andreas fault at Wallace Creek, California, *Geol. Soc. Am. Bull.*, **95**, 883–896.

Singer, B. S., 1992. Correction for distortions of magnetotelluric fields: limits of validity of the static approach, *Surv. Geophys.*, pp. 309–340.

Siripunvaraporn, W. & Egbert, G. D., 2009. WSINV3DMT: Vertical magnetic field transfer function inversion and parallel implementation, *Phys. Earth Planet. In.*, **173**(3-4), 317–329.

Siripunvaraporn, W., Egbert, G. D., Lenbury, Y., & Uyeshima, M., 2005. Three-dimensional magnetotelluric inversion: data-space method, *Phys. Earth Planet. In.*, **150**(1-3), 3–14.

Sternberg, B. K., Washburne, J. C., & Pellerin, L., 1988. Correction for the static shift in magnetotellurics using transient electromagnetic soundings, *Geophysics*, **53**(11), 1459–1468.

Stock, J. & Molnar, P., 1988. Uncertainties and implications of the late Cretaceous and Tertiary position of North America relative to the Farallon, Kula, and Pacific plates, *Tectonics*, **7**(6), 1339–84.

Tauber, S., Banks, R., Ritter, O., & Weckmann, U., 2003. A high-resolution magnetotelluric survey of the Iapetus Suture Zone in southwest Scotland, *Geophys. J. Int.*, **153**, 548–568.

Thatcher, W., 1990. Present-day crustal movements and the mechanics of cyclic deformation, in *The San Andreas fault system, California: U.S. Geological Survey Professional Paper*, vol. 1515, pp. 189–205, U.S. Geological Survey.

Thomas, A. M., Nadeau, R. M., & Bürgmann, R., 2009. Tremor-tide correlations and near-lithostatic pore pressure on the deep San Andreas fault., *Nature*, **462**(7276), 1048–51.

Thurber, C., Zhang, H., Waldhauser, F., Hardebeck, J., Michael, A., & Eberhart-Phillips, D., 2006. Three-Dimensional Compressional Wavespeed Model, Earthquake Relocations, and Focal Mechanisms for the Parkfield, California, Region, *B. Seismol. Soc. Am.*, **4B**(96), S38–S49.

Tikhonov, A. N., 1950. On determining electrical characteristics of the deep layers of the earth's crust, *Dokl. Akad. Nauk SSSR*, **73**(2), 295–297.

Titus, S. J., DeMets, C., & Tikoff, B., 2006. Thirty-Five-Year Creep Rates for the Creeping Segment of the San Andreas Fault and the Effects of the 2004 Parkfield Earthquake: Constraints from Alignment Arrays, Continuous Global Positioning System, and Creepmeters, *B. Seismol. Soc. Am.*, **96**(4B), S250–S268.

Toppozada, T. R., Branum, D. M., Reichle, M. S., & Hallstrom, C. L., 2002. San Andreas Fault Zone, California: M $\geq$ 5.5 Earthquake History, *B. Seismol. Soc. Am.*, **92**, 2555–2601.

Torres-Verdín, C. & Bostick, F. X. J., 1992. Principles of spatial surface electric field filtering in magnetotellurics: Electromagnetic array profiling (EMAP), *Geophysics*, **57**(4), 603.

Tournerie, B., Chouteau, M., & Marcotte, D., 2007. Magnetotelluric static shift: Estimation and removal using the cokriging method, *Geophysics*, **72**(1), F25.

Tuncer, V., Unsworth, M. J., Siripunvaraporn, W., & Craven, J. A., 2006. Exploration for unconformity-type uranium deposits with audiomagnetotelluric data: A case study from the McArthur River mine, Saskatchewan, Canada, *Geophysics*, **71**(6), B201–B209.

Türkoğlu, E., Unsworth, M., & Pana, D., 2009. Deep electrical structure of northern Alberta (Canada): implications for diamond exploration, *Can. J. Earth Sci.*, **46**, 139–154.

Unsworth, M., 2010. Magnetotelluric Studies of Active Continent-Continent Collisions, *Surv. Geophys.*, **31**, 137–161.

Unsworth, M. J. & Bedrosian, P. A., 2004. Electrical resistivity structure at the SAFOD site from magnetotelluric exploration, *Geophys. Res. Lett.*, **31**(12), 10–13.

Unsworth, M. J., Malin, P. E., Egbert, G. D., & Booker, J. R., 1997. Internal structure of the San Andreas fault at Parkfield, California, *Geology*, **25**(4), 359.

Unsworth, M. J., Egbert, G. D., & Booker, J. R., 1999. High-resolution electromagnetic imaging of the San Andreas fault in Central California, *J. Geophys. Res.*, **104**(B1), 1131–1150.

Usui, T., Nakamura, E., Kobayashi, K., Maruyama, S., & Helmstaedt, H., 2003. Fate of the subducted Farallon plate inferred from eclogite xenoliths in the Colorado Plateau, *Geology*, **31**(7), 589–592.

ed. Wallace, R. E., 1990. *The San Andreas fault system, California: U.S. Geological Survey Professional Paper 1515*, U.S. Geological Survey.

Ward, S. H. & Hohmann, D. W., 1987. Electromagnetic theory for geophysical applications, in *Electromagnetic Methods in Applied Geophysics*, vol. 1, pp. 131–311, ed. Nabighian, M. N., SEG.

Ward, S. N., 1990. Pacific-North America Plate Motions: New Results From Very Long Baseline Interferometry, *J. Geophys. Res.*, **40**(B13).

Weckmann, U., Magunia, A., & Ritter, O., 2005. Effective noise separation for magnetotelluric single site data processing using a frequency domain selection scheme, *Geophys. J. Int.*, **161**(3), 635–652.

West, G. F. & Edwards, R. N., 1985. A simple parametric model for the electromagnetic response of an anomalous body in a host medium, *Geophysics*, **50**(12), 2542–57.

Wiersberg, T. & Erzinger, J., 2007. A helium isotope cross-section study through the San Andreas Fault at seismogenic depths, *Geochem. Geophys. Geosyst.*, **8**(1), 1–12.

Wiersberg, T. & Erzinger, J., 2008. Origin and spatial distribution of gas at seismogenic depths of the San Andreas Fault from drill-mud gas analysis, *Appl. Geochem.*, **23**(6), 1675–1690.

Wiersberg, T. & Erzinger, J., 2011. Chemical and isotope compositions of drilling mud gas from the San Andreas Fault Observatory at Depth (SAFOD) boreholes: Implications on gas migration and the permeability structure of the San Andreas Fault, *Chem. Geol.*, **284**, 148–159.

Wiese, H., 1962. Geomagnetische Tiefentellurik Teil II: Die Streichrichtung der untergrundstrukturen des elektrischen Widerstandes, erschlossen aus geomagnetischen Variationen, *Pure Appl. Geophys.*, **52**, 83–103.

Wilson, D. S., McCrory, P. A., & Stanley, R. G., 2005. Implications of volcanism in coastal California for the Neogene deformation history of western North America, *Tectonics*, **24**, TC3008.

Working Group on California Earthquake Probabilities, 1995. Seismic Hazards in Southern California: Probable Earthquakes, 1994 to 2024, *B. Seismol. Soc. Am.*, **85**(2).

Xiao, Q., Cai, X., Xu, X., Liang, G., & Zhang, B., 2010. Application of the 3D magnetotelluric inversion code in a geologically complex area, *Geophys. Prospect.*, **58**(6), 1177–1192.

Yerkes, R. F., Levine, P., & Wentworth, C., 1985. Abnormally high fluid pressures in the region of the Coalinga earthquake sequence and their significance, in *The Coalinga, California, Earthquake of May 2, 1983: U.S. Geological Survey Professional Paper*, vol. 1487, pp. 235–257, U.S. Geological Survey.

Zhang, H., Nadeau, R. M., & Toksoz, M. N., 2010. Locating nonvolcanic tremors beneath the San Andreas Fault using a station-pair double-difference location method, *Geophys. Res. Lett.*, **37**, L13304.

Zhao, D., Kanamori, H., & Humphreys, E., 1996. Simultaneous inversion of local and teleseismic data for the crust and mantle structure of southern California, *Phys. Earth Planet. In.*, **93**, 191–214.

Zhdanov, M. S., Fang, S., & Hursán, G., 2000. Electromagnetic Inversion using Quasi-Analytical Approximation, *Geophysics*, **65**, 1501–1513.

Zhdanov, M. S., Green, A., Gribenko, A., & Cuma, M., 2010. Large-scale three-dimensional inversion of EarthScope MT data using the integral equation method, *Phys. Solid Earth. Izv. Akad. Nauk SSSR*, **46**(8), 670–678.

Zoback, M., Hickman, S., Ellsworth, W., & the SAFOD Science Team, 2011. Scientific Drilling Into the San Andreas Fault Zone – An Overview of the SAFOD's First Five Years, *Scientific Drilling*, **11**, 14–28.

Zoback, M. D., 2006. SAFOD penetrates the San Andreas Fault, *Scientific Drilling*, **2**, 32–33.

Curriculum Vitae

For reasons of data protection, the curriculum vitae is not included in the online version.

Aus Gründen des Datenschutzes erscheint der Lebenslauf nicht in der elektronischen Fassung.

Publications and conference paper

Tietze, K. & Ritter, O., 2012. 3D magnetotelluric inversion in practice, *Geophys. J. Int., in rev.*

Weckmann, U., Ritter, O., Chen, X., **Tietze, K.**, & de Wit, M., 2012. Magnetotelluric image linked to surface geology across the Cape Fold Belt, South Africa, *Terra Nova*, **24**(3), 207–212.

Tietze, K. & Ritter, O., 2012. 3D magnetotelluric inversion in practice, *21st IAGA WG 1.2 Workshop on Electromagnetic Induction in the Earth*, Darwin (Australia).

Tietze, K. & Ritter, O., 2012. 3D magnetotelluric inversion in presence of a 2D regional conductivity structure, *72nd annual meeting of the German Geophysical Society (DGG)*, Hamburg (Germany).

Tietze, K. & Ritter, O., 2012. Resolution of 3D elongated deep conductive bodies embedded in a 2D background conductivity structure by 3D and 2D magnetotelluric inversion, *Proceedings of the 24th Schmucker-Weidelt-Colloquium on Electromagnetic Depth Sounding*, Neustadt / Weinstr. (Germany).

Weckmann, U. & **Tietze, K.**, 2011. On the Applicability of 3D Magnetotelluric Inversion to Real World Data Sets, *General Assembly International Union of Geodesy and Geophysics*, Melbourne (Australia), *invited*.

Tietze, K. & Ritter O., 2011. Large conductors at the San Andreas fault go missing and reappear – experiences with 3D magnetotelluric inversion, *24th Schmucker-Weidelt-Colloquium on Electromagnetic Depth Sounding*, Neustadt / Weinstr. (Germany).

Tietze, K., Ritter O., & Becken, M., 2010. Magnetotelluric 3D inversion models from the San Andreas Fault near Parkfield, California, *Fall Meeting of the American Geophysical Union*, San Francisco (USA).

Weckmann, U., Ritter, O., Chen, X., **Tietze, K.**, & de Wit, M., 2010. Deep crustal structures of the Cape Fold Belt, South Africa, *Fall Meeting of the American Geophysical Union*, San Francisco (USA).

Tietze, K., Ritter, O., & Becken, M., 2010. Magnetotelluric 3D inversion models from the San Andreas Fault near Parkfield, California, *20th IAGA WG 1.2 Workshop on Electromagnetic Induction in the Earth*, Giza (Egypt).

Brändlein, D., Ritter, O., Weckmann, U., & **Tietze, K.**, 2010. A permanent array of magnetotelluric stations located at the South American subduction zone in Northern Chile, *20th IAGA WG 1.2 Workshop on Electromagnetic Induction in the Earth*, Giza (Egypt).

Brändlein, D., Ritter, O., Weckmann, U., & **Tietze, K.**, 2010. A permanent array of magnetotelluric stations located at the South American subduction zone in Northern Chile, *General Assembly European Geosciences Union*, Vienna (Austria).

Tietze, K., Ritter, O., Becken, M., Bedrosian, P. A., Weckmann, U., & Muñoz, G., 2010. Magnetotelluric 3D inversion models from the San Andreas Fault near Parkfield, California. *70th annual meeting of the German Geophysical Society (DGG)*, Bochum (Germany).

Becken, M., **Tietze, K.**, & Ritter, O., 2010. Source field effects in magnetic transfer functions?, *70th annual meeting of the German Geophysical Society (DGG)*, Bochum (Germany).

Brändlein, D., Ritter, O., Weckmann, U., & **Tietze, K.**, 2010. A permanent array of magnetotelluric stations located at the South American subduction zone in Northern Chile, *70th annual meeting of the German Geophysical Society (DGG)*, Bochum (Germany).

Chen, X., Weckmann, U., & **Tietze, K.**, 2010. From forward modelling of MT phases over 90° towards 2D anisotropic inversion, *70th annual meeting of the German Geophysical Society (DGG)*, Bochum (Germany).

Tietze, K., Ritter, O., & Weckmann, U., 2010. Substitute models for static shift in 2D, *Proceedings of the 23rd Schmucker-Weidelt-Colloquium on Electromagnetic Depth Sounding*, Seddiner See (Germany).

Chen, X., Weckmann, U., & **Tietze, K.**, 2010. From forward modelling of MT phases over 90° towards 2D anisotropic inversion, *Proceedings of the 23rd Schmucker-Weidelt-Colloquium on Electromagnetic Depth Sounding*, Seddiner See (Germany).

Ritter, O., Weckmann, U., & **Tietze, K.**, 2009. Electrical conductivity of the Cape Fold Belt, South Africa, *11th SAGA Biennial Technical Meeting and Exhibition 'Ancient Rocks to Modern Techniques'*, Swaziland.

Nube, A., Weckmann, U., Ritter, O., Chen, X., Deacon, J., MacLennan, S., Moodley, L., DeWit, M., Willkommen, G., Barth, R., Streich, R., & **Tietze, K.**, 2009. Magnetotelluric measurements across the southern Barberton greenstone belt: data analysis, *11th SAGA Biennial Technical Meeting and Exhibition 'Ancient Rocks to Modern Techniques'*, Swaziland.

Bibby, H. M., Heise, W., Bennie, S. L., Caldwell, T. G., Seebeck, H., **Tietze, K.**, Junge, A., & Cole, J. W., 2008. Investigation of an active caldera: magnetotelluric survey of Okataina Caldera, New Zealand, *19th IAGA WG 1.2 Workshop on Electromagnetic Induction in the Earth*, Beijing (China).

Tietze, K., Weckmann, U., Beerbaum, J., Hübert, J., & Ritter, O., 2008. MT measurements in the Cape Fold Belt, South Africa. *Proceedings of the 22nd Schmucker-Weidelt-Colloquium on Electromagnetic Depth Sounding*, Děčín (Czech Republic).

Weckmann, U., Jung, A., Branch, T., **Tietze, K.**, & Ritter, O., 2007. Electrical conductivity anomalies in the Namaqua Natal Mobile Belt and the Beattie magnetic anomaly: Do they have a common source?, *10th SAGA Biennial Technical Meeting and Exhibition*, Wild Coast Sun (South Africa).

Tietze, K., Bibby, H., Junge, A., & Bennie, S., 2006. A Magnetotelluric Profile Across the Eastern Rim of the Okataina Caldera, North Island, New Zealand, *18th IAGA WG 1.2 Workshop on Electromagnetic Induction in the Earth*, El Vendrell (Spain).

Erklärung

Hiermit versichere ich, dass ich die vorliegende Dissertation selbständig ohne Hilfe Dritter verfasst habe. Andere als die angegebenen Quellen und Hilfsmittel wurden nicht verwendet. Die den benutzten Quellen wörtlich oder dem Sinn nach entnommen Abschnitte sind als solche kenntlich gemacht. Dies gilt auch für Zeichnungen, Skizzen, bildliche Darstellungen und dergleichen, sowie für Quellen aus dem Internet. Die Dissertation hat in dieser oder ähnlicher Form weder ganz noch in Teilen einer in- oder ausländischen Hochschule zum Zwecke der Promotion vorgelegen.

Teile von Kapitel 3 wurden bei *Geophysical Journal International* eingereicht und sind zur Veröffentlichung akzeptiert unter Voraussetzung einer Überarbeitung des Manuskripts.

Teile von Kapitel 4 sind veröffentlicht in: Tietze, K., Ritter, O., & Weckmann, U., 2010. Substitute models for static shift in 2D, *Proceedings of the 23rd Schmucker-Weidelt-Colloquium on Electromagnetic Depth Sounding*, Seddiner See (Germany), ISSN 2190-7021.

Berlin, 14. November 2012 _____